Localized States in the Spacer Layer of Spintronic Nanodevices

THÈSE de DOCTORAT

pour obtenir le titre de
Docteur de l'Université de Strasbourg
Discipline/Spécialité: Physique

Université de Strasbourg
École Doctorale de Physique et Chimie-Physique (ED-182)
CNRS-Institut de Physique et Chimie des Matériaux de Strasbourg(IPCMS), UMR-7504

présentée par
KANDPAL Lalit Mohan

soutenue le : July 06, 2021

JURY :

DIRECTEUR de THÈSE:

Dr. BOWEN Martin	Directeur de Recherche, CNRS-Institut de Physique et Chimie des Matériaux de Strasbourg(IPCMS), et Université de Strasbourg

RAPPORTEURS:

Dr. GROLLIER Julie	Directrice de Recherche, Unité Mixte de Physique CNRS-Thales, et Université Paris Saclay
Dr. VUILLAUME Dominique	Directeur de Recherche, CNRS-Institut d'Électronique de Micro-électronique et de Nanotechnologie (IEMN), et Université de Lille

EXAMINATEUR :

Dr. FIX Thomas	Chargé de Recherche, CNRS-iCUBE et Université de Strasbourg

Acknowledgment

This thesis represents a long-held dream of mine to pursue my Ph.D. in cutting-edge experimental research, working on state-of-the-art research facilities, and learning the latest and upcoming technologies in the market. My heartfelt gratitude and thanks to Dr. Martin Bowen (Research Director, CNRS-IPCMS, University of Strasbourg, France), my doctoral advisor, for providing me the opportunity to work in his research team, believing in my abilities, fostering my potential, and guiding me to turn my dream into reality. I was not only benefitted from your deep knowledge of condensed matter physics and command on spintronics but also got the habit of seeing things critically, one of the essential qualities of a researcher. I thank you very much for organizing my lodging well in advance of my arrival in Strasbourg. Due to your friendly behavior and democratic values, I was able to develop a one-to-one relationship with you. The quality time that we spent in Luxembourg, Florence, and Uttarakhand further enriched this relationship. I shall remain indebted to you in my entire life for providing me an excellent Ph.D. training that certainly helped me to grow as an independent researcher. I would also like to thank my former head of the department (DMONS), Late Dr. Eric Beaurepaire (Research Director, CNRS-IPCMS, University of Strasbourg, France), a pioneer in ultrafast magnetism, for forwarding my profile to Martin for this Ph.D. position. Eric will always be remembered as a great scientist and a humble person. May his soul rest in peace!

My sincere thanks to Dr. Julie Grollier (Research Director, CNRS-Thales, University Paris-Saclay, France) and Dr. Dominique Vuillaume (Research Director, CNRS-IEMN, University of Lille, France), leading experts in inorganic and organic spintronics research, respectively for reviewing my Ph.D. thesis within the due time. I also thank Dr. Thomas Fix (Scientist, CNRS-ICUBE, University of Strasbourg, France), another jury member for his valuable comments on my thesis and for arranging my Ph.D. defense in due time. Thomas, your friendly advice on my remaining work to get published is invaluable. Thanks Martin for constituting such a high-level Ph.D. jury.

I recall my arrival in Strasbourg: It was Dr. Etienne Urbain (Ph.D. student in our research team), who came to receive me at Gare Centrale de Strasbourg. Thanks, Etienne! for welcoming me to the beautiful city of Strasbourg (Capitale de Noël and seat of the Européen Parliament). I started my Ph.D. working with Etienne to help him with his remaining experiments. My thanks to Dr. Filip Schleicher, a postdoctoral researcher and colleague of mine for introducing me to cleanroom processing. From Filip, I also learned the technicalities of the FERT setup, a magnetotransport measurement setup dedicated by Martin to his doctoral advisor Professor Albert Fert (Nobel prize winner in Physics, 2007). I found Filip a very supportive, warm, and social person. Thanks for helping us even when you had moved to Institute Jean Lamour, Nancy. Filip, I enjoyed working with you a lot. My special thanks to Dr. Jacek Arabski, a senior engineer in our research team, for his technical support on Ar^+ ion etching. Jacek was very friendly to all of us and would take care as a senior family member. Thank you for sharing your knowledge of French and Polish delicacies to me. I wish you a very happy and healthy post-retirement life.

I would also like to thank Dr. Fabrice Scheurer for the technical help in fixing the Auger electron detection assembly, attached in-situ with the Ar^+ ion etching system. Thanks to our team efforts (myself, Fabrice, and Martin) that we could be able to repair and use that Auger electron spectroscopy unit for almost next two more years. My sincere thanks to Professor Wolfgang Weber for providing your Auger electron spectroscopy unit when our Auger detector's Channeltron plate (electron multiplier) was almost dead. I appreciate your help highly. I am a great admirer of your deep knowledge of the subject, and sense of humor. I like the way you explain the toughest topics of physics in a very simple language. My gratitude and thanks to Dr. Samy Boukari for the wonderful scientific discussions and for helping me in some of the magnetotransport measurements performed on hybrid spintronic nanodevices. Your critical comments during the group meetings helped me a lot to grow scientifically. Thanks to our departmental (DMONS) engineers: Mr. Daniel Spor, Mr. Christophe Kieber, Mr. Benôite Leconte, Dr. Victor Da Costa, Mr. Manuel Acosta, and Dr. Benôite Gobaut for the technical help. Thank you Dr. Yves Henry for arranging basic necessities at the office.

Thanks to Dr. Kostantine Katcko (now at IMEC, Belgium), my colleague and a Ph.D. student in our research team for explaining the technicalities of multi-functional magnetotransport bench (BMF), capable to cool the sample down to 10K under the magnetic field of 2T with an added feature of optical excitation by an external LASER source. Thanks to Dr. Ufuk Halisdemir, a former Ph.D. student in our research team, and Martin for the automation of BMF, and for equipping it with an external LASER source. A big thanks to Dr. Beata Taudul (now at Sorbonne University, Paris) another Ph.D. student in our research team, for the DFT support on MgO-based spintronic research. You were always available to discuss the results, at prior short notice. Being a theoretician, your eagerness to understand the experiments and trying your best to implement those conditions in your calculations helped us to support our experiments well. I found you a very soft-spoken lady, willing to help without any expectations in return, and overall a good human being. I always enjoyed the scientific and general discussion with you. I also thank Mr. Franck Ngassam Nyakam, another Ph.D. student in our research team, and Professor Mébarek Alouani for the DFT support on organic spintronics research.

Since the experimental research work presented in this thesis is of very fundamental nature and at the same time has relevance in the spintronic industry, therefore necessitates a highly specialized international scientific collaboration. I thank our external collaborators for the first part of my thesis: Professor Michel Hehn, and his team (from Institute Jean Lamour, University of Lorraine, Nancy, France) for providing the MTJ stacks that were later processed by us into the microscale MTJ devices using the UV-photolithography technique at STnano cleanroom facility at my home institute CNRS-IPCMS, University of Strasbourg. These microscale UV-lithographically processed MTJ devices were subsequently measured on our multifunctional magnetotransport bench (BMF). Thanks to STnano cleanroom facility staff: Mr. Romain Bernard, Dr. Sabine Seigwald, and Dr. Hicham Majjad for providing me a solid training on cleanroom processing. Special thanks to Romain and Sabine for revealing me the hidden technicalities of cleanroom processing that can only be acquired after a large working experience. I learned a lot with you guys and on top of that, you never made me feel that I am away from my home. Thanks to the friendship that we developed over these years. I further extend my sincere thanks to Dr. Luc Thomas (TDK-Headway Inc., USA), Dr. Ricardo Ferreira, Dr. Tim Boehnert, and Professor Paulo Freitas (all three from International Iberian Nanotechnology Laboratory-Portugal), and Dr. Pranab Kishor Muduli (IIT-Delhi, India) for sending us the spin-transfer torque (STT) ready MgO-based nanopillar MTJ devices. We also received the STT ready nanopillar MTJ devices from Professor Johan Åkerman (University of Gothenburg, Sweden), however, due to the relatively lower resistance of these devices, we could not be able to achieve the objectives of our research project. Thanks, Johan for providing nanopillar MTJ devices to us. Thanks to Dr. Akash Kumar (now at the University of Gothenburg, Sweden) with whom I performed spin-torque ferromagnetic resonance (ST-FMR) experiments on nanopillar MTJ devices at Spin Dynamics Laboratory led by Dr. Pranab Kishor Muduli at IIT-Delhi. We used to have great time both in India and France. Thanks to Pranab and his team for providing great hospitality during our visit to IIT-Delhi. I also thank Ms. Pankhuri Gupta (IIT-Delhi) for helping us with additional ST-FMR data fitting. Thanks to Dr. Filip Schleicher, Dr. Elmer Nahuel Monteblanco, and Dr. Daniel Lacour (all three from Institute Jean Lamour, University of Lorraine, Nancy, France) for the transport measurements on TDK-Headway nanopillar MTJ devices. Thanks again Daniel for helping me with the theoretical calculations for the barrier heights (not included in this thesis) performed using your own developed computer code.

To reach our goals on the organic spintronics research, described in the second part of this thesis, our main concern was to protect the organic molecular layer used as a spacer between the two ferromagnetic (FM) electrodes in a trilayer stack from the resists and solvents being used during the conventional nanolithography process such as electron beam lithography. We, therefore, developed an alternative lithography process called 'nanobead processing' which is unique in the sense that there is no photoresist and solvent used, thanks to Etienne! for demonstrating this experimentally. To further refine the nanobead processing, I used atomic force microscope (AFM) nanomanipulations for controlling the number and the location of deposited silica nanobeads (used as a shadow mask). My sincere thanks to our internal collaborator Dr. Mircea Rastei (CNRS-IPCMS), for guiding me on AFM-nanomanipulation techniques and therefore helping me to achieve my objectives. Your dedication to both research and teaching motivates me a lot. I always saw you full of energy and warmness. In the nanobead processing, the size of the nanopillar is directly proportional to the diameter of the silica nanobead being used as a shadow mask during Ar^+-ion etching step, therefore, to achieve the desired size of nanopillar, I collaborated with Dr. Damien Mertz (CNRS-IPCMS) and was able to optimize the diameter of the silica nanobead from 100-500nm. Thanks a lot, Damien! for teaching me the 'surfactant mediated sol-gel reaction' to synthesize and subsequently optimizing the size of silica nanobeads, helping me in transmission electron microscopy (TEM) imaging, dynamic light scattering (DLS) measurements, UV-visible, zeta potential and Fourier transform infrared (FTIR) spectroscopy techniques. In addition to your scientific support, I also thank you for the moral support you provided me during my Ph.D. Thanks for being a good friend. Our discussions on science to societal issues during our travel from ‘Arago’ to ‘Gare Centrale’ in the bus-G, after office hours, also helped me a lot to learn from you. Sometimes when we had to work till late evening to finish our experiments; you had to run to catch your train, my sincere apologies for that!

AFM-nanomanipulation becomes a very time-consuming process when one has to implement this to craft the arrays of vertical junctions for example 21 junctions in a hybrid stack and 240 MTJs in a MgO-based inorganic stack, therefore I implemented another approach ‘microfluidic pen lithography technique’ proposed by my doctoral advisor Martin to me. Thanks Martin! for this awesome proposal. I would also like to extend my sincere thanks to Professor Bernard Doudin (CNRS-IPCMS) for providing me all the required equipment such as an optical bench, sample stage with two axis translation and an in plane rotation degrees of freedom, optical microscope with large working distance, digital camera with desired zoom, LED light source, microfluidic injector, micropipettes, and two mechanical manipulators with three axis translational and rotational degrees of freedom, to develop the ‘microfluidic pen lithography’ setup.

I would like to thank another Ph.D. student, Dr. Bhavishya Chowrira for a collaborative work on ‘spintronic/quantum engine’ (not included in this thesis). In addition to the nanofabrication work that I did on ‘spintronic/quantum engine’, I thank you Martin for choosing me for the measurement part carried out for this research at DEIMOS beamline at synchrotron SOLEIL, Paris. Thanks to our team efforts and technical assistance by DEIMOS staff: Dr. Philippe Ohresser, Dr. Edwige Otero, and Dr. Fadi Choueikani that made it possible to finish our measurements within the timeslot of 24X7 hours. Thanks to Dr. Loic Joly, and Elmer Nahuel Monteblanco, with whom I enjoyed working on night shifts. It was a great experience for me to work in such a state-of-the-art and one of the most advanced research facilities in the world. I thank the SOLEIL supporting staff for providing a nice accommodation inside the SOLEIL campus and delicious French meals during my stay there.

I must acknowledge my colleague and Ph.D. student, Dr. Sambit Mohapatra (now at C2N, Paris), for his help on AFM imaging at the beginning of my Ph.D.. It was nice to share an apartment with you during the ‘International School on Magnetism and Synchrotron Radiation 2018’, organized by Franco-German scientific collaboration at a picturesque village of ‘Mittelwihr’ located in a culturally rich Alsace region. I always enjoyed discussing various topics of scientific and societal importance with you. Thanks for providing me an intellectual company.

During my stay at Mittelwihr, I was able to interact with so many researchers and professors; one of them is Professor Stephen Blundell (Oxford University, United Kingdom), whose books on physics I used to read during my university courses/research work in India. Indeed it was a great honor for me that after my first interaction with Stephen, I used to be regularly invited by him for the dinner cum scientific discussion, during my stay at Mittelwihr. We would often go for the evening walks to the vineyards and forest nearby and discuss about latest scientific developments, geography, history, western classical music and cultures of Alsace and UK. Thanks, Stephen! for inspiring me to pursue a quality research work. Thanks again to Late Dr. Eric Beaurepaire for the foundation of this school. Thanks to Dr. Fabrice Scheurer for smooth running of this school in 2018. I would highly recommend this school to the Ph.D. fellows who are working on magnetism, spintronics and synchrotron radiation physics.

I would like to thank my dear friends from CNRS-IPCMS: Dr. Senthil Kumar Kuppuswamy, Dr. Matthieu Picher, Dr. Shyam Kanta Sinha, Dr. Garen Avedissian, Mr. Khaled Rassoul, Mr. Frank Ngassam Nyakam, Dr. Gladice Magnifouest Tchinda, Dr. Guillaume Chaumy, Dr. Dris Ihiawakrim, Dr. Nathaly Ortiz, Ms. Mariana Moreira, Ms. Vinavadini Ramnarain, Mr. Othman Darouich, Mr. Christian C. Carmona-Vargas, and Dr. Gisele Dalmônico, for the socio-cultural exchange, and for providing a great company during my Ph.D..

My sincere thanks to Ms. Véronique Wernher, Ms. Catherine Bonin, Ms. Sophie Siegel, Ms. Joelle Lacava, Mr. Miguel Monlouis, Mr. Ali Amir, Professor Aziz Dinia, and Dr. Pierre Rabu, for the administrative support during my Ph.D.. Thanks to ‘Indo-French Center for the Promotion of Advanced Research’/ ‘Center Franco-Indien pour la Promotion de la Recherche Avancée’ (IFCPAR/CEFIPRA) for funding my Ph.D. through ‘Campus France’.

Finally, I would like to thank my family: grandmother, mother, late father, elder sister, and younger brother, for all the necessary support they provided me to reach my goals. I can’t imagine this thesis without you! Thanks to my nephew for providing cheerful moments in between.

I dedicate this Ph.D. manuscript to my first and best ever friends: my beloved mother Mrs. Munni Kandpal and my late father Mr. Devaki Nandan Kandpal. Thanks for always inspiring us to become better human beings; what matters the most in the end.

“All truths are easy to understand once they are discovered; the point is to discover them.”

−Galileo Galilei

Contents

Résumé en Français

Partie I : Impact des États Localisés induits par la Vacance d'Oxygène sur le Couple de Transfert de Spin

Introduction

La découverte du spin de l'électron est considérée comme l'une des percées de la physique moderne qui a permis d'expliquer le phénomène du magnétisme et a ouvert la voie au développement de la physique quantique. Ces dernières années, le degré de liberté du spin de l'électron a été largement utilisé pour transporter l'information dans les dispositifs électroniques. Ces dispositifs électroniques complétés par un degré de liberté de spin électronique supplémentaire sont communément appelés dispositifs spintroniques[1].

Ces dispositifs spintroniques sont généralement des dispositifs à trois couches contenant deux électrodes ferromagnétiques (FM), séparées soit par une fine couche métallique non magnétique (NM), soit par une couche isolante/diélectrique. La première classe de dispositifs spintroniques est connue sous le nom de vanne de spin[2,3] tandis que la seconde est connue sous le nom de jonctions tunnel magnétiques (MTJ)[4–6]. Dans l'un ou l'autre de ces dispositifs spintroniques, la direction de magnétisation de l'une des électrodes FM est épinglée par une couche antiferromagnétique (AFM) sous-jacente de sorte qu'elle reste magnétiquement fixe tandis que l'autre électrode FM est autorisée à faire tourner sa direction de magnétisation sous un champ magnétique appliqué de l'extérieur. La première et la seconde électrode FM sont respectivement appelées couches fixe/référence et libre. Sous l'application d'un champ magnétique externe, l'alignement magnétique mutuel entre les deux électrodes FM peut ainsi passer d'un état parallèle (P) à un état antiparallèle (AP) ou vice-versa. Pour les spin-valves et les MTJ, les états/configurations magnétiques P (AP) offrent un chemin de résistance faible (élevé) aux électrons qui traversent le dispositif. Cette manipulation de la résistance due à un champ magnétique appliqué de l'extérieur à travers ces dispositifs spintroniques est appelée effet de magnétorésistance (MR) et plus spécifiquement magnétorésistance géante (GMR) et magnétorésistance à effet tunnel (TMR) pour les spin-valves et les MTJ, respectivement. Pour observer ces effets, la couche mince qui sépare les deux électrodes ferromagnétiques joue un rôle important. Dans les dispositifs à valve de spin, la fine couche métallique non magnétique offre une diffusion diffusive dépendant du spin, tandis que dans les MTJ, la fine couche isolante/diélectrique assure le filtrage de spin et de symétrie des électrons entrants polarisés en spin. Parmi les deux dispositifs spintroniques susmentionnés, les jonctions tunnel magnétiques (MTJ)[2,3], en raison de leur robustesse et de leur grande réponse[7,8] au champ magnétique appliqué[4,5], restent l'un des candidats les plus privilégiés pour les applications technologiques. L'effet TMR permet aux

MTJ de détecter un champ magnétique externe ou un élément d'information sous la forme d'un bit magnétique en commutant sa configuration magnétique mutuelle (P/AP) et de la convertir en un signal ou une sortie électrique. Contrairement à l'effet TMR, la configuration magnétique (P/AP) d'un MTJ peut également être commutée par un courant électrique appliqué à travers le dispositif. Ce phénomène est appelé effet de couple de transfert de spin (STT) [9,10]. Dans l'effet STT, un courant d'entrée d'une densité suffisamment élevée (J >10^7 A.cm^{-2})[9,10] après avoir traversé la couche ferromagnétique fixe (FM) constitutive d'un MTJ se polarise en spin avec un moment angulaire de spin non nul. Ce courant polarisé en spin, suivi d'un effet tunnel dépendant du spin à travers une fine couche isolante ou barrière tunnel, induit la précision de l'aimantation et transfère par conséquent le couple de spin sur l'aimantation de la couche ferromagnétique libre. En raison du transfert du couple de spin, la magnétisation de la couche ferromagnétique libre, en fonction de l'intensité du courant de commutation, soit : (a) précesser avec amortissement ou (b) précesser avec un grand angle en régime permanent ou (c) augmenter continuellement et rapidement l'angle de précession conduisant à une inversion magnétique[11,12]. Le scénario (b) trouve son application dans la génération ou la détection des signaux de radiofréquence dans le spectre des micro-ondes (gamme GHz) et les dispositifs utilisés pour cela sont appelés nano-oscillateurs à couple de spin (STNO), tandis que le scénario (c) est utilisé pour commuter la magnétisation de la couche libre et donc l'alignement magnétique mutuel de P à AP ou vice-versa dans un dispositif MTJ, remplissant ainsi le critère pour les mémoires magnétiques à accès aléatoire (MRAM)[13].

Ces dernières années, la recherche sur les STT a suscité un grand intérêt pour des applications de dispositifs stratégiques tels que la détection/perception de micro-ondes[12], les synapses artificielles[14], l'informatique neuromorphique[15] et les mémoires magnétiques à accès aléatoire (MRAM) de nouvelle génération[13]. Dans les MRAM à base de STT, l'exigence d'un courant électrique avec une densité suffisamment importante (~10^7 A.cm^{-2}) est généralement réalisée en abaissant la surface de section transversale de la MTJ dans le régime nanométrique, grâce aux techniques de nanolithographie de pointe qui ont rendu ce travail possible. Lorsque la section transversale du MTJ est réduite, le courant critique (I_C : la quantité de courant d'entrée nécessaire pour observer le STT) diminue également. Étant donné que la stabilité thermique d'une information stockée ou d'un bit dans un MTJ est déterminée par le rapport entre l'énergie d'anisotropie (k_u.V) et l'énergie thermique (k_B.T), la réduction de la section transversale entraîne une diminution de la stabilité thermique. Cette réduction de l'I_C par la diminution de l'aire de la section transversale du MTJ, coûte la stabilité thermique de l'information stockée surtout quand la constante d'anisotropie (k_u) de l'électrode ferromagnétique est petite. Pour un matériau ferromagnétique existant, k_u peut être augmenté en diminuant l'épaisseur et en transformant son anisotropie en anisotropie magnétique perpendiculaire (PMA). Le choix d'une électrode ferromagnétique PMA permet donc d'obtenir une stabilité thermique et une meilleure évolutivité mais coûte en I_C car l'augmentation de k_u augmente également le I_C.[16] Pour briser ce cercle vicieux, c'est-à-dire diminuer le I_C et améliorer la stabilité thermique simultanément dans les p-MTJ (où p- désigne l'anisotropie magnétique perpendiculaire), de nouveaux schémas tels que l'inclusion d'une double barrière[17] et d'un polariseur incliné[18] ont été proposés. Les performances spintroniques des MTJ ne dépendent pas seulement de l'électrode ferromagnétique, mais aussi de la qualité de la barrière à effet tunnel, et de l'interface entre la barrière à effet tunnel et l'électrode ferromagnétique. Les progrès réalisés jusqu'à présent dans la recherche sur les STT (mentionnés dans le paragraphe précédent) n'ont pas pris sérieusement en compte la qualité de la barrière à effet tunnel. De plus, il existe encore des énigmes non résolues dans la physique de la MTJ, par exemple la divergence entre la grande valeur TMR de 10000% prédite théoriquement[19] et la valeur TMR la plus élevée de 604% observée expérimentalement[7], le comportement métallique et semi-conducteur dissemblable dans le tracé courant-tension (I(V)) dans les états parallèle (P) et antiparallèle (AP) respectivement[20], qui n'a pas d'explication appropriée à ce jour. À partir des calculs théoriques effectués sur des MTJ d'une section transversale de 100x100 nm^2, Halisdemir et al. [21] ont révélé que même pour la barrière de MgO la plus fine d'une épaisseur de 0,7 nm, la densité de courant requise pour piloter le STT ne peut être atteinte que si les hauteurs de barrière sont bien inférieures à 3,9eV (la hauteur de barrière du MgO intrinsèque/libre de défauts/idéal). À partir des expériences de microscopie à force atomique à pointe conductrice (CT-AFM), les auteurs[21] ont conclu que la combinaison d'un TMR élevé et d'un produit R.A. faible, qui sont les exigences clés pour observer l'effet STT, est due à la réduction des hauteurs de barrière effectives offertes aux électrons de tunnel dans la couche de tunnel du MgO par les états localisés induits par la vacance d'oxygène. Ces résultats sont également soutenus par les rapports précédents[22–27] dans lesquels les hauteurs de barrière effectives extraites des mesures de magnétotransport effectuées sur les MTJ à base de MgO se sont avérées très faibles par rapport au MgO intrinsèque. De plus, la spectroscopie d'absorption des rayons X (XAS) ainsi que les mesures CT-AFM réalisées par Studniarek et al. [28] sur les MTJ à base de MgO ont révélé que les inhomogénéités structurelles dues aux lacunes d'oxygène dans le MgO entraînent une inhomogénéité du courant par effet tunnel sous la forme de points chauds de courant.

États localisés induits par la vacance de l'oxygène dans le MgO

En général, tous les processus de croissance de films minces sont enclins à former des défauts structurels dans l'échantillon, soit sous la forme de dislocations ou de vacances[29,30]. Comme décrit par Gibson et al. [31], les vacances d'oxygène présentent l'énergie de formation la plus faible, et sont donc plus susceptibles de se produire dans le MgO[32]. Les vacances d'oxygène sont formées par le défaut d'un ou deux atomes d'oxygène voisins les plus proches dans une cellule unitaire de MgO. Le premier état de défaut est connu sous le nom d'état de vacance d'oxygène simple ou centre F, tandis que le second est connu sous le nom d'état de vacance d'oxygène double ou centre F_2/M. Ces deux vides d'oxygène dans le MgO donnent lieu à des états localisés proches de l'énergie de Fermi (E_F) dans le diagramme de bande d'énergie. Le calcul théorique[32,33] a révélé que les M-centres produisent des états de liaison et d'anti-liaison M_1 et M_2-centres respectivement. D'après les rapports théoriques, le centre F isolé dans le MgO réduit la performance spintronique du dispositif MTJ[34,35] alors que les centres F voisins qui sont séparés les uns des autres par moins de 6Å, donnent lieu à un effet tunnel cohérent[36] améliorant ainsi la performance spintronique. Puisque les centres M sont formés par les deux vacances d'oxygène les plus proches séparées l'une de l'autre par une distance de ~3Å, ils sont donc supposés offrir un transport cohérent aux électrons à effet tunnel polarisés en spin éjectés des électrodes FM.

Certains rapports indiquent que pour un MTJ avec FeCoB comme électrodes FM et MgO comme barrière d'effet tunnel, les états d'énergie à 0,4eV, 0,7eV et 1,1eV en dessous de E_F dans le diagramme de bande d'énergie correspondent aux états M_2, F^{+*} (état F positivement excité) et F-centres, respectivement[26,37]. Cependant, les résultats théoriques combinés aux expériences ont révélé que ces états localisés sous E_F correspondent aux états M_2, F et M_1, respectivement[33,38]. Pour résoudre la divergence concernant les positions énergétiques exactes de ces états localisés sous E_F, nous avons réalisé une expérience dans laquelle nous avons modifié la fonction de travail de l'électrode FM supérieure en la remplaçant de CoFeB à FeB et caractérisé les états localisés en effectuant des mesures $\hat{I}$/TMRrel dans la fenêtre de température de 30K à 300K.

Technique expérimentale : Technique du $\hat{I}$/TMR

La beauté de la technique $\hat{I}$ est qu'elle ne fait aucune hypothèse sur le profil du potentiel de barrière ou la masse effective du porteur de charge. Au lieu de cela, elle examine la polarisation à laquelle la conduction activée thermiquement est maximale et attribue la position énergétique de l'état localisé à la différence d'énergie résultante par rapport à E_F. En termes pratiques, la technique $\hat{I}$ nécessite deux I(V) consécutifs réalisés à deux températures différentes T_1 et T_2 où $T_1 < T_2$. En utilisant la formule, $\hat{I}(V, T) = [\{I(V, T_2)/I(V, T_1)\} - 1]*100$ (%), $\hat{I}$ peut être tracé en fonction de la polarisation appliquée. $\hat{I}(V, T)$ attribue la position de polarisation des maximas dans $\hat{I}$ à la distance énergétique de E_F d'une caractéristique DOS qui a été activée thermiquement lors de l'augmentation de T de T_1 à T_2. La hauteur de barrière effective calculée à l'aide de cette technique est totalement indépendante de l'épaisseur de la barrière[39]. Contrairement aux modèles phénoménologiques (par exemple Simmons[40] ou Brinkman[41]), cette méthode physique de détermination des caractéristiques du paysage potentiel du MTJ ne fait aucune hypothèse concernant la dispersion effective de la masse ou de l'énergie du porteur de charge[39]. En raison du bruit associé aux $\hat{I}$ réalisées dans l'état P pour nos MTJ de 20μm de taille latérale, nous l'avons remplacé par $\mathrm{TMRrel}(V, T) = [\{\mathrm{TMR}(V, T_2)/\mathrm{TMR}(V, T_1)\} - 1]*100$ (%). Puisque la TMR est quantifiée par un changement relatif dans le courant parallèle sur le fond du courant dans l'état antiparallèle, donc lorsqu'elle est incorporée dans la TMRrel peut permettre de visualiser les caractéristiques spectroscopiques comparativement petites avec moins de bruit.

Résultats: Paysage énergétique exact des états localisés induits par la vacance d'oxygène

En remplaçant l'électrode supérieure de $Fe_{0.4}Co_{0.4}B_{0.2}$[26] par $Fe_{0.8}B_{0.2}$ (un matériau à fonction de travail plus élevée), nous avons constaté que tous les états énergétiques situés en dessous de l'E_F à

0,4, 0,8 et 1,1 eV se déplacent de 0,45 eV expérimentalement [voir Fig. 1], vers les énergies plus élevées par rapport à l'E_F[20]. Le décalage énergétique de 0,45 eV pour tous les états d'énergie est dû à la modification de l'énergie de Fermi par le remplacement de l'électrode supérieure. Afin de confirmer les résultats expérimentaux, des calculs DFT ont été effectués pour la situation où l'électrode supérieure a été remplacée de Fe à FeCo[33]. Un décalage de 0,25 eV vers l'E_F a été systématiquement prédit[20].

Les calculs théoriques sont en accord quantitatif raisonnable avec l'expérience. Cela confirme également que les états qui se trouvent sous la E_F à 0,4eV, 0,8eV et 1,1eV correspondent aux états M_2, F et M_1 et sont activés dans la plage d'énergie thermique de 250K < T, 80K < T < 250K et 80K < T < 30K, respectivement. Pris ensemble avec des recherches antérieures[26,33], ces résultats[20] révèlent que les centres F et M favorisent les barrières tunnel dominantes dans des plages de température spécifiques. De plus, les états localisés dus aux vacances d'oxygène (M_2, F, M_1) se situent en dessous de E_F, dans la bande de valence ; cela indique donc que l'effet tunnel est dû aux trous plutôt qu'aux électrons. Cette sous-section permet donc d'identifier les vacances individuelles et leur paysage énergétique, une condition préalable pour explorer l'impact de ces états de défaut sur le STT.

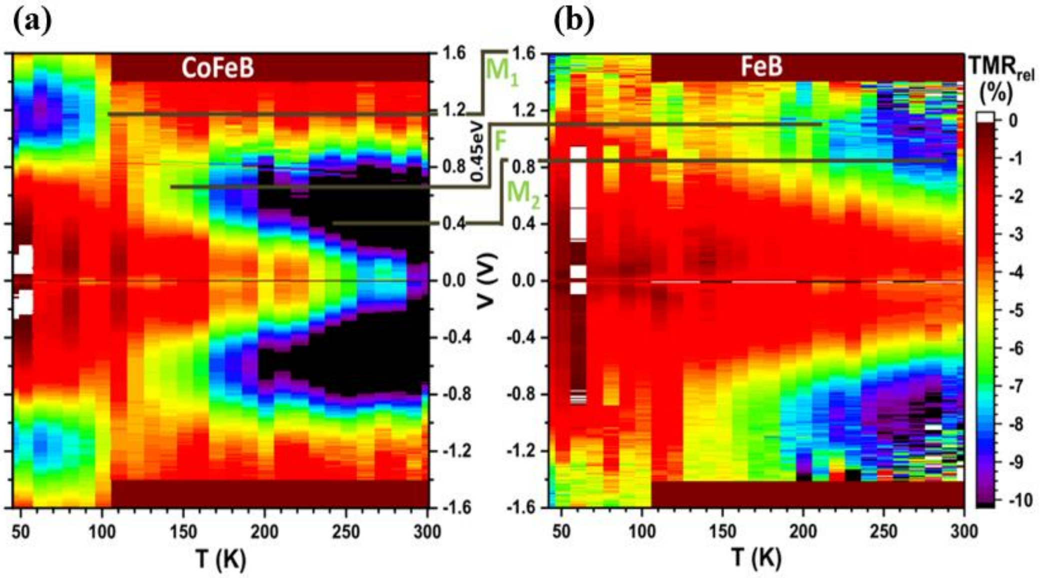

Figure 1. Tracés 3D de TMRrel pour les dispositifs MTJ avec l'électrode supérieure (a) CoFeB et **(b)** FeB. Les axes x, y et z représentent respectivement la température, la polarisation appliquée et l'amplitude du TMRrel. L'échelle de couleur représente l'axe z ou l'amplitude du TMRrel. Le déplacement de 0,45 eV dans les états occupés vers les valeurs d'énergie plus élevées par rapport à l'énergie de Fermi est évident lorsque l'électrode FM supérieure est remplacée par du FeB au lieu du FeCoB.[20]

A partir de calculs de densité de charge, Taudul et al.[33] ont révélé que les centres F et M (M_1 et M_2) ont respectivement des caractères de type p et s. Le consensus général concernant les vacances d'oxygène est qu'elles ont un impact négatif sur les performances spintroniques[23,34,42,43], mais les résultats théoriques[32,33] combinés aux mesures de magnétotransport réalisées[20,26] sur les

MTJ de 20 µm de large avec un produit R.A. ~10^8 Ω.µm^2 ont révélé que la présence des centres M_2 dans MgO améliore les performances spintroniques d'une MTJ. L'amélioration des performances spintroniques en présence du centre M_2 dans le MgO est due : i) à la diminution de la hauteur de barrière effective de 0,4eV, ii) à l'amélioration du filtrage de spin et de symétrie pour les Δ_1 (électrons majoritaires dans la configuration P de la MTJ) offerte par les états M_2 en raison de leur caractère s et iii) à une atténuation (κ) plus faible pour les électrons Δ_1 par rapport au MgO intrinsèque[33]. En réglant correctement les paramètres de croissance et de post-dépôt, on peut ajuster le rapport des vacances d'oxygène M/F dans le MgO et donc les performances spintroniques des dispositifs MTJ[33,37,43]. Comme mentionné précédemment, la pointe conductrice AFM ainsi que les mesures XAS[21,28] ont révélé que ces vacances d'oxygène produisent des points chauds de courant ou des canaux de nanotransport supplémentaires à travers la barrière tunnel de MgO, améliorant ainsi les performances spintroniques du dispositif MTJ. La contribution au transport de ces canaux de nanotransport devient très importante lorsque la taille du dispositif descend à l'échelle nanométrique. La taille des dispositifs STT se situant également à l'échelle nanométrique, il est donc très important, tant du point de vue de la physique fondamentale que de celui des applications technologiques, d'étudier précisément les états localisés dus aux lacunes d'oxygène et leur impact sur l'effet STT.

Résultats : Impact des états localisés induits par la vacance d'oxygène sur le couple de transfert de spin

Pour étudier l'impact de ces nanocanaux de transport dus aux lacunes d'oxygène sur le STT, des mesures de transport en fonction de la température ainsi que la technique $\hat{I}$[39] ont été réalisées sur les MTJs à l'échelle nanométrique façonnés sous forme de nanopilliers verticaux avec un produit R.A. ~20-30 Ω.µm^2 reçus en collaboration avec le professeur Paulo Freitas, INL Portugal et le Dr. Luc Thomas de TDK-Headway Inc. USA. Ces dispositifs MTJ à nanopiliers sont abrégés en MTJ-F et MTJ-H, respectivement. D'après les mesures de courant-tension (I(V)) effectuées sur les MTJ nanopiliers MTJ-F [voir Fig. 2], la commutation STT bistable a été observée de l'état P à l'état AP pour une polarisation négative appliquée et de l'état AP à l'état P pour une polarisation positive appliquée, sur la plage de température de 27K à 297K.

D'après la Fig. 2.a, deux points sont clairs : i) l'état P est " presque ohmique" avec un I(V) presque linéaire alors que l'état AP pour le même MTJ est " semi-conducteur", ii) lorsque la température augmente, on observe une réduction du courant critique (I_C) et de la tension critique (V_C) et iii) la réduction des paramètres STT (I_C, V_C et donc la densité de courant critique $J_C = I_C/A$) en fonction de la température n'est pas la même pour les commutations STT P > AP et AP > P. La Fig. 2.b est l'équivalent en résistance de la Fig. 2.a. Les deux régimes de transport différents à travers les MTJ nanopiliers, c'est-à-dire le transport " presque ohmique " et le transport " semi-conducteur ", ont également été observés dans les mesures I(V) [voir Fig. 3] et R(T) [voir Fig. 4] effectuées dans les états P et AP respectivement.

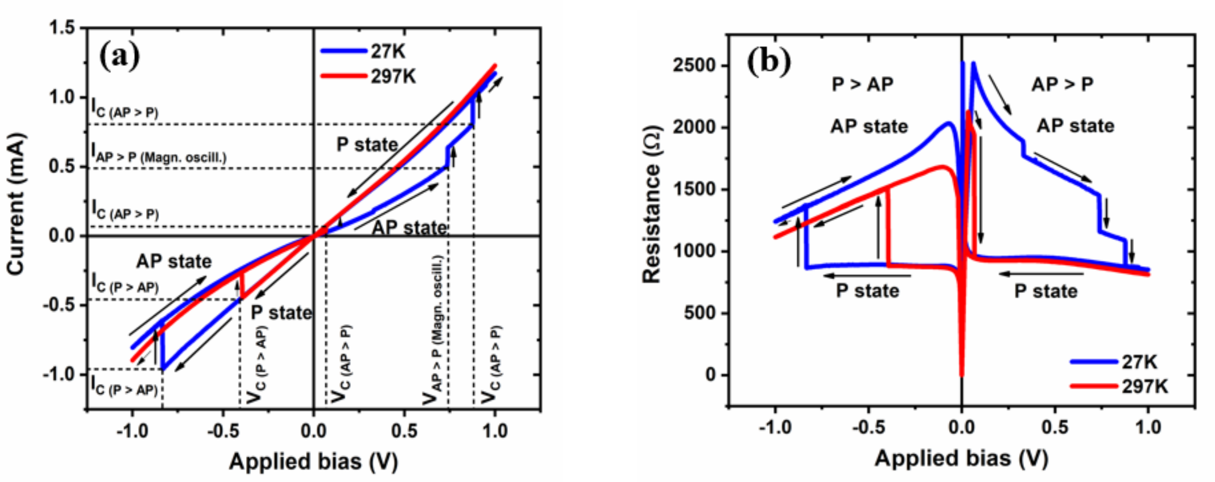

Figure 2. Commutation STT dans un dispositif MTJ-F à deux températures. (a) Tracé I(V) pour le dispositif MTJ-F à 27K (bleu) et 297K (rouge), **(b)** Tracé R(V) équivalent pour (a). Commutation STT de P > AP (AP > P) observée à une polarisation négative (positive) appliquée.

Les panneaux (a) et (b) de la Fig. 3 montrent les I(V)s réalisés dans l'état P (2000 Oe) et l'état AP (-200 Oe) représentant les régimes de transport "presque ohmique" et "semi-conducteur" des nanopiliers MTJ-Fs, respectivement.

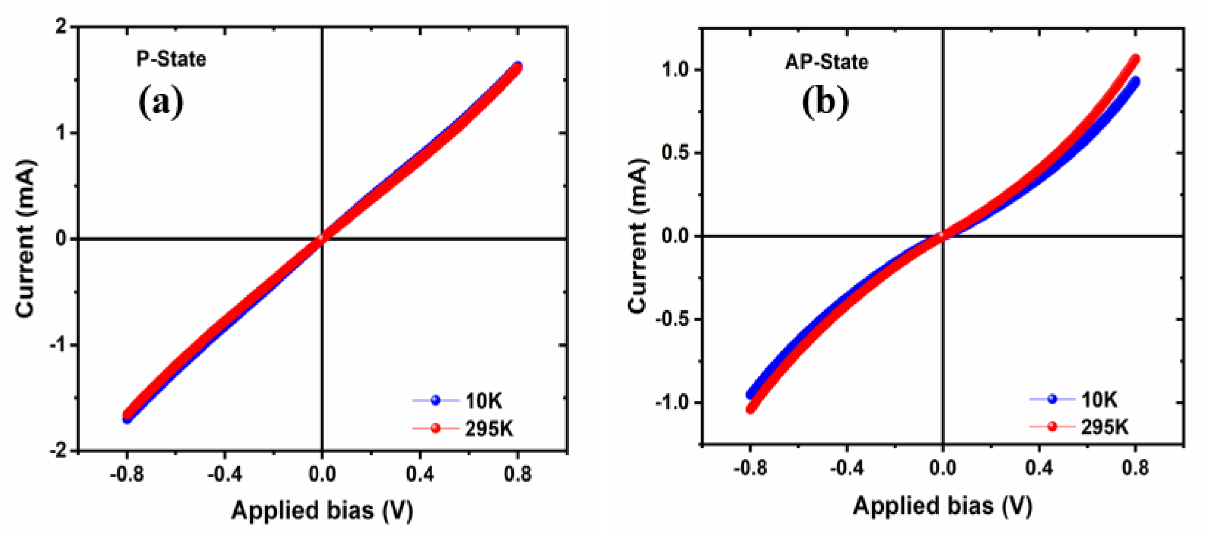

Figure 3. I(V)s réalisés pour le dispositif MTJ-F à, (a) l'état P (2000 Oe) et **(b)** l'état AP (-200 Oe). La courbe bleue (rouge) représente les mesures effectuées à 10K (295K).

La Fig. 4 montre la distribution de la résistance en fonction de la température pour les dispositifs nanopiliers MTJ-F et MTJ-H, confirmant les transports "presque ohmiques" [panneau (a)] et "semi-conducteurs" [panneau (b)] dans les états P et AP respectivement. Le transport "presque ohmique" dans l'état P pourrait être dû aux états Δ_1 disponibles au niveau de l'E_F.

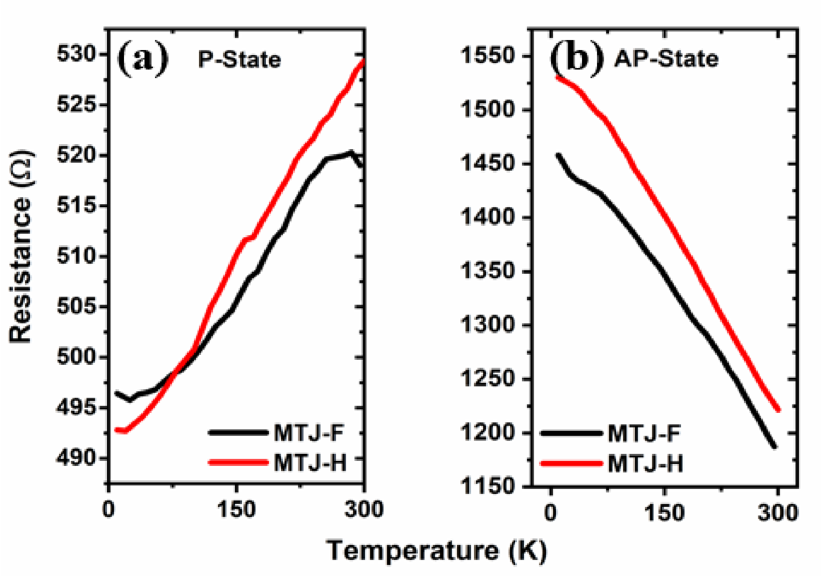

Figure 4. **Tracé de résistivité en fonction de la température mesurée à 100 mV de biais appliqué**, pour les dispositifs nanopiliers MTJ-F (noir) et MTJ-H (rouge) dans leurs états respectifs **(a)** P et **(b)** AP.

Afin d'explorer l'impact des états localisés induits par les vacances d'oxygène sur le STT, nous avons effectué des I(V)s à chaque pas de 10K sur la plage de température de 27K - 300K. La plage de température de 27K-300K fournit les énergies thermiques requises pour exciter les vacances d'oxygène M_2, F et M_1. La Fig. 5 montre la distribution en fonction de la température des paramètres STT (V_C, I_C et J_C) pour la commutation STT P>AP et AP>P, extraite des I(V)s en fonction de la température réalisés. Les messages importants sont i) La valeur de $|J_C|$ dépend fortement de la température. Lorsque la température augmente, $|J_C|$ diminue pour la commutation P > AP et AP > P. ii) Pour la commutation P > AP et AP > P, trois régions thermiques ont été observées, celle de 27K-77K (marquée par I), la deuxième de 77K-257K (marquée par II), et enfin la troisième de 257K-297K (marquée par la région III). La région I n'est pas affectée par la température, sauf une petite déviation pour la commutation P > AP dans la figure de gauche. La dépendance de la température de $|J_C|$ est évidente à partir de la région II. ii) A partir de la région II, la pente absolue, $|d|J_{C\,(AP > P)}|/dT|$ est plus grande que $|d|J_{C\,(P > AP)}|/dT|$. La pente absolue de $|J_C|$ devient plus importante dans la région III (à l'approche de la température ambiante).

Comme troisième point : iii) , nous observons que $|J_{C\,(P > AP)}| < |J_{C\,(AP > P)}|$ après 77K. À 27K, les valeurs de $|J_{C\,(P > AP)}|$ et $|J_{C\,(AP > P)}|$ ont été mesurées respectivement à 2,922x10^6 A/cm^2 et 2,857x10^6 A/cm^2, ce qui indique qu'il n'y a pas de différence significative entre la commutation P > AP et AP > P. La différence de $|J_C|$ pour la commutation P > AP et AP > P devient plus significative à T = 297K, avec les valeurs mesurées de $|J_{C\,(P > AP)}|$ et $|J_{C\,(AP > P)}|$ de 1,458x10^6 A/cm^2 et 9,696x10^4 A/cm^2 respectivement. Nous observons une différence marquée dans la dépendance de la température entre $|J_{C\,(P > AP)}|$ et $|J_{C\,(AP > P)}|$. Alors que $|J_{C\,(P > AP)}|$ diminue d'un facteur ~3 entre 27K et 297K, $|J_{C\,(AP > P)}|$ diminue d'un facteur 30.

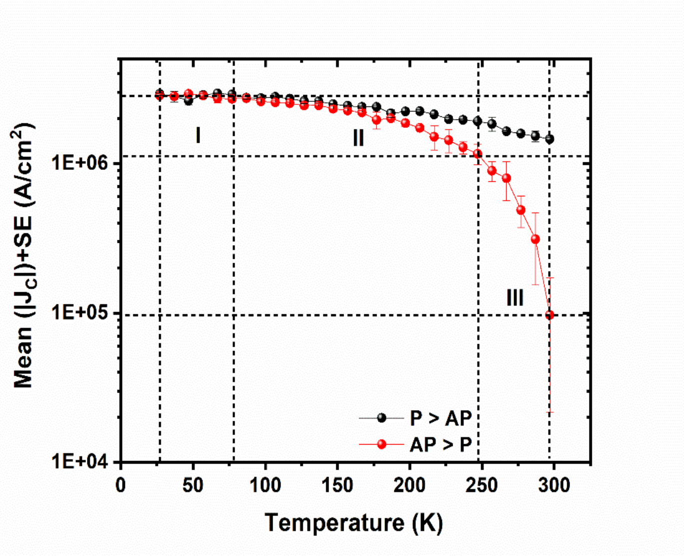

Figure 5. Tracé de la densité de courant critique |J_C| pour les dispositifs MTJ-F à **(a)** P > AP, **(b)** AP > P, commutation STT.

La caractéristique commune du |J_C| dépendant de la température est qu'il diminue avec l'augmentation de la température pour la commutation STT P>AP et AP>P après 77K. A première vue, on pourrait penser que les états localisés induits par la vacance d'oxygène sont activés aux énergies thermiques correspondantes et qu'en abaissant la hauteur de la barrière, on diminue l'exigence de J_C pour la commutation STT. Cependant, cette hypothèse ne correspond pas au régime de transport 'presque ohmique' et 'semi-conducteur' observé dans les états P et AP respectivement, ce qui indique que les états disponibles pour les électrons Δ_1 à E_F sont présents uniquement dans l'état P. Puisque J_C est directement proportionnel à l'énergie d'anisotropie magnétique (E) des électrodes FM, décrit mathématiquement par la formule: $J_C = 2\alpha\gamma eE.t/\mu_B.g(P,\eta)$ et que E varie avec la température par une tendance similaire, nous nous référons donc que la variation de J_C en fonction de la température est due à l'anisotropie magnétique des électrodes FM. Cependant, cela n'explique pas la différence observée dans les valeurs de J_C pour la commutation P>AP.

Afin de caractériser les états localisés dus aux lacunes d'oxygène dans les MTJ nanopiliers, nous avons effectué une spectroscopie $\hat{I}$ et une résonance ferromagnétique à couple de spin (ST-FMR) [voir Fig. 6]. Le panneau (a) de la Fig. 6 montre les spectres $\hat{I}$ du dispositif nanopillaire MTJ-H. Nous observons que l'amplitude de la résonance ferromagnétique de spin-torque est très faible. Nous observons que l'amplitude de la $\hat{I}$(V, T) est négative pour l'état P alors qu'elle est positive pour l'état AP. Ceci confirme expérimentalement que le transport dans l'état P est "presque ohmique" alors que dans l'état AP il est "semi-conducteur". De plus, dans l'état P, les larges pics d'états localisés apparaissent initialement à 0,6V, se déplacent vers 0,4V sous E_F à température ambiante et leur queue se croise à EF. Ces caractéristiques n'apparaissent que pour l'état P plutôt que pour l'état AP. Les dispositifs MTJ-F avec un produit R.A. presque similaire, mesuré par la technique ST-FMR à température ambiante, ont révélé que le rapport entre le couple hors du plan et le couple dans le plan présente également un large pic centré à 0,4 V. L'origine de ce pic n'est cependant pas claire. L'origine de ce pic n'est cependant pas bien comprise mais présente une caractéristique similaire de $\hat{I}$s à l'état P.

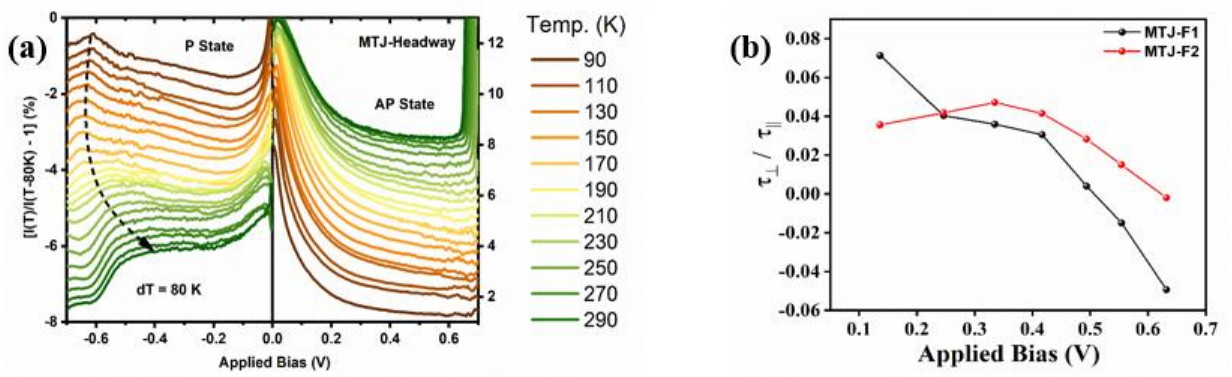

Figure 6. (a) Tracés I-hat ($\hat{I}$-) plots calculés à partir de I(V)s consécutifs réalisés à $\Delta T = T_2 - T_1 = 80K$, à l'état P (à gauche) et à l'état AP (à droite) pour le dispositif MTJ-H. Le grand saut dans $\hat{I}_{AP}$ (V>0) est dû à l'effet STT lui-même. **(b) Rapport du couple hors plan sur le couple dans le plan** (calculé à partir du rapport de torkance respectif) par rapport à la polarisation appliquée pour les dispositifs MTJ-F1 (noir) et MTJ-F2 (rouge).

Pour confirmer nos résultats expérimentaux, nous avons effectué des calculs DFT sur un système Fe|MgO|Fe assez simple. L'épaisseur du MgO a été maintenue à 5ML, ce qui correspond bien à la valeur expérimentale de 0,6-0,9 nm. Afin d'exclure toute possibilité d'états lacunaires induits par le métal (MIGS) dans le MgO en raison de l'électrode Fe provoquant un transport "presque ohmique" dans l'état P, les calculs de densité d'états (DOS) ont été effectués pour ladite MTJ avec du MgO intrinsèque/libre de défauts. Pour les MTJs Fe|MgO(5ML)|Fe avec MgO sans défaut, les MIGS se sont avérés être présents seulement jusqu'au 2ème ML de MgO à partir de l'interface Fe|MgO. L'absence de MIGS au 3ème ML de MgO à partir de l'une ou l'autre des interfaces Fe|MgO ne fournit donc pas le chemin de connexion le moins résistif aux électrons par effet tunnel pour présenter un transport "presque ohmique".

En se référant aux diagrammes $\hat{I}$ [Fig. 6.a], les larges pics $\hat{I}$ qui se déplacent également vers E_F indiquent que les états d'énergie localisés induits par la vacance d'oxygène ne sont pas isolés mais interagissent entre eux. De plus, les états localisés induits par la vacance d'oxygène ne sont pas à l'E_F et ne peuvent donc pas expliquer le transport "presque ohmique" observé dans l'état P d'une MTJ. Nous avons donc testé l'hypothèse selon laquelle l'hybridation de plusieurs vides d'oxygène élargirait l'état fondamental d'antibondage M_2 du vide d'oxygène double (à ~0,4eV en dessous de l'E_F pour les électrodes FeCoB), de sorte qu'une queue d'états intersecterait l'E_F. Nous avons donc envisagé une chaîne en zig-zag de lacunes d'oxygène (ZZCOV) couvrant la jonction [voir la Fig. 7.a]. Cela correspondrait également à la description d'un hotspot à l'échelle nanométrique, comme en témoignent les expériences CT-AFM[28,44]. La Fig. 7.b montre les tracés DOS zoomés à l'état P pour la MTJ Fe(1-4ML)|MgO(5ML)|Fe(5-7ML) à 3 ML de MgO près de E_F sans (lignes solides) et avec (lignes pointillées) ZZCOV. D'après la Fig. 7.b, sans ZZCOV, le DOS à E_F est presque nul, et en incorporant ZZCOV, le DOS à E_F augmente significativement. Cela suggère un transport amélioré et donc un transport "presque ohmique" dans l'état P de nos dispositifs MTJ.

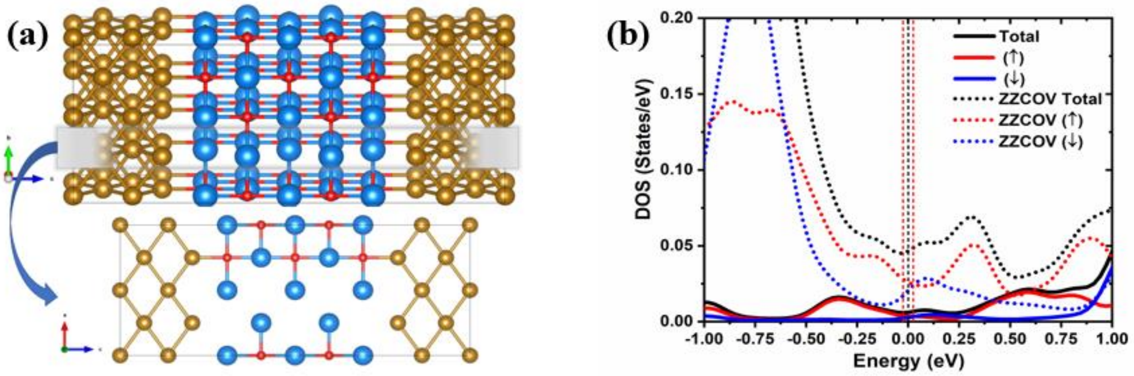

Figure 7. (a) Chaîne en zigzag d'une vacance d'oxygène unique (ZZCOV) introduite dans la couche à effet tunnel de MgO de 5 ML d'épaisseur prise en sandwich entre les électrodes de Fe, et **(b) tracés DOS** d'une MTJ Fe(1-4ML)|MgO(5ML)|Fe(5-7ML) à 3 ML de MgO avec du MgO idéal/sans défaut (lignes solides) et du MgO avec ZZCOV (lignes en pointillés courts) à l'état P.

Afin de confirmer davantage les deux types de transport distincts observés, c'est-à-dire "presque ohmique" et "semi-conducteur" dans les états P et AP, respectivement, les calculs de densité de charge ont également été effectués pour les MTJ Fe|MgO(5ML)|Fe avec ZZCOV dans MgO [voir Fig. 8, 9]. En comparant les Fig. 8.a et 8.b, il est très clair que la densité de charge des électrons majoritaires (vers le haut) dans l'ensemble de la monocouche de MgO 5ML est assez élevée par rapport aux électrons minoritaires (vers le bas) dans l'état P, ce qui suggère un transport "quasi-ohmique" pour les électrons majoritaires (vers le haut) dans l'état P. La densité de charge plus faible pour les électrons minoritaires (vers le bas) dans l'état P est très élevée. La densité de charge réduite pour les électrons minoritaires (descendants) dans les 5ML de MgO à l'état P fait référence au transport "semi-conducteur" pour les électrons respectifs dans leur état magnétique respectif. Le tracé de la densité de charge pour les électrons minoritaires dans l'état P ne semble pas être cohérent avec les tracés DOS [Fig.8.b]. Cette incohérence pour les électrons minoritaires pourrait être due à la rupture de la symétrie par l'incorporation de ZZCOV dans la couche tunnel de MgO.

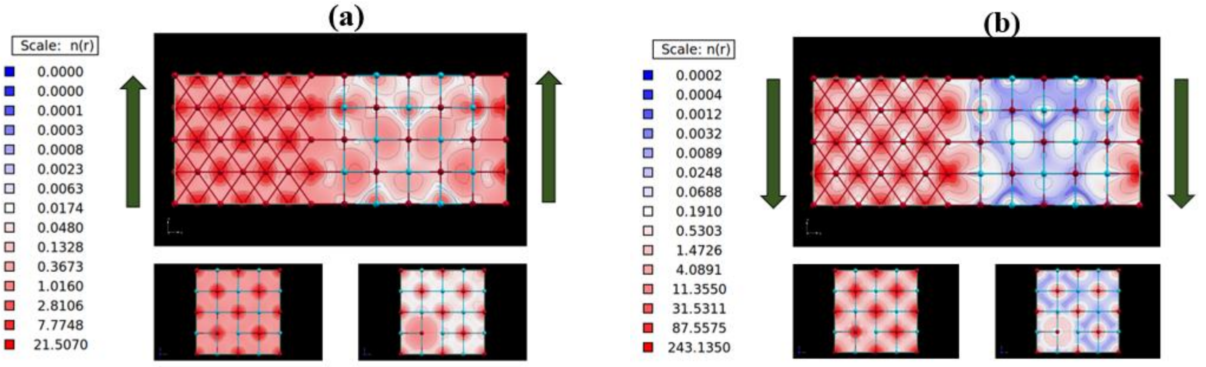

Figure 8. Tracés de densité de charge calculés pour la MTJ Fe|MgO(5ML)|Fe avec la chaîne de vacances F-oxygène dans la barrière à effet tunnel MgO pour **(a)** les électrons de spin supérieur majoritaires et **(b)** les électrons de spin inférieur minoritaires, à l'état P.

Les Fig. 9.a et 9.b représentent les tracés de densité de charge calculés pour les électrons de spin majoritaire (haut) et minoritaire (bas) respectivement dans leur état AP. En partant du côté gauche, les premiers 3ML correspondent à l'électrode de Fe, les 5ML suivants au MgO, et les 3ML à l'extrême droite correspondent à l'électrode de Fe droite. En raison des conditions limites périodiques prises en considération, le nombre de monocouches de Fe après l'interface MgO n'affecte pas les calculs de densité de charge.

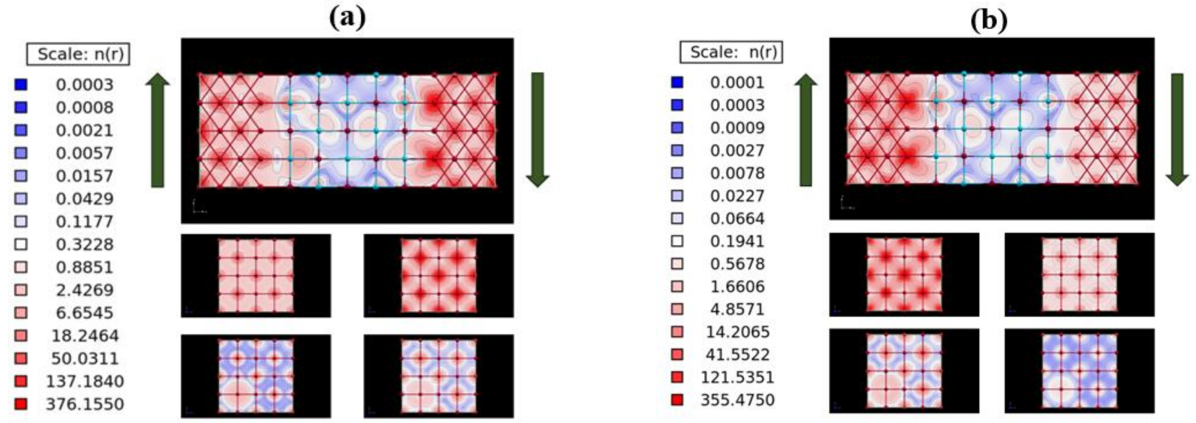

Figure 9. Tracés de densité de charge calculés pour la MTJ Fe|MgO(5ML)|Fe avec la chaîne de vacances F-oxygène dans la barrière à effet tunnel MgO pour **(a)** les électrons de spin supérieur majoritaires et **(b)** les électrons de spin inférieur minoritaires, dans l'état AP.

Pour les Fig.9.a et b, en descendant vers la structure supercellulaire, dans la première rangée, le panneau de gauche représente la densité de charge du Fe gauche, et le panneau de droite représente la monocouche de Fe droite à l'interface du MgO. Tandis que dans la dernière rangée vers le bas, le panneau de gauche est pour la densité de charge de la monocouche de MgO gauche, et le panneau de droite est pour la monocouche de MgO droite à l'interface. D'après les deux structures supercellulaires pour les électrons majoritaires (vers le haut) et minoritaires (vers le bas) dans leur état AP, la densité de charge dans la couche à effet tunnel de MgO est trop faible, ce qui montre le comportement semi-conducteur du MTJ dans l'état AP.

Conclusion partielle

Dans la première partie de cette thèse, nous avons étudié expérimentalement l'impact des lacunes d'oxygène sur le STT dans nos dispositifs MTJ nanopillaires obtenus auprès de deux laboratoires différents. Nous avons également effectué des calculs ab-initio pour expliquer nos résultats. En rassemblant ces données, nous avons dressé le tableau suivant du magnétotransport à travers les nano-MTJ de MgO qui présentent un STT.

Nous avons tenté d'interpréter le transport "presque ohmique" dans l'état P du MTJ, et "semi-conducteur" dans l'état AP, comme résultant d'un point chaud à l'échelle nanométrique constitué d'une chaîne en zigzag de lacunes d'oxygène (ZZCOV). Ce nanoobjet génère un DOS sur chacune des barrières de MgO de 5ML d'épaisseur à $E-E_F < -0,4$eV qui peut expliquer les caractéristiques spectroscopiques expérimentales trouvées dans les données $\hat{I}$- et ST-FMR : a) la chute plus prononcée de l'amplitude négative de $\hat{I}$ dans l'état P du MTJ ; et b) le changement de la tendance du rapport de couple (dérivé du rapport de torkance). Ce DOS croise E_F et est beaucoup plus fort que tout DOS résiduel induit par MIGS. Cela peut expliquer le comportement de transport "presque ohmique".

Nous ne sommes pas en mesure d'expliquer de manière élégante pourquoi le ZZCOV génère un comportement "presque ohmique" pour l'état P de la MTJ et non pour l'état AP. En effet, le DOS apparaît à E_F pour les deux états magnétiques des MTJ. L'explication de la symétrie est impossible car le ZZCOV brise la représentation du groupe de symétrie. Néanmoins, les tracés de transmission révèlent une transmission P beaucoup plus importante que pour l'état AP (non montré ici, pour plus de détails voir le chapitre correspondant). De plus, la transmission pour AP s'effectue le long d'une direction X-K diffuse, alors que la transmission P se produit principalement au point X. Il est possible que cela génère une plus grande quantité d'énergie dans la transmission. Il est possible que cela génère un transport plus diffus dans l'état AP, qui serait thermiquement activé (non montré ici, pour plus de détails, voir le chapitre correspondant). Cela expliquerait le $\hat{I}$- positif et les données R(T) semi-conductrices. Cela pourrait également expliquer l'énergie d'activation thermique supérieure d'un ordre de grandeur à la température élevée de l'effet STT AP > P par rapport à l'effet STT P > AP. En d'autres termes, cela pourrait expliquer la diminution de l'ordre de grandeur de la densité de courant critique de l'effet AP > P STT. L'effet P > AP STT diminue beaucoup plus faiblement avec l'augmentation de la température car cette diffusion est beaucoup plus atténuée. La transmission calculée donne une valeur TMR de 106% qui est proche des valeurs expérimentales de 136% à 297K. Pour conclure, l'image dominante est que le produit R.A. faible et le TMR élevé qui sont les conditions clés pour l'effet de couple de transfert de spin (STT) sont les résultats de trous d'épingle/états de vide induits par le métal. Notre travail révèle qu'il s'agit plus probablement du résultat d'une voie de nanotransport telle qu'une chaîne en zigzag de lacunes d'oxygène (ZZCOV) qui traverse la barrière de MgO de la jonction. Cette explication rend compte de manière satisfaisante de presque toutes les observations expérimentales (magnétotransport, ST-FMR), en conjonction avec les calculs DFT. Nous espérons que nos résultats et la lacune de cette étude encourageront les chercheurs de l'industrie et de l'université à explorer davantage les vacances d'oxygène et leur impact sur la STT.

Partie II: Spintronique à travers les Nanodispositifs Inorganiques-Organiques ou Hybrides

La deuxième partie de cette thèse traite des dispositifs spintroniques inorganiques-organiques ou hybrides. Ces dispositifs comprennent une couche d'espacement moléculaire organique prise en sandwich entre les deux électrodes ferromagnétiques inorganiques. L'intérêt pour la spintronique organique ou moléculaire vient de l'attente que, en raison du faible couplage spin-orbite[45] et du transport électronique à travers les orbitales π-délocalisées[46,47], ces espaceurs organiques peuvent favoriser un grand temps de relaxation du spin (plusieurs ordres de grandeur par rapport aux espaceurs inorganiques), ce qui est une clé pour préserver la polarisation du spin sur de grandes distances. Outre l'amélioration des performances de la spintronique, l'incorporation de molécules organiques dans les dispositifs spintroniques apporte de nombreux avantages pratiques tels que la flexibilité, la possibilité de fabriquer des dispositifs polyvalents en utilisant le génie chimique, et le faible coût qui est un facteur crucial pour la commercialisation des dispositifs[46].

Introduction

Le premier dispositif spintronique hybride à géométrie latérale présentant des propriétés de soupape de spin avec un MR négatif a été démontré par Alek Dediu[45] en 2002. En 2010, Barraud et al. ont rapporté des dispositifs hybrides verticaux de quelques dizaines de nm^2 de taille, en utilisant la technique de nanoindentation basée sur l'AFM avec 300% de MR positif à 2 K[46]. Le signe du MR observé indiquait que le transfert de charge polarisé en spin à l'interface métal/molécule ferromagnétique pouvait provoquer un changement du signe de la polarisation en spin (P). Cela a été confirmé par des expériences ultérieures[48–50], qui ont également révélé que cette P pouvait être très grande[51] à/au-delà de la température ambiante. Ces effets interfaciaux sont surnommés "spinterface"[52,53].

L'inversion, et les très grandes valeurs de P, observées pour la "spinterface" peuvent être comprises par le fait que la molécule isolée avec des niveaux d'énergie discrets, lorsqu'elle est adsorbée sur un métal FM, s'hybride avec les états d'énergie du métal FM. Cette hybridation fournit une durée de vie finie (τ) aux niveaux moléculaires avec une certaine probabilité de s'échapper vers le métal, conduisant à l'élargissement (Γ) dans les niveaux d'énergie qui peut être quantifié à partir du principe d'incertitude d'Heisenberg ($\Gamma \geq \hbar/2\tau$). De plus, le niveau d'énergie du côté moléculaire se déplace de l'énergie du vide ε_0 à $\varepsilon_{\mathrm{eff}}$. Selon la force de couplage, l'élargissement des niveaux d'énergie peut être compris entre meV et eV. En première approximation, cet élargissement est directement proportionnel à la densité d'états (DOS) du métal FM. Pour les métaux FM, il y a toujours un déséquilibre dans la DOS résolue en spin pour les porteurs de charge, donc le décalage des niveaux d'énergie et l'élargissement du niveau d'énergie sont inégaux pour les niveaux d'énergie de spin haut et bas.

La polarisation de spin effective (P_{int}), de ce système ou de la "spinterface" est une somme de la polarisation de spin du métal FM et de la première monocouche. En considérant les deux scénarios (i) lorsque $\Gamma \gg \Delta E$, où $\Delta E = E_F - \varepsilon_{eff}$, est la position énergétique par rapport à l'énergie de Fermi, conduit à l'inversion de la polarisation de spin du métal ferromagnétique alors que (ii) lorsque $\Gamma \ll \Delta E$, conduit à la très grande MR. Les scénarios susmentionnés suggèrent que la polarisation de spin de la "spinterface" dépend fortement de l'hybridation dépendant du spin et que l'on peut accorder la polarisation de spin avec la force de couplage entre le métal FM et la molécule organique. [54] Il a été observé que la première monocouche se couple fortement à la "spinterface" via un échange ferromagnétique conduisant à l'effet de durcissement magnétique[55]. Serri et al.

ont signalé un fort couplage antiferromagnétique dans la couche moléculaire de CoPc avec une énergie d'échange de 100 K[56]. Une étude comparative dans les bicouches Co|MPc en sélectionnant l'ion métallique pour former la chaîne de spin a été rapportée par Boukari et al. a révélé qu'en augmentant le moment magnétique de l'atome M central dans la couche MPc, une amélioration sur le biais d'échange a été observée.[55]

Barraud et al. ont également rapporté les premières expériences sur l'impact des chaînes de spin moléculaires portées par les molécules de phtalocyanine métallique sur le transport polarisé en spin[57,58]. Ce travail a introduit les notions de spectroscopie de spin-flip[59], normalement étudiées dans des jonctions modèles assemblées à l'aide d'un STM, aux dispositifs à l'état solide. En effet, ils ont lié les augmentations de conductance observées à l'ouverture d'un canal de courant dû aux excitations de spin. Pourtant, bien que ce canal de courant supplémentaire soit censé être entièrement polarisé en spin en raison des règles de transition[60], l'impact sur le MR n'a pas été discuté.

Nous avons étendu ce travail aux dispositifs verticaux d'un diamètre de 500 nm qui ont été fabriqués à partir de l'empilement de tricouches Fe|CoPc|Co (de bas en haut) cultivé in-situ. Des techniques conventionnelles de nanolithographie sont utilisées pour fabriquer des nanopiliers verticaux avec l'utilisation de solvants qui peuvent dégrader la couche moléculaire. Une grande partie de cette thèse expérimentale a donc été consacrée à l'amélioration d'une technique de lithographie alternative[61] basée sur la lithographie de nanosphères[62]. Dans cette technique de lithographie alternative que nous appelons le 'traitement des nanobilles', des nanobilles de silice sont utilisées comme masque d'ombre pour définir les nanopiliers, en dessous. La motivation derrière le développement du "procédé nanobille" était de protéger la couche d'espacement organique de l'empilement hybride à trois couches de la résine photosensible et des solvants organiques (couramment utilisés dans les techniques de nanolithographie standard telles que la lithographie par faisceau d'électrons et les techniques de nanoindentation basées sur l'AFM).

Technique expérimentale utilisée pour réaliser des dispositifs spintroniques hybrides à base de nanopilliers: Traitement des nanobilles

Pour définir les dispositifs spintroniques à nanopiliers verticaux, le "traitement des nanobilles" se compose de quatre étapes. Dans la première étape, les nanobilles de silice sont dispersées sur la surface supérieure de la couche de recouvrement d'un empilement hybride. Le dépôt de ces nanobilles de silice sur la surface supérieure d'un empilement hybride à trois couches peut être réalisé soit par des impulsions ultrasoniques suivies de "nanomanipulations au microscope à force atomique (AFM)" (le long des directions latérales dans le plan), soit par des techniques de "lithographie microfluidique au stylo" (avec des gouttelettes très localisées d'un volume de picolitre d'éthanol contenant des nanobilles de silice). Les nanomanipulations AFM et la technique de lithographie par stylo microfluidique permettent un meilleur contrôle de l'emplacement précis et de la concentration des nanobilles à déposer. Dans la deuxième étape de la lithographie, la gravure sèche contrôlée (fraisage par ions Ar^+, suivi par spectroscopie électronique Auger in situ) préserve la structure sous les nanobilles de silice et transforme ainsi l'empilement de tricouches hybrides en un réseau de nanopiliers verticaux.

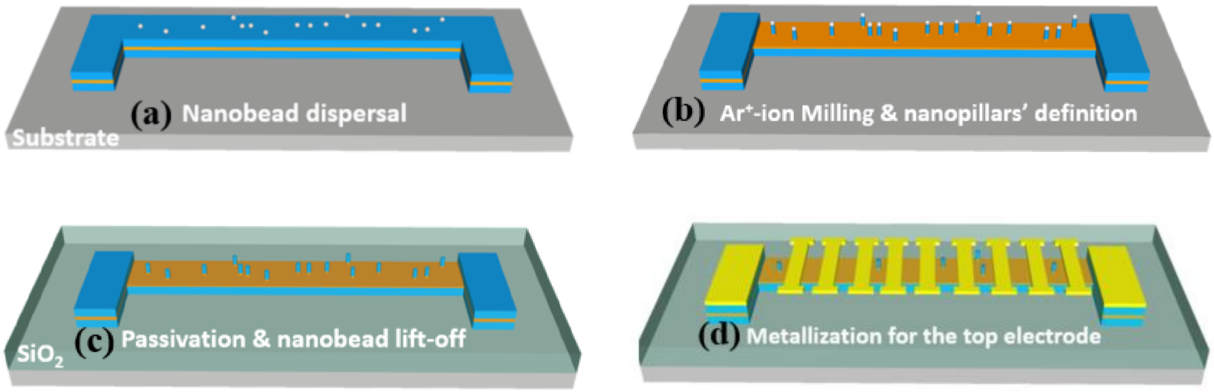

Figure 10. Présentation schématique du processus des nanobilles. (a) Étape I : dispersion de nanobilles de silice sur la surface supérieure de l'empilement de tricouches hybrides, ces nanobilles de silice servent de masque d'ombre pour l'étape II, **(b)** Étape II : étape de gravure par ions Ar^+ pour fabriquer les nanopiliers, **(c)** Étape III : étape de décollement des nanobilles et de passivation pour encapsuler les nanopiliers, **(d)** Étape IV : étape de métallisation pour déposer les électrodes supérieures.[63]

Pour protéger les nanopilliers verticaux gravés contre les courts-circuits, un mince film de silice servant de couche de passivation est déposé lors de la troisième étape du traitement des nanobilles. L'épaisseur de la couche de passivation est maintenue plus petite que le rayon des nanobilles de silice de sorte que les nanobilles de silice puissent être facilement soufflées par le jet de gaz Argon pendant le processus de décollage à sec. Dans la quatrième étape, des électrodes en or sont déposées pour réaliser des contacts supérieurs. Après avoir effectué un traitement des nanobilles en quatre étapes, les nanopiliers hybrides sont maintenant prêts à être mesurés. Dans le processus de traitement des nanobilles, la section transversale du nanopilier est directement proportionnelle à la taille de la nanobille de silice utilisée, donc en sélectionnant soigneusement la taille de la nanobille de silice, la taille souhaitée du nanopilier peut être obtenue. En réglant correctement les paramètres de réaction, j'ai réussi à synthétiser des nanobilles de silice d'un diamètre compris entre 100 et 500 nm.

Résultats : Codage de l'information sur l'état excité d'une chaîne de spin moléculaire

Les mesures effectuées sur plusieurs nano-jonctions verticales Fe|CoPc|Co et Fe|CoPc|Fe révèlent des caractéristiques similaires à celles rapportées par Barraud et al. [57,58], comme la présence de MR due à un renversement de l'aimantation à de grands champs effectifs. Ceci a été interprété comme la conséquence d'un biais d'échange au niveau de la bicouche métal ferromagnétique/chaîne de spin moléculaire (MSC)[55,64–66]. D'après les mesures de transport effectuées à un champ magnétique de +2T appliqué de l'extérieur sur des nanopiliers verticaux de 500 nm de section en Si|SiOx||Cr(5)|Fe(50)|CoPc(20)|Co(10)|Cr(5), une augmentation soudaine de la conductance différentielle a été observée après une certaine valeur de la polarisation appliquée ou de la tension de seuil (V_{th}) [voir Fig. 11]. Cette augmentation soudaine de la conductance différentielle est due à l'ouverture de canaux excités par retournement de spin supplémentaires au sein de la chaîne de spin moléculaire CoPc à couplage antiferromagnétique. Cette technique électrique de caractérisation des excitations par retournement de spin dans une chaîne antiferromagnétique est connue sous le nom de spectroscopie inélastique par effet tunnel (IETS).

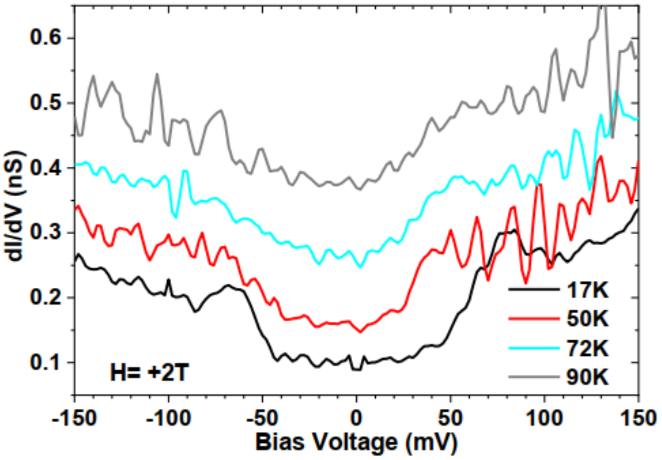

Figure 11. Excitation par retournement de spin. Données de conductance différentielle ou dI/dV(V) à H= +2T pour différents points de température (T) acquises pour la nanopillar de taille 500nm fabriquée à partir d'un empilement de Si|SiOx||Cr(5)|Fe(50)|CoPc(20)|Co(10)|Cr(5).[63]

Après la procédure de refroidissement par champ (FC) à -1T, les mesures de magnétotransport effectuées à une polarisation appliquée de 58mV à 60K, ont révélé trois unités magnétiques distinctes dans nos dispositifs. Le premier saut de résistance près de H = 0T est dû à l'inversion de magnétisation de l'unité magnétique supérieure [flèche verte supérieure sur la Fig. 12.a]. Cette unité comprend l'électrode supérieure Co FM avec l'électrode voisine CoPc MSC en dessous [Fig. 12.b]. À l'interface de la jonction supérieure (Co|CoPc), on suppose que les atomes métalliques diffusent[67] dans la couche moléculaire située en dessous avec un empilement moléculaire[65] différent de celui de l'interface inférieure de la jonction (Fe|CoPc). Cette unité supérieure complexe à anisotropie magnétique modérée est représentée schématiquement par un segment semi-transparent à l'intérieur de l'encadré vert supérieur de la Fig. 12.b. Le renversement de cette unité supérieure se produit par rapport à une unité magnétiquement dure composée de l'"unité inférieure" (électrode Fe formant une "spinterface" (Fe|CoPc) avec le 1er ML de la molécule de CoPc) et de l'"unité centrale" (chaîne de spin moléculaire (MSC) antiferromagnétique du CoPc couplée à l'unité inférieure par un mécanisme de biais d'échange[55,64–66,68–71]). Dans l'état fondamental de l'unité centrale, les unités inférieure et centrale représentent collectivement une seule entité magnétique, c'est-à-dire l'"unité dure" dont les propriétés physiques bien caractérisées peuvent expliquer nos principaux résultats. Cette "unité dure" est représentée schématiquement à la Fig. 12.b par la boîte verte pleine du bas, relativement plus grande, contenant une boîte jaune-vert. Dans son état fondamental, l'aimantation de cette unité dure inférieure est représentée par la flèche verte solide et épaisse. Cependant, le MSC CoPc couplé antiferromagnétiquement, lorsqu'il est dans son état d'excitation électrique, se sépare de l'"unité inférieure" et agit comme une unité magnétique distincte à l'état stable. L'état électriquement excité du CoPc MSC est représenté schématiquement sur la Fig. 12.b, tandis que sa présence dans notre dispositif est conceptualisée par la flèche jaune-verte et la boîte de la Fig. 12.b. Cette "unité centrale" présente une très faible anisotropie magnétique et est couplée par échange à l'électrode Fe inférieure avec une énergie d'échange J_{12}^{MSC}. Cette énergie d'échange J_{12}^{MSC} conduit à la polarisation d'échange[55,64–66,68–71] qui peut commuter l'orientation magnétique de l'unité centrale (CoPc MSC) dans son état excité au 2ème point de commutation H ≈ 1.1T [voir flèche jaune/verte sur la Fig. 12.a].

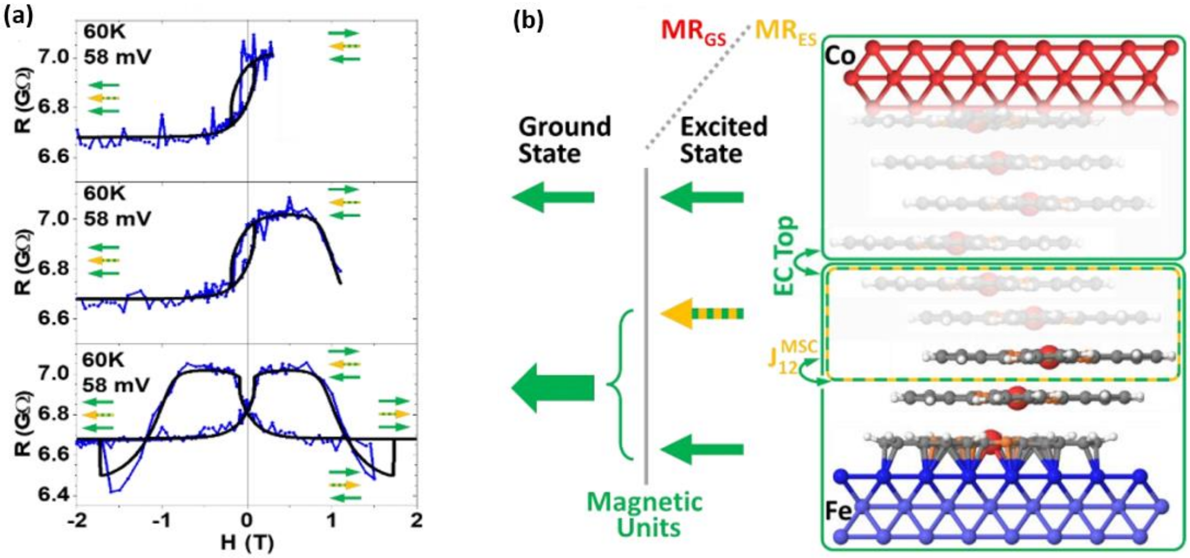

Figure 12. Magnétorésistance par retournement de spin. (a) Les mesures de magnétotransport effectuées à T=60K et V=58mV révèlent trois commutations de résistance dues à l'inversion de magnétisation de trois unités magnétiques (flèches vertes et vertes/jaunes). **(b)** Schéma des unités magnétiques contribuant au MR_{GS} et au MR_{ES}. Dans l'état fondamental, la chaîne de spin moléculaire de CoPc forme une unité relativement plus dure avec l'interface Fe|CoPc et l'électrode inférieure de Fe (représentée par la grande boîte verte inférieure qui contient également une boîte verte/jaune), cependant, dans son état excité à spin inversé, la chaîne de spin moléculaire de CoPc agit comme une unité magnétique distincte (représentée par la boîte verte/jaune et la flèche) avec un champ coercitif et contribue uniquement au MR_{ES}. La partie imparfaitement contrôlée de la jonction apparaît semi-transparente. Les termes de couplage ECTop et J_{12}^{MSC} du modèle macrospin entre les unités centrales et supérieure/inférieure sont représentés. Voir les textes pour plus de détails. L'ajustement [représenté par la ligne noire dans le panneau (a)] a été effectué en utilisant les paramètres K_t/M_t =0.26T, θ_{Mt}=60^0, K_b/M_b =4.95T, θ_{Mb}=-4^0, ECTop=-0.05T, J_{12}^{MSC} =1.28T, R_0=6.68GΩ, MR_{GS} =-2.4% et MR_{ES} =5.1%.[63]

Le troisième changement de la résistance au champ positif plus élevé de la Fig. 12.a est dû à l'inversion de l'"unité inférieure" composée de l'électrode de Fe et de la "spinterface" formée entre la couche supérieure de Fe et le 1er ML de la molécule de CoPc, qui est représentée par la flèche verte inférieure de la Fig. 12.a et la flèche verte inférieure fine de la Fig. 12.b. Le couplage d'échange entre l'"unité supérieure" et l'"unité magnétique centrale" est indiqué par le paramètre ECTop. En outre, les données de magnétotransport en fonction de la polarisation ont révélé que les excitations par retournement de spin dans l'"unité magnétique centrale" (CoPc MSC) peuvent être induites en appliquant une tension de polarisation supérieure à la tension de seuil (V_{th}). Le canal de transport de spin qui traverse les états quantiques de base et excités de la chaîne de spin génère deux termes de magnétorésistance, MR_{GS} et MR_{ES}, respectivement.

Une image claire de la MR_{GS} et de la MR_{ES} est montrée dans la boucle R(H) tracée à une polarisation appliquée de 80mV pour le point de température 17K [voir Fig. 13.a]. De plus, il est clairement visible sur la Fig. 13 que la réduction de la polarisation appliquée entraîne la diminution de la MR_{ES} et finalement sa disparition à 20mV. Des résultats similaires sont obtenus pour la polarisation négative appliquée (données non présentées). La dépendance de la conductance différentielle (dI/dV) par rapport à la polarisation, représentée sur la Fig. 13.g (ligne grise), montre une amplitude presque constante de la dI/dV dans la plage de polarisation appliquée de $-35mV < V < 35mV$. Une forte augmentation de la dI/dV est observée après $|V|>35mV$ avec un pic centré autour de $|V|\approx 70mV$. L'amplitude du dI/dV augmente encore pour des valeurs de polarisation appliquées plus élevées. Cette dépendance du biais de la dI/dV ressemble à la littérature précédente[57,59,72] sur le transport assemblé par STM et à l'état solide à travers les chaînes de spin, c'est-à-dire qu'elle est la caractéristique de l'excitation de spin dans la chaîne de spin moléculaire (MSC). De plus, à partir de la Fig. 13.g, nous observons que la magnétorésistance induite par l'excitation de spin (MR_{ES}) à travers la MSC calculée à partir des données R(H) suit la conductance différentielle (dI/dV). À notre connaissance, il s'agit de la première observation d'un signal MR unique qui est poussé à apparaître en raison de la tension de polarisation appliquée, et dont l'amplitude suit la conductance différentielle. On ne s'attend pas à ce qu'une génération de MR interfaciale à une "spinterface", pilotée électriquement[53,73] et due à ce qu'on appelle le "durcissement magnétique"[64,68–71] au-delà d'un seuil de champ électrique, produise un terme de MR qui s'échelonne avec dI/dV[63]. Cela confirme encore que le MR qui suit le dI/dV, est uniquement dû à l'ouverture de canaux de transport de spin-flip supplémentaires à travers le MSC électriquement excité quantiquement.

Le signe opposé de la polarisation de spin (P) du canal de transport de l'état excité à retournement de spin du MSC au canal de magnétotransport de l'état fondamental entraîne l'inversion du signe du MR_{ES} au MR_{GS}. L'inversion observée du signe de la MR n'est pas due à nos définitions de la MR, mais montre l'influence des effets opposés de la MR sur l'inversion de la magnétisation de l'électrode FM supérieure [voir la Fig. 7.5.b]. Si le simple fait d'exciter électriquement le MSC ouvrait un canal de conductance supplémentaire avec la polarisation de spin inversée P, alors le MR de la Fig. 13.e changerait également de signe, mais la forme du R(H) resterait la même. Le deuxième changement de résistance au champ magnétique appliqué H= +1,2T uniquement en présence du courant d'excitation de spin indique la présence d'une troisième unité magnétique qui est liée à l'augmentation de la conductance [comparer les Fig. 13.d et 13.e]. C'est la raison pour laquelle le scénario lié à l'état fondamental [Fig. 13.e] et à l'état excité [Fig. 13.d] des MSC CoPc dans notre dispositif est schématisé par les deux et trois unités magnétiques, respectivement. Ainsi, cette unité magnétique responsable de la MR_{ES} [boîte jaune/verte de la Fig. 12.b] n'est pas seulement entraînée électriquement pour apparaître au-delà d'un seuil de polarisation, mais possède également des propriétés magnétostatiques efficaces (par exemple, son propre champ coercitif).

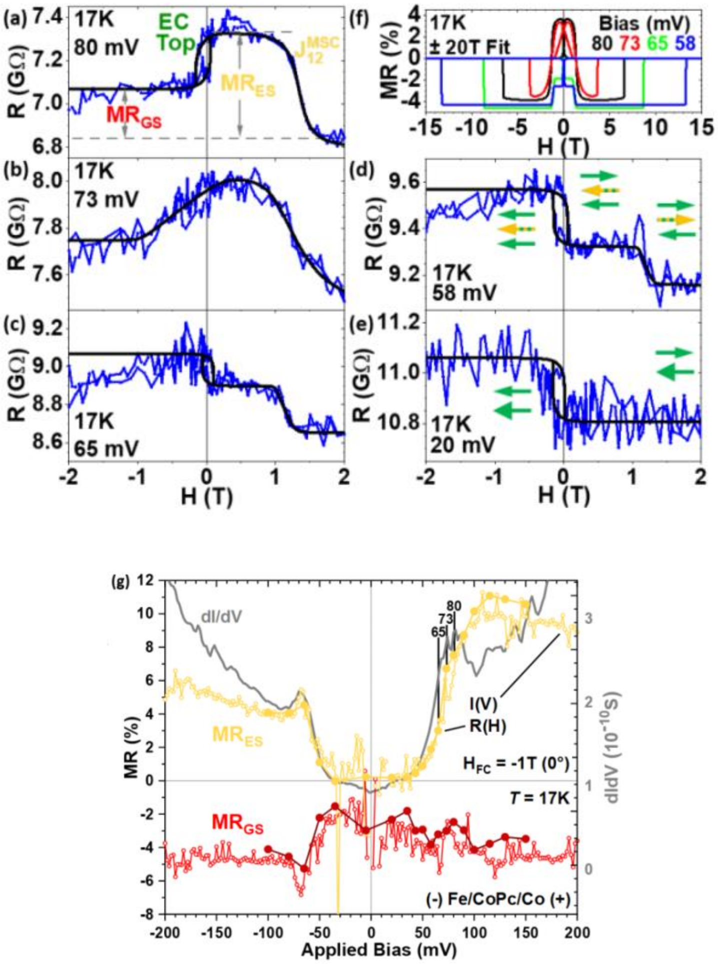

Figure 13. Le début électrique de la magnétorésistance de spin-flip. (a-e) Boucles R(H) expérimentales (bleu) réalisées à 17K pour 20<V(mV)<80 avec les ajustements associés (noir), également représentés dans le **panneau (f)** pour ±20T. Les flèches jaunes/vertes indiquent les trois unités magnétiques distinctes. La plus grande flèche verte dans le **panneau (e)** représente une unité inférieure combinée (CoPc MSC avec Fe|CoPc 'spinterface' et sous l'électrode inférieure Fe) en l'absence d'excitations de spin [voir **Fig. 12.b**]. **(g)** Dépendance du biais de dI/dV, et de MR_{GS}/MR_{ES} déduite des données I(V) et R(H). Le MR_{ES} suit le dI/dV et génère une trace R(H) spécifique.[63]

Pour étudier l'énergétique de la troisième unité magnétique (centrale), les mesures de magnétotransport en fonction de la température ont été effectuées à une polarisation appliquée supérieure à la polarisation de seuil (V_{th}) requise pour observer les excitations de spin-flip dans le MSC. Les tracés R(H) en fonction de la température réalisés à 100mV sur la plage de température

17K < T < 80K sont présentés sur les Fig. 14.a-e. D'après les tracés R(H) réalisés sur 17K < T < 55K (les données à 55K ne sont pas présentées), sous le champ magnétique appliqué H| ≤ 2T, un type de basculement similaire pour l'unité supérieure et inférieure est observé. Les tracés R(H) deviennent symétriques sur la plage de température de 60K ≤ T(K) < 72K [voir également la Fig. 12.a]: ici, l'unité magnétique inférieure bascule également pour |H| ≤ 2T. Un changement net de la contribution du MR_{ES} par rapport au champ appliqué (H) est observé à T≈70K correspondant à l'énergie thermique $E_{crit} = k_B.T$ ≈6meV. A T ≥ 80K, enfin, la boucle R(H) est effondrée, et seule la MR à faible champ est observée jusqu'à 100K.

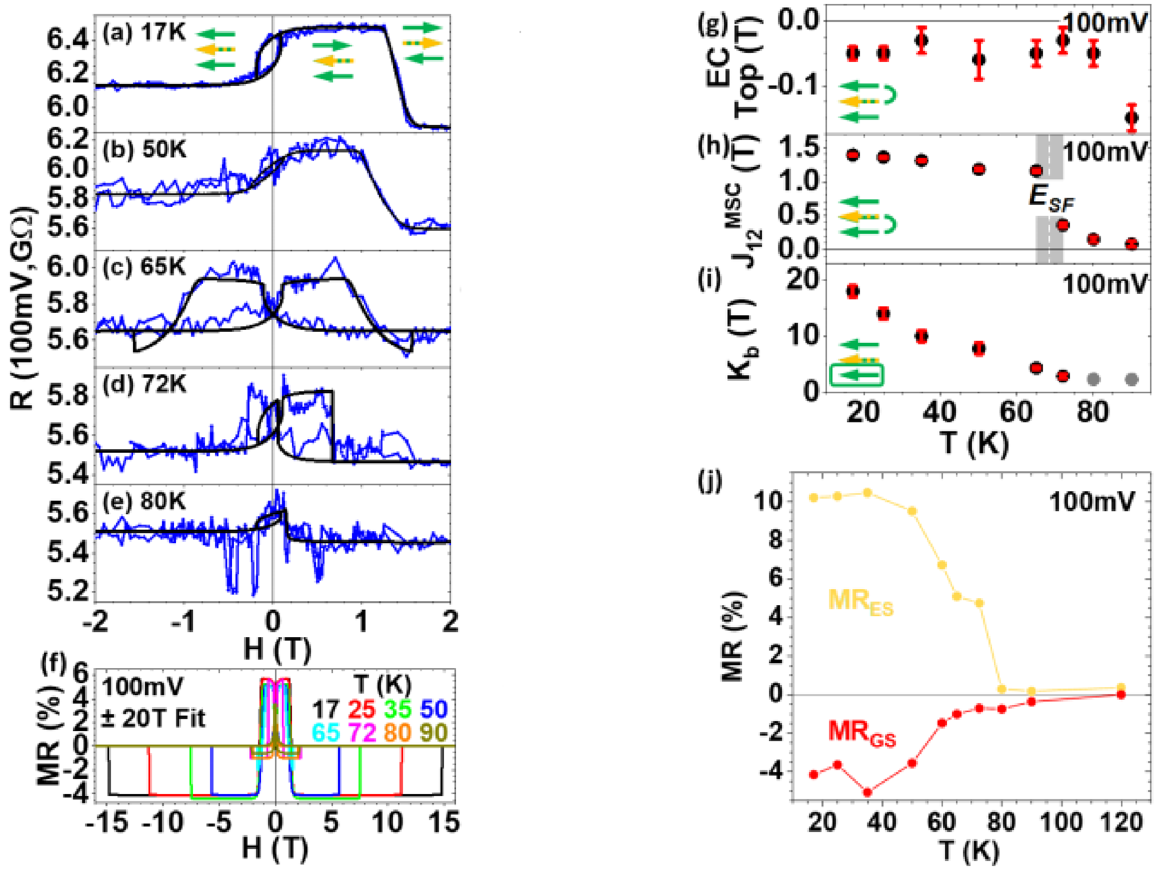

Figure 14. Stabilité thermique de la magnétorésistance de spin-flip. (a-e) Boucles R(H) à 100mV pour 17< T(K) <80. La ligne bleue/noire représente les données expérimentales/ajustements modélisés et est également représentée dans le panneau **(f)** pour ±20T. Dépendances à la température de **(g)** ECTop, **(h)** J_{12}^{MSC}, **(i)** K_b, et **(j)** de MR_{ES} et MR_{GS}. Les données grises dans le panneau **(i)** pour T≥80K sont les valeurs minimales requises pour obtenir R(- 2T)≠R(2T).[63]

Conclusion partielle

Dans ce travail, nous voyons que l'augmentation de la conductance induite par le spin-flip suit l'apparition et l'augmentation d'un terme MR spécifique (MR_{ES}) induit par la polarisation. Ce régime de transport dynamique de spin-flip permet effectivement au CoPc MSC d'agir comme une unité magnétiquement distincte. C'est ce que l'on constate en ajustant les boucles MR à l'aide d'une description phénoménologique à trois macrospins du magnétotransport impliquant trois unités magnétiques. Le signe opposé du MR entre les canaux de transport conventionnel et d'excitation de spin lors de l'inversion de la magnétisation de l'électrode supérieure est expliqué par la physique de l'état excité par retournement de spin par rapport à l'état fondamental[60]. Ce terme supplémentaire de MR est circonscrit par un changement de résistance à des champs magnétiques élevés. Le modèle phénoménologique attribue cet effet à la présence d'une grande énergie d'échange (J_{12}^{MSC}) entre l'électrode inférieure (Fe) et le CoPc MSC dans son état excité. Les études de température montrent que l'énergie d'échange (J_{12}^{MSC}) diminue soudainement d'un ordre de grandeur à T~70K. Les calculs de théorie fonctionnelle de la densité révèlent que l'énergie thermique correspondante de 5,9meV correspond à la barrière d'anisotropie de 6,1meV entre l'état fondamental et le premier état excité du CoPc MSC au sommet de l'électrode Fe. Pris ensemble, ces résultats démontrent que nous avons réussi à isoler une contribution MR due au canal de transport par retournement de spin à travers une chaîne de spin moléculaire dans son état excité. Il s'agit d'une étape importante vers le codage et la transmission d'informations à l'aide de chaînes de spin moléculaires. Contrairement aux dispositifs spintroniques à base de MgO, la présence d'un terme supplémentaire de magnétorésistance à l'état excité (MR_{ES}) ouvre la voie à l'utilisation de ces dispositifs hybrides à l'état solide pour coder l'information sur l'état excité quantique de la chaîne de spin.

Conclusion finale et perspectives

En résumé, ce doctorat a étudié l'impact des états localisés dus aux lacunes d'oxygène dans la barrière de tunnel du MgO dans les MTJ nanopiliers sur le couple de transfert de spin. Ces lacunes en oxygène sont inévitables et donc inhérentes au MgO. Pour caractériser ces vacances d'oxygène et leur impact sur le STT, les mesures de transport sont effectuées sur les MTJ nanopiliers de CoFeB|MgO|CoFeB fournis par deux laboratoires différents (le laboratoire du Prof. P. Freitas à l'INL Portugal et TDK-Headway Inc. USA). Les vacances d'oxygène apparaissent comme des états localisés par rapport à l'énergie de Fermi (E_F) dans le diagramme de bande d'énergie et ont été caractérisées par les techniques $\hat{I}$. Pour nos dispositifs de nanopiliers CoFeB|MgO|CoFeB, les états localisés sont apparus uniquement dans l'état parallèle (P). L'apparition de larges pics des états localisés dans les spectres $\hat{I}$ suggère que ces états sont formés en raison de la chaîne de lacunes d'oxygène plutôt que des lacunes isolées. Dans un modèle simpliste, nous avons supposé que la chaîne est formée à cause des lacunes d'oxygène isolées ou des centres F. Des caractérisations supplémentaires des états localisés dus aux lacunes d'oxygène sont également effectuées en utilisant la technique ST-FMR.

Les expériences de commutation STT en mode continu ont permis d'observer que : i) les états P(AP) de ces dispositifs présentent des caractéristiques "presque ohmiques" ("semi-conductrices"), ii) les paramètres STT (P >AP et AP >P) diminuent avec l'augmentation de la température, et iii) la commutation AP >P se produit à des valeurs de courant critique (tension/densité de courant) relativement plus faibles que la commutation P >AP. Pour savoir si ces résultats sont une conséquence des vacances d'oxygène, les calculs DFT sont effectués. Les tracés de densité de charge, qui intègrent la chaîne de lacunes d'oxygène en zigzag (ZZCOV, déduite de la technique de spectroscopie $\hat{I}$) formée en raison de la chaîne de lacunes d'oxygène uniques ou du centre F dans la couche de MgO, ont permis d'aborder avec succès le transport "presque ohmique" et semi-conducteur dans les états P et AP respectifs. La diminution des paramètres STT (P >AP et AP >P) avec une augmentation de la température pourrait être liée à la variation de l'anisotropie magnétique des électrodes FM en fonction de la température. Bien que l'incorporation de ZZCOV dans les calculs DFT explique les deux modes de transport différents observés, à savoir le transport "presque ohmique" et le transport semi-conducteur dans les MTJ nanopiliers aux états P et AP respectifs, elle n'a pas pu expliquer explicitement pourquoi la commutation AP >P se produit à une densité de courant critique d'entrée relativement plus faible que sa contrepartie P >AP. Pour conclure, dans nos dispositifs nanopiliers CoFeB|MgO|CoFeB avec un produit R.A de ~20-30 $\Omega.\mu m^2$, les faibles hauteurs de barrière (~0,7/0,4eV, mesurées expérimentalement à partir des tracés $\hat{I}$, et ~0. 45eV, calculés théoriquement à l'aide de l'ajustement de Brinkman) et un TMR élevé (~136 %) conduisant au STT sont plus probablement les résultats d'une voie de nanotransport telle qu'une chaîne en zig-zag de lacunes d'oxygène qui enjambe la barrière de MgO de la jonction.

Dans la deuxième partie de la thèse, nous avons montré comment les dispositifs spintroniques basés sur des molécules organiques (utilisées comme couche active ou couche d'espacement) peuvent offrir des avantages supplémentaires par rapport à leurs homologues inorganiques. Pour réaliser expérimentalement ces dispositifs spintroniques inorganiques-organiques ou hybrides à base de molécules organiques, j'ai conçu une nouvelle configuration pour une technique de lithographie alternative appelée "traitement des nanobilles", j'ai optimisé chimiquement la taille de la nanosphère de silice utilisée comme masque d'ombre (pour définir le nanopilier en dessous) et j'ai réalisé d'innombrables processus de gravure à sec pour fabriquer les jonctions de nanopiliers hybrides. Pour contrôler le nombre de nanobilles de silice déposées (servant de masque d'ombre pendant l'étape de gravure) et leur emplacement précis sur le dessus de la surface de recouvrement des empilements hybrides, des nanomanipulations AFM ont également été réalisées. Afin d'améliorer encore le traitement des nanobilles, la configuration de la "lithographie par trempage" a été conçue, optimisée et démontrée pour obtenir des nanopiliers hybrides fonctionnels. Ces dispositifs nanopillaires hybrides traités ont été étudiés pour les applications de "codage de l'information"[63] et de "récolte d'énergie"[74]. Parmi les études susmentionnées, cette thèse ne contient que la première, c'est-à-dire l'application "codage de l'information" de ces dispositifs. Les dispositifs nanopiliers tricouches de 500nm de section, utilisés dans cette étude contiennent deux électrodes FM Fe (en bas) et Co (en haut) séparées par une couche moléculaire CoPc (couche d'espacement). En utilisant la technique de spectroscopie à effet tunnel inélastique (IETS) réalisée sur les jonctions des nanopiliers Fe|CoPc|Co, en dessous d'une température correspondant à l'anisotropie magnétique de la chaîne de spin moléculaire, la chaîne de spin peut être excitée électriquement. L'état excité par retournement de spin induit électriquement de la molécule de CoPc provoque une inversion du signe du spin total des molécules de CoPc et donc du couplage d'échange (J) entre les molécules de CoPc adjacentes. L'inversion de J modifie les corrélations magnétiques (AFM → FM) entre les molécules adjacentes de CoPc et contribue à un terme supplémentaire de magnétorésistance (MR) c'est-à-dire MR_{ES} (état excité MR). Ce terme de MR supplémentaire c'est-à-dire MR_{ES} a le signe opposé à la MR de l'état fondamental (MR_{GS}), et suit spectroscopiquement la conductance différentielle (dI/dV) des excitations de spin-flip. Puisque le MR code le signal d'entrée magnétique en un signal de sortie électrique, la présence du terme MR supplémentaire, c'est-à-dire le MR_{ES}, dans ces dispositifs spintroniques hybrides apporte des avantages supplémentaires par rapport aux dispositifs spintroniques à base de MgO ou d'autres homologues inorganiques. En outre, ce terme MR_{ES} n'apparaît qu'à partir d'une certaine valeur de polarisation appliquée (nécessaire pour entraîner les excitations de retournement de spin dans les molécules de CoPc) ; il est donc entraîné électriquement et peut donc être considéré comme une alternative potentielle au couple STT/orbite de spin.

On a constaté que ces nanodispositifs hybrides avec des états de défaut (centres paramagnétiques Co^{2+}) dans la couche intercalaire CoPc génèrent de l'énergie spontanée à température ambiante[74]. L'origine de l'effet observé est de nature quantique et ces dispositifs sont donc connus sous le nom de "moteurs quantiques" ou "moteurs spintroniques"[51,75,76]. Le mécanisme de fonctionnement de ces moteurs spintroniques n'est cependant pas très clair. Nous espérons que ce travail de recherche[74], y compris les travaux de recherche antérieurs effectués par d'autres groupes, inspirera d'autres chercheurs à mieux comprendre le mécanisme de fonctionnement de ces dispositifs afin d'augmenter leur efficacité ou leur rendement. Nous espérons que cette direction de recherche sera capable d'atténuer la crise énergétique de notre société jusqu'à un certain point.

Références:

[1] Meservey R, Tedrow P M and Fulde P 1970 Magnetic Field Splitting of the Quasiparticle States in Superconducting Aluminum Films *Physical Review Letters* **25** 1270–2

[2] Baibich M N, Broto J M, Fert A, Van Dau F N, Petroff F, Etienne P, Creuzet G, Friederich A and Chazelas J 1988 Giant Magnetoresistance of (001)Fe/(001)Cr Magnetic Superlattices *Physical Review Letters* **61** 2472–5

[3] Binasch G, Grünberg P, Saurenbach F and Zinn W 1989 Enhanced magnetoresistance in layered magnetic structures with antiferromagnetic interlayer exchange *Physical Review B* **39** 4828–30

[4] Jullière M 1975 Tunneling between ferromagnetic films *Physics Letters A* **54** 225–6

[5] Miyazaki T and Tezuka N 1995 Giant magnetic tunneling effect in Fe/Al2O3/Fejunction *Journal of Magnetism and Magnetic Materials* **139** L231–4

[6] Moodera J S, Kinder L R, Wong T M and Meservey R 1995 Large Magnetoresistance at Room Temperature in Ferromagnetic Thin Film Tunnel Junctions *Physical Review Letters* **74** 3273–6

[7] Ikeda S, Hayakawa J, Ashizawa Y, Lee Y M, Miura K, Hasegawa H, Tsunoda M, Matsukura F and Ohno H 2008 Tunnel magnetoresistance of 604% at 300K by suppression of Ta diffusion in CoFeB⁄MgO⁄CoFeB pseudo-spin-valves annealed at high temperature *Applied Physics Letters* **93** 082508

[8] Dieny B, Prejbeanu I L, Garello K, Gambardella P, Freitas P, Lehndorff R, Raberg W, Ebels U, Demokritov S O, Akerman J, Deac A, Pirro P, Adelmann C, Anane A, Chumak A V, Hiroata A, Mangin S, Onbaşlı M C, Finocchio G, Diaz L L, Chantrell R, Chubykalo-Fesenko O and Bortolotti P Opportunities and challenges for spintronics in the microelectronic industry 26

[9] Slonczewski J C 1996 Current-driven excitation of magnetic multilayers *Journal of Magnetism and Magnetic Materials* **159** L1–7

[10] Berger L 1996 Emission of spin waves by a magnetic multilayer traversed by a current *Physical Review B* **54** 9353–8

[11] Krishnan K M 2016 *Fundamentals and applications of magnetic materials* (Oxford, United Kingdom: Oxford University Press)

[12] Ralph D C and Stiles M D 2008 Spin transfer torques *Journal of Magnetism and Magnetic Materials* **320** 1190–216

[13] Kent A D and Worledge D C 2015 A new spin on magnetic memories *Nature Nanotechnology* **10** 187–91

[14] Krzysteczko P, Münchenberger J, Schäfers M, Reiss G and Thomas A 2012 The Memristive Magnetic Tunnel Junction as a Nanoscopic Synapse-Neuron System *Advanced Materials* **24** 762–6

[15] Torrejon J, Riou M, Araujo F A, Tsunegi S, Khalsa G, Querlioz D, Bortolotti P, Cros V, Yakushiji K, Fukushima A, Kubota H, Yuasa S, Stiles M D and Grollier J 2017 Neuromorphic computing with nanoscale spintronic oscillators *Nature* **547** 428–31

[16] Sbiaa R and Piramanayagam S N 2017 Recent Developments in Spin Transfer Torque MRAM *physica status solidi (RRL) - Rapid Research Letters* **11** 1700163

[17] Choi J-Y, Lee D, Baek J-U and Park J-G 2018 Double MgO-based Perpendicular Magnetic-Tunnel-Junction Spin-valve Structure with a Top Co2Fe6B2 Free Layer using a Single SyAF [Co/Pt]n Layer *Sci Rep* **8** 2139

[18] Mojumder N N and Roy K 2012 Proposal for Switching Current Reduction Using Reference Layer With Tilted Magnetic Anisotropy in Magnetic Tunnel Junctions for Spin-Transfer Torque (STT) MRAM *IEEE Trans. Electron Devices* **59** 3054–60

[19] Mathon J and Umerski A 2001 Theory of tunneling magnetoresistance of an epitaxial Fe/MgO/Fe(001) junction *Phys. Rev. B* **63** 220403

[20] Schleicher F, Taudul B, Halisdemir U, Katcko K, Monteblanco E, Lacour D, Boukari S, Montaigne F, Urbain E, Kandpal L M, Arabski J, Weber W, Beaurepaire E, Hehn M, Alouani M and Bowen M 2019 Consolidated picture of tunnelling spintronics across oxygen vacancy states in MgO *J. Phys. D: Appl. Phys.* **52** 305302

[21] Halisdemir U, Schleicher F, Kim D J, Taudul B, Lacour D, Choi W S, Gallart M, Boukari S, Schmerber G, Davesne V, Panissod P, Halley D, Majjad H, Henry Y, Leconte B, Boulard A, Spor D, Beyer N, Kieber C, Sternitzky E, Cregut O, Ziegler M, Montaigne F, Arabski J, Beaurepaire E, Jo W, Alouani M, Gilliot P, Hehn M and Bowen M 2016 Oxygen-vacancy driven tunnelling spintronics across MgO *Spintronics IX* vol 9931 (International Society for Optics and Photonics) p 99310H

[22] Yuasa S, Nagahama T, Fukushima A, Suzuki Y and Ando K 2004 Giant room-temperature magnetoresistance in single-crystal Fe/MgO/Fe magnetic tunnel junctions *Nature Materials* **3** 868–71

[23] Miao G X, Park Y J, Moodera J S, Seibt M, Eilers G and Münzenberg M 2008 Disturbance of Tunneling Coherence by Oxygen Vacancy in Epitaxial Fe/MgO/Fe Magnetic Tunnel Junctions *Physical Review Letters* **100**

[24] Mitani S, Moriyama T and Takanashi K 2003 Fe/MgO/FeCo(100) epitaxial magnetic tunnel junctions prepared by using *in situ* plasma oxidation *Journal of Applied Physics* **93** 8041–3

[25] Parkin S S P, Kaiser C, Panchula A, Rice P M, Hughes B, Samant M and Yang S-H 2004 Giant tunnelling magnetoresistance at room temperature with MgO (100) tunnel barriers *Nature Materials* **3** 862–7

[26] Schleicher F, Halisdemir U, Lacour D, Gallart M, Boukari S, Schmerber G, Davesne V, Panissod P, Halley D, Majjad H, Henry Y, Leconte B, Boulard A, Spor D, Beyer N, Kieber C, Sternitzky E, Cregut O, Ziegler M, Montaigne F, Beaurepaire E, Gilliot P, Hehn M and Bowen M 2014 Localized states in advanced dielectrics from the vantage of spin- and symmetry-polarized tunnelling across MgO *Nature Communications* **5** 4547–55

[27] Teixeira J M, Ventura J, Araujo J P, Sousa J B, Fernández-García M P, Wisniowski P and Freitas P P 2010 Evidence of spin-polarized direct elastic tunneling and onset of superparamagnetism in MgO magnetic tunnel junctions *Phys. Rev. B* **81** 134423

[28] Studniarek M, Halisdemir U, Schleicher F, Taudul B, Urbain E, Boukari S, Hervé M, Lambert C-H, Hamadeh A, Petit-Watelot S, Zill O, Lacour D, Joly L, Scheurer F, Schmerber

G, Da Costa V, Dixit A, Guitard P A, Acosta M, Leduc F, Choueikani F, Otero E, Wulfhekel W, Montaigne F, Monteblanco E N, Arabski J, Ohresser P, Beaurepaire E, Weber W, Alouani M, Hehn M and Bowen M 2017 Probing a Device's Active Atoms *Adv. Mater.* **29** 1606578

[29] Kittel C 2012 *Introduction to Solid State Physics, 8ed* (Wiley)

[30] David N, University C and Ashcroft N W 2003 *Solid State Physics* (New Delhi: Cengage)

[31] Gibson A, Haydock R and LaFemina J P 1994 Stability of vacancy defects in MgO: The role of charge neutrality *Phys. Rev. B* **50** 2582–92

[32] Taudul B, Bowen M and Alouani M Impact of single and double oxygen vacancies on electronic transport in Fe/MgO/Fe magnetic tunnel junctions *arXiv:1904.02554 [cond-mat.mtrl-sci]* 32

[33] Taudul B, Monteblanco E N, Halisdemir U, Lacour D, Schleicher F, Montaigne F, Beaurepaire E, Boukari S, Hehn M, Alouani M and Bowen M 2017 Tunneling Spintronics across MgO Driven by Double Oxygen Vacancies *Advanced Electronic Materials* **3** 1600390

[34] Velev J P, Belashchenko K D, Jaswal S S and Tsymbal E Y 2007 Effect of oxygen vacancies on spin-dependent tunneling in Fe⁄MgO⁄Fe magnetic tunnel junctions *Applied Physics Letters* **90** 072502

[35] Velev J P, Zhuravlev M Ye, Belashchenko K D, Jaswal S S, Tsymbal E Y, Katayama T and Yuasa S 2007 Defect-Mediated Properties of Magnetic Tunnel Junctions *IEEE Transactions on Magnetics* **43** 2770–5

[36] McKenna K P and Blumberger J 2012 Crossover from incoherent to coherent electron tunneling between defects in MgO *Physical Review B* **86** 245110

[37] Schleicher F, Halisdemir U, Urbain E, Lacour D, Gallart M, Boukari S, Montaigne F, Beaurepaire E, Gilliot P, Hehn M and Bowen M 2015 MgO magnetic tunnel junctions of enduring F-type upon annealing *Journal of Physics D: Applied Physics* **48** 435004

[38] Taudul B, Bowen M and Alouani M 2020 Impact of single and double oxygen vacancies on electronic transport in Fe/MgO/Fe magnetic tunnel junctions *Journal of Applied Physics* **128** 143902

[39] Rottländer P, Hehn M and Schuhl A 2002 Determining the interfacial barrier height and its relation to tunnel magnetoresistance *Physical Review B* **65**

[40] Simmons J G 1963 Generalized Formula for the Electric Tunnel Effect between Similar Electrodes Separated by a Thin Insulating Film *Journal of Applied Physics* **34** 1793–803

[41] Brinkman W F, Dynes R C and Rowell J M 1970 Tunneling Conductance of Asymmetrical Barriers *Journal of Applied Physics* **41** 1915–21

[42] Lu Y, Tran M, Jaffrès H, Seneor P, Deranlot C, Petroff F, George J-M, Lépine B, Ababou S and Jézéquel G 2009 Spin-Polarized Inelastic Tunneling through Insulating Barriers *Physical Review Letters* **102**

[43] Teixeira J M, Ventura J, Araujo J P, Sousa J B, Wisniowski P, Cardoso S and Freitas P P 2011 Resonant Tunneling through Electronic Trapping States in Thin MgO Magnetic Junctions *Physical Review Letters* **106**

[44] Kim D J, Choi W S, Schleicher F, Shin R H, Boukari S, Davesne V, Kieber C, Arabski J, Schmerber G, Beaurepaire E, Jo W and Bowen M 2010 Control of defect-mediated tunneling barrier heights in ultrathin MgO films *Applied Physics Letters* **97** 263502

[45] Dediu V, Murgia M, Matacotta F C, Taliani C and Barbanera S 2002 Room temperature spin polarized injection in organic semiconductor *Solid State Communications* **122** 181–4

[46] Barraud C, Seneor P, Mattana R, Fusil S, Bouzehouane K, Deranlot C, Graziosi P, Hueso L, Bergenti I, Dediu V, Petroff F and Fert A 2010 Unravelling the role of the interface for spin injection into organic semiconductors *Nature Physics* **6** 615–20

[47] Anon 2009 Why going organic is good *Nature Materials* **8** 691–691

[48] Xu W, Szulczewski G J, LeClair P, Navarrete I, Schad R, Miao G, Guo H and Gupta A 2007 Tunneling magnetoresistance observed in La0.67Sr0.33MnO3/organic molecule/Co junctions *Appl. Phys. Lett.* **90** 072506

[49] Vinzelberg H, Schumann J, Elefant D, Gangineni R B, Thomas J and Büchner B 2008 Low temperature tunneling magnetoresistance on (La,Sr)MnO3⁄Co junctions with organic spacer layers *Journal of Applied Physics* **103** 093720

[50] Ciudad D, Gobbi M, Kinane C J, Eich M, Moodera J S and Hueso L E 2014 Sign Control of Magnetoresistance Through Chemically Engineered Interfaces *Adv. Mater.* **26** 7561–7

[51] Katcko K, Urbain E, Taudul B, Schleicher F, Arabski J, Beaurepaire E, Vileno B, Spor D, Weber W, Lacour D, Boukari S, Hehn M, Alouani M, Fransson J and Bowen M 2019 Spin-driven electrical power generation at room temperature *Commun Phys* **2** 116

[52] Sanvito S 2010 The rise of spinterface science: Molecular spintronics *Nature Physics* **6** 562–4

[53] Cinchetti M, Dediu V A and Hueso L E 2017 Activating the molecular spinterface *Nature Mater* **16** 507–15

[54] Delprat S, Galbiati M, Tatay S, Quinard B, Barraud C, Petroff F, Seneor P and Mattana R 2018 Molecular spintronics: the role of spin-dependent hybridization *J. Phys. D: Appl. Phys.* **51** 473001

[55] Boukari S, Jabbar H, Schleicher F, Gruber M, Avedissian G, Arabski J, Da Costa V, Schmerber G, Rengasamy P, Vileno B, Weber W, Bowen M and Beaurepaire E 2018

Disentangling Magnetic Hardening and Molecular Spin Chain Contributions to Exchange Bias in Ferromagnet/Molecule Bilayers *Nano Lett.* **18** 4659–63

[56] Serri M, Wu W, Fleet L R, Harrison N M, Hirjibehedin C F, Kay C W M, Fisher A J, Aeppli G and Heutz S 2014 High-temperature antiferromagnetism in molecular semiconductor thin films and nanostructures *Nature Communications* **5** 3079–87

[57] Barraud C, Bouzehouane K, Deranlot C, Kim D J, Rakshit R, Shi S, Arabski J, Bowen M, Beaurepaire E, Boukari S, Petroff F, Seneor P and Mattana R 2016 Phthalocyanine based molecular spintronic devices *Dalton Transactions* **45** 16694–9

[58] Barraud C, Bouzehouane K, Deranlot C, Fusil S, Jabbar H, Arabski J, Rakshit R, Kim D-J, Kieber C, Boukari S, Bowen M, Beaurepaire E, Seneor P, Mattana R and Petroff F 2015 Unidirectional Spin-Dependent Molecule-Ferromagnet Hybridized States Anisotropy in Cobalt Phthalocyanine Based Magnetic Tunnel Junctions *Physical Review Letters* **114** 206603

[59] Chen X, Fu Y-S, Ji S-H, Zhang T, Cheng P, Ma X-C, Zou X-L, Duan W-H, Jia J-F and Xue Q-K 2008 Probing Superexchange Interaction in Molecular Magnets by Spin-Flip Spectroscopy and Microscopy *Physical Review Letters* **101** 197208

[60] Loth S, Lutz C P and Heinrich A J 2010 Spin-polarized spin excitation spectroscopy *New J. Phys.* **12** 125021

[61] Urbain E 2017 *Utilisation de semi-conducteurs organiques comme barrière tunnel pour l'électronique de spin* These de doctorat (Université de Strasbourg)

[62] Wang W G, Pearse A, Li M, Hageman S, Chen A X, Zhu F Q and Chien C L 2013 Parallel fabrication of magnetic tunnel junction nanopillars by nanosphere lithography *Scientific Reports* **3** 1948

[63] Katcko K, Urbain E, Ngassam F, Kandpal L, Chowrira B, Schleicher F, Halisdemir U, Wang D, Scherer T, Mertz D, Leconte B, Beyer N, Spor D, Panissod P, Boulard A, Arabski J, Kieber C, Sternitzky E, Da Costa V, Hehn M, Montaigne F, Bahouka A, Weber W, Beaurepaire E, Kübel C, Lacour D, Alouani M, Boukari S and Bowen M 2021 Encoding Information on the Excited State of a Molecular Spin Chain *Adv. Funct. Mater.* **31** 2009467

[64] Raman K V, Kamerbeek A M, Mukherjee A, Atodiresei N, Sen T K, Lazić P, Caciuc V, Michel R, Stalke D, Mandal S K, Blügel S, Münzenberg M and Moodera J S 2013 Interface-engineered templates for molecular spin memory devices *Nature* **493** 509–13

[65] Gruber M, Ibrahim F, Boukari S, Isshiki H, Joly L, Peter M, Studniarek M, Da Costa V, Jabbar H, Davesne V, Halisdemir U, Chen J, Arabski J, Otero E, Choueikani F, Chen K, Ohresser P, Wulfhekel W, Scheurer F, Weber W, Alouani M, Beaurepaire E and Bowen M 2015 Exchange bias and room-temperature magnetic order in molecular layers *Nature Materials* **14** 981–4

[66] Mallik S, Mattauch S, Dalai M K, Brückel T and Bedanta S 2018 Effect of magnetic fullerene on magnetization reversal created at the Fe/C60 interface *Sci Rep* **8** 5515

[67] Fourmental C, Bellec A, Repain V, Lagoute J, Chacon C, Girard Y, Rousset S, Dappe Y J, Vlad A, Resta A, Garreau Y and Coati A 2019 Deep metallic interdiffusion in a model ferromagnetic/molecular system *Phys. Rev. Materials* **3** 083603

[68] Jo J, Byun J, Lee J, Choe D, Oh I, Park J, Jin M, Lee J and Yoo J 2020 Emergence of Multispinterface and Antiferromagnetic Molecular Exchange Bias via Molecular Stacking on a Ferromagnetic Film *Adv. Funct. Mater.* **30** 1908499

[69] Bairagi K, Bellec A, Repain V, Fourmental C, Chacon C, Girard Y, Lagoute J, Rousset S, Le Laurent L, Smogunov A and Barreteau C 2018 Experimental and theoretical investigations of magnetic anisotropy and magnetic hardening at molecule/ferromagnet interfaces *Phys. Rev. B* **98** 085432

[70] Mundlia S, Chaudhary S, Peri L, Bhardwaj A, Panda J J, Sasmal S and Raman K V 2020 Robust Monolayer Exchange-Bias Effect in Molecular Crane-Pulley Response at Magnetic Surface *Phys. Rev. Applied* **14** 024095

[71] Moorsom T, Alghamdi S, Stansill S, Poli E, Teobaldi G, Beg M, Fangohr H, Rogers M, Aslam Z, Ali M, Hickey B J and Cespedes O 2020 π -anisotropy: A nanocarbon route to hard magnetism *Phys. Rev. B* **101** 060408

[72] Muenks M, Jacobson P, Ternes M and Kern K 2017 Correlation-driven transport asymmetries through coupled spins in a tunnel junction *Nat Commun* **8** 14119

[73] Studniarek M, Cherifi-Hertel S, Urbain E, Halisdemir U, Arras R, Taudul B, Schleicher F, Hervé M, Lambert C-H, Hamadeh A, Joly L, Scheurer F, Schmerber G, Da Costa V, Warot-Fonrose B, Marcelot C, Mauguin O, Largeau L, Leduc F, Choueikani F, Otero E, Wulfhekel W, Arabski J, Ohresser P, Weber W, Beaurepaire E, Boukari S and Bowen M 2017 Modulating the Ferromagnet/Molecule Spin Hybridization Using an Artificial Magnetoelectric *Adv. Funct. Mater.* **27** 1700259

[74] Chowrira B, Kandpal L, Mertz D, Kieber C, Joly L, Monteblanco E, Bahouka A, Vileno B, Bernard R, Garcia H P, Elidrissi S, Gavara M, Sternitzky E, Costa V D, Hehn M, Montaigne F, Choueikani F, Ohresser P, Lacour D, Weber W, Boukari S and Bowen M 2020 Spintronic harvesting of thermal fluctuations on paramagnetic molecular centers around a phase transition *arXiv:2009.10413v2, *The first two authors contributed equally*

[75] Hai P N, Ohya S, Tanaka M, Barnes S E and Maekawa S 2009 Electromotive force and huge magnetoresistance in magnetic tunnel junctions *Nature* **458** 489–92

[76] Miao G-X, Chang J, Assaf B A, Heiman D and Moodera J S 2014 Spin regulation in composite spin-filter barrier devices *Nat Commun* **5** 3682

General Introduction and Thesis Organization

Electrons carry the charge and spin degree of freedom. The devices that use only the charge degree of freedom for their operation are known as electronic devices. Supplementing these electronic devices by the additional 'spin degree of freedom' forms a new class of devices that are popularly known as 'spintronic devices'. These devices serve as one of the key components for complex computation, information encoding, and various types of electrical and magnetic sensors, etc. Typically these spintronic devices are trilayer structures made of two FM electrodes separated by either a non-magnetic metal or a dielectric. During the course of this thesis, we are more interested in the latter devices. These devices are called magnetic tunnel junctions (MTJs). The dielectric layer that is sandwiched between the two FM electrodes acts as a tunneling layer and mostly is a thin layer of MgO. The thickness of the MgO thin film layer and the cross-section of the MTJ defines the R.A product of these devices and tuned according to the role of devices either to be used for the sensors or the information encoding processes. As nothing in this nature a defect-free, the MgO thin layer in these devices is prone to contain defects, mainly the oxygen vacancies.

The general consensus regarding the defect states is that they degrade the spintronic performance of the devices[1,2], which is not always true[3,4]. This thesis is an attempt to understand how the localized states induced by the defects (that are either inherent or implemented by choice) in the spacer layer of the nanospintronic devices can impact their spintronic performance. The nanospintronic devices that are studied in the first part of the thesis are the inorganic devices i.e. the nanopillars of CoFeB|MgO|CoFeB trilayer stacks and the localized states are formed due to the oxygen vacancies (inherent structural defects) within the MgO tunnel barrier. In the second part of the thesis, the nanospintronic devices are the inorganic-organic hybrid devices i.e. nanopillars crafted out of the Fe|CoPc|Co hybrid trilayer stacks and the defect states are the Co paramagnetic centers (paramagnetic defects implemented by choice) within the spacer layer of CoPc molecular spin chain (spacer layer).

Part-I of the thesis begins with Chapter-1, which provides the theoretical background and state-of-the-art of MgO-based inorganic magnetic tunnel junction (MTJ) devices. This Chapter-1 also includes detailed knowledge of localized states formed due to the oxygen vacancies, and the previously published scientific reports revealing their impact on the TMR[5]. The TMR is quantified as the relative change in the resistance due to the switching of magnetic alignment (magnetic state) of an MTJ from parallel (P) to antiparallel (AP) or vice-versa, caused by an external applied magnetic field. The switching of magnetic state can also be realized by the application of an input current of high enough density (> 10^7 A.cm^{-2}) across an MTJ, via the spin-transfer torque (STT) mechanism[6,7]. The STT effect has been extensively studied and used for the development of faster and high density magnetic random-access memories (MRAMs)[8], neuromorphic computing devices[9,10], microwave generation, and detections[11,12], etc.

Besides the important practical applications, the STT research struggles with some limitations, such as the requirement of the high current density, thermal stability of stored information, endurance, etc. To address these challenges many technical and scientific solutions have been reported but to the best of the author's knowledge, there is not a single report yet, stating clearly how the MgO tunneling barrier quality impacts the STT. Generally, all the thin film growth processes are always vulnerable to form structural defects e.g. dislocations or vacancies. In the case of MgO, due to their lowest formation energy, oxygen vacancies are most likely to occur[13]. These structural defects in the form of oxygen vacancies are manifested energetically by localized states appearing in the energy band diagram and therefore can be characterized either by the photoexcitation measurements such as photoluminescence (PL) spectroscopy[14] or the temperature-dependent magnetotransport measurements such as I-hat ($\hat{I}$) spectroscopy[15]. The PL spectroscopy is not an operando technique therefore does not provide any idea about the impact of localized states on the spintronic performance. On the other hand, the temperature dependent magnetotransport measurements performed in a special protocol i.e. the $\hat{I}$-spectroscopy technique allows one to characterize the localized states involved in transport. On performing additional magnetotransport measurements, these well-characterized localized states can also be excited simultaneously (either electrically, thermally, or optically) and therefore can reflect their contributions in the magnetotransport.

In this thesis, the $\hat{I}$-technique is used to characterize the localized states (due to the oxygen vacancies) within the MgO tunneling layer of CoFeB|MgO|CoFeB inorganic nanopillar devices and the additional magnetotransport measurements chosen to study their impact on spintronic performance is spin-transfer torque (STT). These experiments are also supported by the spin-torque ferromagnetic resonance (ST-FMR) spectroscopy technique[16] and the density functional theory (DFT) calculations[17]. Chapter-1 ends up with the basic physics of the STT and the scientific motivation of part-I of the thesis. Chapter-2 includes the UV-photolithography and nanolithography processes used to fabricate TMR- and STT-capable micropillar and nanopillar devices, respectively. This chapter also includes a detailed description of the $\hat{I}$-spectroscopy and the spin-torque ferromagnetic resonance (ST-FMR) technique. Chapter-3 contains the transport measurements performed on the CoFeB|MgO|CoFeB(FeB) micropillars of R.A product (~ 10^8 $\Omega.\mu m^2$), to characterize the exact energetic positions of the localized states relative to the Fermi energy (E_F), in the MTJ devices. In Chapter-4, these well-characterized localized states are again studied in CoFeB|MgO|CoFeB nanopillars of low R.A product (~ 20-30$\Omega.\mu m^2$) using both the $\hat{I}$-spectroscopy and ST-FMR techniques. To further study the impact of these localized states on the spintronic performance, temperature-dependent STT measurements are performed. The presence of localized states and their impact on the STT is also supported by the density functional theory (DFT) calculations.

Moving to part-II of the thesis, the first chapter, i.e. Chapter-5, begins with the importance of organic or molecular spintronics[18,19]. This chapter progresses with a detailed theoretical description and state-of-the-art on inorganic-organic (FM|organic spacer|FM) hybrid trilayer devices. The interface that is formed due to the hybridization between the available energy states of the FM electrode and the organic spacer layer on either side of these hybrid trilayer devices, carries a net non-zero spin polarization (P_{int}) that is different from that of the FM electrode (P). This is known as the 'spinterface'[20] and is also described in detail. Compared to their inorganic counterparts, i.e. the MgO-based MTJs (discussed in the first part of this thesis), the ability of spinterface to modify the spin polarization[20–22] of the FM electrode provides an additional advantage in tuning the spintronic performance of these hybrid devices. Out of the many chemically engineered organic molecules available, the cobalt-phthalocyanine (CoPc) molecule due to its interesting magnetic properties[23,24] is chosen for the spacer layer. The magnetic properties of the CoPc molecules are borne by the Co^{2+} central metal ion with $3d_z^2$ orbital and total spin of S=1/2[25]. The CoPc molecular film forms an antiferromagnetic (AFM) molecular spin chain (MSC) along the z-axis,[23,24]. In the AFM phase of CoPc MSC, i.e. for temperatures below the MSC's magnetic anisotropy energy, an applied bias larger than the magnetic exchange energy can result in spin-flip excitations[23,26] or the inelastic tunneling of electrons, causing a huge increase in the conductance. If these paramagnetic states are suitably spin-split and are paired with spintronic selectors[27,28], this can result in a spontaneous non-zero output current across the device. The spontaneously generated current or the energy is a manifestation of the quantum effects arising within these devices. These devices are popularly known as quantum or spin engines[29–31].

To realize these quantum effects i.e. the spin-flip excitations/inelastic electron tunneling and the spontaneous energy generation, the trilayer hybrid devices must be reduced dimensionally into the quantum or nanometric scales. One of the most common techniques to craft these nanoscale devices is the electron-beam lithography technique. However, this approach cannot serve the purpose here because of the frequent use of the resist and organic solvents, which can easily degrade the organic molecular spacer layer sandwiched between the two FM electrodes. To overcome this issue, I developed, designed, and optimized a new setup for an alternative lithography technique called 'nanobead processing' based on the nanosphere lithography technique[32]. The detailed description of the 'nanobead processing' is presented in the second chapter of part-II of the thesis i.e. Chapter-6. The nanobead processing not only serves the purpose for the hybrid samples but has also been demonstrated as a suitable technique to fabricate the nanopillar devices of the MgO-based STT capable devices. The third chapter of the second part of my Ph.D. thesis i.e. the Chapter-7, contains the experimental realization of the electrically induced spin-flip excitations in the Fe|CoPc|Co trilayer vertical nanojunctions of the cross-section 500nm[33]. The electrically induced spin-flip excitation produces an excited state magnetoresistance (MR_{ES}) which tracks the differential conductance (dI/dV) and has the opposite sign to the ground state MR (MR_{GS}). This additional excited state MR (MR_{ES}) term has never been reported for the MgO-based or other inorganic spintronic devices and provides an additional resource for information-encoding applications. Finally, Chapter-8 provides a general conclusion, perspective, and future scope of the work done in this thesis.

Part-I

Localized States in Inorganic Spintronic Nanodevices

1.

Theoretical Background

The discovery of spin-transfer torque (STT)[6,7] is considered a giant leap in the development of magnetic random-access memories (MRAMs)[8]. The STT effect has been observed for both spin valves[34,35] and magnetic tunnel junctions (MTJs)[5,36,37] however the more pronounced effect has been observed for the MTJs. Both devices are the trilayer thin-film structures consisting of two ferromagnetic metallic (FM) electrodes separated by a thin layer of nonmagnetic material (for spin valves)/dielectric or insulator (for MTJs). Out of the two ferromagnetic layers, the one which has low coercivity is called the free/soft layer whereas the other with higher coercivity is called the fixed/reference layer. The higher coercivity for the fixed FM layer is generally achieved by either increasing their thickness compared to that of the free layer or by pinning their magnetization direction using synthetic antiferromagnet (SAF) such as IrMn. However, in pseudo spin valves, this coercivity variation is achieved by using two different ferromagnetic materials for the fixed and free layer. The magnetization direction of the free layer can be switched either by the application of an external magnetic field or by the input current of sufficiently high density. The switching of the magnetization direction of the free layer thus flips the mutual magnetic alignment of these trilayer devices from parallel (P) to antiparallel (AP) or vice-versa resulting in a change in the resistance $\Delta R = R_{AP}-R_{P}$. This change in the resistance due to the applied external magnetic field is popularly known as the magnetoresistance (MR) and is quantified by the formula MR(%) = $[(\Delta R/R_{P}) - 1)]*100\%$. This MR is more specifically termed as giant magnetoresistance (GMR) and tunnel magnetoresistance (TMR) for the spin valves/pseudo spin valves and MTJs respectively. Contrary to the MR (GMR/TMR) effect, in STT effect the input current of sufficiently high density when applied to the fixed FM layer gets spin-polarized, and after due to the spin-dependent diffusive scattering across the non-magnetic spacer layer (in case of spin valves and pseudospin valves)/spin-dependent tunneling across a thin dielectric or insulating layer (in case of MTJs) transfers its' angular momentum onto the magnetization of free FM layer. This magnetization precession in the free FM layer thus causes magnetic oscillations or even switching of the magnetization direction of the free layer, resulting in the reversal of mutual magnetic alignment of the devices from P to AP or vice-versa. The STT effect holds a capacity to retain or switch to one of the magnetic states (P/AP) by the application of input current of sufficiently high density, therefore can be utilized for storing the information magnetically. The memory devices that work on this principle are known as magnetic random-access memories (MRAMs) and differs from the conventional RAMs in which the information is stored using charge degree of freedom of electrons.

The advancements made so far in the STT research have been mainly oriented towards lowering the critical current density required for the STT switching, thermal stability of the stored information, increasing the storage density, endurance, etc. These advancements are more related to the MTJ device geometry, the material used for the FM electrodes and their magnetic anisotropies, etc. To the best of our knowledge, there are no reports on how the tunneling barrier quality affects the STT. Therefore, the first part of this thesis is dedicated to how the structural defects (not by choice) more specifically the oxygen vacancies impact the physics of STT. In this chapter, we will describe all the basic physical concepts necessary to understand how the oxygen vacancies impact STT.

1.1 Quantum tunneling

On applying de Broglie's formula λ = h/mv (where λ = wavelength, h= Planck's constant, m = mass of the particle and v = velocity of the particle) for the electrons, provides a wavelength in the order of Å regions which suggests that electron does not only behave like a particle but also as a wave. Later W. Heisenberg showed that the two variables that are canonical conjugate to each other [e.g., position (Δx) and momentum (Δp), energy (ΔE) and time (Δt), and angular momentum (ΔJ) and angular displacement ($\Delta\theta$)] cannot be accurately measured at the same time. These findings along with the concept of the additional spin degree of freedom are the core of non-relativistic quantum physics. According to which, electrons cannot be described just like as a classical object with a certain position at a time but must be described by the probability density ($P = \psi^*.\psi = |\psi|^2$), where $\psi = \psi$ (r, t) is the wave function which depends on the position (r) and time (t). This wavefunction ψ with the propagation along the positive direction of the z-axis, at any point z and time t, can be written as ψ (z, t) = $\exp\{i(k.z-\omega t)\}$. Further simplifying by leaving the time-dependent term, it can be written as ψ (z) = $\exp(ik.z)$.

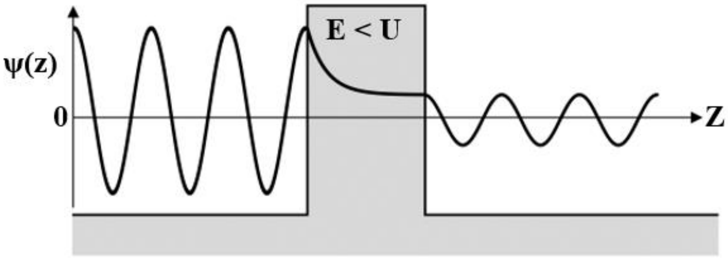

Figure 1.1. Schematic representation of quantum tunneling at the barrier. The tunneling event takes place only when: i) the incoming particle exhibits quantum properties (wave-particle duality), and ii) the energy ($E = \hbar\omega$) of which is less than the barrier height (U), i.e. $E < U$. Along the propagation axis-z, at any point the amplitude of the wave associated with the quantum particle is given by ψ (z) = $\exp(ik.z)$, where ψ is the wavefunction and k is the wave-vector along the propagation axis-z.

According to classical physics, if a classical body does not have enough energy (E) to surmount the energy barrier (U) cannot reach the other side, for example, a ball that does not have enough kinetic energy to surmount the potential energy of the hill will roll down back. However, for the quantum bodies (e.g., subatomic particles with a significant de-Broglie wavelength), this classical picture is no more valid and there is a certain probability of finding these quantum bodies with energy E (< U) to the other side of the barrier height (U) [Fig. 1.1]. This phenomenon is popularly known as *quantum tunneling*.

This basic understanding of quantum tunneling is one of the prerequisites to understand the tunneling mechanism in MTJs. However, in MTJs due to the imbalance in the spin-resolved density of states (DOS) in the FM electrodes, the tunneling process is purely a spin-dependent phenomenon. The spin-dependent tunneling (SDT) will be described in the next subsection.

1.2 Spin-dependent tunneling (SDT)

To calculate tunneling current theoretically, Simmons[38] used an NM|I|NM heterostructure (NM = nonmagnetic metal and I = insulator) with an asymmetrical electrode. Further, Brinkmann[39] extended Simmons's work by incorporating a trapezoidal barrier. These theoretical works completely ignore the spin polarization associated with the ferromagnetic electrodes therefore cannot be appropriate for the MTJs in which the spin-dependent tunneling is prevalent.

In 1972, Meservey et al.[40] reported their transport measurements performed on FM|I|S (where FM and S being the ferromagnet and superconductor respectively) heterostructures. They used an FM electrode (Co, Ni, Fe…) to serve the purpose of spin polarizer whereas the superconducting electrode (Al) on the other side of the tunneling layer (Al_2O_3) was chosen for the spin analyzer/detector. For FM electrodes, the spin polarization (P) at the E_F can be written mathematically as:

$$P\,(E_F) = \frac{(\rho_\uparrow - \rho_\downarrow)}{(\rho_\uparrow + \rho_\downarrow)} \tag{1}$$

Where, ρ is the DOS at the E_F, and up(↑)/down(↓) refers to the majority/minority electrons. In the laboratory experiments, these DOS can be easily extracted out from the second derivative of the conductance i.e., d^2I/dV^2. To understand SDT, the transport experiments performed on a bare aluminum superconductor, NM|I|S (NM being the non-magnetic metal), and FM|I|S (FM being the ferromagnetic metal) heterostructures, and their results are summarized below:

For a bare Al superconductor thin film [Fig. 1.2.a] below its' critical temperature (T_C), the quasiparticle DOS features a gap of 2ΔeV around E_F with characteristic singularities at ±Δ represented by solid and dashed lines[41]. On applying the magnetic field (below to that of the critical magnetic field H_C) along the in-plane direction, the Zeeman splitting appears between DOS of spin ↑ ($-\mu_B.H$ dotted line) and ↓ ($+\mu_B.H$ solid line) quasiparticles. These Zeeman-splitted spin-resolved four sharp features in the DOS will help in determining the contribution of spin ↑/↓ electrons to the tunneling current. If the spin is conserved during the tunneling process, the conductance will be the sum of ↑ and ↓ channels.

For an NM|I|S structure [Fig. 1.2.b], the appearance of four symmetrical peaks indicates that the tunneling process is unpolarized. This is because in metals (M), the DOS at E_F, for both the spin up and down electron is the same, $\rho_\uparrow = \rho_\downarrow$, resulting in a zero-spin polarization.

For FM|I|S structure [Fig. 1.2.c], the appearance of four asymmetrical peaks indicates that the tunneling process is polarized. This is because in ferromagnets (FM), the DOS at E_F, for the spin up and down electron is not the same, $\rho_{\uparrow} \neq \rho_{\downarrow}$, resulting in a non-zero spin polarization. The spin polarization (P) of the FM electrode in terms of the conductance peaks is given by the following formula:

$$P(E_F) = \frac{(\sigma_4 - \sigma_2) - (\sigma_1 - \sigma_3)}{(\sigma_4 - \sigma_2) + (\sigma_1 - \sigma_3)} \tag{2}$$

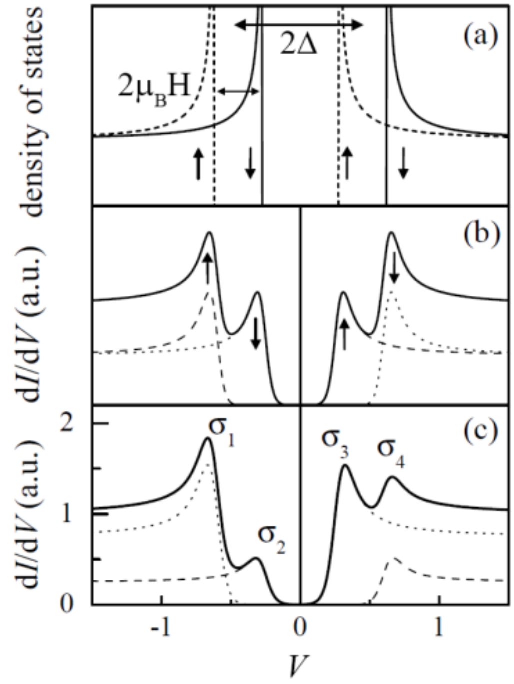

Figure 1.2. Spin dependent tunneling. (a) Zeeman splitted energy levels (± μ_B.H within the 2ΔeV energy gap near E_F for superconductor (Al thin film), **(b)** unpolarized spin tunneling in M|I|S heterostructure with symmetric peaks around E_F, **(c)** spin-polarized tunneling in FM|I|S heterostructures with asymmetric peaks around E_F. The figures are taken from ref [42].

1.3 Tunneling magnetoresistance (TMR) effect

In 1975, Jullière[36] reported the conductance G(V) measurements performed on Fe-Ge-Co junctions. These were the first magnetotransport measurements ever reported for the MTJs. He measured conductance G(V) at both P and AP states of the MTJs and figured out that the conductance is related to the spin polarization of conduction electrons.

To explain his experimental findings, Jullière proposed a theoretical model with the following two assumptions: i) the electron spin remains conserved during the tunneling process i.e., there is no spin-flip event within the barrier, and ii) the probability of the electron's tunneling through the insulating barrier is directly proportional to the number of initial states in the first FM electrode and the available final states in the second FM electrode. According to the first assumption, the electron originating from the first electrode will only be accepted by the second electrode only if the states with the identical spin are available. It allows us to implement a two-current model for the majority and minority electrons. Keeping these two assumptions in mind the conductance (G) in P and AP states can be written as:

$$G_P \propto \rho_1^{\uparrow}.\rho_2^{\uparrow} + \rho_1^{\downarrow}.\rho_2^{\downarrow} \tag{3}$$

$$G_{AP} \propto \rho_1^{\uparrow}.\rho_2^{\downarrow} + \rho_1^{\downarrow}.\rho_2^{\uparrow} \tag{4}$$

Where, G_P and G_{AP} are the tunneling conductance in the MTJs P and AP states respectively, $\rho_i^{\uparrow}$ and $\rho_i^{\downarrow}$ are the DOS of the ferromagnetic electrodes (i =1,2) at E_F for the majority (spin-up) and minority (spin down) electrons, respectively.

The Jullière model is pictorially represented by Fig. 1.3. In the P state [Fig. 1.3.a], the majority electrons (↑) that are in larger number at the emitting FM electrode (left side) finds more available majority (↑) states at the collecting FM electrode (right side) whereas the minority electrons (↓) which are already in smaller number at the emitting FM electrode (left side) finds lesser available minority (↓) states at the collecting FM electrode (right side). Therefore, in the P state of MTJ, $\rho_1^{\uparrow}.\rho_2^{\uparrow} > \rho_1^{\downarrow}.\rho_2^{\downarrow}$.

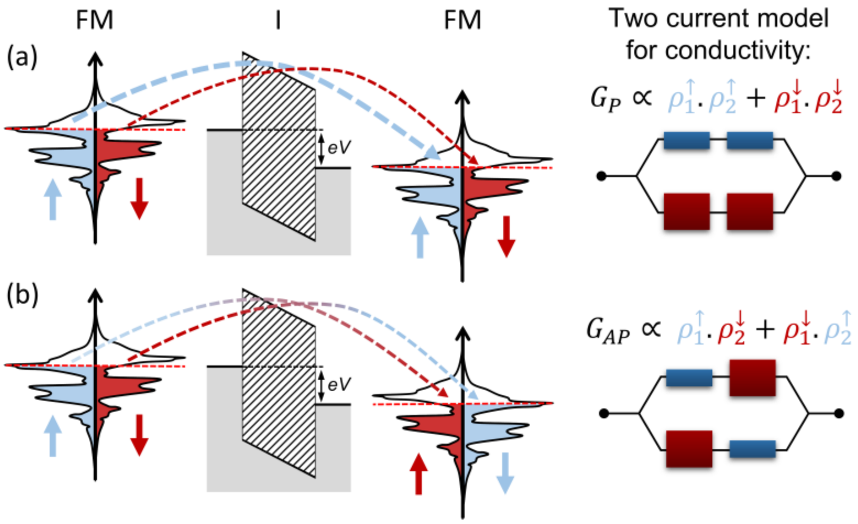

Figure 1.3. Schematic representation of Jullière formalism. The two current model is applied on FM|I|FM trilayer structures, when both the emitting FM electrode (left side) and collecting electrode (right side) are mutually in **(a)** parallel (P) state and **(b)** antiparallel (AP) state. The figures are taken from ref [41].

However, for the AP state [Fig. 1.3.b], due to the reversal of the magnetization direction of one of the FM electrodes, the spin-resolved DOS for that FM electrode gets inverted. In the present scenario for the AP state, we have reversed the spin-resolved DOS for the collecting FM electrode (right side), due to that the majority electrons (↑) of the emitting FM electrode (left side) can only tunnel to the minority states (↓) of the collecting FM electrode (right side) whereas the minority electrons (↓) of the emitting FM electrode tunnel to the majority (↑) states at the collecting FM electrode (right side). Therefore, the total conductance (G) in the P and AP state is not the same. It is clear that the MTJs magnetic state **(**P/AP) alters the spin-polarized DOS of the FM electrodes at E_F and therefore affects the conductance. This difference in the conductance at P and AP states of the MTJs thus leads to the tunneling magnetoresistance (TMR). Mathematically, the TMR for MTJs is expressed by the following formula:

$$\mathrm{TMR} = \frac{\mathrm{G_P} - \mathrm{G_{AP}}}{\mathrm{G_{AP}}} = \frac{\mathrm{R_{AP}} - \mathrm{R_P}}{\mathrm{R_P}} \tag{5}$$

On replacing the G_P and G_{AP} from equation (3, 4) to equation (5) and further using the SP equation (1), the TMR can be written:

$$\mathrm{TMR} = \frac{2\mathrm{P_1P_2}}{1 - \mathrm{P_1P_2}} \tag{6}$$

Where P_1 and P_2 are the spin polarization of the emitting (left side) and collecting (right side) FM electrodes, respectively. For his Fe-Ge-Co junctions, Jullière experimentally measured 14% of TMR. However, for the spin polarization values [P_1(Fe) = 44% and P_2(Co) = 34%] taken from Tedrow and Meserve's measurements on Al-Al_2O_3-Ferro junctions[43], he deduced 26% TMR. Jullière suggested that this difference in the TMR values could be due to the magnetic coupling between the FM electrodes and the spin-flip part of the second-order conductance anomaly[36]. Jullière model was successful to calculate TMR values from the spin polarization of the ferromagnetic electrodes, but it does not take the tunneling barrier into the account. In the next subsection, we will explain how the tunneling barrier plays an important role in determining the TMR.

1.4 Spin and symmetry filtering in crystalline MTJs

From Section 1.3, we have seen that the TMR of an MTJ device in the Jullière approach relies only on the spin polarization of the FM electrodes. Although the Jullière approach[36] was successful for determining the TMR for the MTJs with amorphous barrier e.g., Al_2O_3[5,37], but must be used carefully for the MTJs with crystalline/fully epitaxial structure. In the crystalline solids, the periodic arrangement of the constituent ions produces a periodic potential and thus modifies the electron's wavefunction. For the crystalline FM electrodes, these modified wavefunctions can be grouped according to their symmetries, and tunnels through the available evanescent states within the crystalline barrier (e.g., MgO) with a certain attenuation constant or decay rate. Therefore, during the tunneling process, along with the spin, the symmetry of tunneling electrons also remains conserved. This spin and symmetry conservation of the tunneling electrons give rise to larger TMR for the crystalline MTJs.

To explain the role of spin and symmetry filtering on the magnetoresistive properties of MTJs, we have chosen a very simple trilayer structure Fe|MgO|Fe with perfect crystallinity. The beauty of a defect-free perfect crystalline structure is that its physical properties mostly remain in line with the theoretical calculations. In this section, we will first provide the details of the crystal structure of the entire MTJ. In the second subsection, we will talk about the first principle or *ab-initio* techniques used to describe the third subsection (magnetotransport properties). In the third subsection, we will discuss the conductance of tunneling electrons under the P and AP magnetic state of MTJ.

1.4.1 Crystal structure

In Fe|MgO|Fe MTJ, the iron (Fe) layer act as an FM electrode while the MgO layer serves the purpose of tunneling barrier. The crystalline structure of iron (Fe) below 1180K is body-centered cubic (*bcc*) but above this temperature, it follows the face-centered cubic (*fcc*) structure. Opting the trilayer deposition direction along the (001) direction, the *bcc* Fe structure bears the lattice parameter (a_{Fe}) of 0.287nm [Fig. 1.4.b].

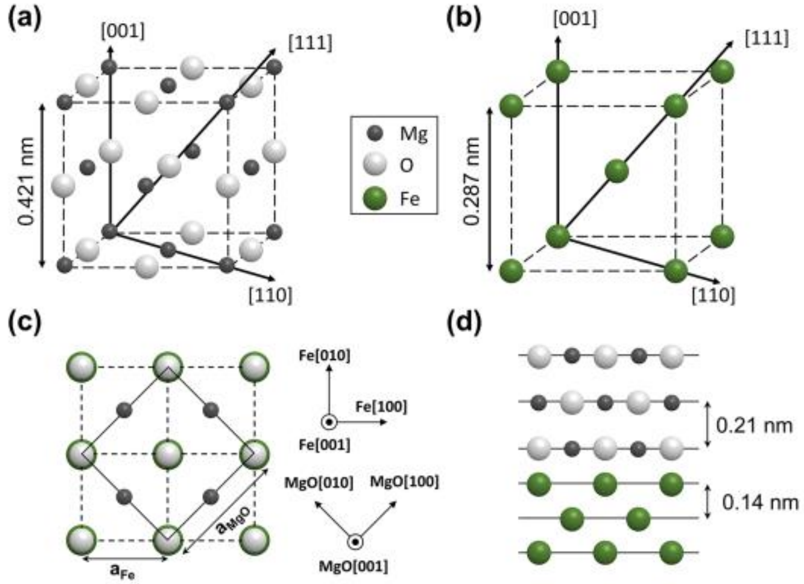

Figure 1.4. Crystal structure of MgO, Fe and Fe|MgO interface. (a) Bulk fcc MgO with lattice parameter 0.421 nm, **(b)** Bulk bcc Fe, **(c)** Fe|MgO interface: fcc MgO(100) with 45^0 rotation along Fe(110) direction. **(d)** Monolayers of MgO (represented with black and white spheres for Mg and O respectively) and Fe (represented with green spheres) with thickness 0.21nm and 0.14nm respectively. The figures are taken from ref [44].

On moving along the (001) direction the next layer to Fe electrode is the tunneling MgO layer. The MgO crystal is formed due to the charge transfer between the Mg and O atoms. In the charge transfer process, the two electrons from the outermost shell ($3s^2$) of Mg ($1s^2$, $2s^2$, $2p^6$, $3s^2$) are transferred to the unfilled p-orbitals of O ($1s^2$, $2s^2$, $2p^4$) atom. In this process, the Mg and O atoms are turned out to the Mg^{2+} (cation) and O^{2-} (anion) with a stable electronic configuration $1s^2$, $2s^2$, $2p^6$. This is also the reason that in the MgO band structure diagram the valence band (VB) and conduction band (CB) are mainly dominated by the states due to the oxygen and magnesium atoms respectively. This charge transfer makes MgO a very stable insulating compound with a direct bandgap of ~7.8eV. The MgO crystal follows the *fcc* (rock salt) structure with the lattice parameter (a_{MgO}) of 0.421nm along the (001) direction [Fig. 1.4.a]. For Fe(100)|MgO(100) structure, due to the significant difference in the lattice parameters between Fe(100) (a_{Fe} = 0.287nm) and MgO(100) (a_{MgO} = 0.421nm), a compressive strain of ~47% is expected from Fe(100) on the MgO(100) layer on top. This huge compressive strain precludes the possibility of the epitaxial growth of Fe(100)|MgO(100) structure. However, the detailed experimental results[45] show that MgO(001) grows epitaxially on top of Fe(001) by rotating itself at the angle of 45^0. This 45^0 rotation of MgO thus minimizes the energy of the trilayer structure and modifies the interface geometry from Fe(001)|MgO(001) to Fe(001)[110]||MgO(001). As a result, the compressive strain exerted by Fe (110) ($a'_{Fe} = \sqrt{2}$ X 0.287nm = 0.406 nm) on MgO (100) (a_{MgO} = 0.421nm) is only 3.7% [Fig. 1.4.c]. Fig. 1.4.d shows the thickness of MgO and Fe monolayers.

1.4.2 First principal approach to Fe|MgO|Fe epitaxial MTJs

From *ab-initio* calculations based on Layered-Korringa-Kohn-Rostoker (LKKR) method[46], Butler et al.[47] calculated the electronic structure of Fe|MgO|Fe MTJ. The LKKR method is based on the density functional theory (DFT) and incorporates the atomic sphere approximation (ASA). This method applies to the periodic (crystalline/epitaxial) solids in which the translational symmetry is preserved. In the crystalline/epitaxial solids, the periodic arrangement of constituent ions produces a periodic potential, due to which the electrons occupy certain states in the energy band. Independent electrons, each of which obeys a one-electron Schrödinger equation within a periodic potential are known as the Bloch electrons. In LKKR method, the electronic wavefunction is described by the product of two functions: (i) the wavefunction that describes the electrons inside the radius defined by the atomic sphere approximation, where the potential due to on-site atoms is large, and (ii) another function that describes the electron in the interstitial region, where the potential of the on-site atoms is negligible. In crystalline solids, the periodic potential modulates the electronic wave function into the form of plane waves. In crystalline solids, these plane waves serve as the basis set for the electron's wavefunction. Assuming the Fe|MgO|Fe heterostructure as an epitaxial system along the z-direction, focussing on the crystalline Fe electrodes, the basis set of plane waves propagated to the entire structure (consisting infinite layers with translational symmetry) allows calculating the reflection and transmission coefficient at the Fe|MgO interface as a function of four scattering matrices (describing the exchange of electrons with the neighboring layers). After extracting the transmission coefficient for each Bloch states, the total conductance can be calculated using the Landauer-Büttiker fomula[48,49]. In the case of perfect translational symmetry, $k_\parallel$ is conserved and the Landauer-Büttiker formula can be simplified into the following for [50]:

$$G = \frac{e^2}{h}\sum_{k_\parallel,j} T(k_\parallel, j) \tag{7}$$

Where, e = electronic charge, h = Planck's constant, T = transimssion coefficient for respective Bloch state j along the transverse mode ($k_\parallel$). Where $k_\parallel = (k_x, k_y)$ is the projection of k on the x-y plane and z- is the direction of the tunneling current perpendicular to the trilayer structure.

1.4.3 Density of states (DOS) plots

Following the formalism mentioned in Section 1.4.2, the spin-resolved tunneling conductance can also be determined for both parallel (P) and antiparallel (AP) magnetic configuration of the MTJ. For Fe|MgO|Fe MTJ with eight monolayers of MgO, the tunneling conductance in the P and AP states are shown by Fig. 1.5.

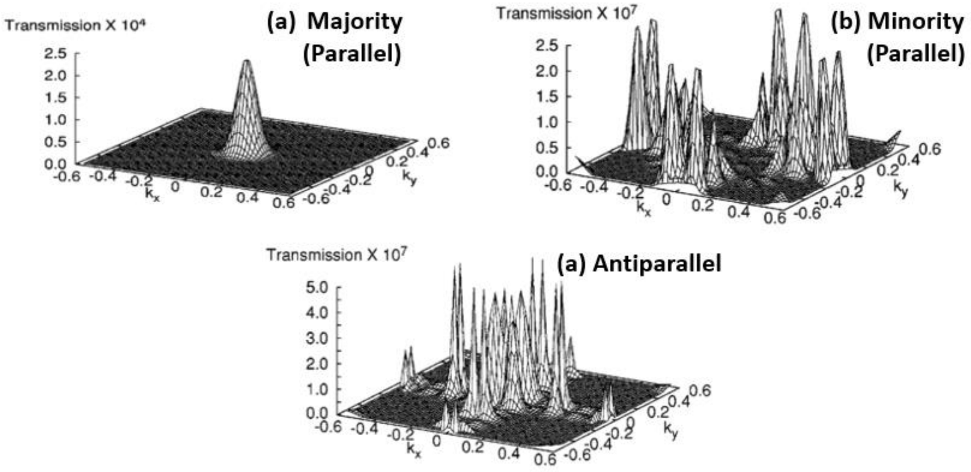

Figure 1.5. $k_\parallel$ resolved conductance plots for Fe|MgO|Fe junction with eight monolayers of MgO for **(a)** majority electrons in the parallel state, **(b)** minority electrons in the parallel state, and **(c)** antiparallel state. The figures are taken from ref [47].

For P state the conductance maxima due to the majority (spin-up) electron are centered at only $k_\parallel = (0,0)$ [Fig. 1.5.a] whereas for the minority (spin down) electrons the conductance peaks are dispersed in the k_x - k_y plane [Fig. 1.5.b]. Moving to the AP state [Fig. 1.5.c], the conductance distribution looks like a blend of both majority and minority conductance distribution in the P state. Further, a significant difference of three orders in the conductance amplitude was observed between the P (majority) and P (minority)/AP state. Due to the significant difference observed in the conductance amplitude between P and AP state, the TMR becomes more pronounced along $k_\parallel = (0,0)$ direction.

1.4.4 Complex band structure and decay parameter (κ)

Considering a simple picture of free electron model in which the electrons are tunneling through a potential barrier of height U, the decay in the wave function is given by exp(-κd), where d is the barrier thickness and the decay constant $\kappa = \sqrt{(2m/\hbar^2)\,(U - E_F) + k_{\parallel}^2}$. This simple expression based on the free electron model for the decay rate however is not correct because it gives a single value of the decay constant irrespective of the symmetries of tunneling electrons. In their detailed theoretical treatment, Butler et al.[51] showed that in addition to the value of $k_{\parallel}$, the decay rate also depends on the symmetries of the tunneling electrons. According to them, the decay parameter (κ) for $k_{\parallel}$ = (0, 0) could be written as:

$$\kappa^2 = \frac{2m}{\hbar^2}\,(U - E_F) - \frac{\langle\phi|\frac{\partial^2}{\partial x^2} + \frac{\partial^2}{\partial y^2}|\phi\rangle}{\langle\phi|\phi\rangle} \tag{8}$$

Where, $\phi(x, y)$ is the amplitude/planar component of the wavefunction $\psi(x, y, z) = \phi(x, y)$. exp-($\kappa$.z). The variation of $\phi(x, y)$ is assumed to be oscillatory. The second term of the above equation is positive and depends on the number of nodes in the planar amplitude $\phi(x, y)$. The higher the number of nodes, the more important $\phi(x, y)$ term is. At the interface, for a given wavefunction, the number of nodes can be determined considering the symmetries in the calculations. These nodes define the curvature in the plane and subsequently decide the decay rates. Fig. 1.6 shows the grouping of different orbitals according to the electronic symmetry.

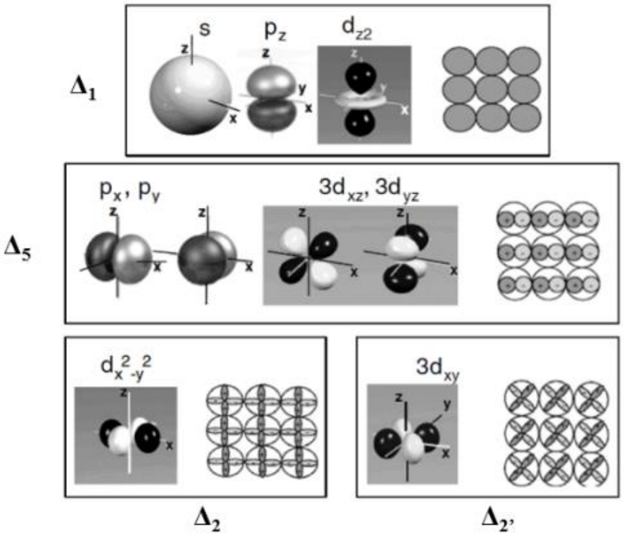

Figure 1.6. The atomic-like orbitals are grouped according to their symmetry properties along the propagation direction (001) in z-axis. In each panel, the extreme right figure represents the corresponding transverse nodes. The figures are taken from ref [52].

Where, g is associated to the planar amplitude $\phi(x,y)$ with a mathematical relation $\phi(x,y) = \exp(ig.\rho)$, ρ being a vector in the x-y plane and g a vector of corresponding reciprocal space. In the tunnel junctions, the Bloch states originating from the FM electrodes match at the interface with the evanescent states caused by the tunneling barrier. Considering the MTJ as an epitaxial system, the k- vector can be decomposed into two parts $k_{||}$ and k_z. The transverse component $k_{||}$ in the plane (k_x, k_y) remains conserved whereas the k_z with complex value ($k_z = q+i\kappa$, where q is the real part and κ is the attenuation constant which decays exponentially exp($-\kappa$d) propagates along the z-direction. Mavropoulos and Dederichs[53,54] showed that the decay rates for the different Bloch symmetry groups tunneling from the electrodes highly depends on the complex k_z vector of the MgO crystal for the corresponding symmetry.

The decay rates (κ) with the Bloch states/electronic symmetries are further classified in Table 1.1. The smaller decay rate ($\kappa_{\Delta1}$) for the Δ_1 symmetry compared to that of the Δ_5 symmetry ($\kappa_{\Delta5}$) at the Fermi level E_F, suggests that the electrons with Δ_1 symmetry within the barrier decay slower than that of the Δ_5 symmetries. The symmetries Δ_2 and $\Delta_{2'}$ are not represented here because of their much smaller decay rate. The MgO barrier preserves the spin and symmetry of the incident Bloch waves during the tunneling process and thus acts as a symmetry filter[55] for the coherent transport.

Bloch state	**Corresponding orbitals**	**Decay parameter (κ)**
Δ_1	s, p_z, $d_{3Z^2-r^2}$	$\sqrt{(2m/\hbar^2)\,(U-E_F)}$
Δ_5	p_x, p_y, d_{xz}, d_{yz}	$\sqrt{(2m/\hbar^2)\,(U-E_F)\,+\,g_1^2}$
Δ_2	$d_{x^2-y^2}$	$\sqrt{(2m/\hbar^2)\,(U-E_F)\,+\,g_1^2}$
$\Delta_{2'}$	d_{xy}	$\sqrt{(2m/\hbar^2)\,(U-E_F)\,+\,g_2^2}$

Table 1.1. The atomic-like orbitals are grouped according to their Bloch states/electronic symmetries and the decay parameter (κ) along the propagation direction (001) in the z-axis.

Fig. 1.7.b refers to the symmetry resolved complex band structure of MgO along Γ-X line in the first Brillouin zone of the reciprocal space [Fig. 1.7.a]. For the dominant tunneling, we are much interested in the decay parameters at the Fermi level E_F.

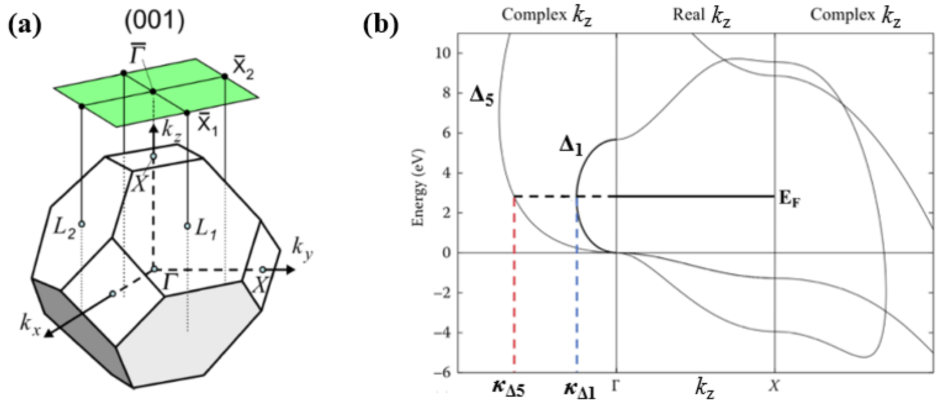

Figure 1.7. Brillouin zone and complex band structure. (a) Brillouin zone of the *fcc* MgO and **(b)** corresponding complex band structure (CBS) with the attenuation constant $\kappa_{\Delta 1} << \kappa_{\Delta 5} << \kappa_{\Delta 2'}$. The figures are taken from ref [53].

1.4.5 Coherent transport and TMR

These different decay rates of the corresponding Bloch symmetries within the MgO tunnel barrier decides the conductance in the MTJ's respective P and AP state. Fig.1.8 shows the total density of states (TDOS) plots for a Fe|MgO(8ML)|Fe epitaxial system in its parallel (P) and antiparallel (P) state[55]. In the P state, the tunneling between the two Fe electrodes is observed for similar spins (majority-majority and minority-minority) electrons [Fig.1.8.a, b]. In the majority-majority tunneling for P state [Fig.1.8.a], all three symmetry groups Δ_1 (s, p_z, $d_{3Z^2-r^2}$), Δ_5 (p_x, p_y, d_{xz}, d_{yz}), and $\Delta_{2'}$ (d_{xy}) are present in the majority channel of both the electrodes. Since the decay rate for the tunneling electrons of $\Delta_{2'}$ symmetry is the highest among all, therefore it doesn't reach the collecting electrode through 8ML of MgO hence doesn't contribute to the conductance.

In the minority-minority tunneling for the P state [Fig.1.8.a], the Δ_5, Δ_2 ($d_{x^2-y^2}$), and $\Delta_{2'}$ are present in the left Fe electrode but only Δ_5 and Δ_2 could reach the right Fe electrode. Therefore, the parallel conductance (G_P) can be written as the sum of all the contributing symmetry resolved conductances:

$$G_P = G_{\Delta_1}^{\uparrow\uparrow} + G_{\Delta_5}^{\uparrow\uparrow} + G_{\Delta_5}^{\downarrow\downarrow} + G_{\Delta_2}^{\downarrow\downarrow} \qquad (9)$$

However, in the antiparallel (AP) state of MTJ for majority-minority tunneling, the available states for the Δ_1 symmetry electrons are missing at the Fermi level (E_F) in the collecting Fe electrode therefore the Δ_1 symmetry will continue to decay in the collecting electrode with almost zero contribution to the total conductivity. Similarly, for minority-majority tunneling, there are no Δ_2 states available at the Fermi level (E_F) in the emitting Fe electrode hence no contribution from the respective symmetry on the total conductivity. In this scenario, the total conductance (G_{AP}) for the

MTJs AP state is only due to the Δ_5 majority-minority (↑↓) and minority-majority (↓↑) tunneling, which could be written mathematically as:

$$G_{AP} = G_{\Delta_5}^{\uparrow\downarrow} + G_{\Delta_5}^{\downarrow\uparrow} \qquad (10)$$

After obtaining G_P and G_{AP}, the TMR can be calculated using the formula: TMR = $[(G_P/G_{AP})-1]$. The difference in the conductance between P (G_P) and AP (G_{AP}) magnetic state is mainly due to the dominance of fully spin-polarized Δ_1 symmetry in the P-state. The conductance difference of three orders between the P and AP state for Fe|MgO(8ML)|Fe MTJ [see Fig. 1.5], thus predicts a huge TMR value.

Finally, the symmetry and spin-resolved tunneling approach by including the role of tunneling barrier for the MTJ operation, thus explains the observed difference in the G_P and G_{AP} leading to the TMR very well.

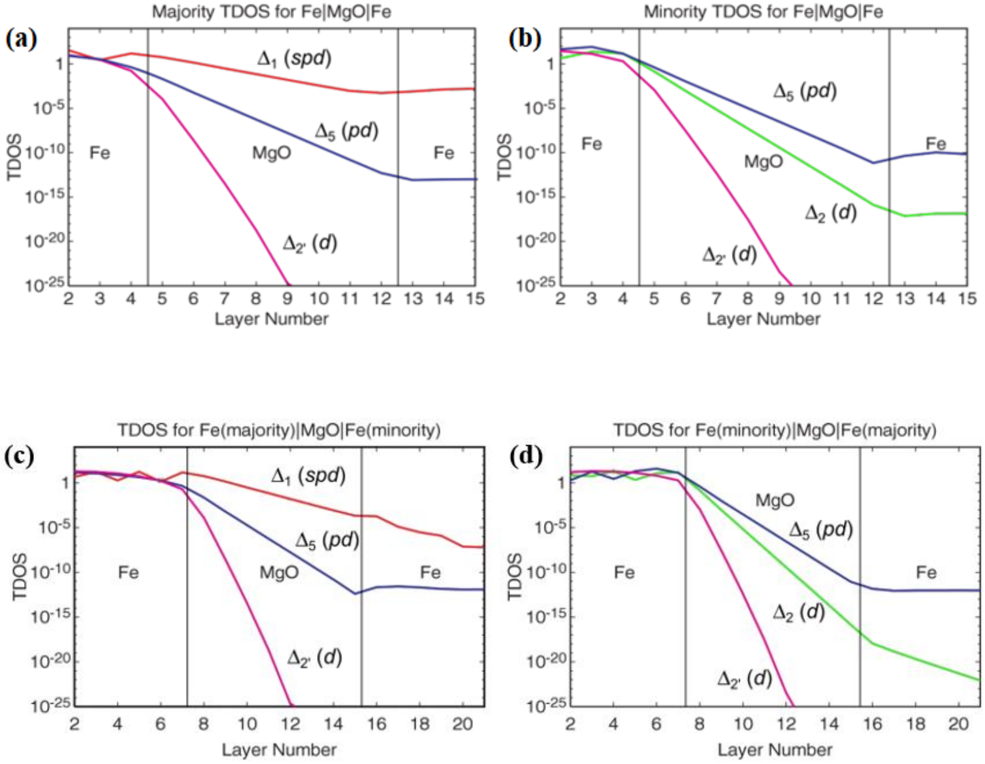

Figure 1.8. Symmetry, spin and layer resolved total density of states (TDOS) plots along k|| = (0,0) for Fe|MgO(8ML)|Fe MTJ in **(a)** P-state, majority-majority tunneling **(b)** P-state, minority-minority tunneling, **(c)** AP state, majority-minority tunneling and **(d)** AP state, minority-majority tunneling. The figures are taken from ref [55].

1.4.6 Choice of the FM electrodes and TMR

From Jullière approach we have understood that the TMR of MTJ devices is directly proportional to the spin polarization at the Fermi energy (E_F) of the FM electrodes. Later, symmetry and spin filtering formalism show that in addition to the spin polarization of the FM electrodes, the tunnel barrier with crystalline structure allows tunneling only those electrons from FM electrodes whose Bloch symmetries matches the evanescent states at the interface. These tunneling symmetries Bloch waves/electrons within the tunneling layer (MgO) also decay at a certain rate.

In 2004 Zhang and Butler[56] theoretically studied the impact of spin polarization of FM electrode on the TMR of MgO-based crystalline/fully epitaxial MTJs. They predicted 5000%, 13000% and 34000% TMR for Fe|MgO|Fe, Co|MgO|Co and FeCo|MgO|FeCo respectively. This drastic increase in the TMR while replacing the FM electrodes from Fe to Co, can be explained by the symmetry and spin-resolved band structure at the Fermi energy (E_F). The band structure for both materials along the direction Γ-H is represented by Fig. 1.9. From the band structure plots, all the states for Co are totally spin-polarized at the Fermi energy (E_F). For both Fe and Co, the Δ_1 state is present for only majority (↑) while the Δ_2 symmetry is present for minority (↓) channels. Further, Δ_5 and $\Delta_{2'}$ symmetries are present for both majority (↑) and minority (↓) channels for Fe but for only minority (↓) channels for the Co. Consequently, the TMR is mainly due to the parallel majority spin (↑) conductance and dominated by the Δ_1 symmetries with the slowest decay rate thus enhancing the conductance (G_P) in the P state. The enhancement in the conductance (G_P) in the P state thus drastically increases the TMR on replacing FM electrode from Fe to Co. Further replacing FM electrode to FeCo, the reflection of all the states at $k_{||}=0$ in the antiparallel state further decreases the antiparallel conductance (G_{AP}) thus increases the overall TMR.

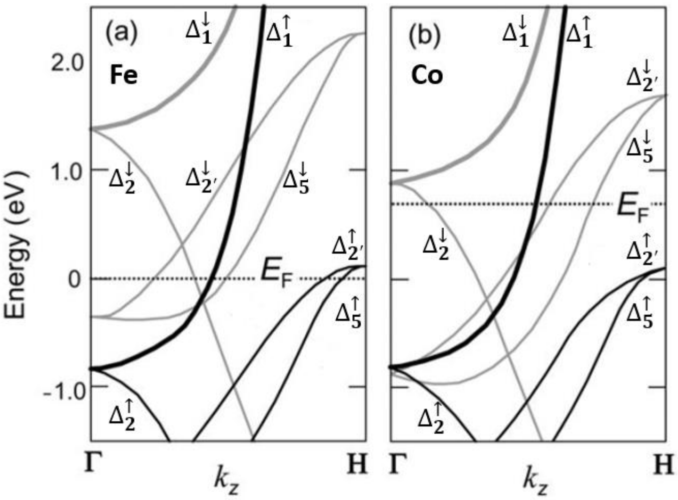

Figure 1.9. Spin and symmetry resolved band structure of **(a)** Fe and **(b)** Co electrodes. The figures are taken from ref [57].

1.5 Evolution of tunneling spintronics

The theoretical research on tunneling spintronics in MTJs was initiated with comparatively simple Fe(001)|MgO(001)|Fe(001) crystalline/fully epitaxial structures. Several theoretical research groups predicted a very large TMR for these MTJs. In 2001, M. Bowen et al. reported the first sizeable TMR of 27% (60%) at room temperature (30K) for the sputtered/laser-ablated Fe(001)|MgO(2nm)|FeCo(001) single crystal epitaxial junctions[58]. Two years later in 2003, Faure-Vincent et al.[59] reported an increased TMR up to 67% at room temperature for MBE grown Fe(001)|MgO(001)|Fe(001) MTJs. In 2004 Yuasa et al. grown single-crystal Fe(001)|MgO(001)|Fe(001) MTJs using the molecular beam epitaxy (MBE) technique[60]. The reported TMR for these MBE-grown MTJs was up to 70%[60]. To utilize the spintronic properties of MTJs for technological applications, efforts were made to mass-produce them. The very slow deposition rate (1µm/h)[61] of the MBE technique although is a key to grow highly epitaxial multilayer structures but at the same time limits itself to be used for mass production. Thanks to the sputtering technique! due to which the mass production of these MTJ devices could be possible. In the same year 2004 when Yuasa et al. published their experimental findings (in the same volume no. 3 of *Letters to Nature*!), Stuart.S.P. Parkin et al. reported a very large TMR up to 220% at room temperature for their sputter and ion-beam grown TaN|IrMn|CoFe|Fe|MgO|CoFe|TaN and TaN|IrMn|CoFe|CoFe|MgO|CoFe|Mg textured MTJs on top of Si/SiO_2 substrate[62]. In 2005 Djayaprawira et al.[63] fabricated MTJs of Ta|PtMn|CoFe|Ru|CoFeB|MgO|CoFeB|Ta|Ru structure, exhibiting TMR values up to 230% at room temperature. In their experiments Djayaprawira et al.[63] revealed that after the MTJ growth followed by the annealing step (360^0C for 2h), CoFeB electrodes were essentially amorphous with some parts crystallized. They assumed that the high annealing temperature might be the reason for the partial crystallization of amorphous CoFeB electrodes. Surprisingly the MgO layer showed a good crystalline structure with a (001) fiber texture [63]. In the same year 2005, Yuasa et al. [64] reported their experimental findings intended for CoFeB|MgO|CoFeB MTJs. From the RHEED patterns, they found that MgO layer grown on an amorphous CoFeB layer has an amorphous structure up to the MgO thickness (t_{MgO}) of 4ML and begins to crystallize with (001) preferred orientation when $t_{\mathrm{MgO}} \geq$ 5ML [64]. By annealing, an amorphous CoFeB layer grown on MgO (001) crystallizes in a body-centered-cubic (bcc) structure with (001) orientation because MgO (001) acts as a template to crystallize CoFeB [64]. The amorphous structure of bottom CoFeB layer at the interface with antiferromagnetic layer (IrMn) below it, also serves as a buffer layer and preserves the structure of the layers grown above. In MTJs the annealing process also pins/fixes the magnetization direction of the bottom FM electrode by the exchange coupling with the underlying synthetic antiferromagnetic IrMn film. However, the magnetic decoupling between the two FM electrodes in the MTJs is mainly achieved by the insertion of insulating layer (tunneling barrier) in between but pinning/fixing the magnetization of the bottom electrode allows to achieve perfect P or AP state within a certain limit of applied magnetic field.

Although the annealing step is necessary to improve the crystallinity at the interfaces and to pin the magnetization of the bottom ferromagnetic electrode (using the antiferromagnetic layers such as IrMn) but at higher temperatures ($\geq 450^0$C) but also diffuses the elements from the bottom layers (such as Ta, Pt, Mn, Ru, etc.) to the interface and thus decreasing the TMR[65]. Hayakawa et al. showed that the higher annealing temperatures (450^0C) for their pseudo spin valves of CoFeB|MgO|CoFeB trilayer structure, improves the TMR up to 472% at room temperature and 804% at 5K. These experimental TMR values were close to the theoretical values exceeding 1000% predicted by Mathon and Umerski, however for the Fe(001)|MgO(001)|Fe(001) crystalline/fully epitaxial MTJs[66]. The incorporation of amorphous CoFeB electrode in the MTJs with annealing step at high temperature, thus tremendously improved the TMR.

Efforts were also made to increase TMR by adopting FM electrodes with high spin polarization (SP) into the MgO-based MTJs. Due to the high spin polarization of cobalt (Co) compared to that of Fe at the Fermi energy (E_F), it seems that Co electrodes could lead to higher TMR in the MgO based MTJs [Section 1.4.6] but the hexagonal closed packed (hcp) structure of Co which is very different to the bcc crystal structure of Fe, limits its integration in the MgO based MTJs. To find a balance between the desire for high spin polarization and the preferred bcc structure of FM electrode (required for high symmetry and spin filtering) the idea of Co doping in Fe electrodes was proposed. Lee et al.[67] comparatively studied the effect of Co doping (x=14%, 25%, 50%, and 75%) on their $(Co_xFe_{100-x})_{80}B_{20}$|MgO|$(Co_xFe_{100-x})_{80}B_{20}$ MTJs of pseudospin valve structure. Following the annealing step at 450^0C for 1h, they measured TMR up to 500% at room temperature for 25% Co doping. Cross-sectional high-resolution transmission electron microscopy (HRTEM) characterizations revealed that at Co doping of 25%, the interface between the top FM electrode and MgO i.e., MgO |$(Co_{25}Fe_{75})_{80}B_{20}$ crystallized to bcc structure along the (001) direction for the entire region [67]. In this experiment an optimum balance between the favored bcc geometry and high spin polarization of the FM electrode was achieved by 25% Co doping, yielding a TMR of 500% at room temperature.

Later in 2006 Ikeda et al.[68] made a breakthrough by reporting a record TMR up to 604% at room temperature for their Ta|$Co_{20}Fe_{60}B_{20}$|MgO| $Co_{20}Fe_{60}B_{20}$|Ta MTJs of the pseudospin valve structure. In addition to the Co doping, Ikeda et al. made the bottom FM layer thick to avoid Ta diffusion at the $Co_{20}Fe_{60}B_{20}$|MgO interface during the annealing step performed at 500^0C. The improvement in the interface quality was also confirmed by X-ray diffraction (XRD) measurements.

1.6 Defects in CoFeB|MgO|CoFeB MTJs

Despite the success achieved so far on MTJ device engineering thus increasing their TMR, the experimental TMR however could not reach the values predicted theoretically[56,68]. Further, from the device engineering point of view, there is always a possibility that the structural defects such as stacking faults, grain boundaries, point defects (vacancies and interstitials), and compound point defects (Schottky and Frenkel pairs) could grow in the material thus altering its ideal crystal structure [69,70]. Here we will briefly describe the different kinds of defects that can be present in the MTJ devices.

1.6.1 Interface oxidation

In Fe|MgO|Fe MTJs, the oxygen atoms of MgO are located on top of the Fe layer [Fig. 1.4.c]. Although the Mg-O bond is more favorable energetically than the Fe-O bond, Meyerheim et al. [71] reported the presence of Fe-O layer at the Fe|MgO interface. Using the LKKR method, Zhang et al. [72]calculated the conductance for Fe|FeO_x|MgO(8ML)|Fe as a function of the oxygen concentration (x) and found a significant drop in the parallel conductance on increasing the concentration of oxygen. DOS plots [72] revealed this drop in the parallel conductance was due to the lowered density of Δ_1 electrons at the Fermi energy (E_F). Contrary to the parallel conductance, the antiparallel conductance (dominated by Δ_5 electrons) was barely affected by the oxygen concentration (x) thus causing a drop in the TMR. These theoretical results were later supported by the experiments performed by Bonell et al. [73]. However, the experimentally measured drop in the TMR[73] was not found that much drastic as predicted by the calculations[72]. In their concluding remark, Bonell et. al. [73] suggested that although interface oxidation has a negative impact on TMR, they are not the principal source of the discrepancies between the theory and experiment.

1.6.2 Grain boundaries

In polycrystalline samples, the area that preserves a single crystalline structure is known as the grain. These grains are randomly oriented and seem to be separated by the regions where the atoms are randomly distributed or do not preserve the crystallinity. This noncrystalline region, separating two neighboring grains is known as the grain boundary or grain wall. The thickness of the grain boundary is very crucial in determining the electrical and lattice (phonon) properties of the material.

These grain boundaries are also present in the commercial CoFeB|MgO|CoFeB MTJs with textured MgO (001) barrier. To investigate the role of grain boundaries on the transport Mizuguchi et al.[74] performed in-situ scanning tunneling microscopy (STM) measurements on the polycrystalline MgO (001) barrier grown on top of the CoFeB electrode. They found that the tunneling current flows uniformly despite the existence of the grain boundaries within the MgO (001) tunneling barrier therefore the grain boundaries do not considerably affect the overall spintronic performance of the MTJ device. Experiments combined with *ab-initio* calculations[75] also revealed that these grain boundaries buried within the MgO can lower the MgO band gap locally down to 3eV. Due to the lowered symmetry at the grain boundaries, the symmetry filtering effect is not that effective as ideal MgO resulting in the overall TMR. This model is very simple and does not take the band structures of CoFeB electrode and MgO (that are the core of the MTJ device operation) into account therefore seems to be inefficient.

1.6.3 Boron diffusion

From the symmetry and spin filtering approach, we have seen how important the FM|MgO interface and the tunneling barrier (MgO) are in determining the spintronic performance of the MTJ devices. We have seen that, incorporating CoFeB as FM electrode in MgO based MTJs, has significantly increased the TMR[68] but there are possibilities that during the annealing step, boron (B) being a comparatively light element might diffuse from CoFeB electrode: (i) to the MgO interface or within the MgO layer (as an interstitial) [76–78], and (ii) and segregate into neighboring Ta layers, resulting in a sharp and impurity-free clean CoFeB|MgO interface [79,80]. Several theoretical reports with contradictory results have been published for the boron (B) diffusion and its impact on the spintronic performance of the MTJs. According to Burton et al.[81] the diffusion of B at the interface reduces the conductance through the Δ_1 channel thus reducing the TMR. Han et al.[82] using ab-initio calculation showed that the B diffusion within the MgO reduces the effective bandgap thus enhances the tunneling current and TMR of the MTJ device. A different situation was conceived by Bai et al. according to which the interface between CoFeB and MgO consists a $Mg_3B_2O_6$ phase [78]. The above calculations seem to be interesting, but they lack the barrier energy calculations required for the migration of boron (B) across the interface. Therefore, it is not clear whether the results reached are realistic. Recent experiments however revealed that boron (B) is not found within the MgO barrier[79,83,84].

1.6.4 Oxygen vacancies

These are the most common point defects that can be present in any oxide material. The presence of the oxygen vacancies in MgO gives rise to a variety of interesting optical[14], catalytic, and transport properties that are absent in the ideal crystalline solid[85]. Since MgO is an ionic compound therefore there are chances of forming vacancies (neutral or charged) due to both magnesium (Mg) and oxygen (O). Within a MgO unit cell, the vacancies formed due to the single Mg and O are represented by V and F-centers respectively. These vacancies can be single V and F- centers and or paired P (due to the two nearest neighboring Mg and O atoms within a MgO unit cell) and F_2 or M-centers (due to the two nearest neighboring oxygen atoms within a MgO unit cell) [Fig. 1.10].

Gibson et. al.[13] theoretically calculated the formation energies for all the possible point defects due to the oxygen and magnesium vacancies in the MgO. They found that the oxygen vacancies exhibit the lowest formation energy among all, therefore are more likely to occur in MgO. The theoretically calculated formation energies for different types of vacancies within the MgO crystal are tabulated in Table 1.2. These defect states create additional energy levels within the nominal bandgap of MgO, in turn, lower the effective barrier heights for the tunneling electrons in an MTJ. Electrons tunneling through these energy levels with lowered barrier height might encounter different scattering rates compared to that of an ideal barrier. Moreover, these defect states can mix symmetries of the electron wave function and might have a negative impact on the spintronic performance[85].

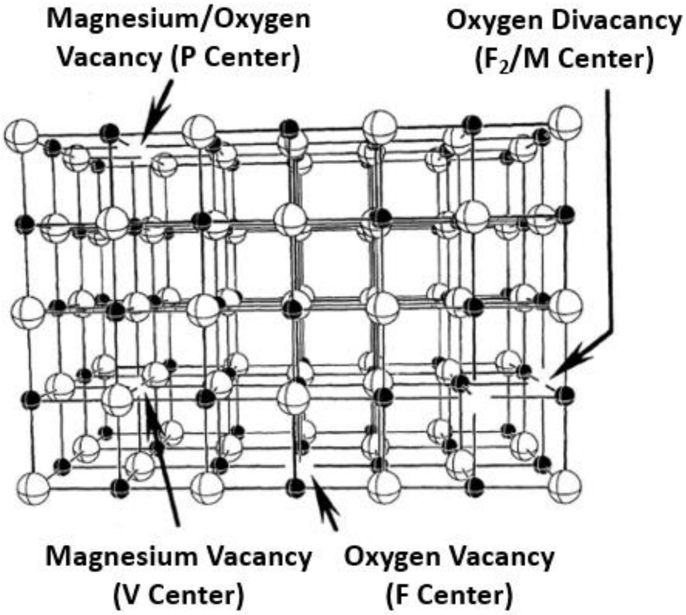

Figure 1.10. Different types of point defects (vacancies) due to the Mg and O atoms within the MgO crystal.

For the tunneling electrons, these defect states within MgO serve as preferred transport paths and can be probed experimentally [Chapter-2]. Table 1.3 summarizes, the experimental values of the MgO barrier heights in MTJs with varying thickness of MgO and different FM electrodes. It is clear from Table 1.3 that the experimentally measured values of the barrier heights of the MgO are much lower than its nominal bandgap (3.9 eV).

Defect	**F**	**F^+**	**F^{2+}**	**F_2/M**	**V**	**V^-**	**V^{2-}**	**P**
Formation Energy (eV)	1.82	3.67	5.47	3.23	13.82	14.83	16.35	3.48

Table 1.2. Calculated formation energies for different types of possible point defects within the MgO crystal. Values are taken from ref [13] and the table is taken from ref [85].

These lowered barrier heights are in fact originated due to different kinds of oxygen vacancies (neutral as well as charged states) within the MgO tunneling layer. The lowered barrier height of 1.1 eV is associated with the single oxygen vacancy F/F^+. Out of the oxygen vacancies mentioned in Table 1.3, the double oxygen vacancy (F_2 or M-center) with a barrier height as low as 0.4 eV seems to be very interesting for the spintronic application[86]. The motivation of the first part of my thesis is to investigate the role of these oxygen vacancy-induced localized states on the spin-transfer torque (STT) therefore these oxygen vacancy states will be described here followed by the STT mechanism and the previous reports (if any) linking both.

MTJ	**TMR (%)**	**Barrier height (eV)**	**t_{MgO} (nm)**	**Reference**
Fe|MgO|Fe	180_{RT} (247_{20K})	0.39	2.3	Ando [60]
Fe|MgO|Fe	130_{RT} (190_{1K})	0.38/0.82*****	2.5	Münzenberg [87]
Fe|MgO|FeCo	$23_{4.2K}$/20_{70K}	0.9	2.6	Takanashi [88]
FeCo|MgO|FeCo	120_{RT} -220_{RT}	1.1-1.7	2-3	Parkin [62]
FeCoB|MgO|FeCoB	100_{RT}	0.62/0.5******	2.5	Bowen [86]
FeCoB|MgO|FeCoB	165_{RT}	0.45-0.59	1.35	Freitas [89]
FeCoB|MgO|FeCoB	136_{RT} (235_{13K})	0.7/$0.4^{\#}$ and $0.45^{\#\#}$	0.6-0.9	Bowen [Present work]

Table 1.3. Experimental barrier heights for the MTJs with the different electrodes and varying MgO thickness. ***** Barrier heights calculated for the symmetry coherent tunneling process and the normal spin coherent tunneling process, respectively. ** Barrier heights calculated from the $\hat{I}$-measurement performed in parallel and antiparallel magnetic configurations, respectively. $^{\#}$ Barrier height measured experimentally from $\hat{I}$-measurement performed in parallel configuration. $^{\#\#}$ Barrier height calculated using Brinkman fit in the antiparallel configuration.

1.6.4.1 Single oxygen vacancy or F-center

As described in Section 1.4.1, MgO is an ionic compound formed by Mg^{2+} and O^{2-} ions. In MgO, a single oxygen vacancy or F-center can be created by removing one oxygen atom thus leaving the two electrons of O^{2-} (donated by Mg^{2+}) behind. These two electrons left behind remain localized in the oxygen vacancy site to preserve the ionicity of Mg^{2+} and O^{2-} ions required for a chemically stable structure.

To determine the electronic structure of the single oxygen vacancy (F-center) and its impact on the tunneling transport, Velev et al. [1] performed *ab-initio* calculations by incorporating F-center in bulk MgO. The DOS plots for bulk MgO in the ideal form (represented by gray shade) and with F-center (red and blue color) are shown in Fig. 1.11.i. The presence of the F-center in bulk MgO results in two additional peaks in the DOS plot. These two peaks centered at ~1eV below (F*s* represented by the red line) and ~4 eV above (F*p* represented by the blue line) to the Fermi energy (E_F). The electronic state F*s* is located in the valence band of MgO and is localized with double occupancy while the F*p* overlaps with the conduction band and is unoccupied. From charge density plots [Fig. 1.11.a, b] it was revealed that these F*s* and F*p* states exhibit charge distribution of spherical or *s*-character and *p*-character respectively and both of them hybridize with the *p*-states of neighboring oxygen atoms.

The F*s* electronic state hybridizes with the nearest neighbor oxygen atoms only therefore appears as a strongly localized sharp state in the DOS plot [Fig. 1.11.a]. Contrary to F*s*, the electronic state F*p* partially overlaps with the conduction band and interacts with the oxygen atoms far away therefore found to be less localized [Fig. 1.11.b].

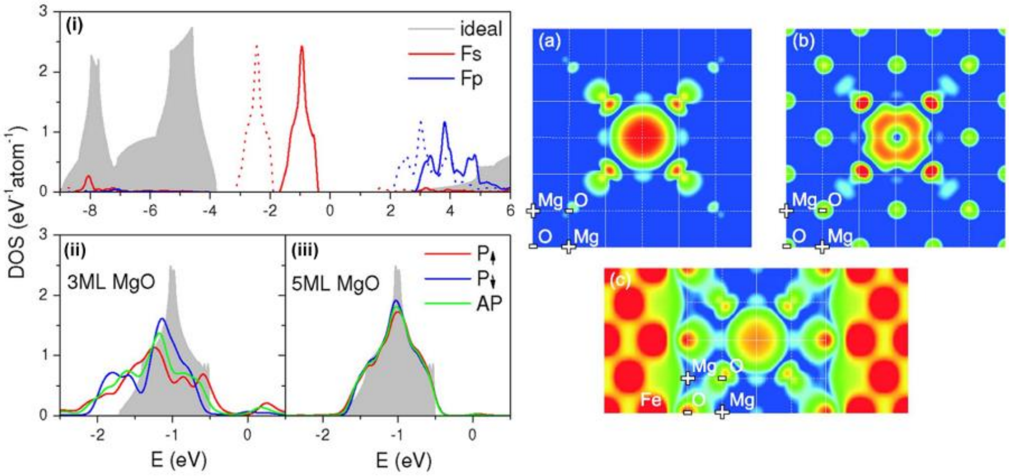

Figure 1.11. DOS plots of MgO with and without single oxygen vacancy or F-center. (i) Ideal MgO (gray shade) and F-MgO (red, and blue). Spin resolved DOS plots for (ii) Fe|F-MgO(3ML)|Fe and (iii) Fe|F-MgO(5ML)|Fe in parallel and antiparallel state. The figures are taken from ref [2].

To know how these localized states due to the F-centers modifies the barrier height of MgO within the MTJs, Velev et al. [2] further performed *ab-initio* calculations for Fe|F-MgO|Fe trilayer structures. They created F-center in the middle layer of MgO [3ML, represented by Fig. 1.11.ii and 5ML, represented by Fig. 1.11.iii] in Fe|MgO|Fe trilayer structure and compared the F*s* DOS calculated in both parallel (spin-resolved) and antiparallel state with the F*s* DOS of the bulk F-MgO (represented by gray shade). For 3ML MgO, broadening in the F*s* DOS was observed [Fig. 1.11.ii], however, increasing the thickness of MgO to 5ML the F*s* DOS recovered its shape [Fig. 1.11.iii]. This broadening in the F*s* DOS for 3ML is a result of strong coupling between the FM electrode and the F-center. These theoretical results suggest, to avoid strong coupling between the FM electrode and the oxygen vacancies, both must be apart of each other by at least 2ML thickness of MgO. The calculated charge density for Fe|F-MgO(5ML)|Fe is shown in Fig. 1.11.c. From the charge density plot, it is clear that similar to bulk F-MgO, F*s* in Fe|F-MgO(5ML)|Fe, interacts with the nearest neighbor oxygen atoms.

1.6.4.1.1 Impact of F-centers on coherent transport

Velev et al.[2] calculated the spin-dependent conductances for Fe|F-MgO(5ML)|Fe in both parallel and antiparallel states [Fig. 1.12.a, b, c]. The corresponding energies of the electronic states due to the F-center created in the third monolayer of MgO, in resonance with the energies of tunneling electrons produce two conductance peaks at 1eV and 3.5eV below and above the Fermi energy (E_F) respectively. The conductance peak below 1eV from the E_F is of *s*-character and lies in the valence band while the peak corresponding to the energy 3.5eV above E_F is of *p*-character and lies in the conduction band (not shown). In the resonance, the conductance for Fe|F-MgO(5ML)|Fe increases for both spin channels (majority and minority) in P and AP state, as a result, the difference between G_P and G_{AP} decreases. This lowered difference in G_P and G_{AP} for Fe|F-MgO(5ML)|Fe compared to that of the defect-free or ideal structure thus decreases the TMR.

Away from the resonance, the conductance for Fe|F-MgO(5ML)|Fe structure in the P-state due to the majority electrons $\Delta_1^{\uparrow}$ decreases 5-7 times compared to its defect-free/ideal counterpart structure. However, the conductance calculated in the AP state and for minority electrons ($\Delta_1^{\downarrow}$) in the P state, away from the resonance is not affected and follows the corresponding conductances calculated for defect-free/ideal structure. Therefore, away from the resonance, the decrease in the G_P for majority electrons ($\Delta_1^{\uparrow}$) thus further lowers the difference between G_P and G_{AP} for Fe|F-MgO(5ML)|Fe compared to that of the defect-free or ideal structure thus leading to a further decrease in the TMR [Fig. 1.12.d]. This reduction in the conductance of the majority channel in the P state is due to the inelastic tunneling induced by the oxygen vacancies, allowing scattering to the states with $k_{\parallel} \neq (0,0)$ leading to more attenuation.

In order to support the scattering interpretation, the complex band structure (CBS) of bulk MgO with and without F-center was calculated. Fig. 1.12.e plots the decay rate of Δ_1 states as a function of energy in bulk MgO for ideal (represented by the black line) and F-MgO (represented by the dotted red line). At resonance (-1eV), a strong reduction in the decay rate was observed. However away from resonance, an increase in attenuation constant/decay rate (κ) was witnessed. In addition to that the probability density $\psi^*.\psi = |\psi|^2$ calculated as a function of MgO barrier thickness (t_{MgO}) for the Δ_1 symmetry electrons for the Fe|F-MgO|Fe system (represented by red dotted line) was found lower than that of the ideal Fe|MgO|Fe structure (represented by the black line).

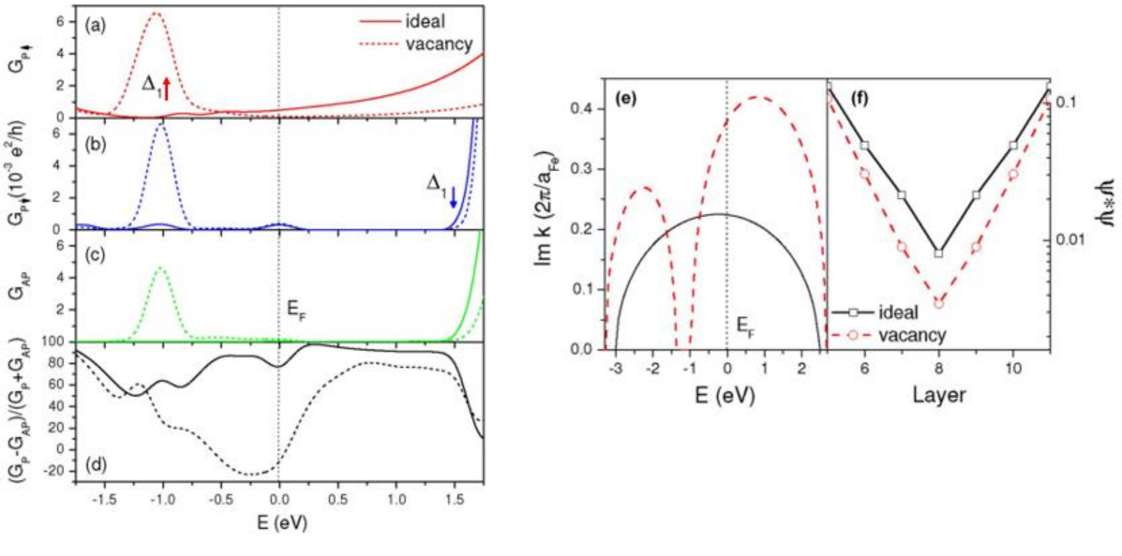

Figure 1.12. Resonant conductance plots for (a) majority $\Delta_1^{\uparrow}$ state in P state, **(b)** minority $\Delta_1^{\downarrow}$ in P state, **(c)** AP state. For all these three figures the dotted line represents the Fe|MgO(5ML)|Fe system with F-center and in its defect-free/ideal form. **(d)** Depiction of lowered TMR due to the enhanced asymmetry in the G_P and G_{AP} caused by the F-center (dotted black line) and the TMR for the ideal structure (solid black line). **(e)** Calculated attenuation constant/decay parameter (κ) for bulk MgO with F-center (red dotted line) and defect-free/ideal MgO. **(f)** Calculated probability density ($\psi^*.\psi = |\psi|^2$) as a function of tunnel barrier thickness for Fe|MgO|Fe system with MgO with F-center (red dotted line) and defect-free/ideal MgO (black solid line). The figures are taken from ref [2].

In an MTJ, the decrease in TMR is closely related to the concentration of the F-centers within the MgO. In 2014, using *Î*- and $\mathrm{TMR}_{\mathrm{rel}}$ spectroscopy techniques, Schleicher et al.[86] confirmed the presence of these single oxygen vacancy or F-centers (F^0 and F^+) in their MTJs of Ta(5)|Co(10)|IrMn(7.5)|FeCoB(4)|MgO(2.5)|FeCoB(4.5)|Ta(5)|Pt(5) multilayer structure grown on top of the Corning 1737 glass substrate. They further experimentally demonstrated that the observed decrease in the TMR is due to the contribution of these defect states in the transport.

In the next section, we will see how these single oxygen vacancies (F-centers) can be harnessed to improve the spintronic performance of the MTJ device.

1.6.4.2 Double oxygen vacancy or M-center

The higher concentration of oxygen vacancies within the MgO forms a variety of complicated vacancy structures. At higher concentrations, out of the possible oxygen vacancy structures, the simplest one is the double oxygen vacancy or M-center formed as a result of the hybridization between the two nearest neighbor single oxygen vacancies. These M-centers can also be charged (M^+) or in their excited states (M*). In 2012 Mckenna and Blumberger[3] calculated the electron transfer rates between the two adjacent F-centers F^0 and F^+ separated by a distance *d* using the *Marcus theory*[90]. In order to apply Marcus theory, the key parameters i.e., electronic coupling matrix element (H_{ab}) and the reorganization energies (λ) were calculated using the constrained density functional theory (CDFT)[3]. The panels a, b, and c in Fig. 1.13 respectively represents the electronic coupling matrix element (H_{ab}), reorganization energy (λ), and the electron transfer rate (k_{et}) as a function of the separation (d) between the adjacent single oxygen vacancies along the different crystallographic directions. From panel (a), it was expected that the electronic coupling matrix element (H_{ab}) should decrease exponentially (represented by the red line) with the separation between the consecutive F vacancies (d), however it was observed that the values of H_{ab} deviate significantly from the expected behavior. The authors linked this observed abnormal behavior in H_{ab} with the intrinsic magnetic anisotropy of the system. In fact, the electron coupling between the consecutive defects along the [110] direction (as shown in panel (a)) was found larger than the consecutive defects that are much closer but along different directions. This larger electronic coupling along [110] direction is due to the mixing of *p*-orbitals of the oxygen atoms (that are extended towards [110] direction) with the *s*-like electronic wave function of the defects resulting in a large charge density along [110] crystallographic direction.

From panel (b), the reorganization energy (λ) is found to be very large for the *d* values less than 5Å. This is due to the overlapping and opposing ionic distortion fields. λ becomes smaller for distances larger than 5Å and increases slowly with defect separation.

From panel (c), the calculated electron transfer rate between the adjacent F-centers exhibits three different tunneling regimes: (i) *non-adiabatic* for the adjacent F-centers that are separated by the distance (d) more than 11Å. In this region on increasing *d*, the electron transfer rate (k_{et}) decreases exponentially due to the weak electronic coupling between the adjacent F-centers, (ii) *adiabatic* for the adjacent F-centers that are separated by the distance between 6 Å and 11Å. In this region, the electron transfer rate (k_{et}) does not follow the monotonic exponential behavior (as seen for the non-adiabatic regime) because the electron transfer rate now depends on both the electronic coupling (H_{ab}) and the strong increase in the reorganization energy (λ) which in turn defines the electron transfer activation energy, and finally the (iii) *coherent* regime for the adjacent F-centers that are separated by the distance (d) less than 6Å. This regime is characterized by negative activation energy, meaning that the electron is delocalized in the two defect sites. In this case, the electron transfer mechanism crosses over from incoherent to coherent tunneling. This was the first report[3] indicating that the pair of oxygen vacancies or M-centers can preserve the coherent tunneling and the symmetries of the incoming or tunneling electrons within the MgO. However, these results were obtained for the bulk-MgO, and not for the real MTJs with MgO as a tunneling barrier, but provided an indication to the spintronic community that the defect states due to the oxygen vacancies can be harnessed to improve the spintronic performance of the MTJ devices.

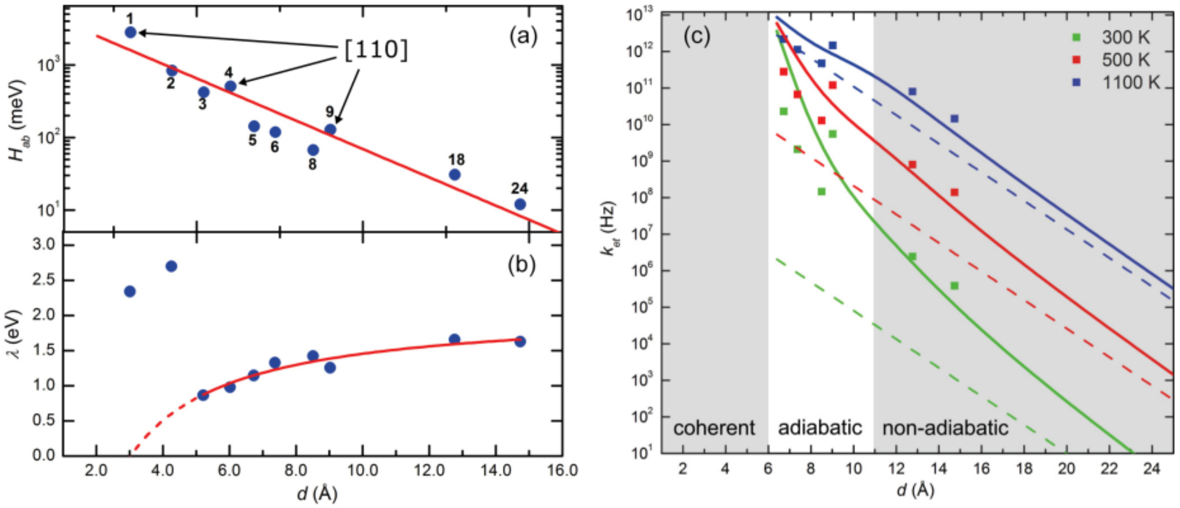

Figure 1.13. Theoretically calculated plots for (a) Electronic coupling matrix element (H_{ab}), **(b)** Reorganization energy (λ), and the **(c)** Electron transfer rate (k_{et}) between the oxygen vacancies F^0 and F^+, as a function of the separation between (*d)* within the bulk-MgO. The figures are taken from ref [3].

1.6.4.2.1 Electronic structure and impact of M-center on coherent transport

Recently, Taudul et al.[4,85,91] implemented these defects into the MTJ structures and systematically studied their impact on the TMR. In their first report[4] they created M-centers within the bulk-MgO and at the middle monolayer of MgO in FeCo|MgO(7ML)|FeCo MTJs. From the density of states (DOS) calculations performed for bulk-MgO [Fig. 1.14.a], the incorporation of double oxygen vacancy (M-center)**,** results in the formation of two occupied energy levels at 1.1eV and 0.4eV below the Fermi energy (E_F). The occupied energy levels centered at 1.1eV and 0.4eV below E_F are denoted by M_1 and M_2 centers respectively. From charge density plots [inset of Fig. 1.14.a], both M_1 and M_2 energy states exhibit a spherical charge distribution (s-character but) with bonding and antibonding nature respectively. Similar to the energy states created by the F-centers below to the Fermi energy [Section1.6.4.1] these M_1 and M_2 states are also localized. In addition to the energy levels below E_F, two additional unoccupied energy states of *p*-character are also observed above E_F. Further incorporating the double oxygen vacancy (M-center) at the 4th ML of MgO within FeCo|Co|MgO(7ML)|Co|CoFe MTJs they found the position of the M_2 energy level at ~0.3eV. Due to the low barrier heights of 0.4eV (in bulk MgO), 0.3eV (present multilayer structure), and *s*-character these M_2 defects could enhance the already favored spin-polarized tunneling for the incoming Δ_1 symmetry electrons from the FM electrode.

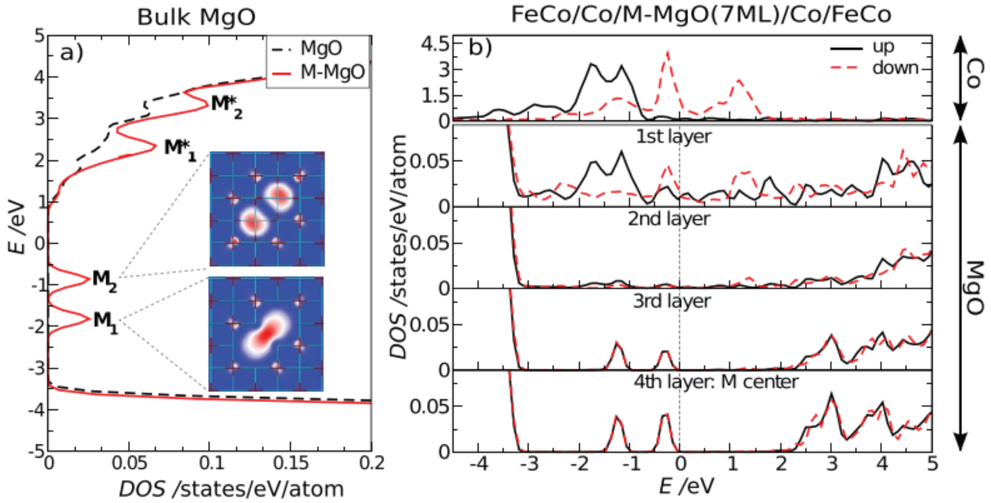

Figure 1.14. Theoretically calculated DOS plots for MgO with and without double oxygen vacancy or M-center. (a) DOS plot (with charge densities in inset) for M-center created within bulk-MgO resulting two localized states M_1 (bonding) and M_2 (antibonding) located at 0.4eV and 1.1eV below Fermi energy (E_F), **(b)** Layer-projected, and spin-polarized DOS plots for FeCo|Co|MgO(7ML)|Co|CoFe with M-center at middle monolayer (4th) of MgO. The figures are taken from ref [4].

Further, they plotted the complex band structures (CBS) for FeCo|Co|MgO(7ML)|Co|CoFe structure with M-centers [in x-y plane, and y-z plane represented by panel (a) and (b) respectively] and F-centers [panel (c)]. In each panel, they compared the abovementioned CBS with that of the ideal (defect-free) bulk MgO (represented by the dashed blue lines) [Fig. 1.15]. They calculated the decay constants (κ) for the Δ_1 symmetry tunneling electrons due to the M_1, M_2, and F-centers. The decay constants (κ) are determined by the value of $|\mathrm{Im}(k)|$ (where $k = q + i\kappa$, please see Section 1.4.4) at which the respective CBS loop due to the corresponding defect states (M_1, M_2, F) cut the Fermi energy (E_F).

For M_2 centers lying in the plane (*x*-*y*) perpendicular to the propagation direction of tunneling electrons (*z*), the calculated decay constant for the Δ_1 symmetry tunneling electrons, $\kappa_{\text{M-MgO}} \approx \kappa_{\text{MgO}}$ [Panel (a)]. Contrary, for the M_2 centers lying partly along the propagation direction of tunneling electrons (*y*-*z* plane), the decay constant $\kappa_{\text{M-MgO}} < \kappa_{\text{MgO}}$. This increase in the decay parameter due to the M_2 center (lying partly along the propagation direction) for the Δ_1 symmetry tunneling electrons thus enhances their transmission in the P-state, resulting in an increased TMR.

These theoretical findings were also confirmed by the transport measurements performed on the MTJs made up of Ta(5)|Co(10)|IrMn(7.5)|FeCoB(4)|MgO(2.9)|FeCoB(4.5)|Ta(5)|Pt(5) stack. The bracketed numbers denote the thickness of corresponding layers in nm. During the growth process, the MgO barrier was formed by sputtering Mg in a pure Ar partial pressure, followed by oxidation in an O_2 atmosphere. Stacks were post-annealed in an in-plane magnetic field of 200 Oe for 1 h at an annealing temperature (Ta) of at least 200 °C to magnetically pin the lower electrode thanks to the IrMn antiferromagnetic layer.

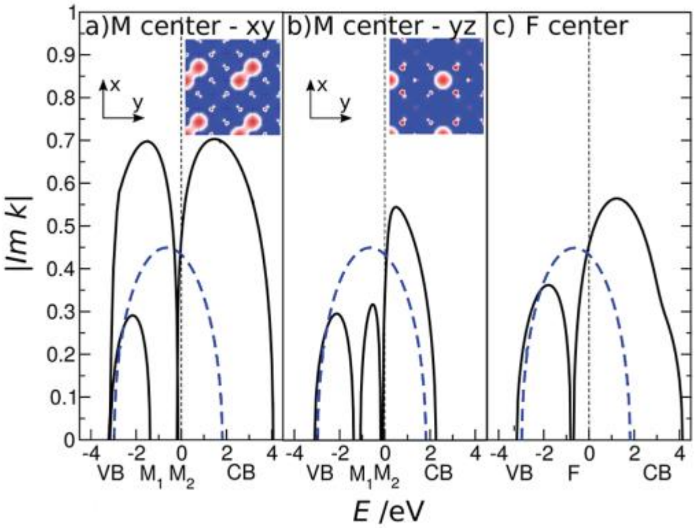

Figure 1.15. Complex band structures (CBS) for FeCo|Co|MgO(7ML)|Co|CoFe M-centers [in x-y plane, and y-z plane represented by panel (a) and (b) respectively] and F-centers [panel (c)]. In each panel, the dashed blue line represents the CBS of ideal MgO. The multilayer structure is grown along the (001) plane in the *z*-direction therefore panel **(a)** indicates that the M-centers in the respective panel lying in the plane transverse to the propagation direction of electrons while panel **(b)** represents the scenario in which the M-centers are partly along the propagation direction of tunneling electrons. The inset figures in the panel **(a)** and **(b)** represent corresponding charge densities for the M_2 center. The figures are taken from ref [4].

By increasing the annealing temperature (Ta) from 200^{0}C to 300^{0}C, the authors observed an increase in the TMR from 20% to 70%. The annealing is widely thought to promote symmetry-polarized tunneling by improving the MgO texture and extending it to the first otherwise amorphous MTJ electrodes beyond the interfaces. However, the authors have shown that the annealing temperature can also be used to reduce the weight of the F/M centers. As we already know that the F/F^{+}* centers reduce the spintronic performance[86] of the MTJ devices [also Section 1.6.4.1.1] while from the present theoretical calculations the M_2 centers are expected to increase the TMR. These F and M_2 centers show their signatures in the $\hat{I}$- measurements at 0.7eV (for the temperature range of 80K< T<250K) and 0.4 eV below (for the temperature range T>250K) to the Fermi energy (E_F = 0V) respectively.

For 200^{0}C annealed MTJ, the $\hat{I}$-measurements (P and AP) performed in the temperature range 80K< T <250K [Fig. 1.16.a] and T >250K [Fig. 1.16.c] exhibits two peak at 0.7eV [Fig. 1.16.a] and 0.4eV [Fig. 1.16.c] respectively. The $\hat{I}$-peak at 0.7eV and 0.4eV corresponds to the charged single oxygens vacancy excited state (F^{+*}) and antibonding double oxygen vacancy state (M_2) localized states respectively. The mixture of these defect states might be the reason for the low TMR (20%).

In contrast, MTJs with T_a =300 °C do not exhibit a signature of the F^{+*}-mediated barrier height state within the expected 80< T <250 K range [Fig. 1.16.b]. Since this state is *p*-like[1,86] this means that annealing has strongly attenuated the Δ_5 transmission channel. Instead, within 80< T <250 K, a weak signature of an M_2-mediated barrier height was observed. This signature, which endures for T >250K [Fig. 1.16.d], is present in the MTJ's P state but not the AP state. This means that the enhanced spintronic response of the MTJs annealed at T_a =300^{0}C compared to those with T_a =200^{0}C is in part due to a Δ_1 tunneling transmission channel in the MTJ's P state that is driven by the M_2-defined barrier height. This explanation is also supported by an inelastic electron tunneling spectroscopy signature at 0.4eV measured[92] in only the MTJ's P state that was tentatively attributed[86] to the M ground state. Finally, this decrease in the ratio of F to M-centers upon increasing T_a is consistent with formation energy for the M center that is 116 meV lower than that of two separate F-centers.

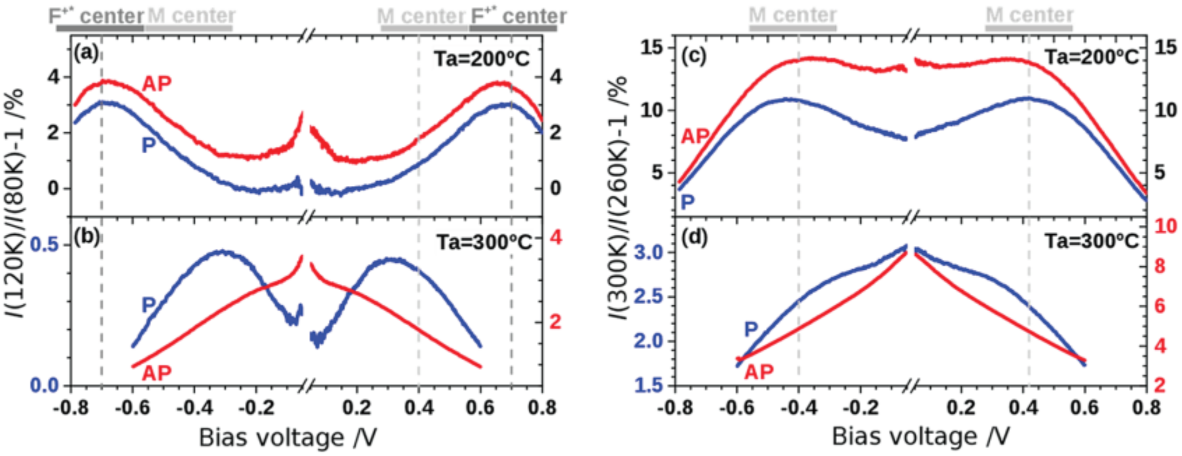

Figure 1.16. Ihat ($\hat{I}$)-measurements performed in both P and AP states for MTJs with Ta(5)|Co(10)|IrMn(7.5)|FeCoB(4)|MgO(2.9)|FeCoB(4.5)|Ta(5)|Pt(5) structure, at the temperature range 80K< T<250K (panel a, and b), and T>250K (panel c, and d) to probe the F and M_2 defect states respectively. The figures are taken from ref [4].

1.7 Transmission across the Fe|MgO|Fe MTJs

In this section, we will briefly describe the transmissions calculated by Taudul et al.[85,91] for the Fe|MgO(5ML)|Fe junctions with defect-free (ideal)-MgO and isolated F- and M-center within the 3rd ML of MgO. The authors calculated the ballistic conductance using the Landauer-Büttiker formula[48,49]:

$$G(E_F) = \frac{e^2}{h} \sum_{n,\boldsymbol{k},\sigma} T_{n,\boldsymbol{k},\sigma} (E_F) \tag{11}$$

Where, $T_{n,\boldsymbol{k},\sigma} (E_F)$ is the total transmission at the Fermi energy (E_F) and the summation is over all n bands crossing the E_F for each $\boldsymbol{k}$ point and spin σ. The electron transmission was evaluated using the scattering-based approach with a plane wave basis set and ultrasoft pseudopotential (USPP) scheme as implemented in the PW_{COND} module[93] of the Quantum Espresso (QE) package[94]. Fig. 1.17 shows the transmission values calculated in 2-dimensional Brillouin zone (BZ) for the Fe|MgO(5ML)|Fe, with defect-free or ideal MgO. Panel (a) and (b) represent the majority channel (spin ↑ electrons) and minority channel (spin ↓ electrons) for the P state while the extreme right panel (c) is for the transmission in the AP state of MTJ. From Fig. 1.17, in the parallel state of MTJ, the majority electron transmission is centered at the Γ-point and dominated by Δ_1 symmetry while the transmission for the minority electron was found at the edges with two order lowered values than the majority electrons. The AP state however seems to be a mixture of both majority and minority transmissions in the P state.

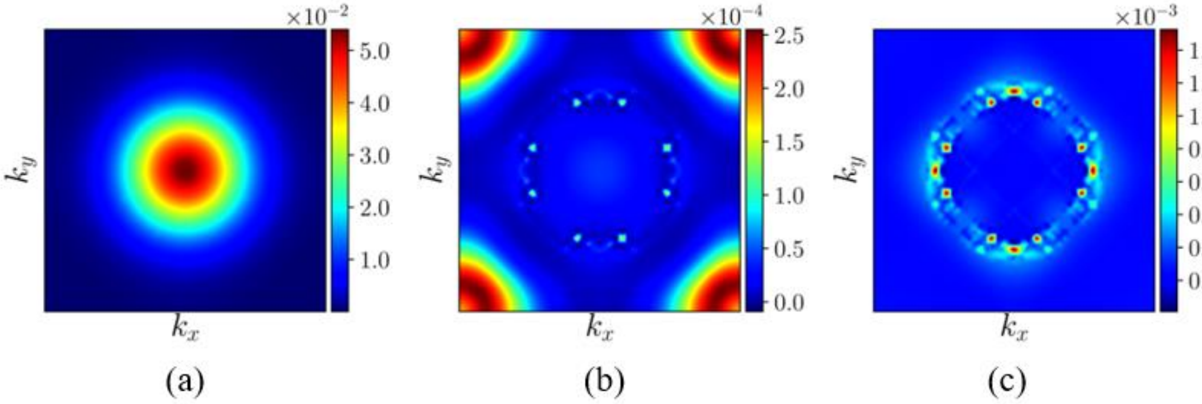

Figure 1.17. Transmission in the two-dimensional Brillouin zone (2D BZ) across an ideal Fe|MgO(5ML)|Fe junction in its P magnetic state for **(a)** the spin-up channel, **(b)** the spin-down channel, and **(c)** in its AP magnetic state. The figures are taken from ref [91].

Further Taudul et al.[91] created isolated F- and M-centers at the 3rd layer of MgO in Fe|MgO(5ML)|Fe junctions respectively shown by the top three (a, b, c) and bottom (d, e, f) three panels in Fig. 1.18. As compared to the ideal MgO case, the BZ transmission distribution for minority channel or ↓ spin electrons in P state (P↓) is slightly affected by the presence of F- and M-centers [see Table 1.4]. However, a significant amount of difference (one order lowered) in the transmission for the spin-up channel (P↑), was observed for both F- [Fig. 1.18.a] and the M-centers [Fig. 1.18.d]. The transmission (P↑) calculated for the F-center [Fig. 1.18.a] contains minima at the center Γ-point with maxima along k_x and k_y directions at the edges of 2D BZ, suggests that the F-center scatters tunneling electrons to the states with higher k-vectors. The electrons are scattered symmetrically in each direction due to the spherical symmetry of a single oxygen vacancy. On the other hand, the P↑ transmission in the presence of the M-center becomes broadened in the 2D BZ but maintains the symmetric maximum at the vicinity of the Γ-point. This clearly suggests that, while the transmission across an F center is reduced by an order of magnitude due to transport across k≠ 0 states, coherent transport that preserves spin and symmetry of the electron wave function is still possible when the M-center is present in the MgO spacer. [91]

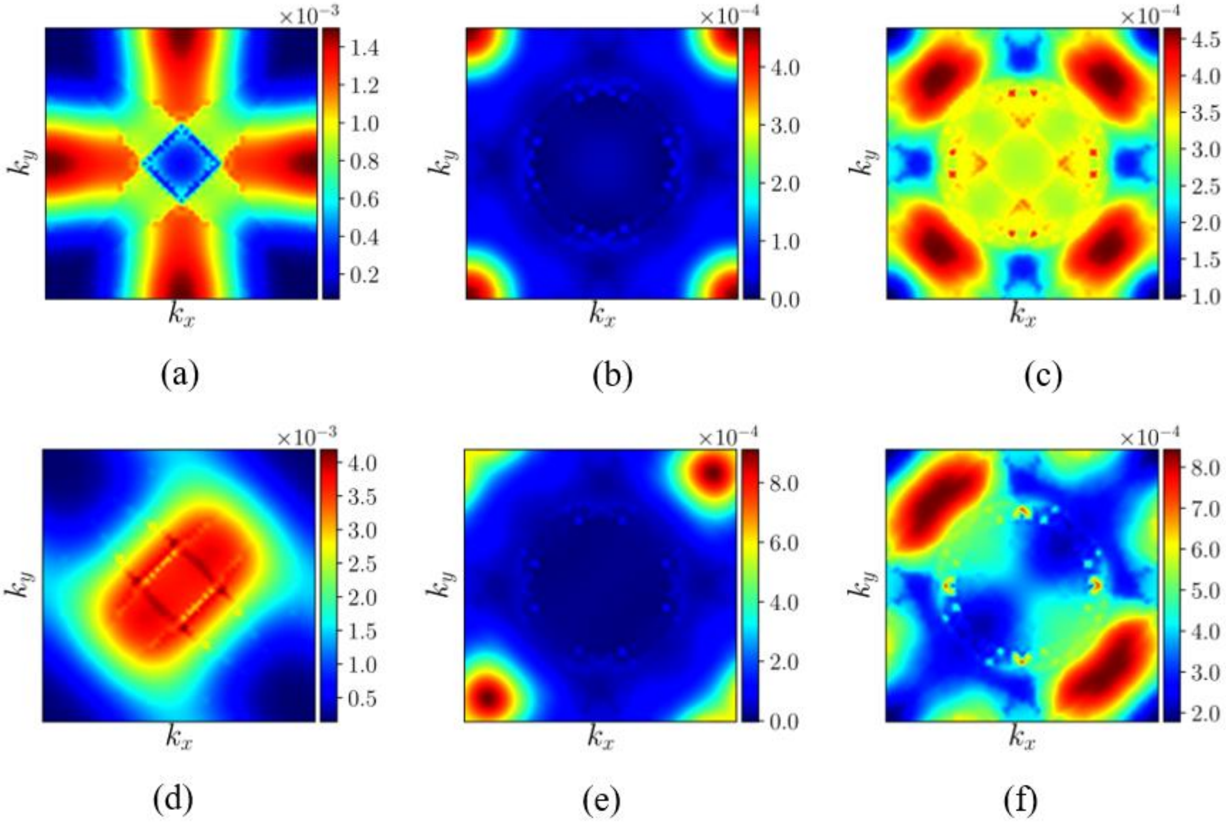

(a) (b) (c)

(d) (e) (f)

Figure 1.18. Transmission in the two-dimensional Brillouin zone (2D BZ) across Fe|MgO(5ML)|Fe junction with isolated F-center [top panels (a, b, c)] and M-center [bottom panels (d, e, f)] at 3rd monolayer of MgO. The extreme left and middle panels (for both top and bottom) represent the majority channel (spin ↑ electrons) and minority channel (spin ↓ electrons) for the P state while the extreme right panel (for both top and bottom panel) is for the transmission in the AP state of MTJ. The figures are taken from ref [91].

Table 1.4 summarizes the theoretically calculated transmissions for P↑, P↓, and in AP state for Fe|MgO(5ML)|Fe junctions with defect-free (ideal)-MgO and isolated F- and M-center within the 3rd ML of MgO. We observe that while F- and M- centers promote a reduction in total P↑ transmission, both centers promote an increase in both the P↓ and AP total transmissions. Furthermore, the transmission distribution in the AP configuration changes significantly from that of an ideal MgO junction. While introducing defects (F- and M- centers) reduces the TMR, the TMR is found larger compared to F centers[91].

Fe|MgO(5ML)|Fe	**P-up (P↑)**	**P-down (P↓)**	**AP**	**TMR (%)**
Ideal 5ML MgO	79.00	0.46	1.0	7850
F-center at 3rd ML of MgO	7.21	0.63	3.2	145
M-center at 3rd ML of MgO	17.1	1.47	4.5	315

Table 1.4. **Total spin-polarized transmissions x10^4 and TMR(%) values calculated** for P (↑), P(↓) transmission channels and AP state for Fe|MgO(5ML)|Fe MTJ, without any defects and with F- and M-centers at the 3rd ML of MgO. The table is taken from ref [91].

Physical vapor deposition techniques such as sputtering which is being used to grow MTJs for commercial and technological applications, do not guarantee the perfect crystallinity of MgO (even the growth is done very slowly). This is the reason even after almost 13 years, we could not cross the experimentally measured record TMR of 604% set by Ikeda et al.[68]. Moreover, this record experimental TMR value is also far behind the theoretically calculated one i.e. 10000%[66]. From the detailed ab-initio calculations, supported by the experimental results and the transmission plots [4,85,91] Taudul et al. revealed that whichever type the oxygen vacancy, it certainly decreases the TMR but increasing the proportion of double oxygen vacancies compared to the single ones, always lead to an enhancement in the spintronic performance thus the TMR of the MTJ device. In the next subsection, we will briefly describe the techniques to increase the M/F ratio within the MgO of an MTJ device both during sputtered growth and annealing steps.

1.8 Tuning M/F ratio

The ratio of M- to F-centers in the MgO barrier can be tuned during the sputtering growth and annealing processes. During the sputtering growth of the MgO layer from its bulk MgO target, adding oxygen to the Ar plasma causes the barrier height of nanoscale hotspots measured by conducting tip atomic force microscopy (CT-AFM) to shift from 0.5 eV to 1.1 eV[95]. The additional oxygen gas flow with Ar plasma during the growth process might be filling the oxygen deficiencies and thus turning M-centers (paired oxygen vacancies) into F-centers (single oxygen vacancies) thus decreasing the M/F ratio. Also increasing the annealing temperature (Ta) of MTJ stacks with a MgO barrier grown by oxidizing an Mg layer decreased the barrier height from 0.7 eV to 0.4 eV [see Fig.1.16] and thus increasing the M/F ratio[91]. This can be understood by the fact that the annealing enables F-centers to coalesce into M-centers thanks to much lower formation energy[4]. The larger M/F ratio within the MgO layer for a given MTJ device lowers the effective barrier height. Theoretical calculations[96] revealed that these defect-mediated lowered effective barrier heights significantly reduce the current densities required for observing STT. Thus, a proper ratio of M/F localized states within the MgO layer could play an important role in the development of the strategic devices, relying on the STT effect from STT-MRAMs[8] to artificial synapses[97] and neuromorphic computing[9].

1.9 Spin transfer torque

Contrary to the TMR, in the spin-transfer torque (STT) effect, an input current of sufficient high density (J >10^7 A/cm^2)[6,7] after passing through the constituent fixed ferromagnetic (FM) layer of MTJ gets spin-polarized with a non-zero spin angular momentum. This spin-polarized current, followed by spin-dependent tunneling across a thin insulating layer or tunnel barrier, induces the magnetization precision and consequently transfers the spin torque on the magnetization of the free ferromagnetic layer. For the abovementioned scenario, the fixed and free FM layer acts as a polarizer and analyzer, respectively. In order to address the abovementioned STT event quantitatively, we will first consider the magnetization dynamics of the magnetic moment under an external magnetic field. The magnetization dynamics of a magnetic moment ($\hat{m}$) under an external magnetic field ($\vec{H}_{eff}$) can be described within the macrospin approximation, using the Landau-Lifshitz-Gilbert (LLG) equation:

$$\frac{\mathrm{d}\hat{\mathrm{m}}}{\mathrm{dT}} = -\gamma.\hat{\mathrm{m}} \text{ x } \vec{H}_{eff} + \alpha.(\hat{\mathrm{m}} \text{ x } \frac{\mathrm{d}\hat{\mathrm{m}}}{\mathrm{dT}}) \tag{12}$$

Applying the above LLG equation for an MTJ, thus corresponds: $\hat{m} = \vec{M}/|\mathrm{M_S}|$ to the unit vector parallel to the magnetization direction ($\vec{M}$) of the free FM layer ($\mathrm{M_S}$ being the saturation magnetization of free FM layer), $\gamma = g.\mu_B/\hbar$ is the gyromagnetic ratio (where g, μ_B and $\hbar$ are the Landé factor, Bohr magneton and reduced Planck's constant respectively), and $\vec{H}_{eff}$ is the effective magnetic field around which $\hat{m}$ precesses.

For the spin-transfer torque (STT) event caused by the angular momentum due to the spin-polarized current in MTJ, the above LLG equation takes the following form[16]:

$$\frac{\mathrm{d}\hat{\mathrm{s}}_2}{\mathrm{dT}} = -\gamma.\hat{\mathrm{s}}_2 \text{ x } \vec{H}_{eff} + \alpha.(\hat{\mathrm{s}}_2 \text{ x } \frac{\mathrm{d}\hat{\mathrm{s}}_2}{\mathrm{dT}}) - \beta_{||}.\mathrm{I}.\hat{\mathrm{s}}_2 \text{ x } (\hat{\mathrm{s}}_1 \text{ x } \hat{\mathrm{s}}_2) - \beta_{\perp}.\mathrm{I}.(\hat{\mathrm{s}}_1 \text{ x } \hat{\mathrm{s}}_2) \tag{13}$$

Where, $\hat{\mathrm{s}}_2$ is the unit vector parallel to the average spin direction ($\vec{S}_2$) of the free layer, $\hat{\mathrm{s}}_1$ = unit vector parallel to the average spin direction ($\vec{S}_1$) of fixed/reference/magnetically pinned layer, $\beta_{||}$ = coefficient determining the in-plane torque, $\beta_{\perp}$ = coefficient determining the out-of-plane torque, I = applied current. Both $\beta_{||}$ and $\beta_{\perp}$, depends on the spin polarization and angle between the incoming spin and local magnetic moments in the free layer. In this equation on the right-hand side, the first term ($-\gamma.\hat{\mathrm{s}}_2 \text{ x } \vec{H}_{eff}$), represents magnetic precision of free layer magnetization ($\hat{\mathrm{s}}_2$) around the net effective magnetic field ($\vec{H}_{eff}$), while the second term [$\alpha.(\hat{\mathrm{s}}_2 \text{ x } \frac{\mathrm{d}\hat{\mathrm{s}}_2}{\mathrm{dT}})$] is for the Gilbert damping or damping-torque. It is clear that the magnetic precision induced by the angular momentum of the spin-polarized electrons in the free layer results in two type of torque: the in-plane (Slonczewski) torque (represented by the third term $[-\beta_{||}.I.\hat{s}_2 \text{ x } (\hat{s}_1 \text{ x } \hat{s}_2)]$ and the out-of-plane or field-like torque (represented by the fourth term $[-\beta_{\perp}.I.(\hat{s}_1 \text{ x } \hat{s}_2)]$. Fig. 1.19 summarizes the STT equation schematically.

Due to the transfer of spin torque, the magnetization of the free ferromagnetic layer depending upon the strength of the switching current either: (a) precess with damping or (b) precess with steady-state large angle or (c) continuously and rapidly increase the precession angle leading to magnetic reversal.[11,98]. Case (b) is utilized to generate or detect the radio-frequency signals in the microwave spectrum (GHz range) and the devices being employed for that are called spin-torque nano oscillators (STNOs) while scenario (c) is used to switch the magnetization of the free layer thus the mutual magnetic alignment from P to AP or vice-versa in an MTJ device, thus fulfills the requirement for the magnetic random-access memories (MRAMs)[8]. All these three scenarios are schematically represented by Fig. 1.20.

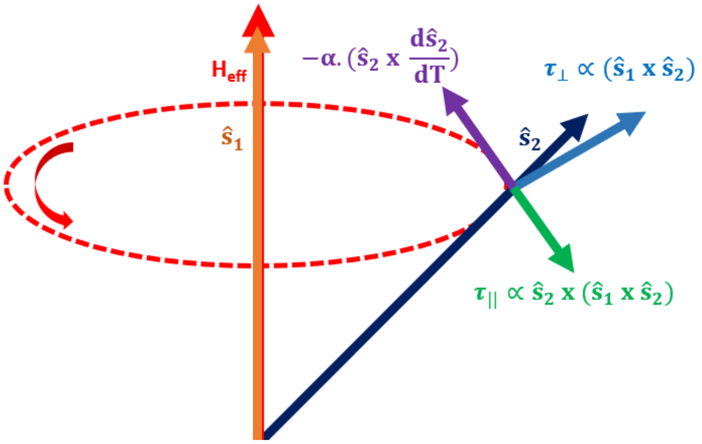

Figure 1.19. Schematic representation of the magnetization dynamics for the STT mechanism in an MTJ.

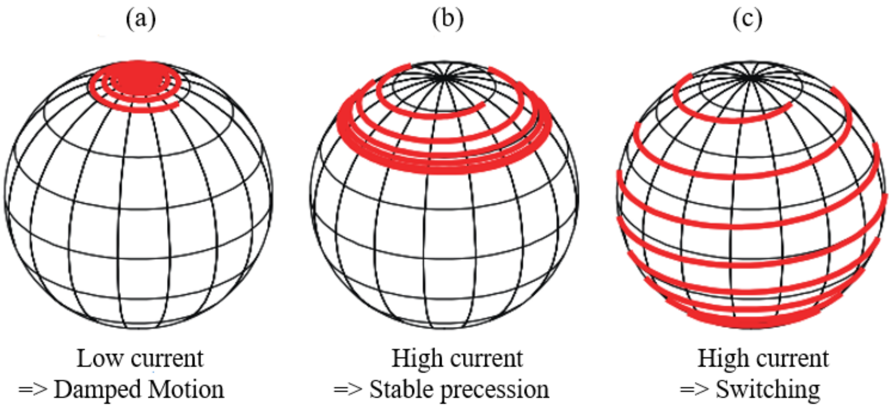

Figure 1.20. Schematic representation of three possible scenarios during STT event: (a) low current leading to the damped motion, (b) high current leading to stable and steady magnetic precession, and (c) High current leading to switching free layer magnetization in MTJs. The figures are taken from ref [11].

1.10 Scientific Motivation

In this chapter, we have covered all the basic concepts and understandings developed so far regarding the MTJ operation. We have also presented a detailed state of the art on how the different types of possible defects within the MTJ can alter its spintronic performance. Amongst all the possible defects, the oxygen vacancies due to the formation of localized states near Fermi energy (E_F) in the energy band diagram of MgO, are found to be the most influential on determining the spintronic performance thus TMR of the MgO based MTJs. The general consensus regarding the single oxygen vacancies (F-centers) is that they negatively impact the transport in MTJs [1,2]. However, from theoretically calculated transmissions, replacing a single oxygen vacancy (F-center) with an isolated double oxygen vacancy (M-center) in MTJs, showed a significant improvement on the theoretically calculated TMR (> x2 times)[91]. These theoretical findings[91] are in line with the theoretical calculations[1–3] and transport experiments[4,86] performed. The localized states due to the double oxygen vacancies (M-centers), enhance the transmissions for the dominant Δ_1 tunneling electrons of spherical charge distribution (s-character) by offering a lowered barrier height of 0.4eV [4,91,92], improved symmetry matching at the FM|MgO interface, and offering smaller decay rate[4] within the MgO tunnel barrier in the parallel state of an MTJ. This increased transmission in the P state, increases the asymmetry between the G_P and G_{AP}, therefore the TMR. The defect-free crystal structure is just a thought of idealism, therefore the associated defects such as oxygen vacancies which are inherent to the oxide materials cannot be completely avoided at the MgO barrier even in its crystalline form. However, one can tune the ratio of double (M-center) to single oxygen (F-center) vacancies i.e., the M/F ratio by a proper control on growth and annealing parameters. The MTJs with increased M/F ratio have shown enhanced TMR[4].

The improved spintronic performance of the MTJs as reflected by the enhancement in the TMR due to the presence of double oxygen vacancies (M-centers), can also benefit the STT research by lowering the critical current density (J_C) required for switching or precession. Although this research topic seems to be quite interesting but remained completely unexplored till the date. There are few reports which talk about the interfacial oxygen vacancies and the STT[99–101], but to our best knowledge, no experimental report has ever been published which unravels the role of oxygen vacancies within the tunneling barrier (MgO) on the STT.

2. Experimental Techniques

In this chapter, we will describe all the experimental techniques from device fabrication to the measurements that are used in Chapter-2 and 3. For the fabrication of microscale devices being used in the Chapter-3, the photolithography technique was used, whereas the nanoscale devices are being used in Chapter-4 were fabricated using the state of the art electron-beam lithography technique and received in collaboration with i) Professor Paulo Freitas' group, International Iberian Nanotechnology Laboratory (INL) Portugal (denoted by MTJ-F) and ii) Dr. Luc Thomas, TDK-Headway Inc., USA (denoted by MTJ-H). Since the microscale devices were fabricated by us at our cleanroom facility using the UV-photolithography technique, the associated technological steps will therefore be described in detail. In contrast, the details of crafting the nanoscale devices will be described only briefly. We will also provide a short description of the experimental setup on which the static magnetotransport measurements were performed and will explain the $\hat{I}$-technique that is used to probe the energy position of the localized states. The details of the spin-torque ferromagnetic resonance (ST-FMR) technique will also be provided, as it was also used in order to calculate the torque ratio of the MTJ devices.

2.1 Microfabrication of the Inorganic MTJs

To avoid any possible contamination during the device fabrication, the complete UV-photolithography process was carried out at the STNano cleanroom facility. The other advantage of working at the STNano cleanroom facility is that it comprises most of the tools needed to process microscale MTJS. The device fabrication part also includes the dry etching part. This was performed at Ar^+ ion etching facility attached with in-situ Auger electron spectroscopy at Department of Nano-Objects (DMONS) of CNRS-IPCMS.

UV-Photolithography

The inorganic multilayer stacks for the MgO-based MTJ devices were grown using the standard sputtering technique by our collaborator Prof. Michel Hehn, at Institut Jean Lamour (IJL), University of Lorraine, Nancy and processed at the cleanroom facility STnano platform of CNRS-IPCMS, Strasbourg. The most common and widely used technique for the fabrication of the micron-sized device is UV-Photolithography or also known as Optical lithography. The UV-photolithography process requires a lithography machine commonly known as a mask aligner. An optical mask or lithography mask with the desired pattern on it is used. In this process, the sample is coated with a specific UV light-sensitive polymer solution called *photoresist*. The basic principle of UV-photolithography is to transfer the desired pattern from the lithography mask to the sample's photoresist layer by shining UV light through the mask.

Photoresist

Depending upon their softening (hardening) due to exposure to UV light, photoresists become soluble (insoluble) to a specific kind of solution called a *developer*. The photoresist that becomes soft after the UV light exposition and soluble to the developer solution are known as a *positive* (+) photoresist, whereas the photoresist that becomes hard after the UV light exposition and insoluble to the developer solution is known as a *negative* (-) photoresist. Common examples of positive photoresist are S1805 and S1813. AZ5214 is a negative photoresist.

Optical mask

The optical mask is a special arrangement of transparent and opaque areas generally called an *image* that is patterned on a *fused quartz substrate*, the mask allows incident UV light to selectively pass through it and transfer the *image* on the photoresist deposited on the sample.

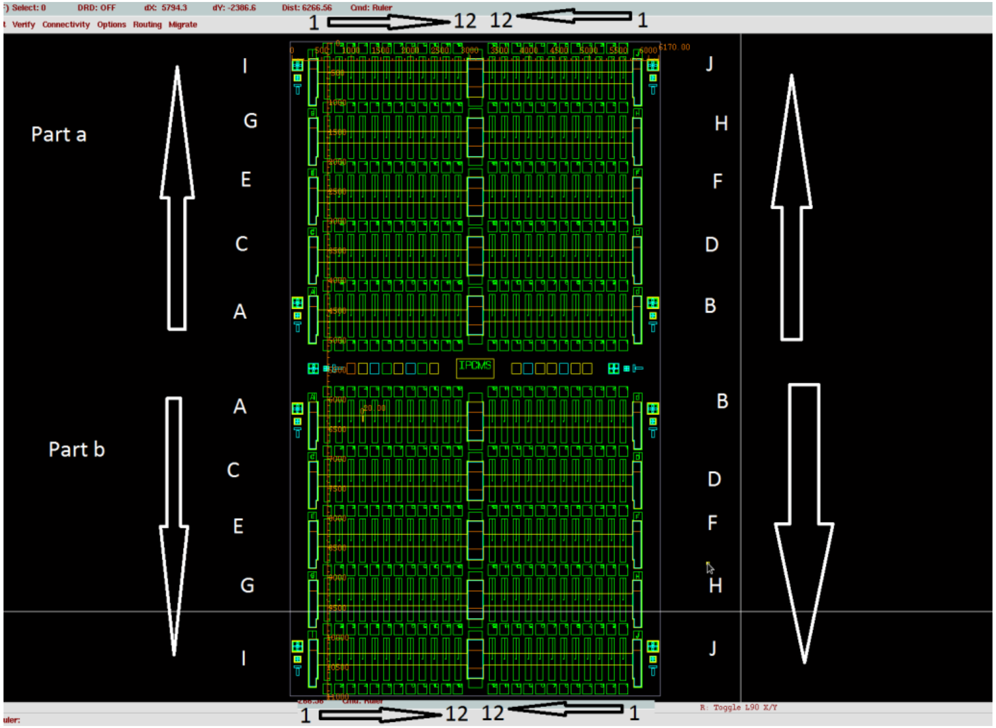

Figure 2.1. General visualization of the lithography mask with all four layers overlapped. For a detailed view please refer to Fig. 2.2.

The image of the optical mask originates from a computerized data file e.g. *Cadence* file, later developed onto fused quartz mask substrate using a photolithography process. The opaque areas are made of thin chromium (Cr) film of a few 10s of nm, while the transparent areas are the fused quartz substrate itself. In order to pattern the stacks for the micron-sized devices, a four-step lithography mask was adapted from Dr. A. Anane's (CNRS-Thales, Université Paris-Sud) design, and further developed through several iterations by F. Schleicher, U. Halisdemir, M. Bowen, and myself from DMONS, CNRS-IPCMS using the *Cadence* software. The optical mask contains two sections: the upper section (a) and the bottom section (b). Each section contains 10 bottom electrodes, each containing 12 top electrodes. In total, for 11x7 mm^2 sample area, 240 devices can be patterned in a single lithography process. To avoid the alignment difficulty during the consecutive lithography steps, the extra 3 mm on both length and width was added as a margin area on the sample. This extra margin was diced out carefully after the device fabrication. The patterned sample further diced into two sections; upper section (a) and lower section (b), both of 7x5 mm^2 in order to glue on the measuring *FERT* chip for the temperature-dependent electrical and magneto-transport measurements.

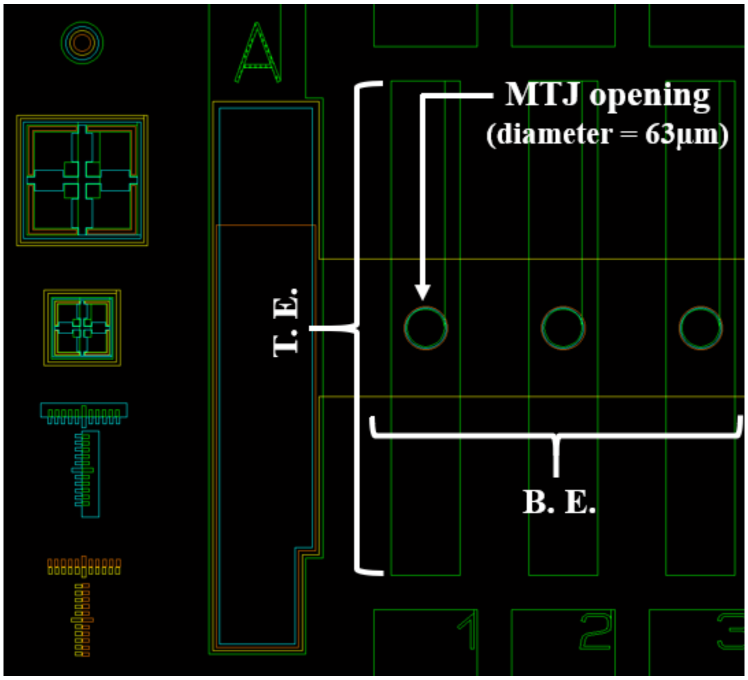

Figure 2.2. Zoomed image by the cadence software of the mask with all four layers overlapped. Colors define the consecutive photolithography steps (fully described in the following section): I- brown, II-yellow, III-blue, and IV-green. Crosses and calipers in the bottom part are essential for precise alignment of steps, especially crucial for step I and III matching.

This mask allows us to pattern 20, 45, and 63 µm diameter vertical pillars. The superposition of all the four lithography steps is depicted in Fig.2.1, whereas Fig.2.2 depicts the detailed image of the device geometry containing horizontal bottom electrode of 200 µm width, perpendicular top electrodes of 100 µm width, junction size (63 µm in the present Fig.2.2) as defined in first lithography step and overlapped alignment marks at the corner.

Dry etching

Sample masking using photolithography can be used to selectively remove the exposed (i.e., resist-free), undesired parts from the sample. One can etch the sample either by dipping it in a reactive solvent or by bombarding it with ions/atoms such as Ar. The etching performed using the reactive solvent is called *wet chemical etching* while the latter is called *dry etching* or *ion beam etching*. In this thesis, we have used the Ar ion etching technique to etch both inorganic and hybrid samples. The Ar^+ etching process takes place inside a vacuum chamber. An applied electric field produces an ionic discharge that ignites the entering Ar gas into Ar^+ ions and electron mixture. The mixture of Ar^+ ions and electrons i.e., *plasma* is confined by a magnetic field and electrically accelerated towards the sample. Due to the collision of Ar^+ ions with the sample, the unprotected area is etched out. To protect the sample from positive charge development during the etching process, these positively charged Ar^+ ions are neutralized, here in our case by an electron-emitting filament. The evacuation of any residual beam charge is achieved by grounding the sample using conductive tape. In order to achieve etching uniformity, the sample was rotated and kept at an angle of 45^0 with respect to plasma.

Further, during a multi-step ion beam etching process to avoid over-etching, at each step the etching rate is controlled by keeping the *etching dose* constant. This *etching dose* is calculated by multiplying the etching current (in mA) by the time (mins) for etching is performed. The etching current is determined by the charged particles caught by the Faraday cup installed within the etching/vacuum chamber. The output (etching current) can be measured with the help of a digital multimeter. The concept of etching dose could provide a rough idea about the etching rate for a given material, but the precise etching rate or exact depth profiling can only be determined with the help of highly sensitive elemental sensing techniques like *Auger* electron spectroscopy. Due to high precision and control over the etching rate, dry etching techniques are preferred over wet chemical etching.

Auger electron spectroscopy

In order to etch precisely, one must know how much and which material has been etched out, and that is done by one of the most sensitive elemental characterization techniques called *Auger* electron spectroscopy. In this spectroscopy technique, the sample is bombarded either by high-energy electrons, ions, or photons. This ejects a core level electron thus leaving a hole therein. To fill this hole, the higher energy outer electrons lose energy. In that process, the energy is emitted either in the form of X-ray (photons) or utilized in emitting an electron from one of the outer levels. An electron removed by the latter process is known as an Auger electron. An Auger electron thus results from a three-electron process and is independent of the way the core hole is created. Auger electrons are the characteristics of an atom from which they are emitted and therefore serve as a fingerprint for the elemental analysis.

The Auger electron spectroscopy attached to the etching chamber uses high-energy electrons of 3 keV to generate core holes. The advantage of using high-energy electrons to generate core holes is that generating and focusing them to a very small spot is relatively easy. To avoid any possible contamination during the etching process, the Auger electron optics are covered by a metallic shutter. Therefore, after the etching process, the sample is transferred to the Auger position, without breaking the vacuum. The Auger electron spectroscopy was performed below 10^{-8} mTorr. The emitted Auger electrons were analyzed in the Cylindrical Mirror Analyzer (CMA) and controlled by either manual mode or by the computer program e.g., Winspectro in remote mode. The *Auger* electrons passing through the analyzer were selected according to their energy ranges (100-800 eV), detected, and further amplified using the Channeltron plate. The amplified signal after the noise filtering works as an input for the computer program, in our case Winspectro. The Auger spectrum of the etched sample is obtained by plotting no. of counts (N) or dN/dE (in derivative mode) with respect to the energy range (E in eV) selected for the analyzer.

Unlike the time-of-flight secondary ion mass spectrometry (TOF-SIMS) based etching systems, in which both the etching and depth profiling is done simultaneously, the detection of Auger electrons in Auger spectroscopy-based etching systems is done after the etching. Therefore, in order not to over etch the sample, the etching is always performed in steps of low etching current dose for small time scales, followed by the Auger measurements after each etching step. That makes the complete process slow as compared to the TOF-SIMS spectroscopy-based etching systems but in case of precision and accuracy, the Auger electron spectroscopy-based etching systems always outperform because of their superior sensitivity.

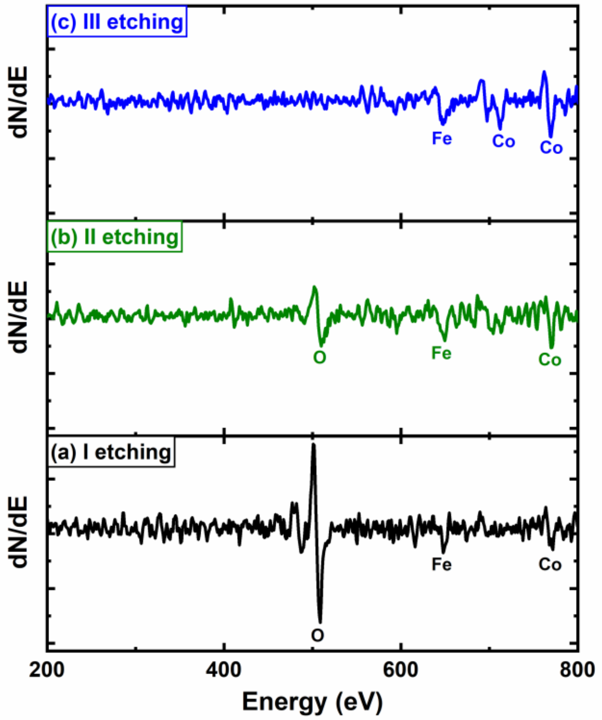

Figure 2.3. 1st order intensity derivative after the subsequent etching of inorganic multilayer stack Glass||Ta(5)|Co(10)|IrMn(7.5)|CoFeB(4)|MgO(2.5)|CoFeB(2.5)|Ta(1)|Pt(1). The numbers inside the bracket represents the thickness in nm. For clarity, only the highest intensity peaks are highlighted. The peaks at [483, 504] eV, [598, 651, 703] eV, and [618, 656, 716, 775] eV corresponds to O, Fe, and Co respectively, with highest intensity peaks at 504 eV, 651 eV, and 775 eV for O, Fe, and Co respectively.

To show how depth profiling is done using Auger electron spectroscopy , the representative stack: Glass||Ta(5)|Co(10)|IrMn(7.5)|CoFeB(4)|MgO(2.5)|CoFeB(2.5)|Ta(1)|Pt(1) was chosen. The numbers inside the brackets denote the thickness in nm and ML stands for monolayer. Fig.2.3 shows the auger scans for depth profiling and results are summarized. In Fig.2.3.a after the first etching of ~5 mA.min, we observe a strong O peak and very small Fe and Co peaks. We conclude that the heterostructure has been etched down to the MgO tunnel barrier layer. In Fig.2.3.b, the scan after a second etching step (~6.8 mA.min) removes few more MgO layers, resulting in a smaller O peak and stronger Fe and Cr peaks when compared with the previous scan. In Fig.2.3.c, Auger analysis after the third step (~4.5 mA.min) is shown: the absence of O peak and presence of Fe and Co peaks from the bottom CoFeB electrode indicates that the MgO layer has been entirely etching.

To pattern the pillars, the sample after the first UV-photolithography step [explained in Section 2.1.1] should be etched out down to the mid-MgO tunnel barrier, therefore Fig.2.3.b shows the correct etching and after that, no further etching was required. Fig.2.3.c is chosen here just to show the case of over-etching. The crucial observation is that the signal from the barrier should decrease between the next-to-last and the last etching steps. This should be accompanied by a strengthening of the signal coming from the lower electrode.

To fabricate the microscale MTJs for the experiments performed in Chapter-3, a four-step UV-photolithography process is used. These four steps are as follows:

2.1.1 Step I: Pillars definition

In this step, both junction (pillars) and bottom electrode pads were defined. A positive photoresist (S1805) was spin-coated on the sample, followed by soft baking to dry out the solvent. The sample was aligned and kept in close contact below the step-I lithography pattern of the optical mask in such a way that, upon shining the UV-light the optical image gets transferred to the sample and later developed by dipping into the developer solution. After the development process, the developer solution was washed away by keeping the sample under running de-ionized water. The sample was dried out and kept safe for the etching process.

During the above lithography step, both pillar/junction and bottom electrode contact pads were protected by the photoresist, while the rest of the sample area was unprotected. In order to pattern the pillar/junction and bottom electrode pads, the multilayer stack was etched down to the mid-MgO layer [Fig.2.3.b]. The choice of etching down to the mid-layer of MgO is to avoid any short-circuiting due to either top electrode residuals or etching-induced redeposition of bottom electrode material on the pillar flanks. During this step, our optical mask allows us to pattern pillars/junctions of three different sizes (diameter): 20, 45, and 63µm. The process of step I is described graphically in Fig.2.4. After this, and each step, the resist is removed in an acetone bath, followed by an ethanol bath. Care is taken to avoid ultrasounds unless necessary, in order to limit any damage to the pillars. That said, any passivation of the resist with ethanol reduces chances of further removal by additional acetone baths. The experience ultimately determines the amount of time spent in the first acetone bath, and the use/power settings of ultrasounds.

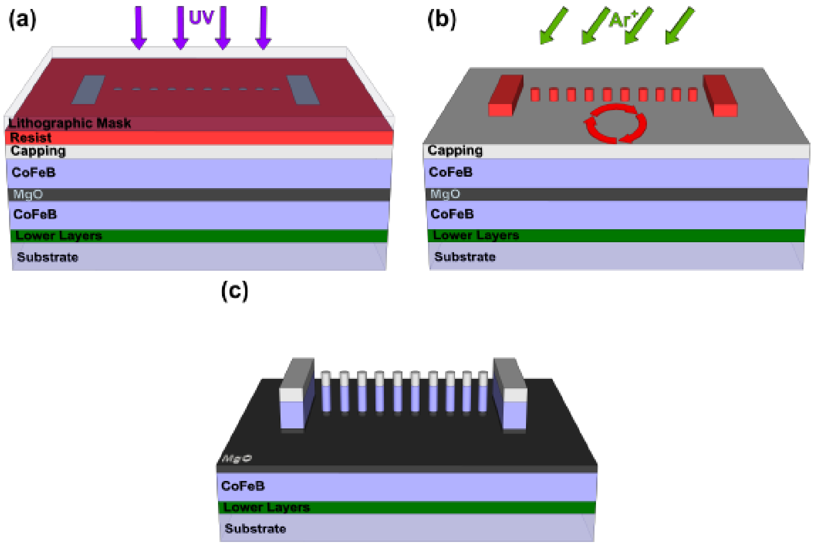

Figure 2.4: Schematics for the photolithography step-I, (a) Photoresist coated multilayer stack, shined under UV light, passing through the desired pattern of the optical mask, **(b)** Developed pattern of photoresist on multilayer stack, keeps the stack beneath safe during the etching process targeted down to the mid-MgO layer, (c) The etching process mentioned in (b), resulting into the vertical pillars and keeps bottom electrode contact pads safe. The figures are taken from ref. [41].

2.1.2 Step II: Bottom electrode definition

In this step, the pattern created during the first step (pillars and contact pads for the bottom electrodes) was preserved by the image developed on the positive photoresist (S1805) layer by shining the UV light through the optical mask.

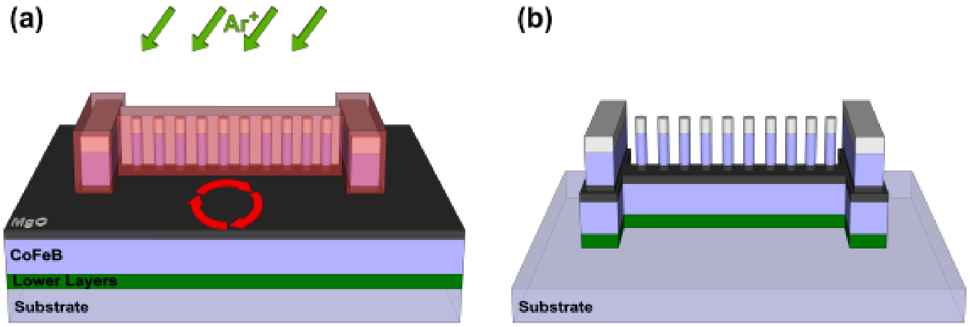

Figure 2.5. Schematics for the photolithography step-II, (a) The step-I pattern is preserved by the developed positive photoresist (pink color) during the Ar ion etching step performed down to the glass (substrate), **(b)** The pattern created containing bottom electrode and pillars and bottom electrode contact pads after the etching process (a). The figures are taken from ref. [41].

In this step, the etching is performed down to the glass (substrate). The appearance of substrate peaks in the Auger spectra must be observed carefully, otherwise over-etching can make the surface of certain substrates conductive, which can impair later measurements. From Fig.2.5, during step II, the bottom electrode is patterned, keeping vertical pillars and bottom electrode contact pads patterned in step I safe.

2.1.3 Step III: Passivation layer deposition

To protect the pattern created in step I (the pillars and the contact pads for the bottom electrode) from the passivation step, a negative photoresist (AZ5214) was selectively developed over the multilayer stack using the optical mask, in such a way that after the deposition of thin silica layer (for passivation purpose) over the entire structure, the lift-off process could easily remove the passivation layer from the top of the pillars and the contact pads of the bottom electrodes whereas keeps the passivation layer remain intact at other parts of the stack for providing electrical insulation. The passivation is done at room temperature by depositing 150 nm of SiO_2 layer using an RF sputtering system (EVA 300+).

The complete process is graphically detailed in Fig.2.6, in which (a) is for how negative photoresist was selectively developed over the entire stack, under the deposition of the silica as a passivation layer, after the lift-off process (b) provides the opening for the pillars and the contact pads for the bottom electrodes.

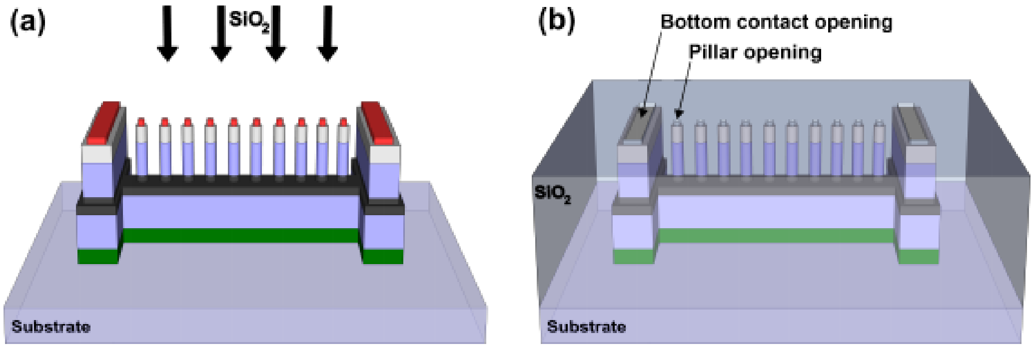

Figure 2.6. Schematics for the photolithography step-III, (a) A negative photoresist is selectively developed over the entire surface to protect pillars and contact pads for the bottom electrode during the passivation layer deposition. **(b)** After the lift-off process, the opening for the pillars and contact pads is achieved. The figures are taken from ref. [41].

2.1.4 Step IV: Metallization process

In this step, to make electrical contacts to the junction/pillar, a thin metallic layer (Al 110nm/Au 35nm) was deposited with the help of an electron beam evaporator (Plassys MEB 550S) machine. Here, the aluminum layer provides better adhesion to the sample.

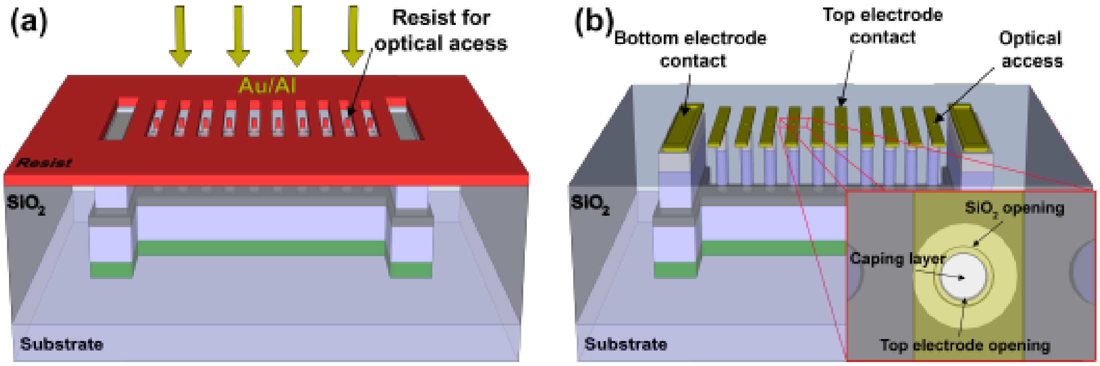

Figure 2.7. Schematics for the photolithography step-IV, (a) Top electrode metal (110nm Al/35nm Au) being deposited using the electron beam evaporation technique on the entire surface that is already selectively developed by negative photoresist, **(b)** Lift-off process, removing the metal (110nm Al/35nm Au) from undesired areas of the surface. The figures are taken from ref. [41].

Before metal deposition, the negative photoresists (AZ5214) was selectively developed over the surface of the stack using the optical mask in such a way that from the rest of the area (other than the pillar, contact pads for bottom electrode, and developed image for the top electrodes), the deposited gold can be easily removed during lift-off process. The top electrodes were deposited in perpendicular geometry to the bottom electrode. For each bottom electrode, 12 top electrodes are deposited at a time. As a feature that was not used in this Thesis, an optical opening in the junctions can be achieved by using the proper design in the optical mask. Step IV is schematized in Fig. 2.7. The aforementioned steps finally yield 240 microscale MTJ devices in 11x7 mm^2 surface area of the multilayer stack. The top view of the processed multilayer stack is shown in Fig. 2.8.

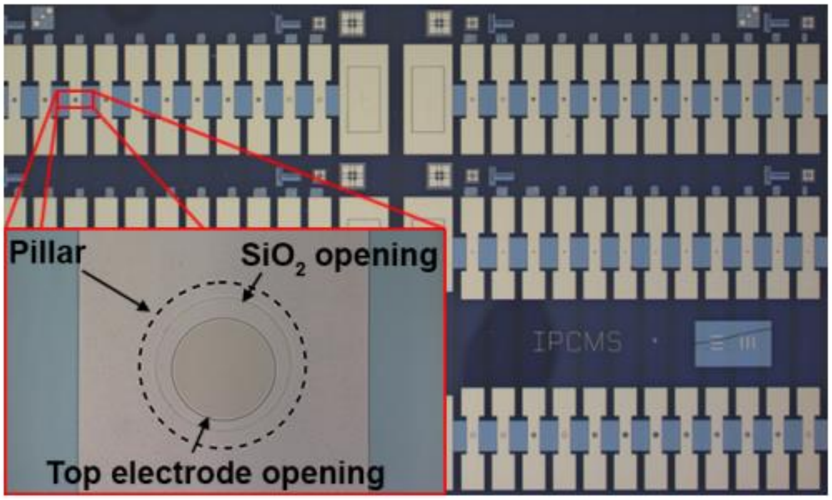

Figure 2.8. 2-dimensional top view of the processed sample after all the four steps. The figure is taken from ref. [41].

2.2 Electron-beam lithography

In spin-transfer torque (STT) experiments, to drive the magnetization dynamics in the free FM layer of an MTJ device, an input current with a sufficiently high density[6,7] is required. This can be achieved by decreasing the cross-sectional area down to the nanometric scale. This miniaturization in the cross-sectional area is generally achieved using electron beam lithography (EBL). The working principle of the EBL is similar to that of UV-photolithography. In both lithography techniques, a polymer layer (sensitive to the incident UV-rays/electron beam) called a resist is coated on the surface of the sample on which the required pattern is desired. In the case of UV-photolithography, the desired image is transferred by shining the UV light through the optical mask, whereas in the case of the EBL this is achieved by the incident electron beam of high energy. In order to remove the charge developed on the sample by the incident electron beam of high energy during the image transfer process, the sample is kept grounded. In both lithography techniques, the incident UV-light/electron beams, are used to soften (harden) the exposed positive (negative) resist layer. The transferred image on the resist layer, after the development process by the developer solution thus produces the desired pattern. The most common resists used for the EBL process are polymethylmethacrylate (PMMA), polybutene-1-sulphone (PBS), polyglycidylmethacrylate coethylacrylate (COP), hydrogen silsesquioxane (HSQ), and SU8. The first two are the positive whereas the last three are the negative resists. The developer solution used is methylisobutylketone (MIBK) and isopropanol (IPA) in 1:1 ratio.

Theoretically, the resolution of the developed pattern is directly associated with the wavelength of the lithographer agent (UV-light in case of the UV-photolithography and electron beam in case of EBL). The electron beam, with a much-lowered wavelength $(\lambda_e = 1.226/\sqrt{V})\ nm$ compared to the UV-light (365 nm, i-line of Hg lamp), can provide a resolution down to 0.1Å by the application of high input voltage of 10keV. However, practically it is impossible to reach a 0.1Å resolution limit because of the choice of the resist and its use during the process. Also, the e-beam setup is an important parameter that limits the final resolution. Generally, 10 nm resolution can be obtained with EBL. These EBL setups can be purchased separately and integrated into the commercially available scanning electron microscope (SEMs) facilities.

In Chapter-4, the nanoscale MTJ devices being used for the STT experiments were also fabricated using the state-of-the-art EBL facility at the International Iberian Nanotechnology Laboratory, Portugal, and TDK-Headway Inc. USA in collaboration with Professor Paulo Freitas and Dr. Luc Thomas respectively. The abbreviation MTJ-F was used for the samples received from Professor Paulo Freitas/Dr. Ricardo Ferreira and MTJ-H for the samples received from TDK-Headway Inc. The details of the MTJ-H devices are kept secret as they are being used for commercial applications by the company TDK-Headway Inc. USA.

The nanopillar MTJ-F device fabrication starts with the deposition of the following stack: Al_2O_3(100)|Ta(3)|CuN(30)|Ta(5)|$Pt_{38}Mn_{62}$(17)|$CoFe_{30}$(2)|Ru(0.85)|$CoFe_{40}B_{20}$(2.6)|MgO(wedge

=0.6-0.9 nm)|$CoFe_{40}B_{20}$(1.4)|Ru(10)|Cu(150)|Ru(30)[102]. The above-mentioned structural sequence from left to the right direction for the multilayer stack progresses from bottom to top on silicon (Si <100>) substrate with native silicon oxide on top. The numbers within the small parentheses represent the thickness of the corresponding material layer. The wedge-deposited MgO layer offers thickness variation of the tunneling barrier and thus the resistance. The top (free) $CoFe_{40}B_{20}$ (1.4 nm) layer has magnetization along an in-plane direction. The square-shaped multilayer stack with dimension 2.2x2.2cm^2 is processed into the nanopillar MTJ devices using state-of-the-art EBL technique.

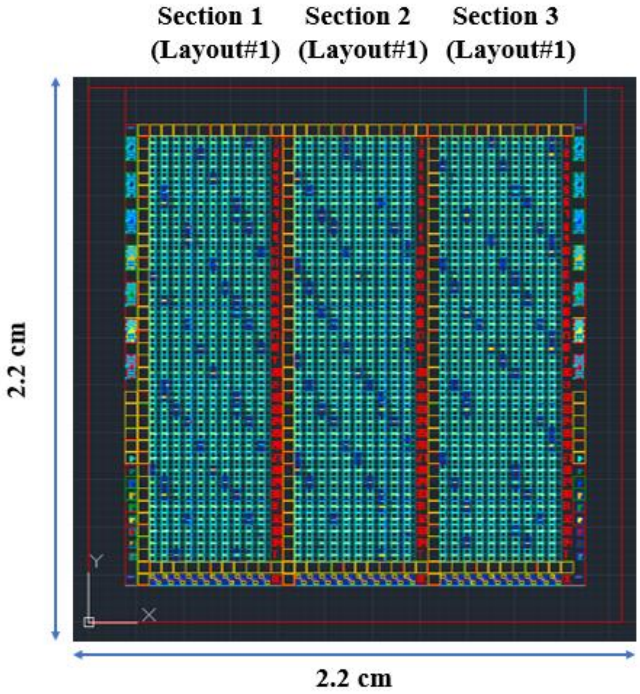

Figure 2.9. Electron beam lithography mask used for fabrication of the nanopillar MTJ-F devices. A complete processed MTJ-F stack contains three sections; i) left, with circular devices, ii) center with elliptical devices and iii) right with both circular and elliptical shape devices. Each section, containing 16 + 01 (test) rows and 10 columns with 170 devices in each section and 510 devices in one processed stack. The numbers written for X and Y are the dimensions of the respective devices in respective directions.

Fig.2.9 shows the EBL mask (with layout#1) used for the EBL process. Each processed stack contains three sections. Each section containing 10 columns and 16 + 01 (test) rows, resulting in 170 nanopillar devices in one section and a total of 510 nanopillar devices in one processed stack. The first section (on the left side) has all the devices in a circular geometry, the second section (right to the first section) contains all the devices in an elliptical shape, while the third section (on the extreme right side) contains circular devices from column 01 to 07 and afterward up to column 10, in an elliptical shape. Fig.2.10.a details all the device dimensions, while panel (b) details the dimensions and geometry of the elliptical devices of section 2 of the processed multilayer stack.

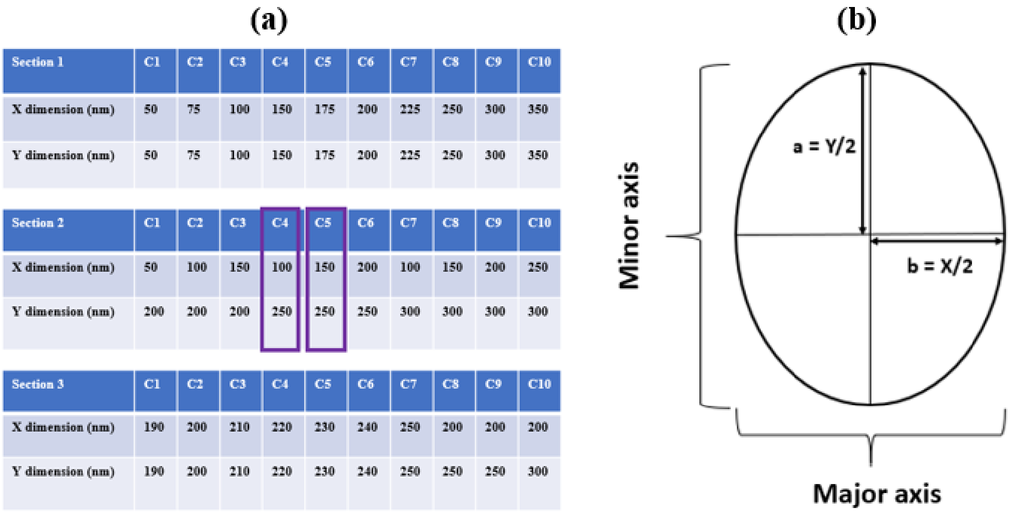

Section 1	C1	C2	C3	C4	C5	C6	C7	C8	C9	C10
X dimension (nm)	50	75	100	150	175	200	225	250	300	350
Y dimension (nm)	50	75	100	150	175	200	225	250	300	350

Section 2	C1	C2	C3	C4	C5	C6	C7	C8	C9	C10
X dimension (nm)	50	100	150	100	150	200	100	150	200	250
Y dimension (nm)	200	200	200	250	250	250	300	300	300	300

Section 3	C1	C2	C3	C4	C5	C6	C7	C8	C9	C10
X dimension (nm)	190	200	210	220	230	240	250	200	200	200
Y dimension (nm)	190	200	210	220	230	240	250	250	250	300

Figure 2.10. Structural details of the MTJ-F nanopillar devices. (a) Dimensions of all the nanopillar devices in nm, **(b)** dimensions, and geometry of the elliptical devices in section 2 of the processed multilayer stack.

The microscopic image of the nanopillar devices is shown in Fig.2.11. The left figure shows an array of the nanopillar devices, while the figure on the right side is a zoomed image of the nanopillar devices. Each device consists of two pads for the bottom and top electrodes, denoted by BE and TE respectively.

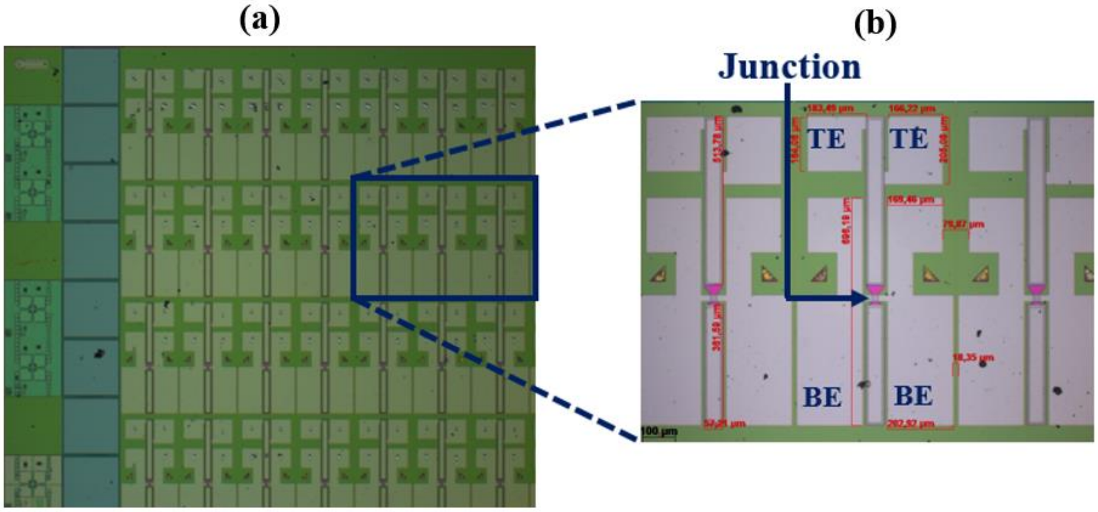

Figure 2.11. Optical image of the MTJ-F nanopillar devices. (a) Microscopic image of the EBL processed multilayer stack taken from an optical microscope, **(b)** Zoomed image of nanopillar MTJs with two contact pads for both top (TE) and bottom electrodes (BE). In the pink part, the area beneath the metallic contact pad is the nanopillar MTJ device.

The device size (cross-sectional area) was tuned using the e-beam lithography technique during the nanofabrication process. In each section, moving from left to right columns, the device size increases. While moving along rows from top to bottom direction, the thickness of the MgO increases and so does the resistance. The thickness of the MgO barrier was controlled by the wedge deposition scheme during the growth process. The wedge deposition scheme together with the e-beam lithography process provides control over one of the most crucial parameters in MTJ physics: The R.A product. The R.A product determines for which application the MTJ devices will be used[103]. For STT-based applications that require a sufficiently large current density to drive the STT effect, the MTJ devices with low R.A products (~1-100 Ω.μm^2) are required. In this chapter, the MTJ-F devices of MgO thickness 0.6-0.9 nm (~5ML), corresponding to an R.A product ranging from 1-40 Ω.μm^2 respectively (in P state at 300 K) were used.

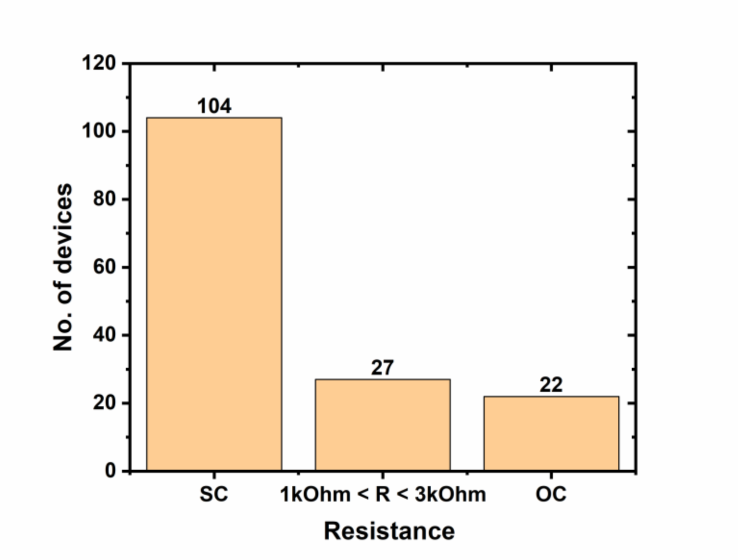

Figure 2.12. Resistance distribution of the MTJ-F elliptical shape nanopillar MTJ devices from section 2 of the processed sample.

Fig.2.12. represents the resistance distribution of the MTJ-F elliptical devices from section 2 of the EBL processed sample. Out of the total 153 devices, only 27 devices exhibit a significant amount of resistance values. In order to probe the localized state and their impact on the STT [Chapter-3 and 4] spanning from Fermi energy to -0.7eV, the devices must have a significant amount of resistance that can help avoid electrical breakdown at corresponding voltages.

The processed sample was diced into 5x7 mm^2 size using the diamond-coated wire saw or the professional dicer was glued on the customized printed circuit board (PCB FERT chip), and bonded in 4-point mode with aluminum wire using the wire-bonder machine. The 4-point or Kelvin mode eliminates the resistances of the connecting wires and therefore measures the true resistance of the junction. The bonded sample is now ready for the magnetotransport measurements. During the measurements, the input bias was applied in such a way that the direction of the flowing electron is from the bottom (fixed) to the top (free) electrode for a positive bias voltage.

2.3 Magnetotransport setup

The magnetotransport measurements were performed on the multifunctional bench (BMF) equipped with a water-cooled 2T cubic and a smaller U-shaped electromagnet. The different geometries of the magnet provide us the flexibility to perform different kinds of experiment like laser excitation, magneto-optical Kerr microscopy, and magnetotransport measurements on the same setup. The sample mounted on the FERT chip is fixed to the cold finger made of copper and covered with the gold-plated shroud with an optical window and cooled down from 300K to 10K temperature using a closed-cycle refrigerator-based cryostat. The temperature of the device is controlled by the cryostat and heater synchronized together by the computer program. Out of the simultaneously connected 5 MTJ devices to FERT chip, a particular device of interest can be selected from using a custom-designed multiplexer. The setup also enables 3-D translational and rotational degrees of freedom to the sample while the cryostat is in the magnet. The cryostat rotation is done manually. During the measurements, to provide a high vacuum, the turbopump remains turned on. The computer program was written by Stephane Dornier, Ufuk Halisdemir, and Martin Bowen on LabVIEW graphical language. Motor coding was written by Stephane Dornier and Martin Bowen. To source the input applied bias and measure the corresponding output current, a Keithley2636 multichannel source meter was used.

2.4 Effective barrier height calculation: $\hat{I}$ spectroscopy

In an MTJ device, the barrier height due to the dielectric layer sandwiched between two FM electrodes plays an important role in the tunneling process. Generally, for an MTJ the barrier heights and the thickness are extracted by fitting the I(V) curves performed in their respective P/AP states, with the Brinkman's or Simmons' formula. Both of these formulas are derived under the framework of WKB approximation and for a perfect potential step within the free electron model. In the presence of defects within the thin insulating layer, the additional energy states start to appear near the Fermi energy (E_F). These additional states, according to their energetic distance from $E_{F,}$ lower the actual barrier heights of the ultrathin insulating layer. The barrier height that is lowered due to the presence of defect states is known as the effective barrier height. In the case of MgO as a dielectric layer between CoFeB electrodes, the barrier height should be 3.9eV theoretically because of its optical bandgap value of 7.8eV. This barrier height has been observed experimentally on defect-free MgO[95]. Since MgO is an oxide material, in which the deficiency of the oxygen atoms produces different kinds of vacancy states, and depending upon the vacancy type the effective barrier height was determined to be much lower than the theoretically suggested values. Depending on the oxygen vacancy type this effective barrier has been reported 0.7eV to 0.4eV below the E_F[95].

In order to calculate the effective barrier heights due to the defect states (that are completely ignored in the previous models i.e. Brinkman's[39] and Simon's[38]), Rottländer et al.[15] proposed a more physical approach. This physical approach utilizes the I(V)s performed at two different temperatures T_1 and T_2 ($T_1 < T_2$) in the thermal energy range of $\Delta E = k_B \Delta T$ to calculate the effective barrier heights. The energetic position (applied bias) at which the $I_{rel}(V,T)$ or $\hat{I}(V,T)$ maxima is observed is the effective barrier height of the MTJ. The $I_{rel}(V,T)$ or $\hat{I}(V,T)$ is calculated using the following formula:

$$\hat{I}(V,T) = \{\frac{I(V,T_2)}{I(V,T_1)} - 1\} * 100\% \tag{14}$$

The $\hat{I}(V,T)$ spectroscopy technique can be understood from Fig.2.13.

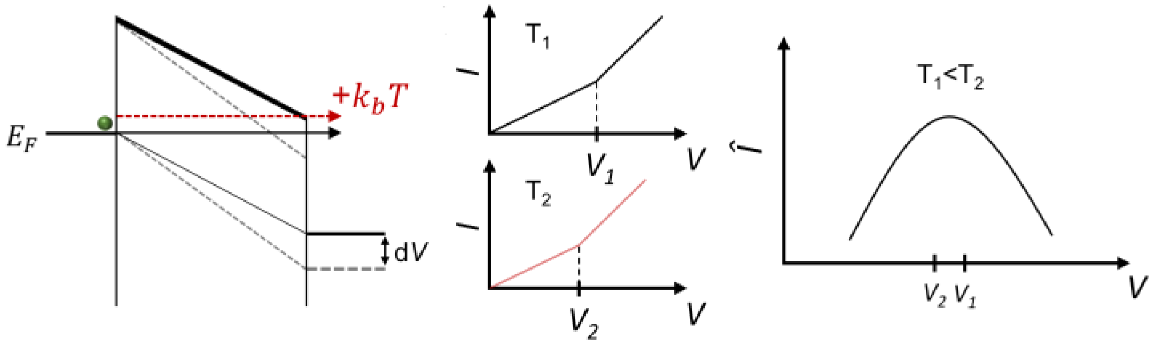

Figure 2.13. Physical description of Î-technique. (a) Applying bias causing a linear potential drop thus lowering of effective barrier height and increase in tunnel current, **(b)** Increasing temperature from T_1 to T_2, provides additional thermal energies to the tunneling electron causes the increased tunneling current at V_2 ($<V_1$), (c) quantified $\hat{I}(V,T)$ for $\Delta T = T_2 - T_1$. The figures are taken from ref. [41].

Similar to $I_{rel}(V,T)$ or $\hat{I}(V,T)$s the TMR_{rel}s can be calculated using the following formula:

$$TMR_{rel}(V,T) = \{\frac{TMR(V,T_2)}{TMR(V,T_1)} - 1\} * 100\% \tag{15}$$

The advantage of replacing $I_{rel}(V,T)$ with $TMR_{rel}(V,T)$ is that the TMR is calculated from both P and AP contribution therefore even a small peak in the $\hat{I}(V,T)$ of P can be easily observed in the background of AP.

2.5 Spin torque ferromagnetic resonance (STFMR) technique

As already been described in the previous sections, the magnetization of the free ferromagnetic layer in nanopillar MTJs can be reversed by flowing a current with a sufficiently high current density ($J > 10^7$ A/cm^2)[6,7] via the STT mechanism. During the STT event, a high-density current when passes through the fixed FM electrode gets spin-polarized. This spin-polarized current after tunneling through the ultrathin barrier when interacts with the free FM layer transfers its' spin angular momentum onto the magnetization of the free layer. This induces the magnetization precession in the free layer causing magnetization reversal of the free FM layer and generation of spin waves in the microwave frequency (GHz) range[104–106]. The devices that work on this principle are known as *spin-torque nano oscillators* (STNOs) and finds application for microwave generation and detections.

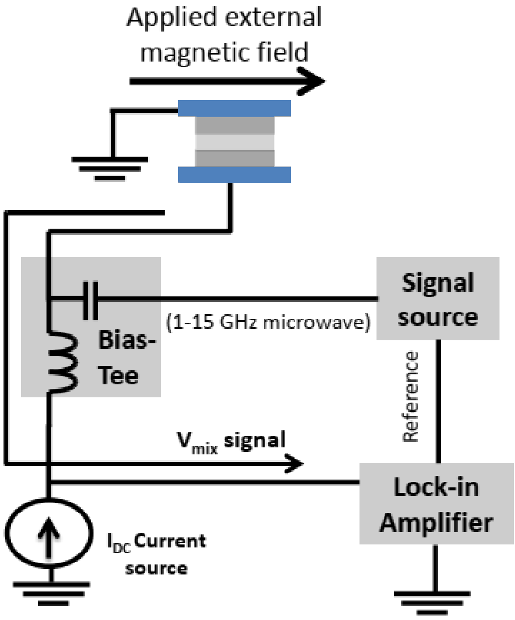

Figure 2.14. Experimental set-up for RFM-STFMR measurements technique. The figure is taken from ref.[107].

As a complementary effect, if an input current in microwave frequency range is applied to the nanopillar MTJ devices, at the resonance frequency corresponding to magnetization precession of the free layer, a d.c. voltage appears. This effect is very similar to the semiconductor p-n diodes commonly used for the rectification process or to convert input a.c. signal to the d.c. output. This spin-torque diode effect[108,109] is widely used in applications as microwave detectors. The STFMR technique[16,109,110], utilizes a similar principle of spin-torque diode effect in which the input radiofrequency current (I_{rf}) at the frequency equal to the precession frequency or at the resonance frequency (f_{rf}) causes the precession of magnetization, thus allowing to probe the dynamical properties of the system. The STFMR technique can be used to study magnetic damping[111], spin-transfer torque[16,109], voltage-controlled anisotropy[112], and magnetic excitations[6,113] in the magnetic nanostructure devices.

STFMR will be used as a complementary technique to examine how oxygen vacancy induced localized states within the MgO tunneling barrier alter spin-transfer torque. We will experimentally extract the in-plane to out of plane torque ratio and compare its bias dependence with the energy position of localized states determined using $\hat{I}$- measurements.

The STFMR experiments were performed at Dr. P. K. Muduli’s group at IIT-Delhi. A small radiofrequency current (I_{rf}) of the form $I_{rf}.\cos(2\pi.f_{rf}).t$ in the microwave frequency (100 MHz to

20 GHz) range was sourced using a Rhode & Schwarz SMB 100A signal generator, and dc current (I_{dc}) were simultaneously applied to the nanopillar MTJ via a bias-tee shown in the **Fig.2.14**.

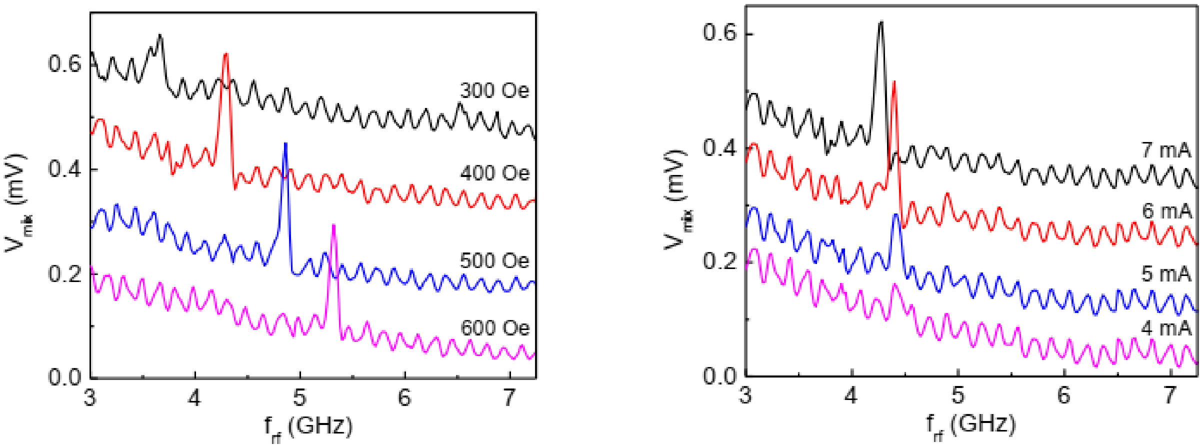

Figure 2.15. A typical RFM- STFMR spectra measured by varying (a) H_{ext} at P_e = -10dBm, **(b)** I_{dc} at H_{ext} = 400Oe and P_e = -10 dBm. The figure is taken from ref.[107].

The most common modulation scheme is the radiofrequency current modulation (RFM), in which the radio frequency signal $I_{rf}.\cos(2\pi.f_{rf}).t$ is modulated on a reference signal of 98 Hz using the signal generator and together with dc current (I_{dc}) applied to the device. The output voltage (V_{mix}) is measured across the lock-in amplifier by sweeping the frequency (100 MHz to 20 GHz range) of the I_{rf} at constant bias current (I_{rf} + I_{dc}) and external magnetic field H_{ext}. The STFMR spectra obtained using the RFM technique is known as radiofrequency current modulation-STFMR (RFM-STFMR), and is schematically represented in Fig.2.14. It is the most common modulation scheme employed in the literature to improve SNR[16,109,110,114].

Fig.2.15.a, and b show the RFM-STFMR spectra acquired on an STNO device at constant external field H_{ext} and constant bias current (I_{rf} + I_{dc}). For RFM-STFMR, the resonance frequency shifts to higher values at higher H_{ext}, while increasing I_{dc} yields no shift in the resonance frequency position but increases the amplitude of V_{mix}. The RFM-STFMR spectra dominated with the background nonmagnetic oscillations due to the change in the I_{rf} during the frequency sweep. The change in I_{rf} with frequency sweep emerges due to the frequency-dependent transmission losses in the rf coaxial cable and formation of the standing waves due to the impedance mismatch between the microwave circuit and sample. Postprocessing is required in order to eliminate the non-magnetic background signal[109,110,114].

In order to remove the non-magnetic background oscillations, present in the RFM-STFMR spectra, Muduli et al.[115] used field modulation (FM) technique[116] in which the static external magnetic field is modulated by a small ac magnetic field of ≤ 5Oe, produced by a pair of additional Helmholtz coils attached to the pair of the poles of the electromagnet. These coils are supplied with an ac voltage at the reference frequency of 98 Hz from a lock-in amplifier, which also measures the voltage, V_{mix}. I_{rf} and I_{dc} are applied simultaneously through a bias-tee to the MTJ nanopillar, which excites the free layer magnetization and causes resistance oscillations. The rectified voltage is measured across the lock-in amplifier at the field modulation frequency[107]. The STFMR technique based on the field modulation technique is known as FM-STFMR and is represented in Fig.2.16.

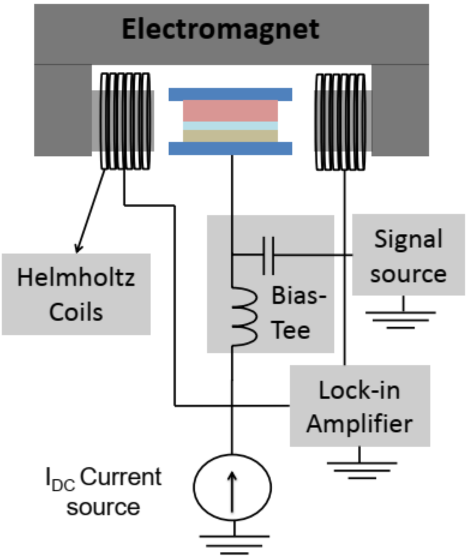

Figure 2.16. Schematic of the FM-STFMR set-up. The figure is taken from ref.[107].

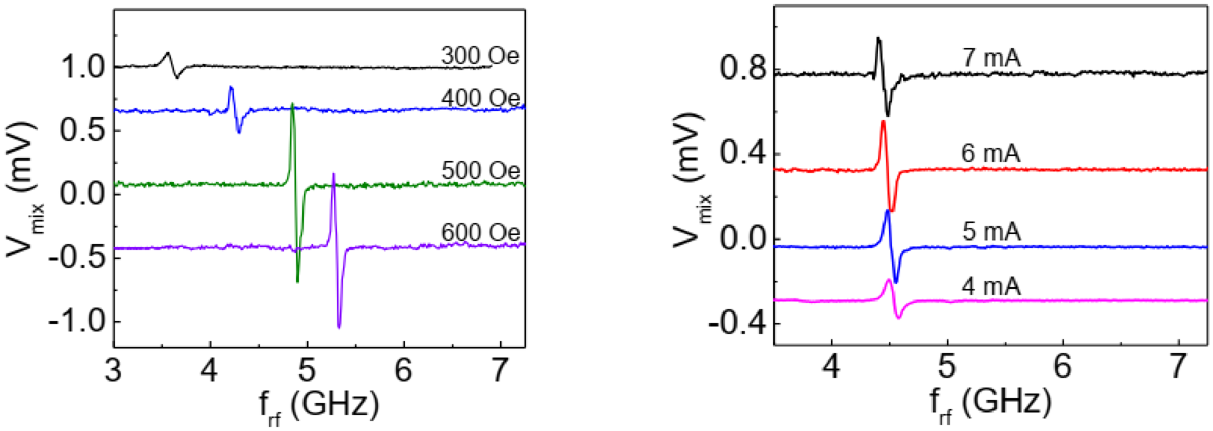

Figure 2.17. A typical FM-STFMR spectra measured by varying (a) H_{ext} at P_e = -10dBm, (b) I_{dc} at H_{ext} =400Oe and P_e = -10 dBm. Figure is taken from ref.[107].

In contrast to the RFM-STFMR spectra in which the peaks are symmetric, the peaks in the FM-STFMR spectra are antisymmetric because of the measured output signal in derivative mode. Likewise, RFM-STFMR, in FM-STFMR, the resonance frequency shifts to higher values at higher H_{ext}, while increasing I_{dc}, makes no shift in resonance frequency position but increases the amplitude of V_{mix}. Using the FM-STFMR technique, the nonmagnetic background oscillations were completely removed from the spectra. Fig.2.17.a, and b represent a typical FM-STFMR spectrum with an almost flat background.

The STFMR spectra from RFM and FM schemes are compared in Fig.2.18. The oscillating frequencies and processional modes in both modulation schemes are close. Due to the larger peak-to-peak voltage (V_{p-p}) and almost flat background, the FM scheme offers much improved SNR compared to the RFM scheme. Muduli et al. reported quite improved SNR of 30.5 dB using the FM scheme as compared to the 17.7 dB from the RFM scheme for the same STNO devices[107].

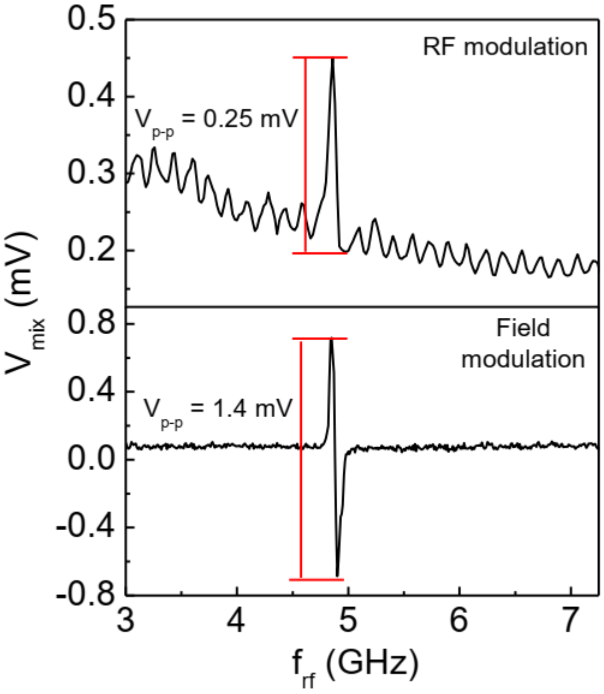

Figure 2.18. Comparison of RFM-STFMR and FM-STFMR spectra measured at H_{ext} = 500Oe and P_e = −10 dBm. The figure is taken from ref.[107].

In the present experiments, the FM-STFMR scheme was implemented for the measurement of in-plane and out-of-plane torkance (a derivative of the torque with respect to the bias) and torque. In STFMR experiments the shape of the signal is given by[109]:

$$V_{mix} = C + V_S S(f) + V_a A(f) \tag{16}$$

Where C is the non-resonant background signal given by:

$$C = \frac{1}{4}\frac{\partial^2 V}{\partial I^2} I_{rf}^2 \tag{17}$$

here I_{rf} is the microwave current, and σ_r is the spectral linewidth. S(f) is the symmetric Lorentzian and A(f) is the antisymmetric Lorentzian given by:

$$S(f) = \frac{1}{1 + (f_{rf} - f_r)^2/\sigma_r^2} \tag{18}$$

and

$$A(f) = \frac{(f_{rf} - f_r)/\sigma_r}{1 + (f_{rf} - f_r)^2/\sigma_r^2} \tag{19}$$

Where σ_r is the spectral linewidth (changes with bias current), and f_r and f_{rf} is the resonance frequency and microwave signal frequency respectively.

The amplitudes of Lorentzian V_s and V_a are a function of spin-torque vectors. The symmetric and antisymmetric amplitudes, containing spin-torque vectors are calculated experimentally using the following equation[109]:

$$V_S = \frac{1}{2}\left(\frac{\partial^2 V}{\partial\theta\,\partial I}\right)\frac{\hbar\gamma\sin\theta}{4eM_S V\sigma_r} I_{rf}^2 \left[\frac{\left(\frac{2e}{\hbar}\right)}{\sin\theta}\right]\frac{d\tau_{\parallel}}{dI} \tag{20}$$

and

$$V_a = \frac{1}{2}\left(\frac{\partial^2 V}{\partial\theta\,\partial I}\right)\frac{\hbar\gamma\sin\theta}{4eM_S V\sigma_r} I_{rf}^2 \left[\frac{\left(\frac{2e}{\hbar}\right)}{\sin\theta}\right]\Omega_{\perp}\frac{d\tau_{\perp}}{dI} \tag{21}$$

Where $\hbar = 1.034\times10^{-34}$ Js is reduced Planck's constant, $\gamma = 1.76\times10^{11}$ Am^2/Js is gyromagnetic ratio for electron, $e = 1.6\times10^{-19}$ C is electron's charge, M_S = saturation magnetization per volume, V = volume, Θ = in-plane field angle, $\tau_{\parallel}$ = in-plane (IP) torque, $\tau_{\perp}$ = out-of-plane (OOP) torque, and

$$\Omega_{\perp} = \frac{\gamma(4\pi M_{eff} + H_{ext})}{2\pi f_r} \tag{22}$$

Where, $4\pi M_{eff}$ is effective magnetic anisotropy, and H_{ext} is the external magnetic field applied during the measurement. The value of the I_{rf} can be calculated by proper knowledge of the impedance mismatch between the sample and microwave circuit using VNA (vector network analyzer). The following formula is used to calculate the value of I_{rf} :

$$\mathrm{I_{rf}} = \sqrt{\mathrm{P_{ac}(W)}}/\mathrm{R_{dc}}(\Omega) \qquad (23)$$

During the measurements, the estimated power loss was around 40%. These formulas will be used in Chapter-4 to calculate the ratio of IP/OOP torque.

3. Localized States in MgO

As already been described in earlier chapters [Chapter-1], the oxygen deficiency within the MgO unit cell leads to the formation of localized states near the Fermi energy (E_F). Experiments[86] combined with ab-initio calculations[4,91] revealed that these localized states near E_F, lower the effective barrier height and promote spin and symmetry filtering, thus impacting the physics of solid-state tunneling transport across the MgO barrier in a magnetic tunnel junction (MTJ).

MTJs have been extensively used for field sensing devices and with the advent of the spin-transfer torque (STT) effect, caught a lot of attention for the development of next-generation magnetic random-access memories (MRAMs). From the scientific literature available so far, these localized states due to the oxygen vacancies within the MgO barrier have never been studied in the context of STT. Therefore, from both basic physics and industrial application point of view it becomes very important to address these localized states and their impact on STT.

From our earlier scientific knowledge [Chapter-1], that these localized states are mainly of three types: M_2 (antibonding double oxygen vacancy), F/F^+ (ground/excited state single oxygen vacancy), and M_1 (bonding double oxygen vacancy) lying below to the E_F. Experiments[4,86] on the MTJs with $Fe_{0.4}Co_{0.4}B_{0.2}$ (FeCoB) as ferromagnetic electrodes pegged the barrier heights 0.4 eV, 0.7 eV and 1.1 eV below to the E_F, to the M_2, F^{+*} and F centers respectively lying at the thermal energy scales of corresponding temperatures of $T > 250$ K, $80 \text{ K} < T < 250$ K and $30 \text{ K} < T < 80$ K respectively. Whereas for the MTJs with FeCo as ferromagnetic electrodes theory[4,91] suggested that these three barrier heights of 0.4 eV, 0.8 eV, and 1.1 eV below to the E_F, could correspond to the M_2, F, and M_1 state, respectively. Inferring that tunneling is proceeding relative to the occupied states. Before heading to the main project dedicated to studying the impact of these localized states on STT (next chapter), the discrepancies between the experiments and theory regarding the exact energetic positions of these localized states relative to the E_F must be resolved.

To resolve the discrepancies regarding the energetic positions of these localized states arising from the experiments and theory, we conceived an experiment followed by *ab-initio* theory in which one of the FM electrode's work function is altered and witnessed how experimental and theoretical barrier height evolves. In present experiments the top FM electrode was replaced from $Fe_{0.4}Co_{0.4}B_{0.2}$ (FeCoB) to $Fe_{0.8}B_{0.2}$ (FeB).

3.1 Device details

The experiment was carried out on the MTJs, processed from the wafer of multilayer structure: Ta(5)|Co(10)|IrMn(7.5)|FeCoB(4)|MgO(2.5)|FM(3)|Ta(1)|Pt(1), where FM denotes the top ferromagnetic electrode and numbers inside the small brackets represent the thickness of respective layers in nm. Left to right direction of multilayer structure indicates, bottom to top layers deposited on Corning 1737 substrates by standard sputtering techniques. A subsequent 300 °C annealing step in an external in-plane magnetic field sets the exchange field of the IrMn pinning layer within the lower electrode and promotes the diffusion of B to crystallize both FeCoB and FeB magnetic electrodes[44]. The growth details have been described in the previous reports[86,117]. In order to ensure no change in the MgO barrier's structure during the growth[118], the lower electrode was kept as it is i.e. FeCoB. The structural properties of the MgO barriers in MTJ stacks with different top FM electrodes e.g. FeCoB and FeB should therefore be comparable, in line with the literature[67].

The MTJs were processed down to the 20 μm diameter using the UV-photolithography technique, as described in the previous chapters [Chapter-2]. The average R.A. product was found to be $5x10^7$ $\Omega \cdot \mu m^2$ and $1x10^8$ $\Omega \cdot \mu m^2$ for the MTJs with FeCoB and FeB top electrodes respectively.

3.2 Electrical and magnetotransport measurements

Figure 3.1, represents the device schematics with the electrical connections. The devices were connected in 4-point mode with positive(negative) contacts on the top(bottom) electrode, such that holes are flowing from top to bottom (or electrons flowing from bottom to top electrode) at positive external applied bias voltage.

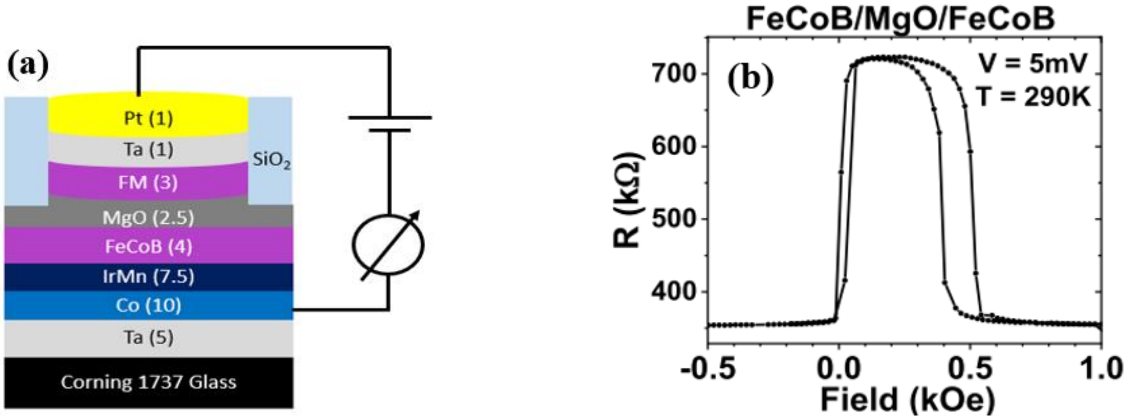

Figure 3.1. Device Schematic and R(H) plot. (a) Schematic of 20 µm circular MTJ device, **(b)** Typical R(H) plot of the MTJ device.[119]

The magnetotransport measurements were performed with a magnetic field applied along the in-plane direction. The following results are representative of previous studies on FeCoB/MgO/FeCoB MTJs[86,120], which we compare with results obtained on six FeCoB/MgO/FeB MTJs. Figure 3.1.b represents the R(H) curve: we observe a large plateau in the MTJ's AP magnetic state due to the IrMn pinning layer. At room temperature, both types of samples exhibit 105% TMR, whereas at 10 K the sample with FeCoB (FeB) exhibits 205% (160%) TMR. The decrease in the observed TMR at low temperature for MTJs with FeB as top electrode is in part due to the presence of additional Δ_5 transport channels at E_F [47,121].

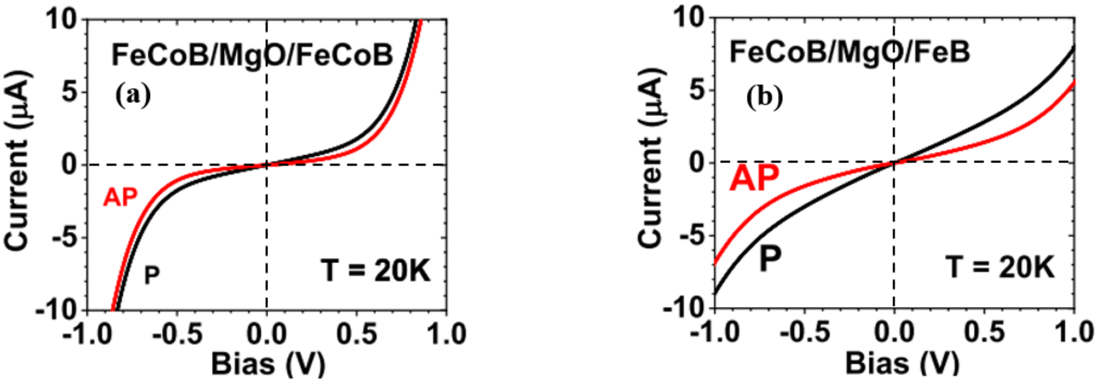

Figure 3.2. I(V)s performed at 20K for the MTJ device with (a) FeCoB, and (b) FeB top electrode. The black and red curve represents P and AP states respectively. [119]

Furthermore, replacing the top FM electrode from FeCoB to FeB introduces $\Delta_{2'}$ and Δ_5 spin up (↑) conduction channels at E_F[122], such that the I(V) characteristics for both P and AP states are more linear at low bias. This can be seen in Figure 3.2.a, and b.

3.2.1 Mapping the localized states experimentally

To precisely locate the energetic positions of the localized states due to the defect states within the barrier, the standard Î-technique[15] [Chapter-2] was employed. The beauty of the Î-technique is that it makes no assumptions on the barrier potential profile or the effective mass of the charge carrier. Instead, it examines the bias at which thermally activated conduction is maximum and ascribes the energy position of the localized state to the resulting energy difference relative to E_F. In practical terms, the Î-technique requires two consecutive I(V)s performed at two different temperatures T_1 and T_2 where $T_1 < T_2$. Using the formula, $\hat{I}(V, T) = [\{I(V, T_2)/I(V, T_1)\} - 1]*100$ (%) formula, Î can be plotted with respect to the applied bias. A peak in the Î, corresponds to 1.2 times the barrier height[15]. The effective barrier height calculated using this technique is completely independent of the barrier thickness[15]. In contrast to phenomenological models (e.g. Simmons or Brinkman)[38,39], this physical method of determining features in the MTJ potential landscape makes no assumption regarding the effective mass or energy dispersion of the charge carrier[15].

Figure 3.3.a, and b shows the Î plots for $\Delta T = 22K$ (21K), calculated from two I(V)s performed at $T_1 = 23K$ (21K) and $T_2 = 45K$ (42K), for the devices with CoFeB (FeB) as a top electrode respectively, in the P magnetic state (i.e., $\hat{I}_p$). The presence of a strong peak in $\hat{I}_p$ near V=0 is due to the thermal activation of the inelastic processes relating to the zero-bias anomaly[123]. In Figure 3.3.a, we observe a strong peak in $\hat{I}_p$ at ±0.9 V. This ±0.9 eV peak for CoFeB corresponds to the M_1 center and is in agreement with the theory[4]. In Figure 3.3.b, for the devices with FeB as the top electrode, however the $\hat{I}_p$ is very noisy, the $\hat{I}_p$ peaks was found around 1.25 eV.

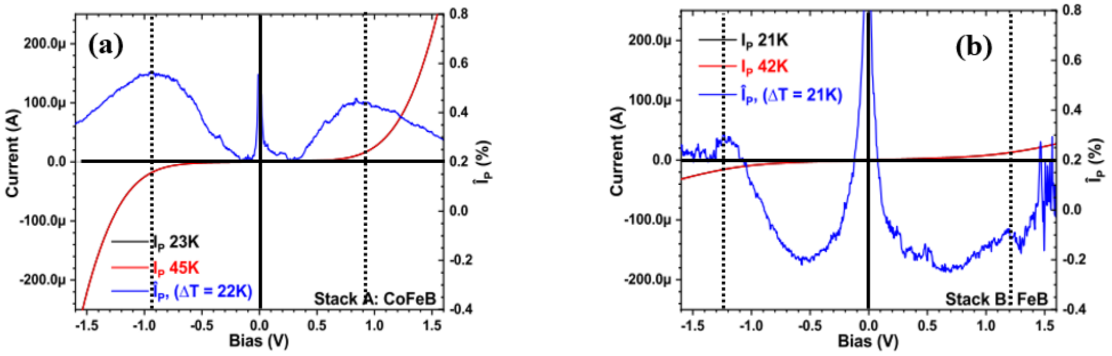

Figure 3.3. I(V)s and Îs performed for the MTJ devices with (a) FeCoB, and (b) FeB as the top electrode. The black and red curve represents the I(V)s performed at 23K, 45K for fig (a) and 21K and 42K for fig **(b)** respectively. The blue curve represents the **Î**s extracted out of that two temperature points.

To overcome the noise issues in the **Î**-technique for the MTJ with FeB as a top electrode, a more refined TMR_{rel} technique[15,86,124] was employed. This technique is based on plotting the relative change in the TMR (TMR_{rel}) values with respect to the applied bias voltage at two given temperature. We define $TMR_{rel}(V, T) = [\{TMR(V, T_1)/TMR(V, T_2)\} - 1] * 100$ (%), where $TMR(V, T) = [\{I_P(V, T)/I_{AP}(V, T)\} – 1]$.

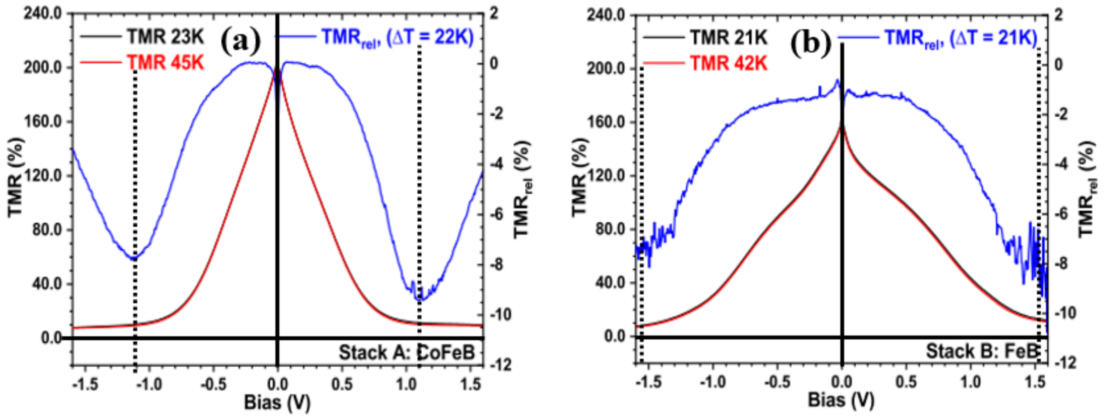

Figure 3.4: I(V)s and TMRrel performed for the MTJ devices with (a) FeCoB, and (b) FeB as the top electrode. The black and red curve represents the TMR(V) measured at 23K, 45K for fig (a), and 21K and 42K for fig (b) respectively. The blue curve represents the TMRrel extracted out from the TMR at these two temperature points.

Since this technique includes I(V)s from both P and AP states for the calculations of the TMR used as an input for $TMR_{rel}(V, T)$, therefore from Figure 3.4.a, and b, it is clearly visible that the TMR_{rel} peaks are smoother with sharper amplitude and a significant reduction in FWHMs is observed as compared to the **Î**-technique. From Figure 3.4.a, for the devices with FeCoB as the top electrode, the TMR(V) traces at 23K and 45K look very similar. The resulting TMR_{rel} contains two pronounced dips centered around ±1.1V. The trend in TMR_{rel} with applied bias is very similar to the **Î**-technique, where the I(V)s at two temperature points 23K and 45K were almost similar but the $\mathbf{\hat{I}}_p$ peaks were found around ~±0.9V.

By changing the top electrode from FeCoB to FeB in the MTJ devices, the TMR_{rel} becomes broader with a TMR_{rel} peak at ±1.55V, at the borderline of the measurement see Figure 3.4.b. The applied bias values were limited up to ±1.6V to avoid device instability issues.

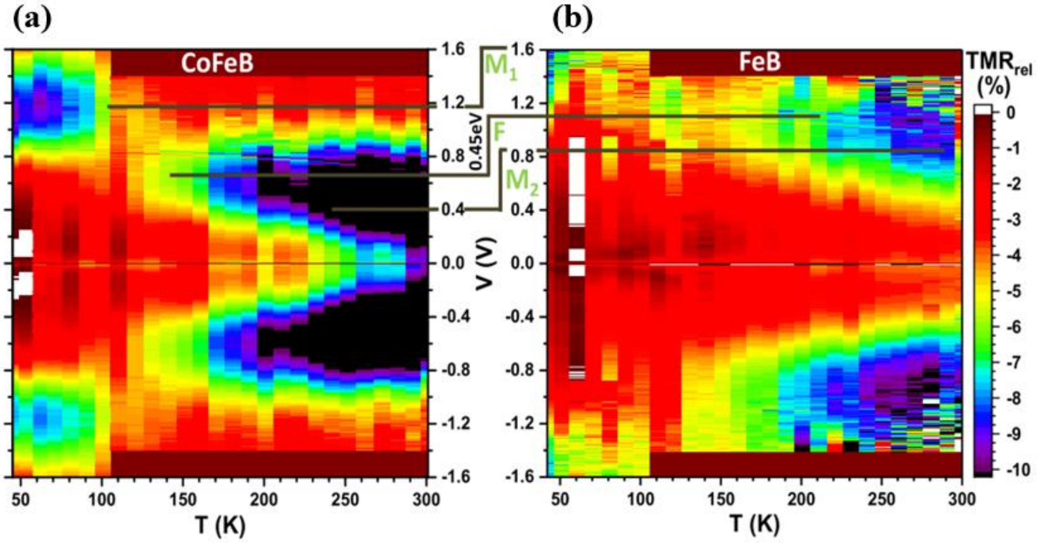

Figure 3.5. TMRrel 3D plots for MTJ devices with the top electrode (a) CoFeB and (b) FeB. The x, y, and z-axis represent the temperature, applied bias, and amplitude of TMRrel respectively. The color scale represents the z-axis or TMRrel amplitude. The shift of the 0.45 eV in the occupied states towards the higher energy values with respect to the Fermi energy is evident when the top FM electrode is replaced from FeCoB to FeB.[119]

Figure 3.5 represents the 3-D color map of TMR_{rel} performed over temperature range 40K-300K at each 9K temperature step for the MTJ devices with (a) FeCoB as the top electrode and (b) FeB as the top electrode. In Figure 3.5, the x, y, and z-axis represent the temperature, applied bias voltage, and amplitude of TMR_{rel}, respectively. The color scale corresponds to the z-axis and the TMRrel amplitude. Referring to Figure 3.5.a, when two FeCoB electrodes are used, the TMR thermal decrease is largest at 1.2 V within 50 K < T < 100 K. For 100 K < T < 250 K, it is at 0.7 V. For T > 250 K, it is at ~0.4 V.

On replacing the top FeCoB electrode with FeB electrode, in Figure 3.5.b the entire set of the features shifts by 0.45 eV to higher energies. Within the experimental error (of 0.04 eV for CoFeB and 0.1 eV for FeB datasets), no asymmetry was found in the energetic positions of the localized states. The increase in the effective barrier height throughout the entire temperature range on replacing the top FM electrode from FeCoB to FeB, concludes that in our MTJs with high R.A product ($\sim 10^8\ \Omega \cdot \mu m^2$), tunneling at low bias is experimentally occurring with respect to occupied states, i.e., holes are tunneling. Therefore, we propose a revised diagram of the potential tunneling landscape induced by oxygen vacancies.

3.3 Mapping the localized states using DFT

In order to confirm the experimental shift of 0.45 eV in the energetic positions of the defect states due to a modification in the MTJ's Fermi level position within the MgO bandgap, *ab initio* calculations of F and M centers' occupied states within MgO (001) were performed while varying the FM electrodes from bcc Fe (001) to FeCo (001) with either a pure Co interface or a FeCo interface [Figure 3.6].

The structural defects due to single and double oxygen vacancies were introduced on the mid-layer of a seven-monolayer thick MgO layer sandwiched between either Fe, FeCo, or Co electrodes. The calculations were performed using the projector augmented plane wave (PAW) method as implemented in the VASP code within the generalized gradient approximation (GGA) with Perdew, Burke, and Ernzerhof (PBE) parametrization. Note that GGA underestimates the bandgap but provides correct quantitative values of the energetic positions of the localized states relative to the Fermi energy (E_F)[4]. The correct bandgap values can be obtained by incorporating the computationally more intensive HSE03 (Heyd–Scuseira–Ernzerhof) hybrid functional[125] into the calculations[4].

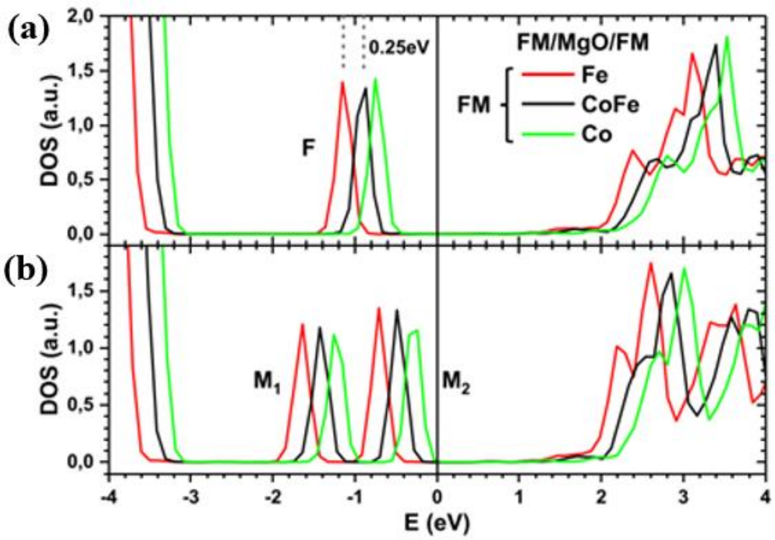

Figure 3.6: **Theoretically calculated DOS of MgO (001) comprising (a)** F centers and **(b)** M_1 and M_2 centers calculated for MTJ stack with a bcc Fe (001) (black), FeCo (001) (red) or Co (001) (green) interface.[119]

Figure 3.6 presents the energy dependence of the density of states (DOS) of the resulting F and M centers as the FM electrode interface is switched from Fe to FeCo to Co. We observe that by replacing the electrode from FeCo (black) to Fe (red), the F-center energy position relative to E_F shifts from -0.9 eV to -1.15 eV, while the M_1/M_2 states shift from -1.42 eV/-0.48 eV to -1.63 eV/-0.71 eV. Thus, we theoretically find that, by switching from FeCo to Fe, the MTJ's Fermi level moves away from the F and M center ground states by 0.25 eV, in a reasonable[96] quantitative agreement with the experiment[126] [Figure 3.5]. The shift in the localized states due to the change in the electrode from FeCoB to FeB was 0.45 eV experimentally while a 0.25 eV shift was predicted. The slight quantitative discrepancy is within the experimental uncertainty (at least ±0.05 eV). The additional theoretical calculations involving MgO sandwiched between Co electrodes reveal a shift of 0.15 eV closer to the Fermi level compared to FeCo.

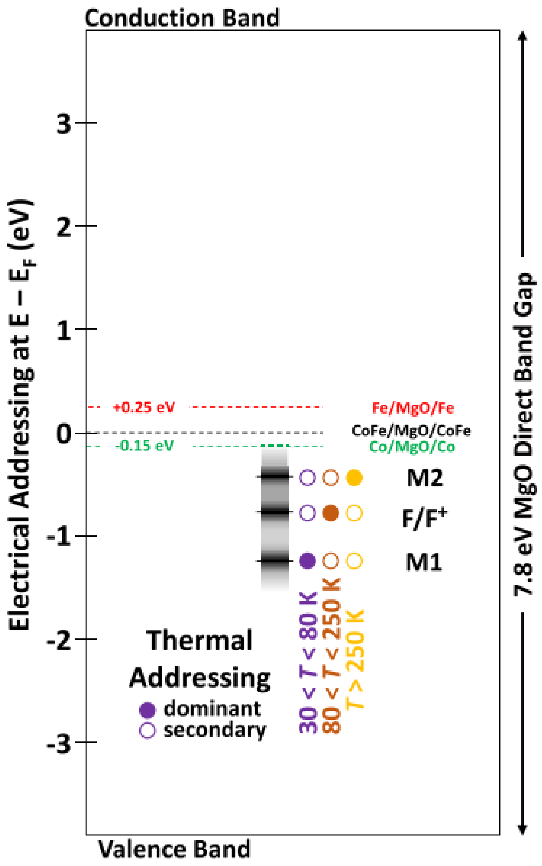

Figure 3.7: Schematic diagram of the energy positions of localized states due to oxygen vacancies in the MgO barrier, relative to the electrode-defined Fermi level. Circles denote the temperature range at which a localized state experimentally dominates the tunneling potential landscape.[119]

The summary of all the theoretical calculations, consistent with the experiment, is presented in Figure 3.7. Switching the top electrode from FeCo to Fe promotes an increase of 0.25 eV in the position of defect states away from the Fermi energy.

3.4 Summary, and perspectives

The magneto-transport experiments combined with *ab-initio* calculations confirm that changing the FM electrode in MTJ devices alters the energetic positions of the occupied/localized states due to the oxygen vacancies with respect to the E_F. This work has provided the correct picture for the energetic positions/effective barrier heights of the localized states within the MTJs comprising CoFeB or FeB as FM electrodes. For an MTJ with FeCoB as FM electrode the energy relative to the E_F at 0.4 eV, 0.7 eV, and 1.1 eV are pegged to the M_2, F, and M_1 states whereas on replacing the top electrode from FeCoB to FeB, all the localized states were shifted to 0.45 eV higher bias value with respect to E_F. *ab-initio* calculations confirm the 0.25 eV shift in localized states to higher bias values with respect to E_F. This shift in the localized states on switching the FM electrode from FeCoB to FeB is due to the modification in the Fermi energy level position within the MgO bandgap. The amplitude of the experimentally and theoretically determined shifts is in reasonable quantitative agreement. Since these localized states lying below E_F are occupied, this means that the tunneling process is mediated by the holes rather than electrons. The MTJs used for this study having an R.A product of around $10^8\ \Omega\cdot\mu\text{m}^2$. For STT studies, MTJs with a much lower R.A product of around 1–100 $\Omega\cdot\mu\text{m}^2$ are used, which suggests the presence of a higher density of interacting oxygen vacancies. From previous scientific reports[4,91], the presence of M_2 center/localized states due to the oxygen vacancies preserves the coherent transport[3] and provides lower effective barrier height. Halisdemir et al.[127] revealed that even for the thinnest barrier, the required current densities for STT can only be achieved if the energetic barrier is much lower than the 3.9eV of intrinsic MgO. This confirms that the defect-induced lower barrier heights/localized states are required for observing STT across MgO-based nanopillar MTJs. In the next chapter, the impact of these localized states due to the oxygen vacancies on STT will be studied extensively.

4. Impact of Localized States on Spin-Transfer Torque

This chapter presents the experimental results and best possible explanations for how the localized states due to the oxygen vacancies within the MgO tunneling layer impact STT. We will start with the transport measurements performed on nanopillar MTJ devices and demonstrate the applied bias-induced bi-stable STT switching from P > AP and AP > P states for the temperature range of 27K-297K. The temperature-dependent STT measurements will provide an insight into how the STT parameters (V_C, I_C, and J_C) evolve with the thermal energies and how do they differ from P > AP and AP > P switching scenarios. The evolution of the STT parameters with respect to the temperature, however, is very complex (due to the magnetic anisotropy variation of the FM electrodes with respect to the temperature, etc...) to link with localized states due to the oxygen vacancies. Nevertheless, the one order-of-magnitude reduction in $|V_C|$, $|I_C|$ and $|J_C|$ at 300 K for AP > P switching compared to the P > AP switching suggests that as soon as the MTJ reaches to its P state, the transport becomes more favorable compared to the AP state. This favored transport in P state for our nanopillar MTJ devices was experimentally observed with linear current-voltage (I(V)) characteristics and 'near ohmic' features ($dR/dT>0$) in temperature-dependent resistivity (R-T) plots [Fig.4.3 and Fig.4.6.a]. While the P state remains 'near ohmic', the AP state of our nanoscale MTJs exhibits a typical semiconducting behavior. The observed 'near ohmic' behavior of our nanopillar MTJs in the P state is contrary to the typical semiconducting behavior of the MTJs, therefore, cannot be understood with the conventional wisdom[52] developed for the MTJs operation. According to the conventional wisdom developed so far, in an MTJ, transmission in the P state is dominated by the Δ_1 symmetry whereas Δ_5 symmetry is dominant for the AP state. This, therefore, offers lower resistance in the P state for the electrons tunneling through the MgO barrier as compared to that of the AP state. This difference in the resistance between the respective magnetic states of an MTJ has been widely utilized in TMR effect-based field sensing devices[103]. The existing knowledge only holds the relative magnetic alignment of FM electrodes accountable for the MTJ operation but does not explain the experimentally observed 'near ohmic' transport in the P state of an MTJ.

Several attempts were made to understand the 'near ohmic' transport in the P state of a given MTJ that includes incorporating pin-holes at the thin MgO barrier [128–131]. These MTJs with pinholes exhibit low TMR values and remain metallic in P as well as in their AP state. Contrary to the MTJs with pinholes, our nanopillar MTJs with an R.A product ranging around 10-30 $\Omega.\mu m^2$ with thin MgO barrier (0.6 – 0.9nm equivalent to 5 ML of MgO) exhibit high TMR values of 136% (235%) at 300K (13K). These distinctive characteristics of our nanoscale MTJs are not coherent with the MTJs devices carrying pinholes, therefore, cannot be explained incorporating pinholes at the tunneling layer. In addition to the ‘near ohmic’ behavior in the P state, the critical current densities ($|J_C|$) required for P > AP and AP > P STT switching for our nanopillar MTJs at room temperature were experimentally found in the order of 10^6 and 10^5A/cm^2 respectively [Section 4.4]. These values are respectively one and two order below the values calculated theoretically by Slonczewski[6]. Following the calculations[96] reported by Halisdemir et. al., even for the thinnest barriers, the required current densities[6] can only be achieved if the energetic barrier height is as much lower than the 3.9 eV for intrinsic MgO[96]. Structural defects[92,132] due to the oxygen vacancies within the tunneling barrier, whose presence has been documented are presumed to underscore these low effective barrier heights[96]. Moreover, with the help of conducting-tip atomic force microscopy (CT-AFM) characterizations, later confirmed with the photoluminescence and *Î*-spectroscopy technique[15], these oxygen vacancies have been found responsible for producing current hotspots[96]. These current hotspots are indeed resulting in an effective lowered barrier height and or thickness[96].

In the progression of this chapter, the observed ‘near ohmic’ behavior in the P state of our nanopillar MTJs will be explained in the context of the oxygen vacancies within the barrier. The appearance of the broad peaks spanning up to E_F in the Î(P) [Fig.4.11 and Fig.4.12] suggests the presence of the electronic states originating from a chain of the oxygen vacancies rather than the discrete localized states[4,91] due to a specific type of oxygen vacancy. To further confirm the presence of states due to the oxygen vacancy chain, the spin-torque ferromagnetic resonance (ST-FMR) technique was also employed. Unfortunately, due to the technical limitation of the setup not capable to reach down to lower temperatures, the complete dynamics over the temperature range of 10K-300K, could not be investigated. The details of the STFMR results will also be presented in this chapter.

To further support our experimental findings, *ab-initio* calculations were performed. For simplicity of the *ab-initio* calculations, bcc-Fe was chosen as the FM electrode at both sides of the MgO (5ML thick) interfaces. We keep in mind from the previous understanding [Chapter-3] that on replacing the FM electrode from the CoFeB to FeB, all the localized states shift 0.45 eV towards the valence band relative to the E_F. In this section, we first check whether metal-induced gap states (MIGS)[133] could be the possible cause for the observed ‘near ohmic’ behavior in the P-state? [Section 4.7.1] From *ab-initio* calculations performed on Fe|MgO(5 ML)|Fe MTJs with intrinsic or defect-free MgO, the MIGS originating within the MgO tunneling layer due to the available *d*-electrons of the FM electrodes generate non-zero DOS at/near to the E_F only up to the 2nd MgO ML from either side of Fe|MgO interface. For ideal MgO, the absence of the MIGS at the 3rd MgO ML does not provide any connecting path for the tunneling electrons. Therefore, for the MTJs with intrinsic/defect-free MgO, rather than the ‘near ohmic’ behavior, the standard semiconducting behavior is observed[95].

Resuming back to the previously made assumption to explain the Î-results, we implemented an alternative theoretical model, in which a zig-zag chain of single oxygen vacancies (ZZCOV of F-centers) was introduced along the propagation direction of the tunneling electrons within the MgO barrier of 5 ML thickness [Section 4.7.1]. Similar to the MTJs with ideal MgO, the MTJs with ZZCOV in the MgO layer features MIGS up to two monolayers from Fe|MgO interface from either side. Contrary to the MTJs with intrinsic/defect-free MgO, incorporating ZZCOV in the MgO layers provides additional localized states and a significant DOS near or at the E_F for the third MgO layer. The interesting thing is that this significant amount of the DOS at the near or at the E_F for the 3rd MgO monolayer may bridge the tunneling electrons and thus explain the 'near ohmic' transport.

The observed 'near ohmic' behavior in the P state was confirmed by the charge density calculations performed for the energy range of $-25meV < E_F < +25meV$ across the MTJ. From the charge density calculations, it was revealed that, for the MTJs with ZZCOV across a 5ML-thick MgO barrier, the majority electrons (↑) in P state offers a significant amount of higher charge density compared to the minority electrons in the same state and majority (↑)/minority (↓) electrons in AP state [Section 4.7.2]. To further support the charge density calculations, transmission probabilities for the same system were calculated for the majority/minority electrons in P and AP states. The transmission plots at the center (3rd) monolayer of MgO with ZZCOV are in line with the charge density calculation results [Section 4.7.3].

The experimental results combined with *ab-initio* calculations confirm the presence of F- oxygen vacancy chain within the MgO layer of the nanopillar MTJ devices and successfully explain the underlying cause of the experimentally observed 'near ohmic' behavior in the P-state of our MTJs and its impact on the STT. All these results will be discussed in detail in this chapter.

4.1 Device details

We measured the two sets of nanopillar MTJ devices: MTJ-F from the Freitas group, and MTJ-H from TDK Headway. The details regarding the nanofabrication process involved for the nanopillar MTJ's, and their design and structure can be acquired from Chapter-2.

4.2 Electrical and magneto-transport measurements

We examined several MTJ-F devices out of which, we will be describing here the representative MTJ-F nanopillar device located at 5th column from the left and 5th row from the top, from section 02 of the processed stack [Chapter-2]. The magnetic field state at which I(V)s were performed was selected carefully so that the chosen magnetic state remains intact over the 25K-295K. The chosen MTJ-F device had an elliptical shape with a major (minor) axis of 250 (150) nm. The measured TMR at 293K (13K) was 136% (235%). The calculated R.A product in P (AP) state was 26.71 $\Omega.\mu m^2$ (63.22 $\Omega.\mu m^2$) at 293 K and 26.20 $\Omega.\mu m^2$ (88.37 $\Omega.\mu m^2$) at 13 K. The field-dependent resistance or R(H) plot is shown in Fig.4.1.a. The 2000 Oe state corresponds to the minimum resistance state or the P state for both 295K (red) and 13K (blue). The AP state or the high resistance state, starts to appear at 21Oe (-200Oe) and remains till -1100Oe (-1295Oe) for RH plots measured at 293K (13K) plots.

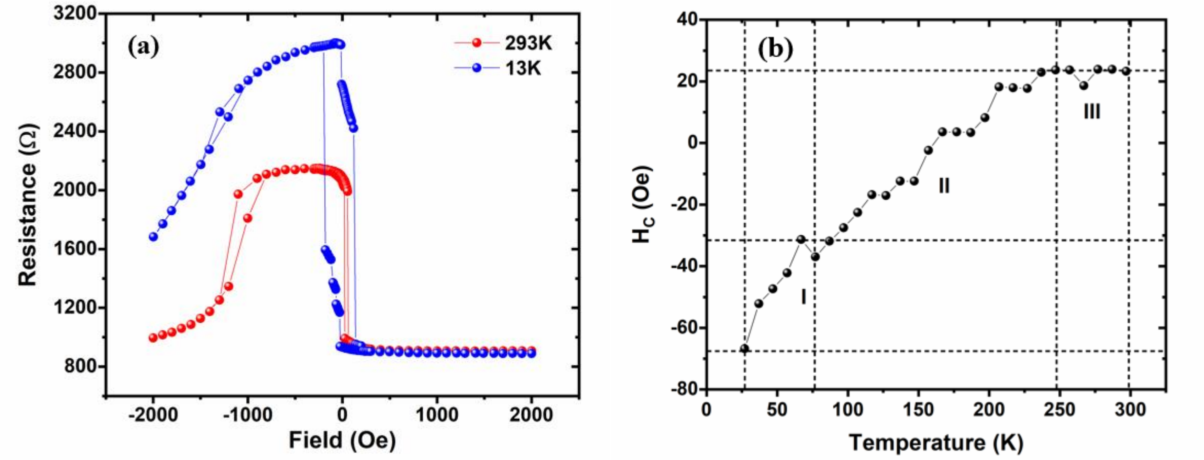

Figure 4.1. A typical magnetotransport performed on MTJ-F device. (a) R(H) plot for MTJ-F device at 13K (blue) and 293K (red). Magnetic state corresponding to 42Oe field remains as P state over the entire temperature range of measurement, **(b)** Temperature-dependent coercivity (H_C) plot.

However, for both the R(H) plots -2000Oe state is not a perfect P state. The observed increase in the TMR at low temperatures is the characteristic feature of the MTJs and is consistent with other MTJ-F devices measured. From Fig.4.1.b as the temperature is increased the coercivity (H_C) also increases. Therefore, in order to get the complete STT data for the temperature range 27K - 297K, the next challenge is to find the field value at which the initial magnetic state (P or AP) does not change with the increase in temperature but can only be switched from one magnetic state to the other (P > AP or AP > P) by applying input current. From R(H) plots performed for the temperature range 27K-297K, it was found that 42Oe field state remains P state for the entire temperature range and can be switched to AP and vice-versa by the applied input current.

4.2.1 Two different transport regimes

STT switching in an MTJ can be visualized in the I(V) measurements by a sudden change in one of its resistance states (P or AP) to the other. To not break the junctions due to the excessive heating caused by the current flowing through, the I(V)s were performed in the range of ±1.0V from 0V with a step of 2mV. In order to avoid the possible jump in the I(V)s due to the range change, all the I(V)s were performed under the auto range off mode by selecting the range manually. The I(V) presented in Fig.4.2 exhibits two different transport regimes i.e., linear with 'nearly ohmic' behavior in P-state and nonlinear with 'semiconducting behavior' in AP state. These distinctive transport regimes in their respective magnetic states (P/AP) can be very clearly seen in Fig.4.3. The observed difference in the I(V) behavior of a given MTJ device in its P and AP states respectively is present for the entire temperature range of 10K-295K. These 'nearly ohmic' and 'semiconducting' transport at the respective P and AP states in our nanopillar MTJs are also featured in the temperature-dependent resistance plots with positive (dR/dT>0) and negative slopes (dR/dT<0) respectively [Fig. 4.6.a].

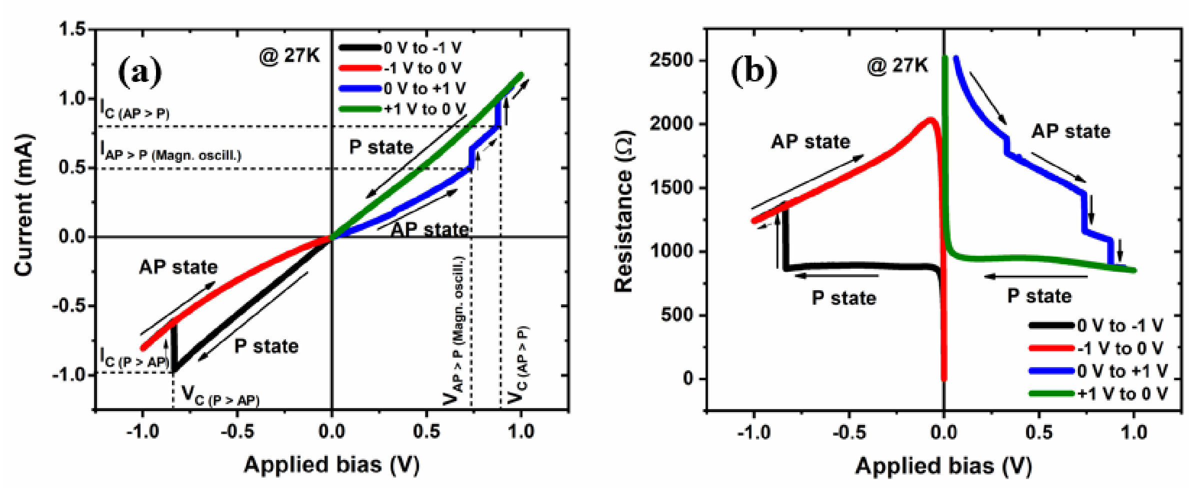

Figure 4.2. STT switching in MTJ-F device. (a) I(V) plot for MTJ-F device at 27 K, **(b)** Equivalent R (V) plot for (a). STT switching from P > AP (AP > P) observed at negative (positive) applied bias.

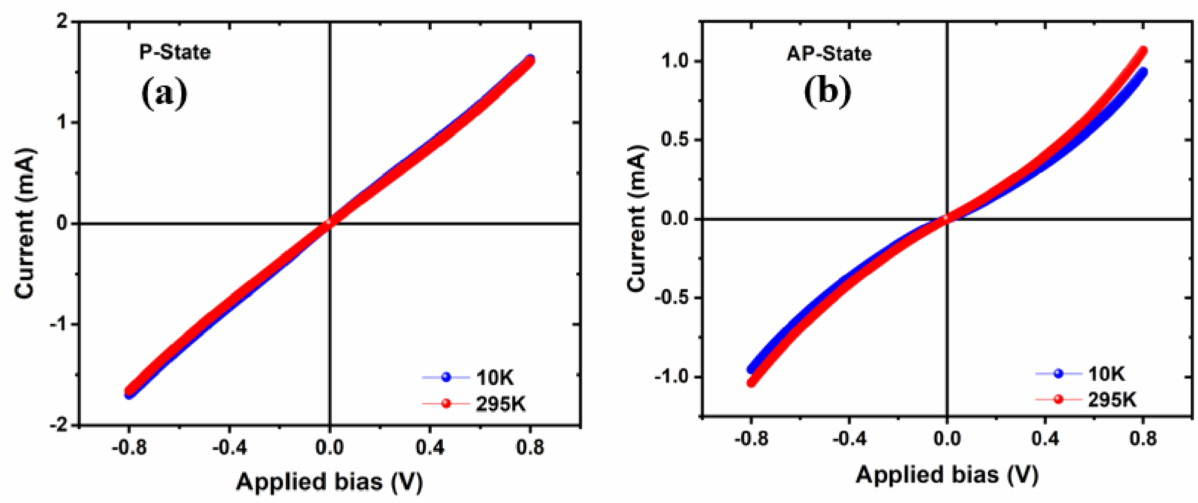

Figure 4.3. I(V)s performed for MTJ-F device at, (a) P state (2000 Oe) and (b) AP state (-200 Oe). The blue (red) curve represents measurements performed at 10K (295K).

The distinct I(V)(T) behavior at P and AP states, suggests that different transport mechanisms are occurring in the respective magnetic states of MTJ. This difference could be purely electronic: the conventional picture of solid-state tunneling (SST) across the MgO barrier is that Δ_1 states dominate transport in the P state, whereas Δ_5 states with a larger barrier height dominate transport in the AP state. However, this difference could also be structural: could the near-Ohmic behavior in the P state be caused by localized states with Δ_1 symmetry that energetically intersect E_F? Out of the aforementioned two hypothesis, the latter gets a proper validation by the experiments (magnetotransport and ST-FMR spectroscopy technique) and theoretical calculations [Section 4.5] that predict a chain of oxygen vacancies can, due to hybridization, energetically broaden the discrete states of the double oxygen vacancy, such that the tail of M_2-like state intersect E_F.

4.2.2 Transport regimes and the evolution of STT parameters

The observed difference in the I(V) behavior also affects the STT parameters (V_C, I_C, and J_C) between P > AP and AP > P switching. From Fig.4.2, I(V) measurement performed for an MTJ-F device at 27K exhibit two STT switching events: i) P > AP switching at $V_{C\ (P > AP)}$ = -0.82V and $I_{C\ (P > AP)}$ = -0.93mA. After switching to the AP state at (-0.82V, -0.93mA), the device remains in the AP state till -1.00V and returning back to 0V. ii) In the positive cycle of applied bias, the device remains in the AP state, till +0.752V. At +0.754V the device switches into an intermediate low resistance state that can be correlated with the magnetic oscillation state. Finally, at +0.878V, the device attains the complete magnetic reversal and switches to the lowest resistance P state, and remains in the P state throughout the entire positive applied bias even during the returning to 0V. The critical voltage and current required for STT switching for AP > P, denoted by $V_{C\ (AP > P)}$ and $I_{C\ (AP > P)}$ were found to be +0.878V and +0.8mA. From P > AP and AP > P switching data, STT switching was found to be asymmetrical which might be due to the different transport behavior at P and AP state. In order to get a complete picture of STT parameters (V_C and I_C) for the entire temperature range of 27K-297K, I(V)s were performed in a similar protocol to that of 27K, for each 10 K steps. Fig.4.4 shows the STT switching at two extreme temperatures 27K and 297K. For a given temperature, a significant difference in the STT parameters was found between P > AP and AP > P switching.

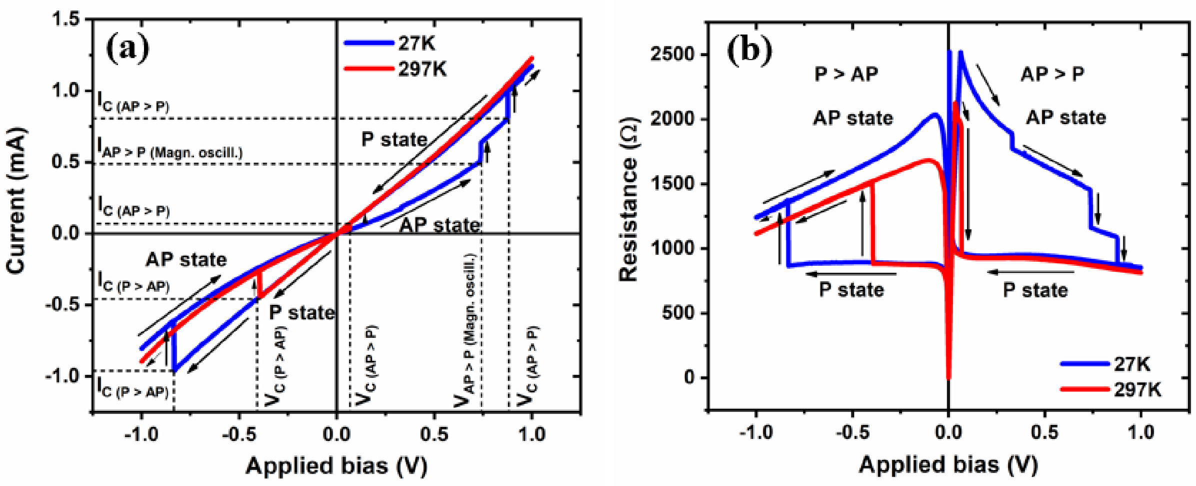

Figure 4.4. STT switching in MTJ-F device at two temperatures. (a) I(V) plot for MTJ-F device at 27K (blue) and 297K (red), **(b)** Equivalent R (V) plot for (a). STT switching from P > AP (AP > P) observed at negative (positive) applied bias

This asymmetry between P > AP and AP > P, STT switching was also observed for the MTJ-H devices for the entire temperature range of 10K-300K. The MTJ-H devices were measured at IJL-Nancy in collaboration with Dr. Daniel Lacour. A representative dataset of MTJ-H devices is shown in Fig. 4.5. The panel (a) of Fig. 4.5, shows the I(V) plots performed for one of the MTJ-H devices, in the applied bias range of ±0.7V from 0V with a step of 5mV. Contrary to the MTJ-F devices, the P > AP (AP > P) switching for MTJ-H devices was observed at positive (negative) sides of the applied bias voltage. This might be due to the electrical contacts with opposite polarity of the applied bias during the transport measurements._The P > AP switching observed for 10K (300K) plot at V_C = 339mV (199mV), I_C = 0.703mA(0.380mA), whereas AP > P switching observed for 10K (300K) was observed at V_C = -663mV (-379mV), I_C = -708mA (-374mA). In Fig. 4.5, panel (b) is the resistance equivalent of I(V)s shown in panel (a).

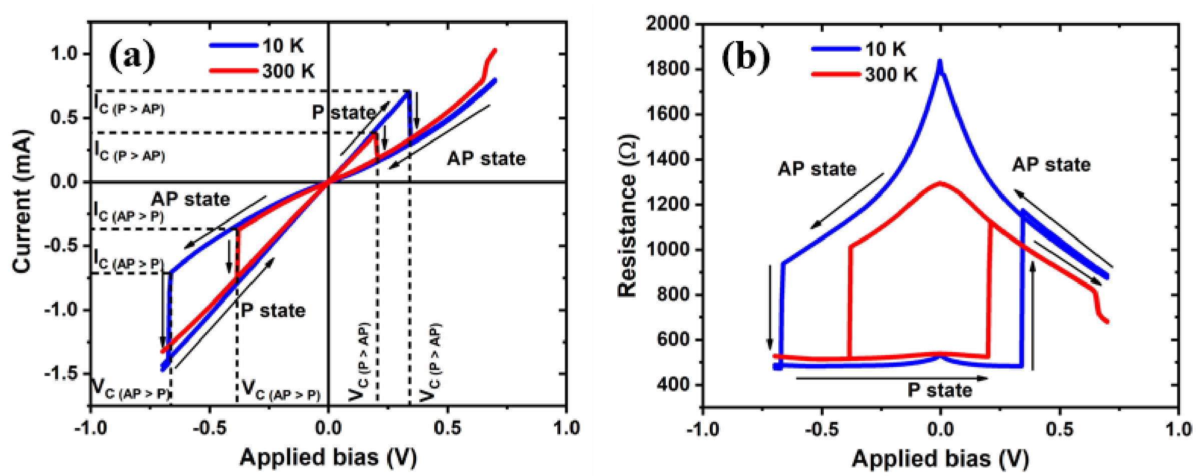

Figure 4.5. STT switching in MTJ-H device at two temperatures. (a) I(V) plot for MTJ-H device at 10K (blue) and 300K (red), **(b)** Equivalent R(V) plot for (a). STT switching from P > AP (AP > P) observed at negative (positive) applied bias

Like the MTJ-F devices, the MTJ-H devices also show metallic I(V) behavior in P state whereas, in its AP state behaves as of a typical MTJ device with semiconducting I(V). Further, the asymmetry in the STT parameters between P > AP and AP > P switching for a given temperature point, and a strong reduction in the STT parameters also resembles with MTJ-F devices. The observed difference in the I(V) behavior between P and AP state is also evident from the temperature-dependent resistance plots [Fig.4.6]. Further, to know how this different transport behavior at P and AP state affects STT, we have extracted the critical current density (J_C) required for P > AP and AP > P switching at each 10K point of the temperature range of 27K-297K. The J_C values were calculated by dividing I_C values by the cross-sectional area of the nanopillar device. This naturally assumes homogeneous current distribution, even though transport is likely proceeding across one or several hotspots. Since P > AP switching in MTJ-F devices occurs at the negative applied bias/current, therefore in order to compare it with the AP > P scenario [Fig.4.4] in which the switching occurs at positive applied bias/current, the absolute values of the negative applied bias/current were taken for P > AP switching. We present in Fig.4.7 the temperature dependence of $|J_C|$ for the AP >P and P > AP STT switching. The important messages are i) $|J_C|$ value strongly depends on the temperature. As the temperature increases, $|J_C|$ decreases for both P > AP and AP > P switching. ii) For both P > AP and AP > P switching, three thermal regions were observed, the one from 27K-77K (marked by I), second from 77K-257K (marked by II), and finally the third from 257K-297K (marked by region III). The region-I is not affected by the temperature, except a small deviation for P > AP switching in the left figure. The temperature dependence of $|J_C|$ is evident from region-II and onward. ii) From region-II and onwards, the absolute slope, $|d|J_{C\,(AP > P)}|/dT|$ is larger than $|d|J_{C\,(P > AP)}|/dT|$. The absolute slope of $|J_C|$ becomes largest at region-III (approaching room temperature).

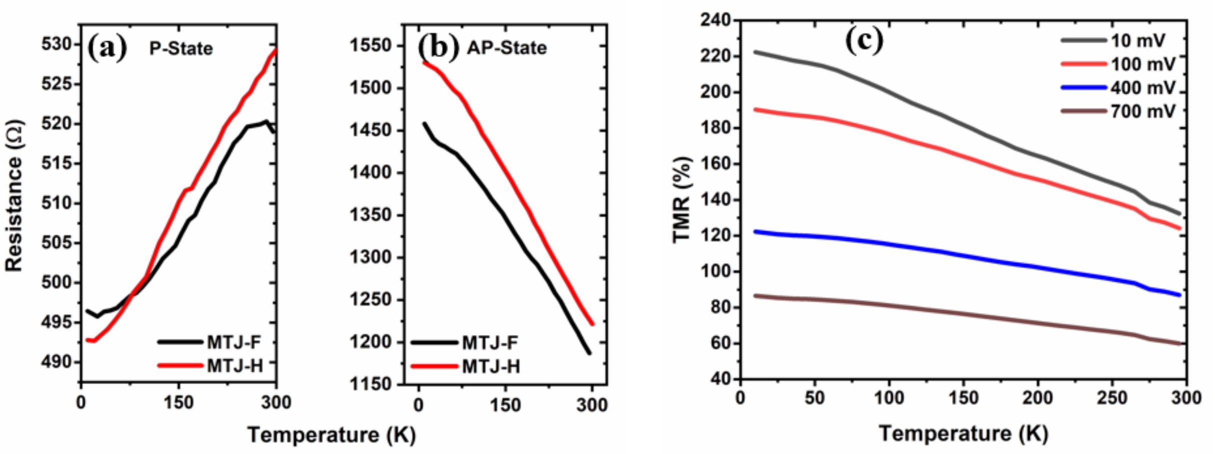

Figure 4.6. Temperature-dependent resistivity plot measured at 100 mV of applied bias, for the MTJ-F (black) and MTJ-H (red) nanopillar devices in their respective (a) P state and (b) AP states. The resistivity plots in P state depicts metallic while in AP state a typical semiconducting behavior, **(c)** Temperature dependent TMR(%) plot for MTJ-F device.

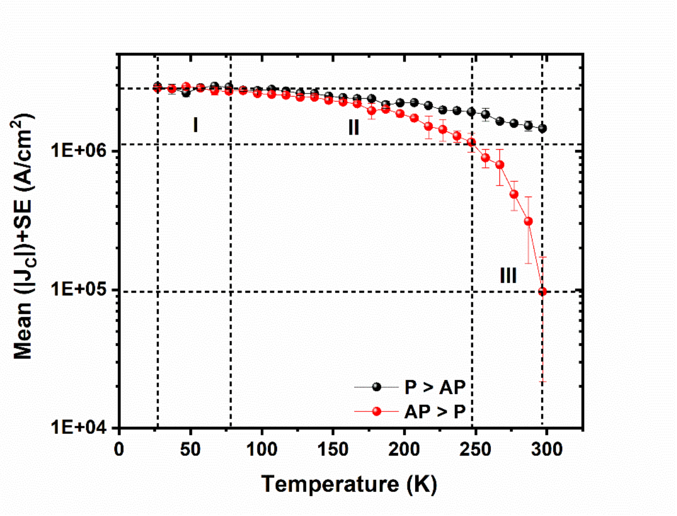

Figure 4.7. Critical current density $|J_C|$ plot for MTJ-F devices at (a) P > AP, (b) AP > P, STT switching.

As the third point: iii) , we observe that $|J_{C\,(P > AP)}| < |J_{C\,(AP > P)}|$ after 77K. At 27K the values of $|J_{C\,(P > AP)}|$ and $|J_{C\,(AP > P)}|$ were measured $2.922\text{x}10^6$ A/cm^2 and $2.857\text{x}10^6$ A/cm^2 respectively, indicating no significant difference between P > AP and AP > P switching. The difference in the $|J_C|$ for P > AP and AP > P switching becomes most significant at T = 297K, with the measured values of $|J_{C\ (P > AP)}|$ and $|J_{C\ (AP > P)}|$ as 1.458×10^{6} A/cm^{2} and 9.696×10^{4} A/cm^{2} respectively. We observe a stark difference in the temperature dependence between $|J_{C\ (P > AP)}|$ and $|J_{C\ (AP > P)}|$. While $|J_{C\ (P > AP)}|$ decreases by a factor of ~3 between 27K and 297K, $|J_{C\ (AP > P)}|$ decreases by a factor of 30.

4.3 Role of magnetic anisotropy on temperature-dependent STT parameters

One possible explanation for the observed decrease in $|J_C|$ with respect to the temperature relates to the temperature dependence of the magnetic anisotropy of the FM electrodes. The critical current density (J_C), for an MTJ device with the cross-sectional area (A), can be written as:

$$J_C = \frac{I_C}{A} \tag{24}$$

Where I_C = critical current required to observe STT and can be expressed as[134,135]:

$$J_C = \alpha \frac{\gamma . e}{\mu_B . g(P, \eta)} M_S . H_K . V \tag{25}$$

Where α = damping parameter, γ = gyromagnetic ratio, e = electronic charge = 1.6×10^{-19} C, μ_B = Bohr magneton, $g(P, \eta)$ = spin efficiency function, a function of spin polarization of the tunneling current and the angle between the fixed and free layer, M_S = saturation magnetization of the free layer, H_K = anisotropy field, and V = A.t = volume of free layer with cross-sectional area A and thickness t.

The magnetic anisotropy energy (E), that acts as an energy barrier between two magnetization direction in a ferromagnetic system, is written as:

$$E = M_S . H_K . V/2 \tag{26}$$

By putting the value of I_C , and E from equation (2) and (3) in equation (1), the current density can be written as a function of the anisotropy energy (E), and spin efficiency function:

$$J_C = 2\alpha \frac{\gamma . e}{\mu_B . g(P, \eta)} E . t \tag{27}$$

From the equation (4), for an MTJ of a given free layer thickness (t), J_C is directly proportional to the anisotropy energy (E), whereas inversely proportional to the spin efficiency function $g(P, \eta)$.

From the temperature-dependent measurements of anisotropy energy (E)/energy density (K), performed on CoFeB/MgO MTJ devices [Fig.4.8], it was found that increasing temperature decreases the anisotropy energy[136,137]. These results combined with equation (4), indicate that increasing the temperature decreases |J_C|.

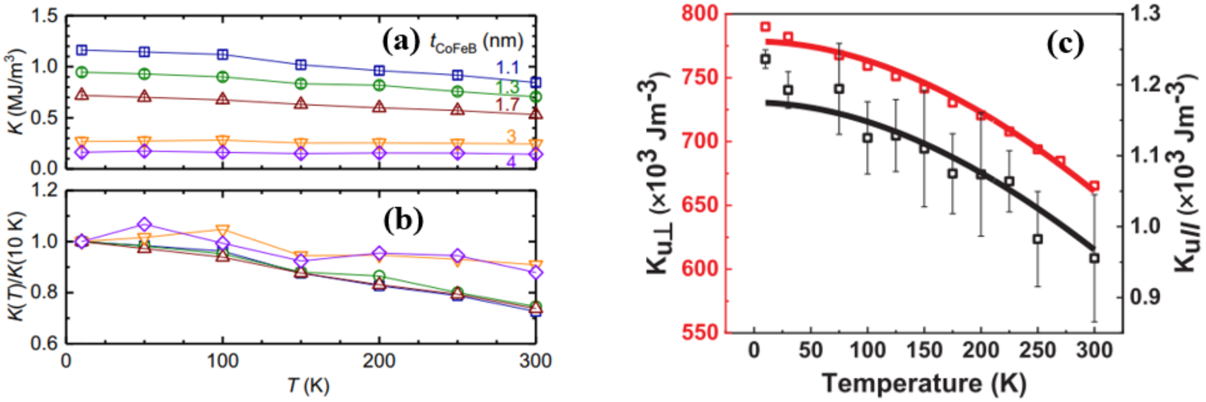

Figure 4.8. Temperature dependence of anisotropy energy density (K). Temperature dependence of **(a)** perpendicular magnetic anisotropy energy density (K), **(b)** normalized K(T)/K(10K) for CoFeB/MgO stacks as a function of CoFeB thickness, **(c)** perpendicular ($K_{u\perp}$) and in plane parallel ($K_{u\parallel}$) anisotropy energy density denoted by the red square and black square lines respectively for CoFeB/MgO junctions. The fig. (a), (b) are taken from ref. [137] and fig. (c) is taken from ref. [136].

Nevertheless, this mechanism cannot explain how with increasing temperature, i) |$J_{C\,(AP > P)}$| decreases much faster than |$J_{C\,(P > AP)}$|, i.e., the two are not the same, and ii) |$J_{C\,(AP > P)}$ decreases by over one order of magnitude.

4.4 Defect-states and the observed difference in the temperature-dependent critical current densities (|J_C|)

We propose that the T dependence of STT parameters is much more pronounced when performing STT from the AP state to the P state because the Δ_1 transport channel involving these states is in principle blocked since there are no Δ_1 states at E_F to accept the tunneling electron [see Chapter-1]. This causes the semiconducting behavior [Fig.4.6.a]. However, in line with the TMR(T) decrease [Fig.4.6.b], increasing T causes the appearance of a Δ_1 channel of transport in the AP state. This is consistent with the increasing linearity of the I(V) in the AP state with increasing temperature, even while the I(V) in the P state remains mostly linear [Fig.4.3]. We, therefore, propose that the increasing thermal activation of the Δ_1 transport channel thanks to the localized states of oxygen vacancies facilitate achieving the P magnetic state for which this Δ_1 transport channel dominates. This causes the effective |$J_{C\,(AP > P)}$| to decrease by over one order of magnitude and can be interpreted as a thermally activated ferromagnetic exchange coupling term between the FM electrodes. This would also be consistent with prior reports[138] indicating that the localized states of oxygen vacancies in MgO can alter the magnetic exchange coupling across an MTJ. The

$|J_C|$ values measured in our experiments are in agreement with the theoretically predicted values by Halisdemir et al. [96] and experimentally measured by Costa et al. [102]

4.5 STT switching scenarios and respective thermal activation energies

The observed difference in the temperature-dependent $|J_C|$ for P > AP and AP > P switching [Section 4.5], is also evident from the activation energies extracted out at the respective STT switching scenarios. $|J_C|$-T plots of respective switching scenarios were fitted with an exponentially decreasing function:

$$J = J_0 . \exp\left(-E_a / k_B . T\right) \tag{28}$$

Where, E_a = activation energy, k_B = Boltzmann constant, and T = temperature. Fitting was done by turning the exponential function into a function $Y = mX + C$, of linear shape. This is achieved by taking the logarithm of $J = J_0 . \exp\left(-E_a / k_B . T\right)$. The logarithmic function:

$$\ln(J) = \ln(J_0) + \left(-E_a / k_B\right) . 1/T \tag{29}$$

on comparing with $Y = mX + C$ thus provides values of activation energy (E_a) as $-m . k_B / (1.6x10^{-19})$ eV, where m = slope of the region for fitting is performed.

We plot $\ln(|J_{C\,(P\,>\,AP)}|)$ and $\ln(|J_{C\,(AP\,>\,P)}|)$ vs 1/T, and their activation energy fits, in Fig.4.9. To obtain general trends, we limited the fitting to two regions. The crossover temperature $(T_{Crossover})$ for both scenarios (P > AP and AP > P switching) is the corresponding temperature at which the two linear fits of completely different thermal energies (27K-77K and 257K-297K) intersect each other.

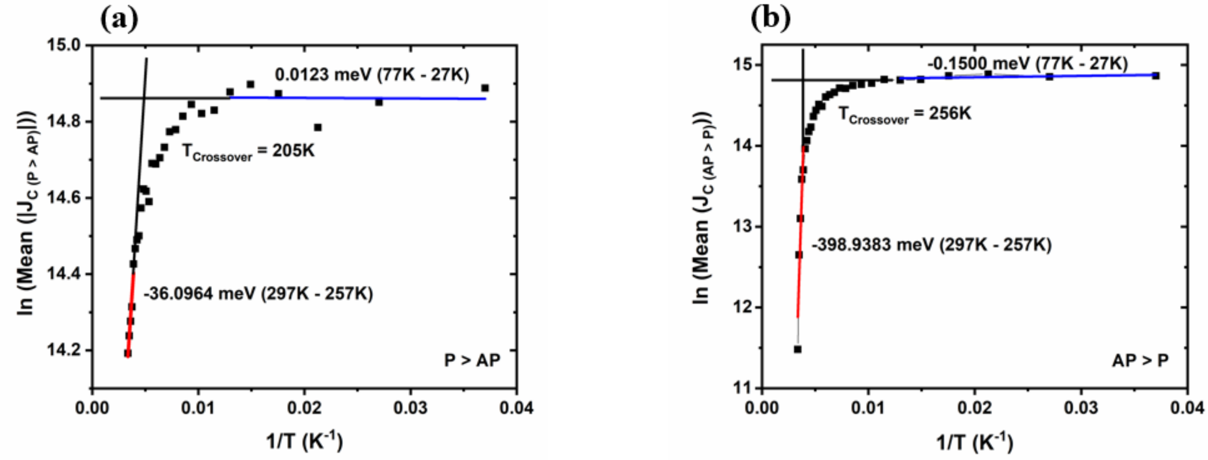

Figure 4.9. Thermal activation energy plots fitted for critical current density($|J_C|$) for (a) P > AP and **(b)** AP > P switching, shows how P > AP and AP > P switching scenarios are different from each other.

We observe that the P > AP and AP > P thermal activation regimes are not energetically similar. For P > AP switching, the E_a value at 27K-77K and 257K-297K is 0.0123 meV and -36.0964 meV with $T_{Crossover}$ of 205K. In contrast, for AP > P switching, the values of E_a for corresponding 27K-77K and 257K-297K regions was -0.1500 meV and -398.9383 meV with $T_{Crossover}$ of 256K. The substantial difference in the calculated thermal energies and crossover temperatures for P > AP and AP > P switching suggests different transport mechanisms for P and AP states.

In Fig.4.10.a, like $|J_C|$ plots, it is obvious to see similar features for the temperature-dependent $|I_C|$ for P > AP and AP > P switching because $|J_C|$ is just a scaled-down value of $|I_C|$ by the common factor of the cross-sectional area of the nanopillar MTJ device. From the $|I_C|$/T plots, P > AP switching was observed at 0.861mA (0.429mA) whereas 0.841mA (0.028mA) current was required in order to see the AP > P switching at 27K (297K) respectively. This data indicates that at low temperature both P > AP and AP > P switching happens for almost similar values of applied current but at high temperature, the difference between the input current required for P > AP and AP > P switching becomes quite significant. Further, from temperature-dependent $|V_C|$ plot [Fig.4.9.b] for the same device, P > AP switching was observed for the applied input bias of 872mV (453mV) whereas 902mV (54mV) of input bias was required for AP > P switching at 27K (297K) respectively.

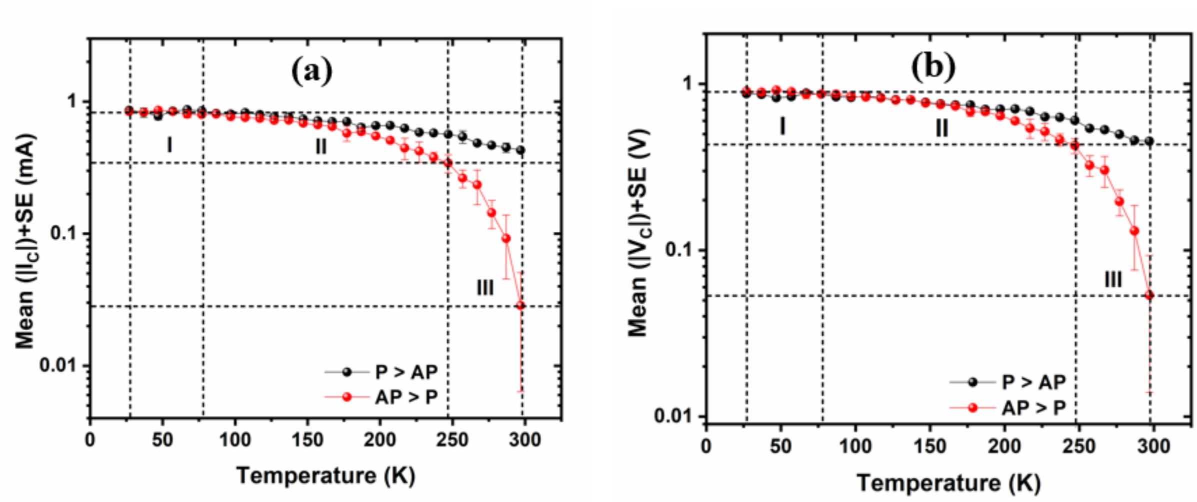

Figure 4.10. Temperature dependent plots for **(a)** $|I_C|$ and **(b)** $|V_C|$ for P > AP (black) and AP > P (red) switching.

The $|V_C|$-T data follows a similar trend as the $|I_C|$-T and $|J_C|$-T data. The observed difference in $|I_C|$, $|V_C|$ values between P > AP and AP > P switching at 297K is consistent with $|J_C|$ values at the respective temperature [please refer to Section 4.4]. In the next section, this observed difference will be supported in the context of our previously made hypothesis of a chain of single oxygen vacancies [please refer to Section 4.2.1 and Section 4.4].

4.6 Mapping the electronic states experimentally

In this section, the details of the localized states present within the MgO tunneling barrier will be extracted out using two techniques. In section 4.6.1, we will examine data acquired using the I-hat ($\hat{I}$-) spectroscopy technique on junctions procured from two different research groups. In section 4.6.2, we will examine data acquired using ST-FMR on two junction set.

4.6.1 Mapping the electronic states using I-hat ($\hat{I}$-) spectroscopy technique

We map the electronic states using consecutive high-resolution I(V)s performed within the thermal energy range of $k_B\Delta T$, thanks to the $\hat{I}$-spectroscopy technique[15] [Chapter-2] in both P (2000Oe) and AP (-200Oe) states. We will see that the $\hat{I}$- for the temperature range of 27K-297K, with chosen $\Delta T = T_2 - T_1 = 80K$ for both MTJ-F and MTJ-H nanopillar MTJ devices shows the presence of localized states spanning from ~-0.7 eV to E_F. The MTJ-F device for which the $\hat{I}$-plot is calculated has an elliptical shape with a major (minor) axis of 250 nm (200 nm). The measured TMR at 295K (25K) was 136% (214%). The R.A product of the device calculated from the resistance data and the cross-sectional area was 20.72 Ω.μm^2 (48.86 Ω.μm^2) at 295K and 19.94 Ω.μm^2 (62.57 Ω.μm^2) at 25K for P (AP) states. The physical characteristics of the device are similar to that of MTJ-F devices for which the STT switching has been already described in Fig.4.4. We present Î-measurements for the MTJ-F junction in Fig.4.11.

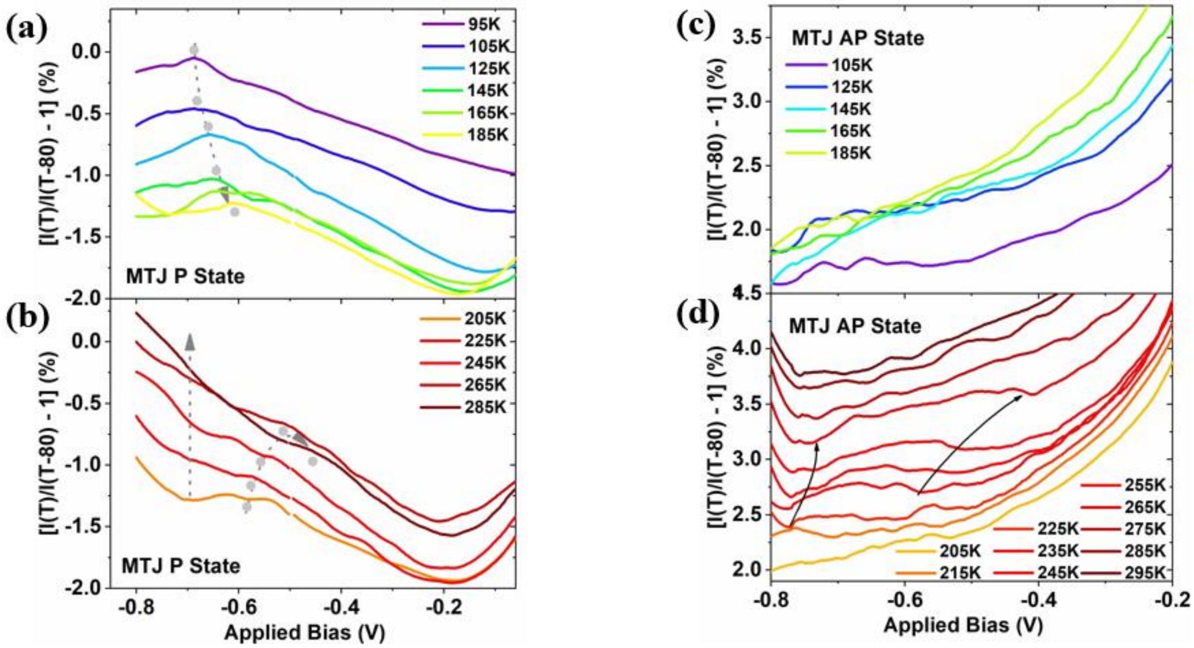

Figure 4.11. I-hat ($\hat{I}$-) plots calculated from consecutive high resolution I(V)s performed at $\mathbf{\Delta T = T_2 - T_1 = 80K}$, for **(a, b)** P state (2000Oe) and **(c, d)** AP state (-200Oe) for MTJ-F device.

In the magnetic P state [panel (a, b)], on increasing the temperature T_2 from 95K to 185K, the broad peak that is centered around -0.7V at T_2=95K, moves towards -0.6V with decreasing amplitude. From T_2=205K to 285K, despite a poor signal-to-noise ratio, we observe that this peak further shifts from -0.6V (205K) to -0.496 eV (285K), against an increasing Irel background. Turning now to the MTJ's AP magnetic state [panel (c, d)], no similar trend is observed. Instead, weak modifications to the Î-spectral fingerprints are seen.

An important point is that the Î amplitude is negative (positive) for the MTJ's P (AP) magnetic state. From the Î values calculated using the formula Î(V, T) = [{I(V, T_2)/I(V, T_1)} - 1]*100 (%) [Chapter-2] for a temperature interval $\Delta T = T_2 - T_1$, ($T_1 < T_2$), the negative amplitude refers to decrease (increase) in the current (resistance) with increase in the temperature thus referring to the metallic transport in the MTJ's P state. Contrary to the P state, the positive amplitude of Î in MTJ's AP state refers to semiconducting transport. These findings are in consistent with the R(T) data shown in Fig.4.6.a, b. Exactly same Î measurement protocol was also used for MTJ-H devices [Fig.4.12]. Like the MTJ-F device, the MTJ-H device's Î data also exhibits a peak centered around -0.6V at T_2=90K. On increasing the temperature T_2, the sharp peak centered at -0.6V shifts towards -0.4V and becomes broader, against an increasing Irel background. Î in the AP-state show no signatures of available states within the range of the applied voltage. Î < 0 for the P state, while Î > 0 for the AP state.

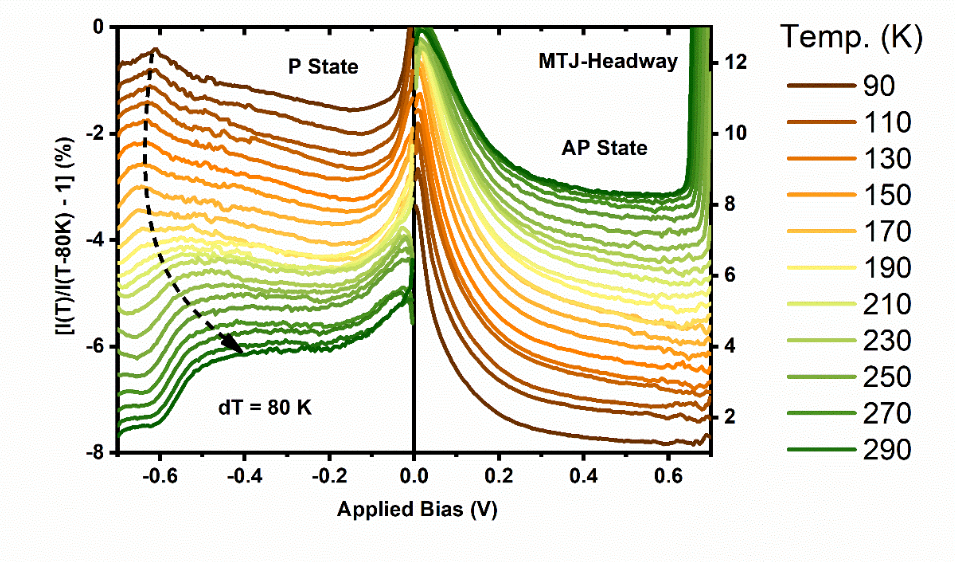

Figure 4.12. I-hat ($\hat{I}$-) plots calculated from consecutive I(V)s performed at $\Delta T = T_2 - T_1 = 80K$, at P state (left) and AP state (right) for MTJ-H device. The large jump in ÎAP (V>0) is due to the STT effect itself.

We thus observe very similar trends in the Î-plots between the two representative devices grown and processed at two different research groups. In particular, the observation of metallic(semiconducting) transport in the junction's P(AP) magnetic states is seen in the Î data. We now interpret the Î data in terms of a potential profile induced by the localized state. The large peak amplitude at 0V can be due to the magnon contribution. Overall, this peak precludes a discussion on the presence of state at E_F. However, the constant, negative amplitude of ÎP up to V=-0.5V at T_2=290K indicates the presence of a constant DOS within 0.5eV of E_F for transport in the MTJ's P magnetic state. For V>-0.5V, a Î- peak to lower negative values is observed at low temperature. The peak thus corresponds to thermally activated transport. As the temperature is increased, it becomes a pronounced decrease to more negative Î- values. This dip suggests the presence of additional DOS that contributes to metallic transport.

From this discussion, it is, therefore, reasonable to infer that states span E_F, thereby explaining the 'near ohmic' behavior in the MTJ's P state. The presence of broad spectral features also suggests that these aren't single oxygen vacancies, but likely hybridized oxygen vacancies. We will address this point in Section 4.7. The localized states spanning from ~-0.7V to E_F in the P-state of the MTJ-F were also probed using the spin-torque ferromagnetic resonance (STFMR) technique.

4.6.2 Mapping the electronic states using spin-torque ferromagnetic resonance (ST-FMR) technique

For this study, we chose two MTJ-F devices denoted by MTJ-F1 and MTJ-F2 of circular cross-sections with radius 110 nm and 125 nm and R.A product (measured at room temperature in P state) 13.27 Ω.µm^2 and 16.10 Ω.µm^2 respectively. The experimental technique of STFMR is already described in the experimental technique chapter [Chapter-2]. The observed TMR for MTJ-F1 and MTJ-F2 at room temperature was found around 110% and 109% respectively. Fig.4.13 shows the R(H) curve at 300 K plotted for the MTJ-F1 and MTJ-F2 devices, respectively. At 300K, the H=1000Oe field state corresponds to the P state while at H=-1000Oe, the devices are in AP state. For both the devices the IP and OOP torkance and torque were calculated using the equations already described in the previous section [Chapter-2].

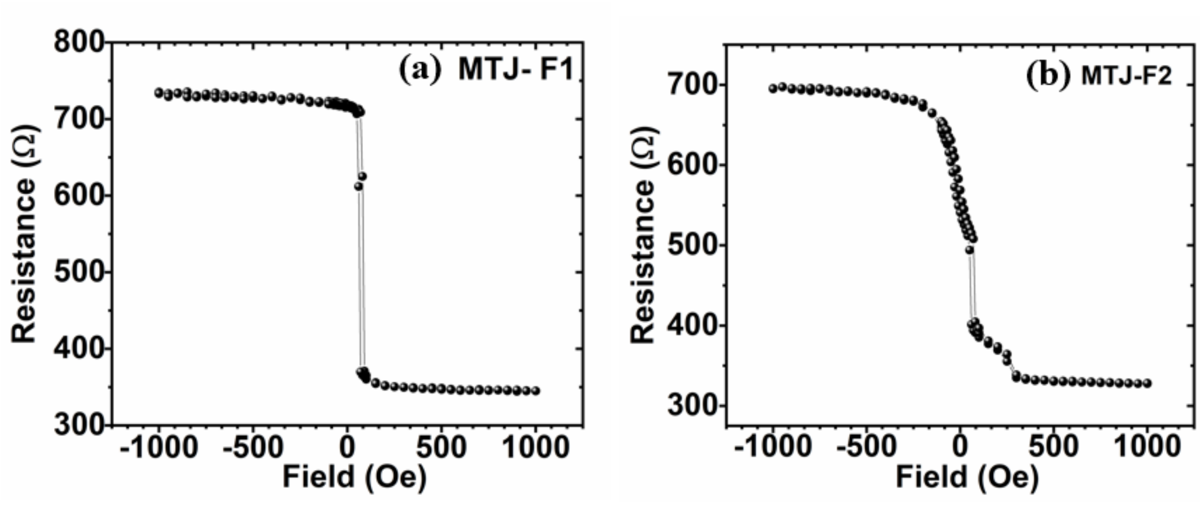

Figure 4.13. R(H) plot at 300 K for (a) for MTJ-F1 device, and **(b)** for MTJ-F2 device.

Fig.4.14 shows the RFM-STFMR spectra for MTJ-F1 and MTJ-F2 devices with varying I_{dc}. The complete RFM-STFMR spectra were obtained for both the devices at H_{app} = 400 Oe and P_{RF} = -10 dBm, in the frequency range of 1- 8 GHz and 1- 6 GHz respectively. The resonance peak in V_{mix} with applied I_{dc} is centered at 4.53 GHz and 3.49 GHz for MTJ-F1 and MTJ-F2 respectively. From both the figures, the resonance peak position doesn't shift with the I_{dc} values.

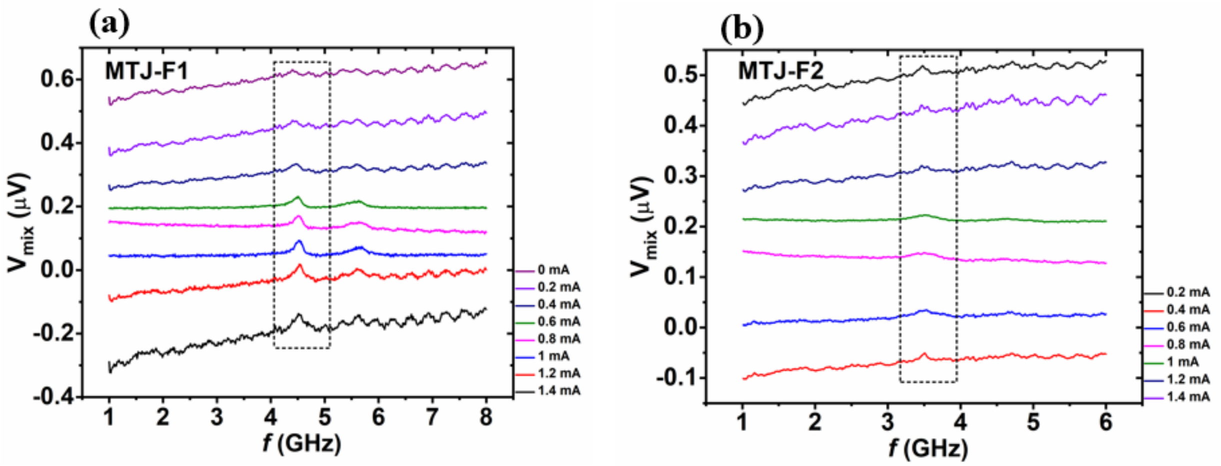

Figure 4.14. RFM- STFMR spectra for (a) MTJ-F1 device and **(b)** MTJ-F2 device, measured by varying I_{dc} at H_{ext} = 400Oe and P_{RF} = -10 dBm.

Modeling the V_{mix} dependence on the applied radiofrequency (f_{rf}), the information regarding the resonance frequencies (f_r), linewidth (σ_r), and magnitude of spin torques (|τ|) can be extracted. In FM-STFMR, the output voltage signal (V_{mix}) measured is equivalent to the first derivative of rectified

RMS voltage signal [$\hat{V}_{mix}(f)$][116]:

$$\hat{V}_{mix}(f) \; = \; B_m \frac{dV_{mix}(f)}{dB} \tag{30}$$

Where B_m is the RMS amplitude of the modulated field. Putting the V_{mix} value from equation (16) [Chapter-2] to equation (30) leads to the following equation[116]:

$$\hat{V}_{mix}\,(f) \approx \; B_m \frac{1}{\sigma_r}\frac{df_r}{dB}(2\,V_S\,S(f))\,A(f) + \; V_a[A^2(f) \; - \; S^2(f)] \tag{31}$$

The equation (31) is used to fit the FM-STFMR spectra, to extract the symmetric V_S and anti-symmetric V_a coefficients, resonance frequency (f_r), and the linewidth (σ_r) for further calculation of torkance and torque.

Fig.4.15 shows the bias dependence (V) of the symmetric (V_s) and antisymmetric voltages (V_a) measured for the MTJ-F1 and MTJ-F2 devices. The applied bias is calculated through I_{dc} divided by the resistance of the MTJ devices in the AP state. The in-plane (IP) torkance ($d\tau_{\parallel}/dI$) and out-of-plane (OOP) torkance ($d\tau_{\perp}/dI$) were calculated from V_s and V_a using the equation (5) and (6) described earlier [Chapter-2]. The various parameters required for the calculations are following: $M_s = 1.36\text{x}10^6$ A/m, $\Omega_{\perp} = \gamma\ (4\pi M_{eff} + H_{app})/2\pi f_r$ with , $H_{app} = 400$ Oe and $f_r = 4.53$ GHz MTJ-F1), 3.49 GHz (MTJ-F2), $I_{RF} = \sqrt{2P_{rf}}\ (1\text{-Ref\%})/R_{dc}$ where, P_{AC} being the rf signal power supplied to the MTJ devices from signal generator during FM-STFMR, the reflection is calculated through S_{11} parameter from VNA. In the present case the reflection was found 10%. $d^2V/dId\theta = (R_{AP} - R_P/2)\sin\theta$, $(dV/dI)_{AP} = R_{AP} + (R_{AP} - R_P/2)\ (1 - \cos\theta)$, $\theta = 5^0$. The R_P and R_{AP} values for the MTJ-F1 (MTJ-F2) extracted from the R(H)s performed at 300 K are 345 Ω (326 Ω), and 726 Ω (695 Ω) respectively.

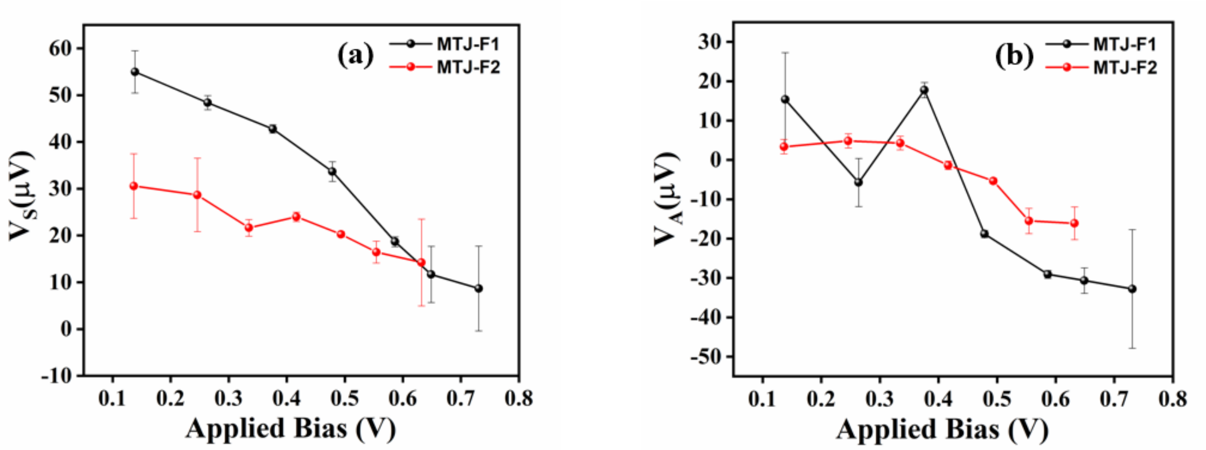

Figure 4.15: Symmetric and antisymmetric components of output voltage. (a) Symmetric component of the output voltage (V_s) and **(b)** Anti-symmetric component of the output voltage (V_a), with respect to the applied bias for MTJ-F1 (black) and MTJ-F2 (red).

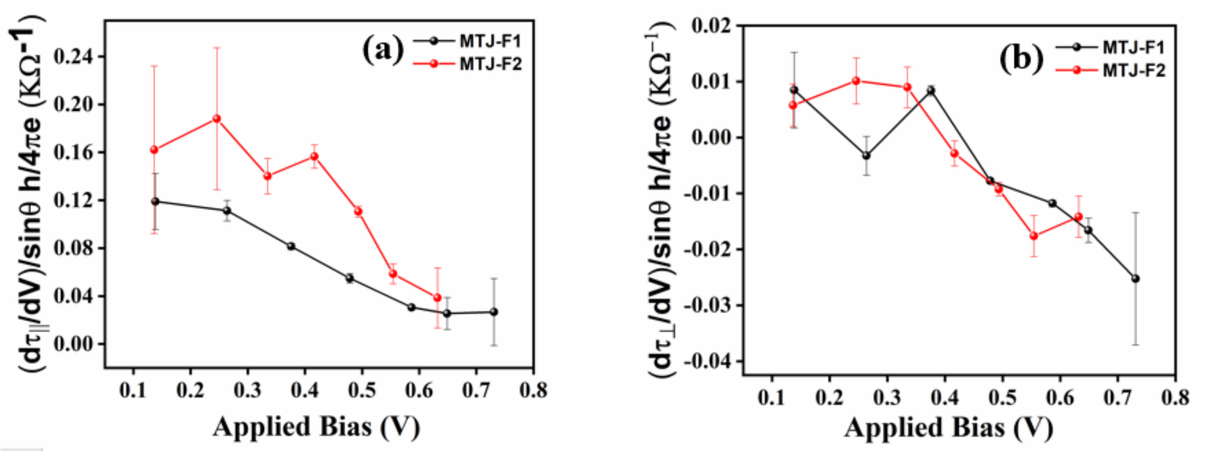

Figure 4.16: Torkance plots. (a) In-plane torkance and **(b)** Out-of-plane torkance, with respect to the applied bias for MTJ-F1 (black) and MTJ-F2 (red) devices.

Fig.4.16.a, b represents the IP and OOP-torkance (derivative of the torque with respect to the current) calculated for both the devices respectively. IP ($\mathrm{d}\tau_{\parallel}/\mathrm{d}I$) and OOP ($\mathrm{d}\tau_{\perp}/\mathrm{d}I$) torkance for both the devices were found linearly decreasing with increasing bias.

Fig.4.17 represents the ratio of OOP to IP-torque, calculated from torkance data [Fig.4.16]. For both MTJs, we observe a general similar trend. For V<0.4V, the ratio is mostly constant. For V >0.4V, the ratio slowly decreases with increasing bias. A larger decrease is observed for MTJ-F2, associated with a change in sign of the torkance ratio. This suggests the implication of other states in transport for V >0.4V, with a different weight of in-plane/out-of-plane orbitals.

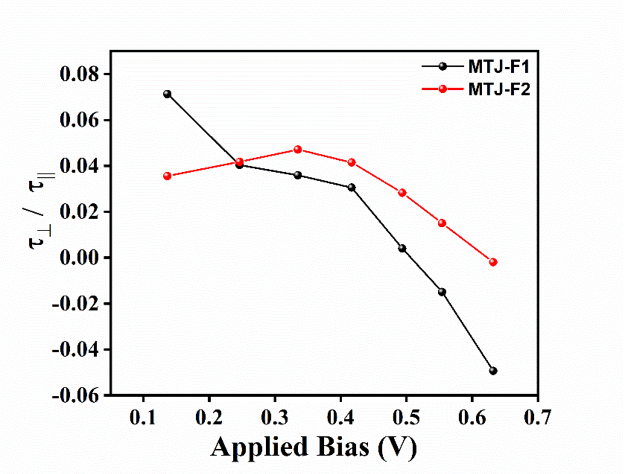

Figure 4.17: Ratio of out-of-plane to in-plane torque (calculated from the respective torkance ratio) with respect to the applied bias for MTJ-F1 (black) and MTJ-F2 (red) devices.

Due to the limitation of the STFMR experimental setup, we were unable to acquire the torque ratio data for the complete temperature range 27K-297K, on which we performed Î measurements. However, the *Î*- and STFMR experiments can be compared at 300K. The change in ST-FMR regime for V >0.4V is matched by a change in Î- spectroscopy for V >0.4V in the MTJ's P magnetic state. To obtain further insight, the following section details the ab-initio calculation using DFT on MTJs with F-oxygen vacancy chain within the MgO tunneling layer.

4.7 Mapping the electronic states with the help of DFT

In this section, we will present *ab-initio* calculations, performed on the MTJ devices for supporting the experimental findings mentioned in the previous sections. These calculations were performed by Dr. (Mme.) Beata Taudul (former Ph.D. candidate in our research group, and currently a Postdoc at the Sorbonne University, Paris), plotted and extensively analyzed by me.

The experimentally fabricated FeCoB electrodes are initially amorphous alloys whose interface with MgO, adopts the latter's (001) texture upon annealing. Nonetheless, the exact arrangement of Fe and Co atoms and the role of boron (B) is not known. Therefore, we decided to consider a simplified scenario with pure Fe electrodes which can still give insight into the nature of the hotspots in the studied pillars. From the earlier knowledge [Chapter-3], switching the FM electrode from CoFeB to Fe only causes the Fermi level to increase by 0.45eV[119]. The geometry of Fe|MgO|Fe supercell was set based on experimental indications: we fixed the lattice constant of MgO to its experimental value (a_{MgO}=4.21Å) and the lateral lattice parameter of the electrode was adjusted to is such that the Fe conventional unit cell was rotated by 45^0 with respect to that of MgO to match the lattice constants of both materials. This choice reflects the experimental evidence[139] that the annealing of the FeCoB/MgO-based MTJs leads to recrystallization of the electrode/barrier interfaces so as to adopt the MgO lattice constant. As a result of the adopted MTJ geometry, the oxygen atoms were placed on top of Fe atoms the Fe-O distance at the interface was set to 2.17Å following previous theoretical studies[1,47]. The MTJ contained 7 monolayers (ML) of Fe electrode separated by 5ML of MgO (~8.42Å which is close to the experimental MgO thickness), the periodic boundary conditions were used in all directions. The sandwiched MgO layer separates the 4ML and 2ML (5th and 7th ML from the extreme left side of the modeled MTJ structure) of Fe on the left and right sides, respectively.

The experimental data (I(V)s, R(T) and Î-plots) indicates 'nearly ohmic' ('semiconducting') transport in the MTJ's P(AP) magnetic state. Prior research has shown that isolated single or double oxygen vacancies do not generate states at E_F[4,85,91]. We, therefore, tested the hypothesis that hybridizing many oxygen vacancies would broaden the antibonding ground state of the double oxygen vacancy (at ~0.4eV below E_F for FeCoB electrodes), such that a tail of states would intersect E_F. We, therefore, considered a zig-zag chain of oxygen vacancies (ZZCOV) spanning the junction [Fig.4.18]. This would also fit the description of a nanoscale hotspot as witnessed using CT-AFM experiments[95,140]. The ground-state calculations were performed within spin-polarized density functional theory (DFT) as implemented in the VASP (Vienna ab initio simulation package)[141,142] with the projector augmented wave method (PAW)[143] and the generalized gradient approximation of Perdew−Burke−Ernzerhof (PBE)[144] for the exchange-correlation potential.

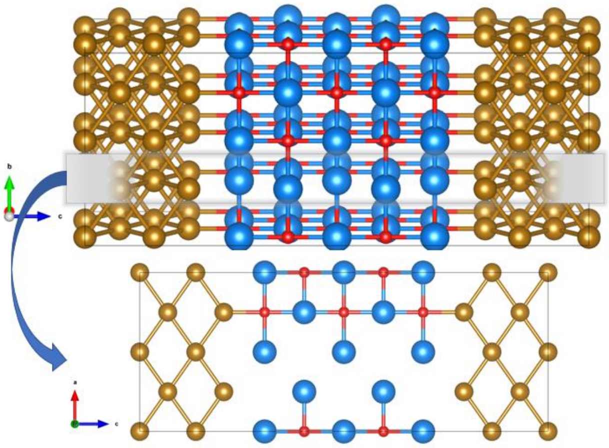

Figure 4.18. Zig zag chain of single oxygen vacancy introduced within the 5 ML thick MgO tunneling layer sandwiched between the Fe electrodes.

The cut-off value for energy was set to 500 eV and the Methfessel-Paxton method for Brillouin zone integration was used. The Fe(7ML)|MgO(5ML) geometry was not relaxed since it is a cumbersome task and should not significantly affect the underlying physics and effects we wanted to study.

4.7.1 Observed near-ohmic transport and metal-induced gap states

In addition to the ab-initio calculations performed for the MTJs containing ZZCOV in the MgO tunneling layer, we have also calculated DOS for the MTJs with intrinsic/defect-free MgO. Fig.4.19 shows the DOS calculated for (a) MTJ with intrinsic/defect-free MgO and (b) MTJ with ZZCOV in the MgO tunneling layer. For both calculations, the thickness of the MgO layer was fixed at 5 ML. From Fig.4.19.a for the intrinsic/defect-free MgO, it is clear that up to the second monolayer of MgO from either side of Fe|MgO interface, the DOS at the E_F is non-zero. This nonzero DOS near/at the E_F up to the 2nd monolayer of MgO from either side of the Fe|MgO interface is due to the available *d*-electrons of Fe are well known as metal-induced gap states (MIGS)[133]. The absence of the MIGS in the 3rd MgO monolayer is evident from a nearly zero DOS at E_F. Since there are not enough states available for the tunneling electrons at the 3rd MgO monolayer therefore for the MTJs with intrinsic/defect-free MgO the typical semiconducting behavior is experimentally observed.

Contrary to the semiconducting behavior as expected and theoretically observed for the MTJs with intrinsic/defect-free MgO, incorporating ZZCOV [Fig.4.18] to the 5 ML thick MgO tunneling layer; in addition to the MIGS up to the 2nd monolayer, a significant non-zero DOS at E_F was found to be available for the 3rd MgO monolayer from either side of Fe|MgO interface. Fig.4.19.b shows the DOS calculated for each layer of the MTJ with ZZCOV in the MgO tunneling barrier. The presence of the non-zero DOS at E_F up to the 2nd MgO monolayer is due to both MIGS and ZZCOV. The presence of a significant nonzero DOS at the E_F in the 3rd monolayer of MgO as compared to that of the intrinsic/defect-free MgO is seen upon comparing panels (a) and (b), and is emphasized in Fig.4.20.a. This significant increase in the DOS at E_F in the 3rd monolayer of MgO due to ZZCOV in the P-state of MTJ confirms the presence of more available states for the tunneling electrons that are expected to provide comparable lower resistive paths to those of the intrinsic/defect-free MgO. The non-zero DOS at E_F in the 3rd monolayer of MgO is in fact due to the localized states spanning up to the E_F, caused by the ZZCOV. Finally, we observe that the increase in DOS on the 3rd ML due to ZZCOV for $E-E_F<-0.4V$ nicely explains the trend toward more negative Î- in the MTJ's P state found experimentally [please see Fig. 4.12]. In fact, this DOS trend is due to ZZCOV is present on all MgO layers. From earlier knowledge[50], the symmetry of the tunneling electrons also plays a crucial role in the transport at their respective magnetic (P/AP) state of an MTJ. To further explore the electronic nature of the energy states by the incorporation of ZZCOV, we have plotted the symmetry resolved DOS plot for the 3rd monolayer of MgO. We notice that, regarding DOSs, $\Delta_1(P)>\Delta_5(P)$ but $\Delta_1(AP)>\Delta_5(AP)$ and collectively $\Delta_1(AP)>\Delta_1(P)>\Delta_5(AP)>\Delta_5(P)$. This collectively implies that $DOS^{AP}(E_F)>DOS^{P}(E_F)$ [see

Fig.4.20.b]. These strange results by incorporating ZZCOV in MgO might be due to the breaking of the structural symmetry in the reciprocal space: This illustrates the limit of discussing magnetotransport across the ZZCOV in terms of electronic symmetries since the ZZCOV isn't a member of the group symmetry representation.

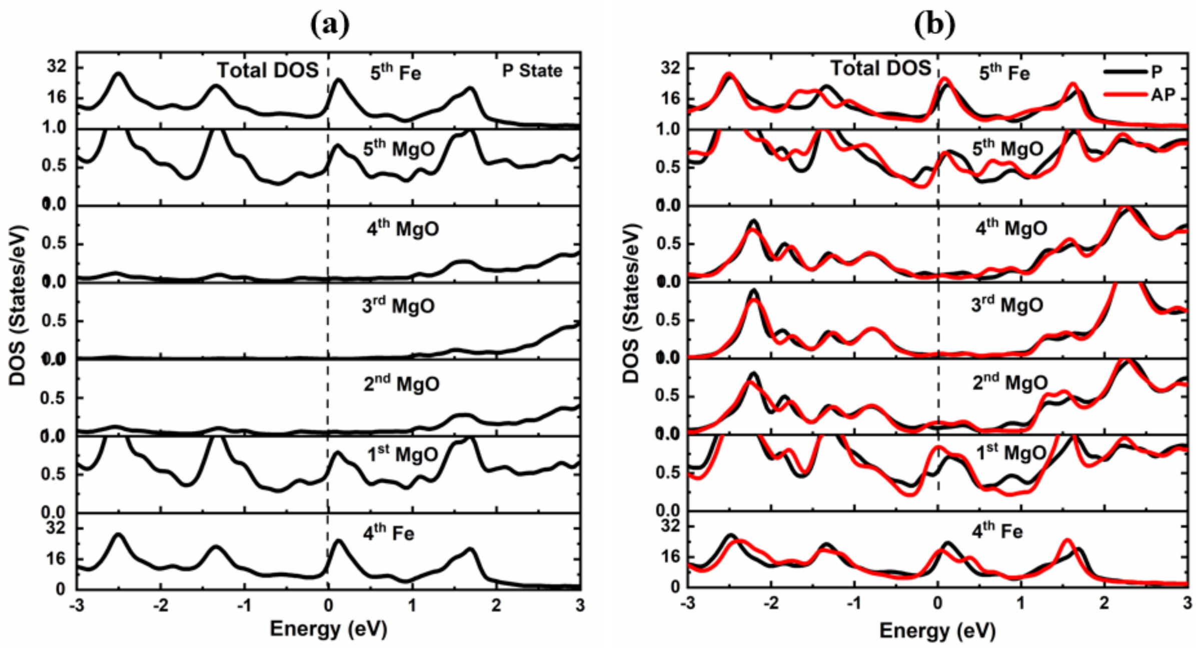

Figure 4.19. Total density of state (DOS) calculated for the Fe(1-4ML)|MgO(5ML)|Fe(5-7ML) MTJ, with **(a)** intrinsic/defect-free MgO, and **(b)** zig-zag F- oxygen vacancy chain within the MgO layer. The bottom 4th Fe monolayer is for the left electrode and the topmost 5th Fe monolayer is for the right-side electrode. The black curve denotes the P state whereas the red curve denotes the AP state. The available d-electrons near the E_F from both sides of the FM electrode can be seen contributing to the metallicity up to the 2nd successive monolayer of MgO tunneling barrier from the interface.

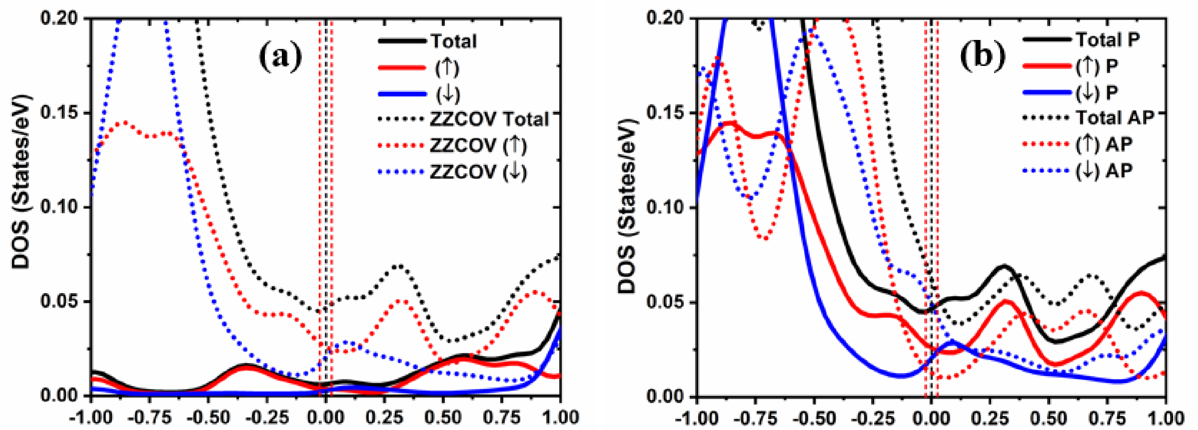

Figure 4.20. DOS plots of a Fe(1-4ML)|MgO(5ML)|Fe(5-7ML) MTJ at 3rd ML of MgO with ideal/defect-free MgO (solid lines) and MgO with ZZCOV (short-dotted lines): (a) in P state, and **(b)** spin resolved DOS in both P and AP states. The dashed vertical lines represent the energy range of E_F ±25meV.

4.7.2 Observed near ohmic transport and electronic charge density plots

As an attempt to visualize explicitly the experimentally observed ‘near ohmic’ behavior in the P state, the charge density calculations were performed in the vicinity of ±25 meV energy range at E_F. Fig.4.21.a and b are the charge density plots calculated for the majority (up) and minority electrons (down) electrons respectively in their P state. Starting from the left side, the first 6ML are of Fe electrode, the next 5ML for MgO, and a single ML at the extreme right is for the right Fe electrode. The color scale in each plot represents the amplitude of the charge density. For each charge density plot (a) and (b), the bottom left panel is for the Fe monolayer and the bottom right panel is for the first MgO monolayer at the interface on the left side. We also plot the up > dn and dn > up cases in the MTJ’s AP state in Fig.4.22.a and b. Here, starting from the left side, the first 3ML are of Fe electrode, the next 5ML for MgO, and the three ML at the extreme right is for the right Fe electrode.

On comparing both Fig.4.21.a and b, it is very clear that the charge density for the majority (up) electrons in the entire 5ML MgO monolayer is quite high compared to the minority (down) electrons in the P state, suggesting ‘near ohmic’ transport for the majority (up) electrons in the P state. The lowered charge density for the minority (down) electrons within the 5ML of MgO in the P state refers to the ‘semiconducting’ transport for the respective electrons in their respective magnetic state. The charge density plot for the minority electrons in the P state does not seem consistent with the DOS plots [Fig.4.20.a]. This inconsistency for the minority electrons might be arising due to the breaking of the symmetry by incorporation of ZZCOV in the MgO tunneling layer.

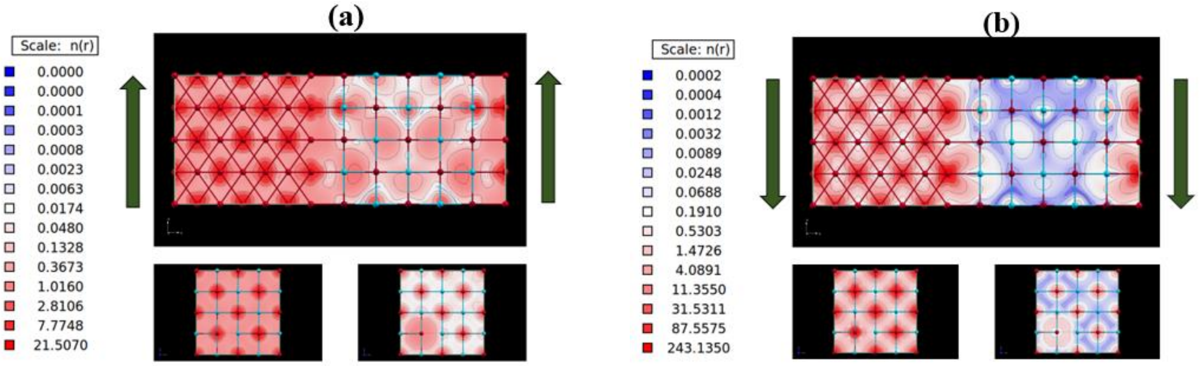

Figure 4.21: **Charge density plots calculated for the Fe|MgO(5ML)|Fe MTJ with F-oxygen vacancy chain within the MgO tunneling barrier** for **(a)** Majority up spin electrons and **(b)** minority down spin electrons, in P-state.

Fig.4.22.a and b represents the charge density plots calculated for the majority (up) and minority (down) spin electrons respectively in their AP state. Starting from the left side, the first 3ML are of Fe electrode, the next 5ML for MgO, and the 3ML at the extreme right is for the right Fe

electrode. Due to the periodic boundary conditions taken into consideration, the number of Fe monolayers after the MgO interface does not affect the charge density calculations. For both Fig.4.22.a and b, from moving down to the supercell structure, in the first row, the left panel is for the charge density for the left Fe, and the right panel is for the right Fe monolayer at the interface of MgO.

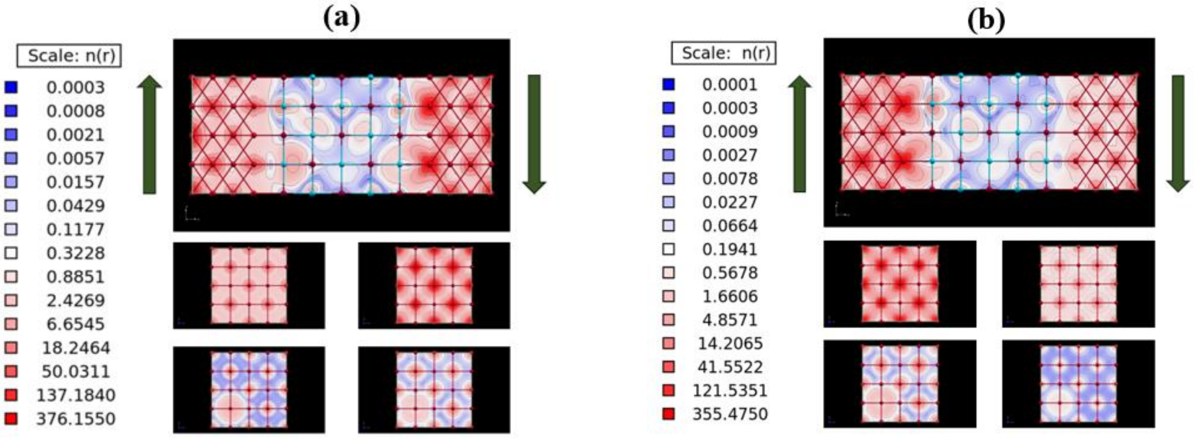

Figure 4.22: **Charge density plots calculated for the Fe|MgO(5ML)|Fe MTJ with F-oxygen vacancy chain within the MgO tunneling barrier** for **(a)** Majority up spin electrons and **(b)** minority down spin electrons, in AP-state.

Whereas in the last row towards the bottom, the left panel is for the charge density of the left MgO monolayer, and the right panel is for the right MgO monolayer at the interface. From both supercell structures for the majority (up) and minority (down) electrons in their AP state, the charge density within the MgO tunneling layer is too weak therefore exhibiting the semiconducting behavior of MTJ in the AP state.

We have attempted to examine the data by looking for a spatial path of transport at E_F ±25meV across the junction. Noting that this exercise was/is difficult since it involves looking at 2D cuts through the 3D data, we did not observe the presence of this path.

4.7.3 Observed near ohmic transport and transmission plots

As a complement to this real-space representation of transport along the zig-zag chain of oxygen vacancy (ZZCOV), we now examine the same in the reciprocal space. The transmission plots calculated on the central 3rd monolayer of MgO are shown in Fig.4.23. The orientation of the MgO layer here is the face-centered cubic (f.c.c.). In the P up channel, transmission occurs at the X-point. This may be expected since the chain was oriented in the x-z plane. However, for the P dn channel, it is at the K-point. The ZZCOV thus appears to filter electrons according to their spin along specific directions in k-space. We find that transport in the AP channel occurs along a diffuse region along the X-K direction. This would correspond to a mixing of the two P spin up (↑) and P spin down (↓) scenario. It would also lead to possible scattering transport, which would be thermally activated. This would explain the positive sign of Î-AP and the semiconducting transport in the AP magnetic state (see Fig. 4.6). The transmission for P(↑) and P(↓) exhibit broad peaks with 5x10^{-2} and 2x10^{-2} amplitudes, respectively. The transmission in the AP state peaks at 2.6E-2. In the present case, the maximum values of the transmissions are higher than the values at respective magnetic states for the spin-up (↑) and spin down (↓) electrons for the intrinsic/defect-free MgO, and isolated F- and M-centers incorporated at the 3rd MgO monolayer[85].

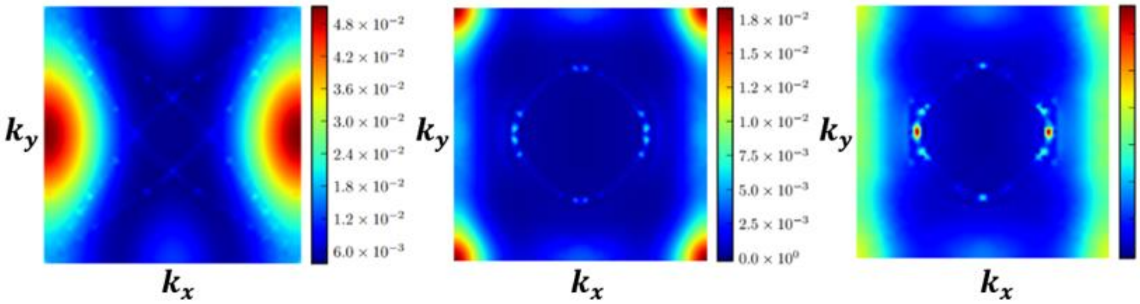

(a) **(b)** **(c)**

Figure 4.23: **Transmission plots at 3rd monolayer of MgO for Fe|MgO(5ML)|Fe MTJ with ZZCOV in the MgO tunneling layer** for **(a)** majority (spin-up) electrons in P state, **(b)** minority electrons (spin down) in P state, and **(c)** AP state.

Considering the enhanced transmission values, we conclude that the metallic conductance observed in our nanopillar MTJ devices can be explained in terms of the ZZCOV in the MgO tunneling layer. Further, the extracted total transmission (conductance) values G_P and G_{AP} for the respective P and AP states are found 1.33x10^{-6} and 6.43x10^{-7} respectively. The TMR value calculated using the formula [(G_P/ G_{AP})-1]*100% was found ~107%. This theoretically calculated TMR value was found to be close to the experimentally observed value (136%) for our nanopillar MTJ devices. It is possible that, due to X-K transmission in the AP state, the corresponding transport could be scattering-dominated, leading to thermally activated transport, i.e., a semiconducting behavior. This would in turn explain the order-of-magnitude larger thermal activation energy found in the AP state at high temperature compared to the P state [see Fig. 4.9].

4.8 Summary, and perspectives

In this chapter we experimentally studied STT switching in our nanopillar MTJs procured from two different research institutes. We also performed ab-initio calculations to help explain our results. Bringing these inputs together, we draw the following picture of magnetotransport across MgO nano-MTJs that exhibit STT.

We have attempted to interpret ‘nearly ohmic’ transport in the MTJ’s P state, and ‘semiconducting’ in the AP state, as arising across a nanoscale hotspot consisting of a zig-zag chain of oxygen vacancies (ZZCOV). This nanoobject generates a DOS on each of the 5ML-thick MgO barrier at

$E-E_F < -0.4$eV that can explain experimental spectroscopic features found in Î- and ST-FMR data: a) the more pronounced dip in negative Î-amplitude of Fig. 4.12 in the MTJ's P state; and b) the change in the trend of the torkance ratio of Fig. 4.17. This DOS intersects E_F and is much stronger than any residual MIGS-induced DOS [Fig. 4.20.a]. This can explain 'nearly ohmic' transport behavior.

We are not able to elegantly explain why the ZZCOV would generate a 'nearly ohmic' behavior for the MTJ's P state and not the AP state. Indeed, the DOS appears for both magnetic states of MTJs. A symmetry explanation is impossible because the ZZCOV breaks the symmetry group representation. Nevertheless, the transmission plots [Fig. 4.23] reveal a much larger P transmission than for AP. Furthermore, the transmission for AP proceeds along a diffuse X-K direction, whereas the P transmission occurs mostly at the X point. It is possible that this can generate more scattering transport in the AP state, which would be thermally activated. This would explain the positive Î [Fig. 4.12] and the semiconducting R(T) data [Fig. 4.6]. It could also explain the order-of-magnitude higher thermal activation energy at the high temperature of the AP > P STT effect compared to the P > AP STT effect [Fig. 4.9]. In other words, it could explain the order-of-magnitude decrease in the critical current density of the AP > P STT effect [Fig. 4.7]. The P > AP STT effect decreases much more weakly with increasing temperature because this scattering is much more attenuated. The calculated transmission yields a TMR value of 106% which is close to the experimental values of 136% at 297K. To conclude, the mainstream picture is that low barrier heights and high TMR leading to spin-transfer torque are the results of pinholes/metal-induced gap states. Our work reveals that this is more likely the result of a nanotransport path such as a zig-zag chain of oxygen vacancies that spans the junction's MgO barrier. This explanation satisfactorily accounts for almost all experimental observations (magnetotransport, ST-FMR), in conjunction with DFT calculations. We hope that our findings and the lacuna in this chapter will encourage researchers from both industry and academia to explore more about oxygen vacancies and their impact on STT.

Part-II

Spintronics across Inorganic-Organic or Hybrid Nanodevices

5. Theoretical Background: Introduction to Organic or Molecular Spintronics

In this chapter, we will provide the key concepts of organic/molecular spintronics. We will first point out the importance of organic spintronics, followed by the physics of organic spintronic devices with cobalt phthalocyanine (CoPc) as a spacer layer. The fundamental knowledge provided in this chapter will help us to understand the experimental results obtained for the CoPc spin chain described in Chapter-7 and will further serve as a foundation to understand the role of paramagnetic defects within spintronics. This chapter is inspired by my former colleague Dr. Kostantine Katcko's Ph.D. thesis[145].

5.1 Why organic or molecular spintronics?

Organic spintronics[18,19] deals with spintronic devices that use organic molecule(s) as an active ingredient. Depending on the spintronic device structure, organic molecules have been used from its single molecular form (e.g., in the break junction devices) to the thin spacer film in organic spin valves[19]. These organic molecules are made of lighter elements such as hydrogen, carbon, nitrogen, etc., therefore produce a weak spin-orbit coupling ($\propto Z^4$, where Z is the atomic number of the element)[146]. The weak spin-orbit coupling (SOC), together with the electronic transport through delocalized π-molecular orbitals, offers large spin lifetimes[147] for the injected spin-polarized electrons. The spin lifetime or spin relaxation time (τ_s) for these organic molecules can reach up to the milliseconds[22,148,149]. The absence of a nuclear magnetic moment in the carbon atom further rules out the possibility of a hyperfine interaction in these molecules.

All these characteristic features preserve the spin coherence of injected spin-polarized electrons within the organic molecules over the large distances. Furthermore, compared to their inorganic counterparts, the organic molecules with the desired structural geometry, physical and chemical properties are also easy to be engineered chemically, which in turn can reduce the production cost of organic spintronic devices. The above-mentioned advantages of organic spintronic devices over the conventional inorganic spintronic devices make them a potential candidate suitable for daily life and industrial-grade applications.

5.2 Electronic structure of the organic molecule

In the organic molecules used as an active ingredient for the spintronic device applications, the intramolecular bonds are strongly covalent, while the intermolecular bonds are due to the weak van der Waals interaction. In inorganic solids, the constituent atoms are strongly hybridized either by ionic, covalent, or metallic bonds and form a continuum of the energy levels called the energy bands (valence or conduction), separated by the Fermi level (E_F). However, within the molecule, the constituent atoms are bound to each other by the strong covalent bonds. Contrary to ionic bonds, covalent bonds are formed by sharing the electrons between the constituent atoms and, depending on the number of shared electrons, can form single (─), double (═) or triple bonds (≡). According to molecular orbital theory (MOT), when two atoms are covalently bonded, the sharing of their electrons is achieved by orbital overlap. Depending on the geometries of the participating orbitals, the overlap can be either from head-to-head or from the lateral side or both. The head-to-head overlap forms the σ-bond whereas the lateral overlap forms the π-bond between the participating orbitals. The σ-bond is a strong bond with highly localized electrons, whereas the π-bond is comparatively weaker and with delocalized electrons. Fig. 5.1 shows the possible σ- and π-bond formed due to the s- and p-orbitals.

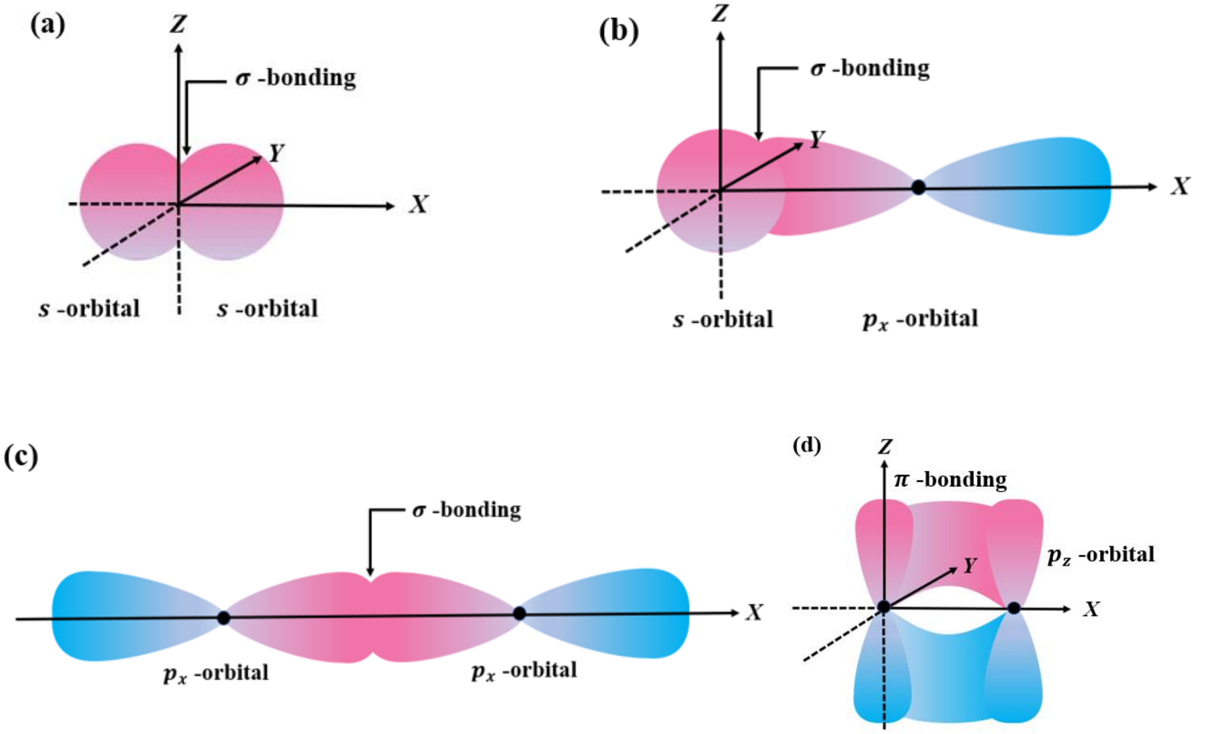

Figure 5.1. Schematic of σ- and π-bond formation. The σ-bond formation due to head-to-head overlap of **(a)** two s-orbitals, **(b)** s- and p_x orbital, and **(c)** two p_x orbitals. The panel **(d)** shows the lateral overlap of two p_z- orbitals forming the π-bond.

It must be mentioned here that after the hybridization of the two orbitals, the two new orbitals are formed. The one with the highest occupancy and smaller energy is called the highest occupied molecular orbital (HOMO) whereas the other with the lowest occupancy and higher energy is called the lowest unoccupied molecular orbital (LUMO). The HOMO and LUMO orbitals are always separated by a finite energy and can be correlated with the valence and conduction bands separated by the Fermi energy in inorganic solids. The hybridization scheme between the two p_z-orbitals forming two new states HOMO and LUMO with π-bonding is shown in Fig. 5.2.

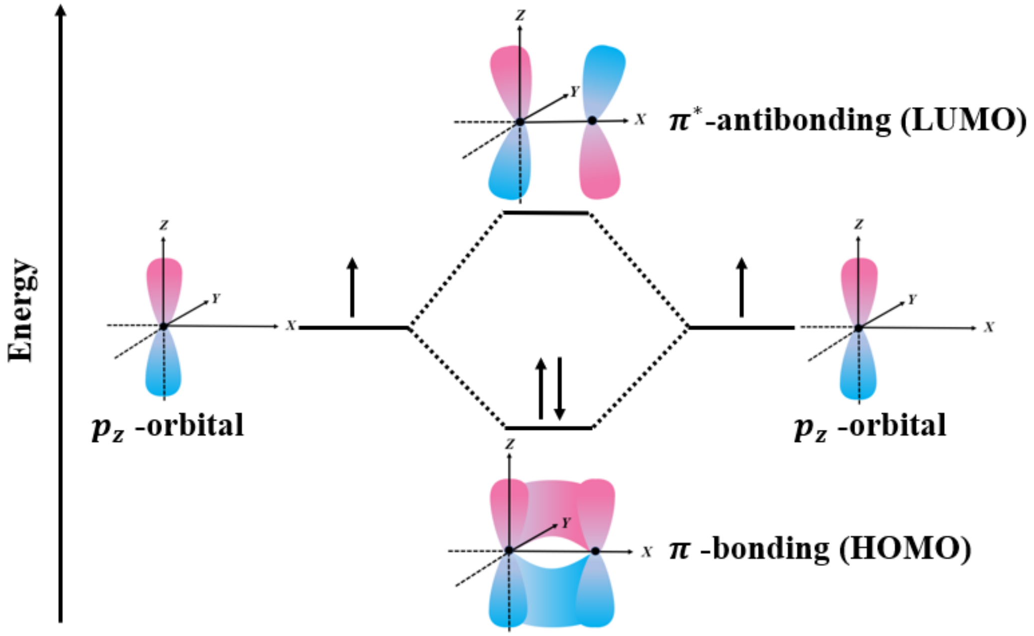

Figure 5.2. Schematic representation of π-bond formation due to the lateral overlap of two p_z-orbitals. The hybridization between the two orbital p_z- orbital, forms two new states: HOMO (bonding) and LUMO (antibonding).

5.3 Transport mechanism in molecular films

This present second half of this thesis deals with the spintronic devices of trilayer structures comprised of two ferromagnetic electrodes separated by a thin organic molecular (spacer) layer. Depending on the thickness, structure of the organic molecule chosen, and the deposition technique used, the spacer layer can be either crystalline, polycrystalline, or amorphous. As described in Section 5.2, the organic molecules are formed by the strong intramolecular covalent bond and associated with the adjacent molecules by weak van der Waals interaction. This causes a weak orbital overlap between the adjacent molecules and hence prevents the delocalization of the electrons between the molecules. Depending on the extent of orbital overlap between the adjacent molecules the transport can be either band-like transport[150] or hopping transport[151].

In band-like transport[150] the strong orbital overlap between the π-orbitals forms a *quasi-continuum of the energy states* or the *energy band* and allows the delocalization of the electrons between the adjacent molecules. On the other hand, in the hopping transport[151] the kinetic energy of the electrons surpasses the potential due to the weak orbital overlap between the π-orbitals and allows them to hop or jump from the localized states of one molecule to the other. The band-like transport is expected for the crystalline/ordered organic molecules at low temperatures only when the *electronic mean free path* (λ_e) exceeds the intermolecular distance (d), while the hopping transport is predominant for the disordered structures and depends on several parameters such as temperature, carrier concentration, defect states, electric field, etc.[152]. These two types of electronic/charge transports are shown in Fig. 5.3.

In addition to charge transport, the molecular spacer layer also affects spin transport in solid-state devices. In 2002, Dediu et al.[18] reported the first trilayer spintronic device using a spin-valve-like structure made of $La_{0.7}Sr_{0.3}MnO_3$ (LSMO) electrodes separated by the sexithienyl (T_6) molecular layer (of thickness ~100-150nm). They experimentally observed a positive magnetoresistance of up to +30% for their lateral devices with a 140 nm channel length. In 2004, Xiong et al.[19] reported an improved magnetoresistance, which they called GMR, of up to - 40% for their macroscale vertical spin-valve devices made of 8-hydroxy-quinoline aluminum (Alq_3) molecule (of thickness ~130-250nm) as an organic spacer layer, and LSMO and Co were chosen for the bottom and top electrodes respectively.

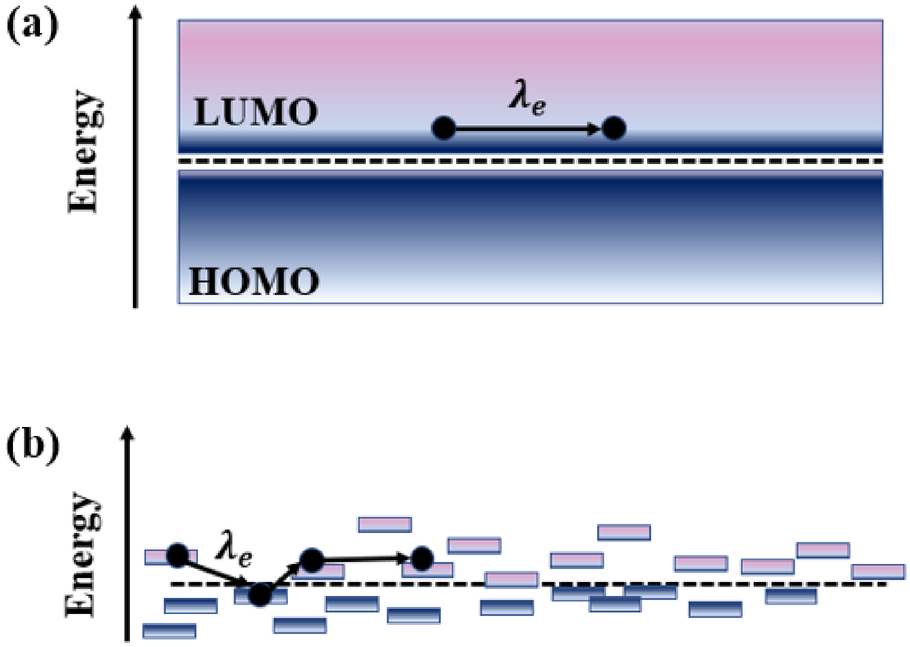

Figure 5.3. Schematic representation of the possible two types of electronic/charge transport in molecules. (a) band-like transport occurs in high crystalline molecules at low temperature when the electronic mean free path (λ_e) exceeds the intermolecular distances (*d*), **(b)** hopping transport in disordered molecules. The figure is adapted from ref[145].

In 2010 Barraud et al[153] reported the highest magnetoresistance of up to +300% at 2K for their nanoscale vertical spin-valve device made of Alq_3 (of thickness ~2nm) as an organic spacer layer, and LSMO and Co was chosen for the bottom and top electrodes respectively. The record positive 300% MR was attributed due to the very small thickness of ~2nm of Alq_3, thus favoring tunneling transport of the spin-polarized electrons across the organic spacer layer. They termed the magnetoresistance obtained for their nanoscale devices as a tunneling magnetoresistance (TMR).

In the above-mentioned experiments, LSMO electrode with high spin polarization[154] is used to inject the spin-polarized current into the spacer or molecular layer (T_6[18]/Alq_3[19,153]). The robustness of LSMO against the environmental oxygen provides an additional advantage over the other ferromagnetic metallic electrodes. In these experiments, the large[18,19] (small[153]) thickness of the molecular spacer layer reflects the hopping (tunneling) transport regime. Furthermore, it was found that the two trilayer devices of similar structures, with large[19] (small[153]) thicknesses of Alq_3 molecular spacer layer sandwiched between the LSMO and Co FM electrode exhibits the negative (positive) MR. These experiments suggest that the thickness of the organic spacer layer not only affects the mode of the charge transport but also the spintronic performance of the device. The change of the MR sign with the thickness of the molecular or the spacer layer is described in the next subsection.

5.4 Spinterface

The change in sign of the observed MR between the Xiong et al.[19] Barraud et al[153] reports indicate a change in the sign of spin polarization of the ferromagnetic metal ($P_{FM} \rightarrow P_{int}$, where P_{FM} and P_{int} are the spin polarization of bare ferromagnetic metal and ferromagnet/molecule interface respectively). This was confirmed by later experiments[155–157], which also revealed that this P_{int} could be very large[29] at/beyond room temperature. These interfacial effects are nicknamed the ‘spinterface’[20,158].

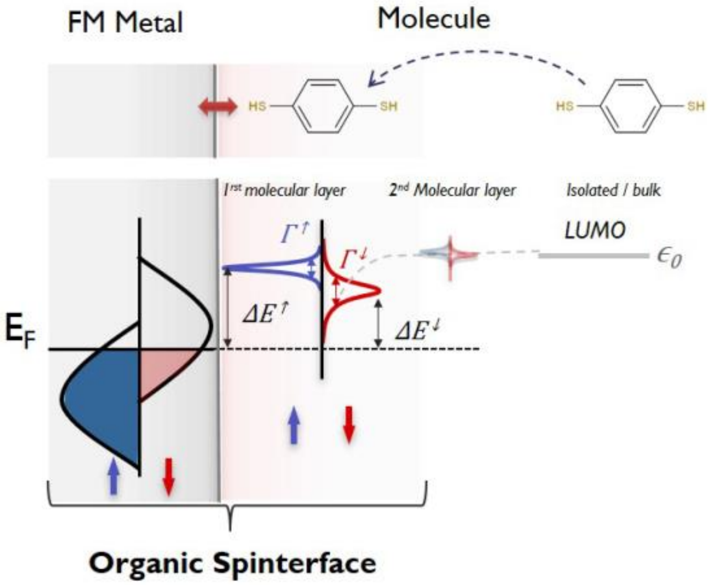

Figure 5.4. Schematic representation of the molecular hybridization at an FM metal interface. Top panel represents the organic molecule approaching towards the FM metal, finally resulting a coupling in between. The bottom panel shows the spin-dependent broadening (Γ, $\Gamma^{\uparrow} \neq \Gamma^{\downarrow}$) and energy shift ($\Delta E$, $\epsilon_{eff}^{\uparrow} \neq \epsilon_{eff}^{\downarrow}$) in the molecular orbitals due to the imbalance in the spin-resolved DOS of the FM metal. The spin-dependent broadening (Γ, $\Gamma^{\uparrow} \neq \Gamma^{\downarrow}$) and energy shift ($\Delta E$, $\epsilon_{eff}^{\uparrow} \neq \epsilon_{eff}^{\downarrow}$) in the molecular orbitals induces a spin polarization (P_{int}) at the interface between the FM metal/organic molecule. The figure is taken from ref[22].

The inversion, and very large values of the spin polarization ($P_{FM} \rightarrow P_{int}$), observed for the spinterface can be understood from the fact that the discrete energy levels of the isolated molecule can, when adsorbed onto an FM metal, hybridize with the energy states of the FM metal. This hybridization provides a finite lifetime (τ) to the molecular levels with a certain probability of escaping to the metal, leading to a broadening (Γ) of the energy levels. This broadening can be quantified from Heisenberg's uncertainty principle ($\Gamma \geq \hbar/2\tau$). Moreover, the energy level of the molecular side shifts from the vacuum energy ϵ_0 to ϵ_{eff}. The shift in the energy level ($\Delta E = \epsilon_0 - \epsilon_{eff}$) and the spin-dependent broadening of the molecular energy levels due to the hybridization between the metallic substrate and the adsorbed molecule is schematically shown in Fig. 5.4. Depending upon the coupling strength, the broadening in the molecular energy levels (Γ) can be ranged between meV to eV. In a first approximation, this broadening is directly proportional to the density of states (DOS) in FM metal. For the FM metals, there is always an imbalance in the spin-resolved DOS for the charge carriers. Therefore the shift in the energy levels (ϵ_{eff}) and broadening in the energy levels (Γ) is unequal for the spin-up (↑) and down (↓) energy levels and becomes spin-dependent i.e. $\epsilon_{eff}^{\uparrow} \neq \epsilon_{eff}^{\downarrow}$ and $\Gamma^{\uparrow} \neq \Gamma^{\downarrow}$.

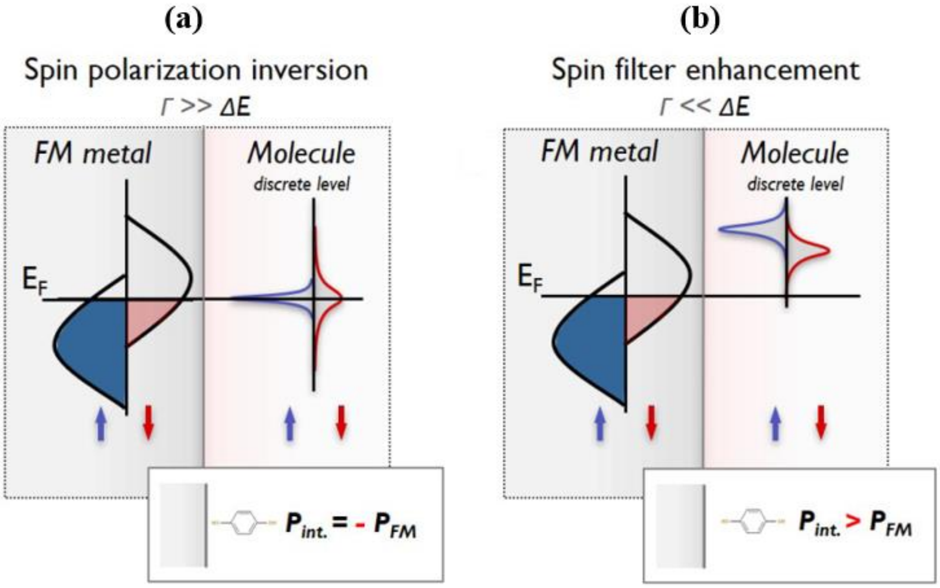

Figure 5.5. Spin polarization inversion and spin filter enhancement (increase in the spin polarization). **(a)** $\Gamma \gg \Delta E$, where $\Delta E = E_F - \epsilon_{eff}$ leading to the inversion of the interface polarization i.e. Pint = -P_{FM}, and the negative magnetoresistance (MR)(b) $\Gamma \ll \Delta E$ leading to the enhancement in the interfacial polarization (Pint > P_{FM}) and therefore larger positive MR. The figures are taken from ref [22].

The effective spin polarization (P_{int}), of this system or the spinterface is a sum of spin polarization of the FM metal and the first monolayer. There are two possible scenarios. (i) When $\Gamma \gg \Delta E$, where $\Delta E = E_F - \epsilon_{eff}$ is the effective molecular energy position relative to the Fermi energy of the substrate metal, this leads to the inversion of spin polarization (P_{int}) of current flowing through the ferromagnetic metal [Fig. 5.5.a]. (ii) When $\Gamma \ll \Delta E$, this leads to a positive and very large spin polarization (P_{int}) and therefore the large magnetoresistance (MR) [Fig. 5.5.b]. The aforementioned scenarios suggest that the spin polarization of the spinterface (P_{int}) is highly dependent on the spin-dependent hybridization and one can tune the spin polarization thanks to the coupling strength between the FM metal and organic molecule.[22] It was observed that the first monolayer strongly couples to the spinterface via ferromagnetic exchange leading to the 'magnetic hardening effect'[159] due to which the topmost monolayer of the bottom FM electrode together with the molecular layer adsorbed on top becomes magnetically anti-aligned relative to the FM layers underneath.

5.5 Transition metal phthalocyanine (MPc) molecules

In the context of a fundamental understanding, and for industrial-grade spintronic device applications, several organic molecules have been studied. Out of the organic molecules studied so far, the metallo-phthalocyanine (MPc) molecules (where M = transition metal), due to the presence of the magnetic atom (M) so their ability to manipulate the spin-polarized current[154], have attracted a lot of attention in recent years. Phthalocyanine (Pc) molecules were first reported in 1907[160]. These molecules are square planar $(C_8H_4N_2)_4$ single decker macrocyclic organic compounds that are composed of four isoindole units linked by the pyrrole nitrogen atoms and exhibit a four-fold axis of symmetry. The molecule has a two-dimensional geometry and a broad ring of 18 π-electrons that is mainly responsible for the charge carrier mobility. The metal-Pc compounds are characterized by a metallic ion that forms covalent bonds with two of the central N-atoms, whereas the other two central N- atoms form coordinate covalent bonds. There are around 70 different phthalocyanine-based compounds discovered up-to-date. When the central point of a Pc molecule is occupied by a transition metal, for instance, a Cobalt Co^{2+} cation, the resulting compound (cobalt-phthalocyanine; CoPc) can acquire magnetic properties. The schematic structure of a CoPc molecule is shown in Fig. 5.6.

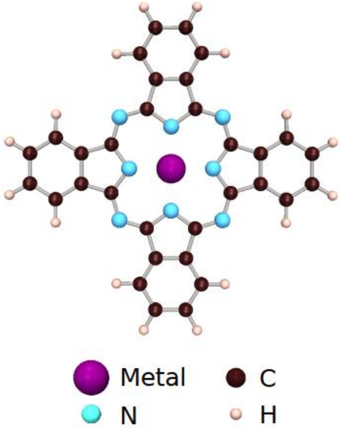

Figure 5.6. Schematic representation of an MPc molecule with a square planar D4h symmetry, where M is the central metal atom and Pc is the phthalocyanine ligand. The figure is taken from ref [161].

In order to understand the basic physics of these CoPc molecule-based spintronic devices and the experimental results obtained [Chapter-7], we now provide a detailed description of these molecules. We have specifically chosen the cobalt-phthalocyanine (CoPc) molecule as a spacer layer for our trilayer FM|organic spacer layer|FM device.

5.5.1 Electronic structure of FM|MPc interface

To understand the magnetic properties of the interface formed between the ferromagnet (Fe) and the organic molecule (CoPc) adsorbed on, Brede et al.[25] performed the DFT calculations and compared the spin and orbital resolved local DOS (SP-LDOS) of an isolated CoPc molecule with the CoPc molecule on the surface of Fe without and with van der Waals interaction. These results are shown in Fig. 5.7. In the case of a free CoPc molecule [see panel (a)], the available d_z^2 states due to the central Co atom for only spin-down electrons at E_F suggests that the magnetic properties of the CoPc free molecule are solely derived from the central metal atom Co. The single electron in the d_z^2 states of Co thus contributes the total spin of S = 1/2 for a free CoPc molecule.

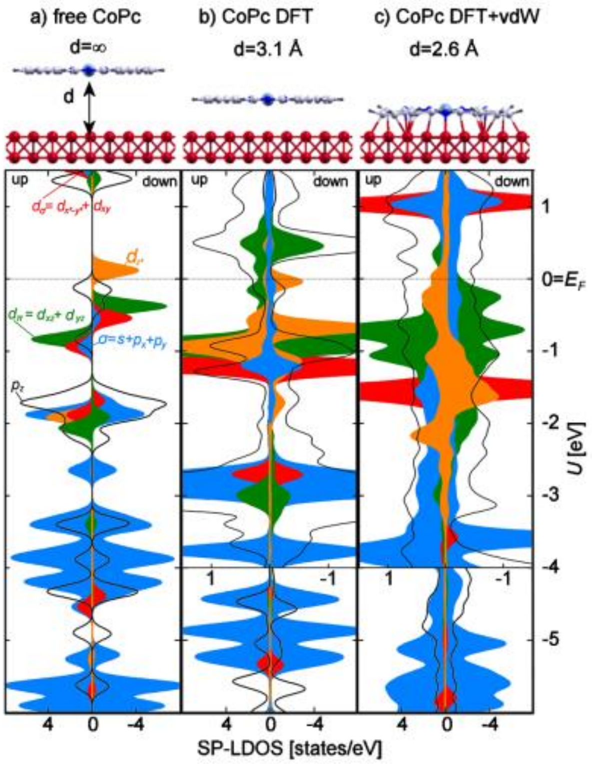

Figure 5.7. The calculated spin-resolved density of states (SP-DOS). (a) For a free CoPc molecule, dz^2 states for spin-down electrons of the Co central metal atom in the CoPc molecule are observed at the Fermi energy. The single electron in the dz^2 orbital gives rise to the total spin angular momentum of an isolated molecule of S = 1/2. **(b)** Case of a CoPc molecule adsorbed on the Fe substrate without any van der Waals (vdW) interactions between. This causes no deformation in the planar geometry of the CoPc molecule. The SP-LDOS shows a strong hybridization between the molecular orbital (MO) of CoPc ($3d_z^2$ of Co) and d-atomic orbitals of the Fe substrate. A transfer of a single electron from Fe to the CoPc causes quenching of CoPc molecular spin i.e. spin S=0. **(c)** Case of a CoPc molecule adsorbed on the Fe substrate with van der Waals (vdW) interactions taken into account. This reduces the distance between the CoPc molecule and Fe by 0.5Å and deforms the CoPc planar geometry. The total spin of CoPc molecule remains S= 0 but spin splitting is recovered. The figure is adapted from ref[25].

The SP-LDOS of a CoPc molecule adsorbed on the Fe substrate, neglecting the van der Waals (vdW) interactions during the relaxation process is shown in Panel (b). In the absence of the vdW interactions, the adsorbed CoPc doesn't deform from its planar geometry and remains flat. The distance between the top monolayer of the Fe substrate and the adsorbed CoPc molecule was calculated 3.1Å. The SP-LDOS shows a strong hybridization between the molecular orbital (MO) of CoPc ($3d_z{}^2$ of Co) and d-atomic orbitals of the Fe substrate. Along the perpendicular, to the molecular plane, the hybridization between the MOs containing the $3d_z{}^2$ atomic orbitals of Co is the strongest followed by the MOs including d_π and p_Z atomic contributions. As compared to the free CoPc molecule the d_σ and σ MOs that are localized in the molecular plane are found to be only slightly broadened. The transfer of an electron from the Fe substrate to the CoPc molecule causes a reduction in the spin splitting of the Fe|CoPc hybrid states and quenches the molecular spin of CoPc molecule to S = 0.

The incorporation of the vdW interactions at the interface reduces the distance between the topmost Fe monolayer and adsorbed CoPc molecule from 3.1Å to 2.6Å [see panel (c)], therefore brings CoPc molecule closer to the Fe substrate by 0.5Å. The incorporation of the vdW interaction distorts the planar geometry of the CoPc molecule [see Fig. 5.8]. The hybridization between the substrate and adsorbed CoPc molecule with vdW completely changes the electronic structure [see panel (c) of Fig. 5.7] to that of without vdW scenario [see panel (b) of Fig. 5.7]. From the SP-LDOS plot [see panel (c)] the MOs of π character strongly hybridize with spin-polarized Fe 3d states of the same symmetry, forming broad spin-split bands. The MOs of σ type are also found to be significantly affected by the interaction with the surface. The molecular spin is annihilated once again (S = 0) as one electron is transferred from the surface to the molecule, but spin splitting is recovered due to local molecule-surface bonding at different parts of the molecule, as mapped in spin-polarized scanning tunneling microscopy (SP-STM).

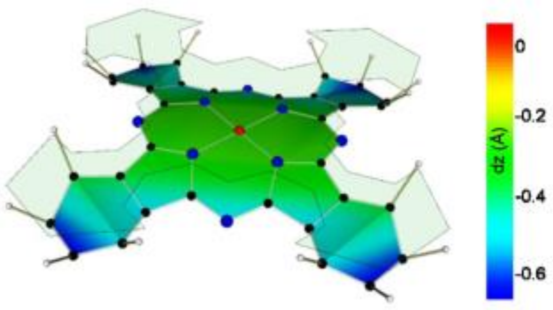

Figure 5.8. Molecular deformation in the adsorbed CoPc molecule due to the vdW interactions at the interface with Fe. The C6 rings and two of the outer N are twisted toward the surface and away from the plane described by the Co ion and four inner N by up to 0.3Å. All H are pointing away from the surface. The figure is adapted from ref[25].

5.6 From MPc molecules to thin films

The polycrystalline structure of the metal-phthalocyanine (MPc) thin films can be found either in the α or β phase. Both α and β phase of the MPc thin films are the results of the column-like structure of MPc molecules stacked along the b-axis. The stacking angle between the adjacent MPc molecules along the b-axis for α and β phase however differs. For CoPc it varies from 65.8^0 to 42.9^0[162]. The α and β phases of CuPc molecules are schematically shown in Fig. 5.9.

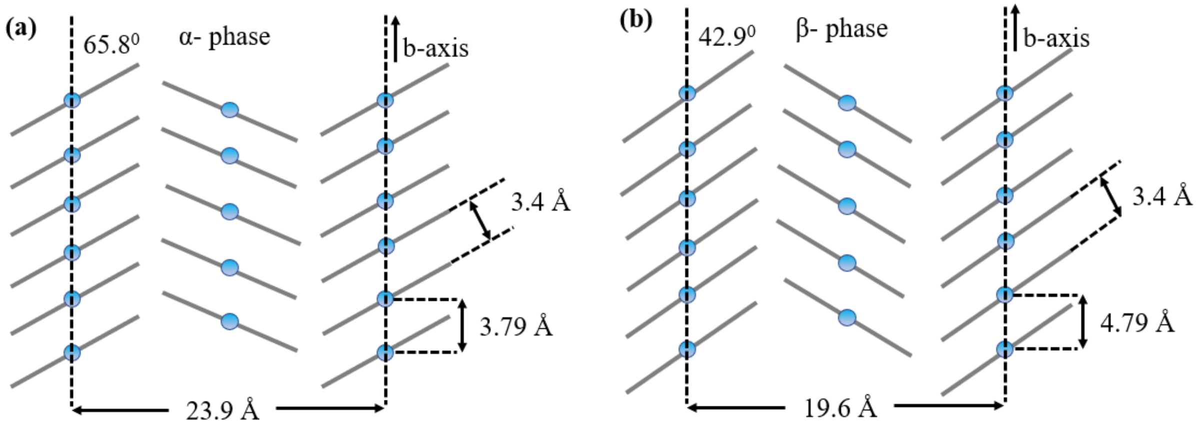

Figure 5.9. α- and β- phase of CuPc stack. Stacking arrangement of CuPc molecule along the b-axis with two different stacking tilt angles of 65.8^0 (left) and 42.9^0 (right) resulting two different phases α- and β- respectively. The figure is adapted from ref[163].

The α and β phase of the MPc thin films can be controlled through the molecular layer's deposition process. Heutz et al.[164] grew CuPc (60nm) thin films over the amorphous Kapton tape substrate in an ultra-high vacuum organic molecular beam deposition (OMBD) chamber and from the XRD measurements reported the structural α phase. They observed that post-growth annealing of CuPc thin films performed at 320^{0}C transforms the α-phase into β phase[164]. The difference in the stacking angle between the α and β phase modifies the intermolecular distance therefore the orbital overlap between the two adjacent vertical M^{2+} ions. The modified orbital overlap due to the structural phase transition (α → β) also influences the magnetic ordering of MPc thin films. Heutz et al.[164] reported that the post-growth annealing step induced structural phase transition (α → β) accompanies a change in the magnetic ordering of CuPc thin films and bulk samples from AFM to the paramagnetic (PM). For MnPc they found that the structural phase transition (α → β) leading to a change in the magnetic ordering from weaker AFM to strong FM[164].

5.6.1 Antiferromagnetic ordering in MPc thin films

In 2008 Chen et al.[23] discussed the superexchange mechanism in cobalt phthalocyanine (CoPc) thin films by low-temperature STM experiments. They used inelastic tunneling spectroscopy (IETS) [see Section 5.6.2] induced by spin-flips along the spin chain to spatially map the spin-flipping channels with sub-molecular precision. They observe that the CoPc molecules form a one-dimensional antiferromagnetic spin chain. From theory and experiments, they revealed that the superexchange between the adjacent $3d_z^2$ orbitals of the Co^{2+} ion is mediated by the e_g orbital of the Pc ring. Furthermore, they experimentally measured a stacking tilt angle of $60^0 \pm 3^0$ which is close to the 65.8^0 stacking tilt angle for the α-phase[162]. The antiferromagnetic ordering in the CoPc thin film is depicted in Fig. 5.10. In 2014 Serri et al.[24] performed the magnetic susceptibility measurements on α-phase CoPc powder and thin films and observed strong AFM coupling with exchange energy (J/k_B) from 77K reaching up to 106K. They confirmed the AFM coupling in the CoPc molecule is due to the superexchange interaction. The exchange energy values (J/k_B) are more than the liquid nitrogen temperature. This is considered one of the milestones in the direction of the MPc based spintronic devices.

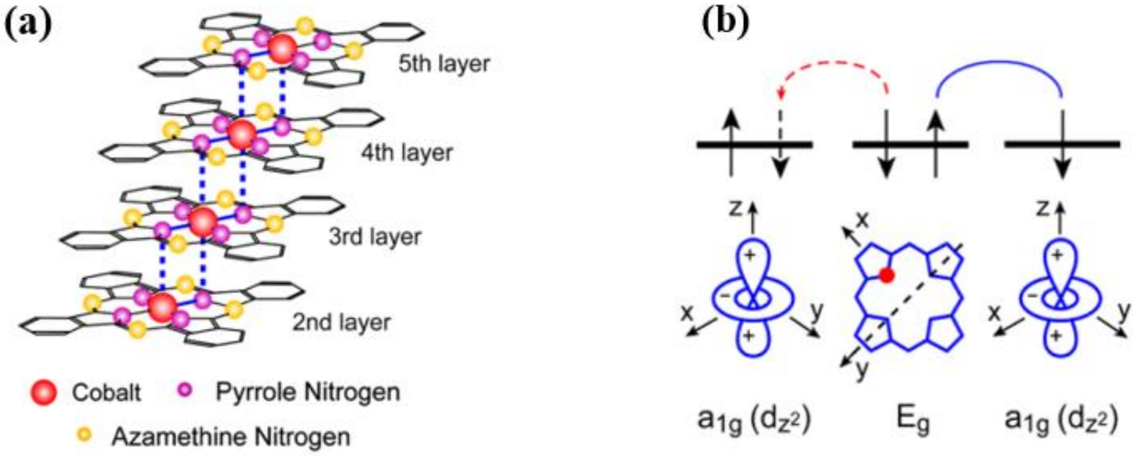

Figure 5.10. Spin-chains and superexchange mechanism. (a) Schematic of superexchange interactions between consecutive CoPc molecules along the one-dimensional chain, **(b)** Spin configuration in superexchange. The superexchange interaction arises due to the hopping of an electron of π-conjugated Pc ring to the $3d_z^2$ orbital of central Co^{2+} ion, the remaining unpaired electron on the π-conjugated Pc ring develops a direct exchange with the neighboring $3d_z^2$ orbital of Co^{2+} ion of another CoPc molecule. This process thus gives rise to an AFM coupling between the adjacent CoPc molecules. The superexchange pathway links the $3d_z^2$ orbitals of two neighboring CoPc molecules along a column across the e_g orbital of the π-conjugated Pc ring of one of the molecules. The figure is taken from ref [23].

In 2015 Gruber et al.[165] reported the antiferromagnetic ordering in MnPc ultrathin molecular films deposited on top of the ferromagnetic thin film sample Cu(100)||Co (7ML) (where Cu is the substrate) at room temperature. In this paper, they reported that the AFM ordering within the MnPc molecule at room temperature is due to the magnetism of the ferromagnetic sample Cu(100)||Co (7ML) on which it was grown, not due to a specific structural phase (α) of MnPc molecule. From X-ray magnetic circular dichroism (XMCD) measurements Gruber et al.[165] found the ferromagnetic (FM) coupling between the Co thin film and the 1st ML of the MnPc [Fig. 5.11.a], while the AFM coupling was observed between the monolayers of the MnPc [Fig. 5.11.b]. These spectacular results at room temperature show the potential of the organic molecules for spintronic device applications.

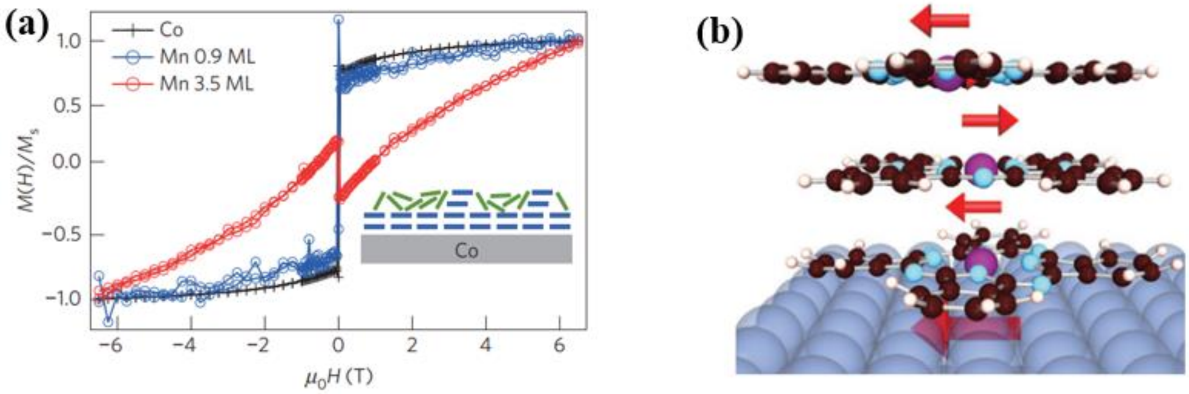

Figure 5.11. Antiferromagnetic ordering of the MnPc molecules and the spin-chain geometry. (a) Normalized magnetization plots obtained using the XMCD intensity at 4.8K for the pure cobalt substrate (black), and 0.9ML(blue line) and 3.5ML (red line) of MnPc deposited on the cobalt substrate. The inset figure schematizes the stacking of 3.5ML of MnPc on Co substrate. The molecules with flat blue lines depict those molecules that are magnetically coupled to Co, whereas the 3rd and 4th ML with green color are disordered and thus exhibit paramagnetic behavior. The black and red colored magnetization curves follow a similar magnetization behavior, which indicates an FM coupling between the Co substrate and the 1st ML of MnPc. **(b)** DFT Calculations of a 3ML MnPc spin-chain on top of Co substrate. The 1st ML of MnPc is pinned by the Co substrate whereas from the 2nd ML onwards AFM ordering is observed. The red arrows show the direction and amplitude of the local spin moments of the respective entities. The Figures are taken from ref [165].

5.6.2 Spin-flip excitations and inelastic electron tunneling spectroscopy (IETS)

For a system containing *N* number of sites with spin $\boldsymbol{S_i}$ at the *i*th site, the magnetic properties can be described by the Heisenberg Hamiltonian (H):

$$H = -J \sum_{i=1}^{N-1} \boldsymbol{S}_i . \boldsymbol{S}_{i+1} \tag{32}$$

where *J* is the exchange parameter, the sign of which determines the magnetic correlation in a solid. A negative (-Ve) *J* corresponds to the AFM coupling, while a positive (+Ve) *J* defines an FM ordering. By altering one or more discrete spin states, one can overcome the exchange parameter *J* or the magnetic correlation in a spin system.

In order to quantify the exchange parameter *J*, Chen et al.[23] performed tunneling transport measurements at the submolecular spatial precision on the 3-5ML thick CoPc films grown on top of the metallic Pb islands, using a scanning tunneling microscope (STM). In their STM measurements the spin-polarized electrons were injected into the antiferromagnetically (AFM) coupled CoPc molecular spin chain (MSC) from the STM tip and finally collected at the metallic substrate (Pb). Due to the absence of the Zeeman splitting and Kondo screening for the molecule adsorbed on the Pb they suggested that the magnetic moment of the 1st ML of CoPc is completely quenched by the substrate. The 1st ML of CoPc thus acts as a buffer to prevent the spins above it from being quenched[23]. A CoPc molecule contains a singly occupied $3d_z^2$ orbital and therefore possesses a net spin of $S = 1/2$. The spin-polarized electrons that are injected to the CoPc molecular spin chain can either be tunneled elastically or inelastically. In elastic tunneling, both energy and spin angular momentum (or the magnetic moment) of the tunneling electrons remain conserved whereas in inelastic tunneling the tunneling electrons interact with their environment and exchange energy and potentially the spin angular momentum[23,26]. In the molecular systems, if the exchanged energy is higher than the exchange parameter J, the spin-chain can be excited by the spin-flip events[23]. During the spin-flip event across a CoPc molecule, the single electron in the $3d_z^2$ orbital with spin up (↑, with spin quantum number $m_s = |+1/2 >$) configuration gets flipped into a spin down (↓, with spin quantum number $m_s = |-1/2 >$) configuration, thus exhibits a spin-flip excitation from $m_s = |+1/2 > \rightarrow m_s = |-1/2 >$. For a 3ML thick CoPc AFM spin chain grown on Pb metal with the quenched magnetic moment of the 1st ML of CoPc, the net spin in the ground state is $S_C = 0$, whereas undergoing a spin-flip excitation ($m_s = |+1/2 > \rightarrow m_s = |-1/2 >$) results a net spin of $S_C = 1$ at the excited state. The energy lost (or exchanged to the molecular layer) during the spin-flip excitation $S_C = 0 \rightarrow S_C = 1$ corresponds to the exchange parameter (J). The spin-flip transition is schematically shown in Figure 5.12.

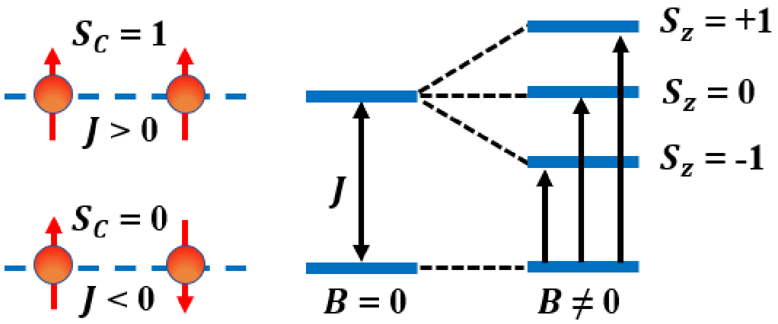

Figure 5.12. Schematic of a singlet state spin-flip excitation leading to singlet→ triplet transition. For a 3ML long spin chain of CoPc with effective spin 1/2 for each ML, the 1st ML magnetization quenched by the ferromagnetic substrate Co, therefore with the next two AFM coupled CoPc molecules, the total effective spin of the 3ML spin chain becomes zero ($S_C = 0$) in the ground state. The excited state due to the spin-flip event turns the total spin of the spin chain equal to one ($S_C = 1$). The energy required to cause $S_C = 0 \rightarrow S_C = 1$ transition is the exchange energy (J). Under the applied external magnetic field, due to Zeeman splitting the triplet state with $S_C= 1$ state further splits into three spin states with spin quantum number $|m_s> = -1, 0, +1$. The figure is adapted from ref [23].

The spin-flip excitations can be probed by a threshold spectroscopy technique; inelastic electron tunneling spectroscopy (IETS) technique. In this technique, the spin-flip excitations correspond to the steps or jumps in the differential conductance (dI/dV, where I is the tunneling current)[23,26]. The threshold voltage (V_{th}) at which the differential conductance step or jump appears corresponds to the excitation energy or the exchange energy (J = ±V_{th}.e). Depending upon the energy of the injected electrons (e.V), two possible tunneling scenarios are shown in Fig. 5.13. The first scenario shown in Fig. 5.13.a1 and a2 represents the elastic tunneling regime when the energy (e.V) of the tunneling electrons is lower than the exchange energy (J), due to which no spin-flip excitations are observed. In terms of the IETS equivalent, this corresponds to the bias voltage lower than the threshold voltage (±V_{th}) and characterized by the flat line in the differential conductance (dI/dV) plot [see Fig. 5.14].

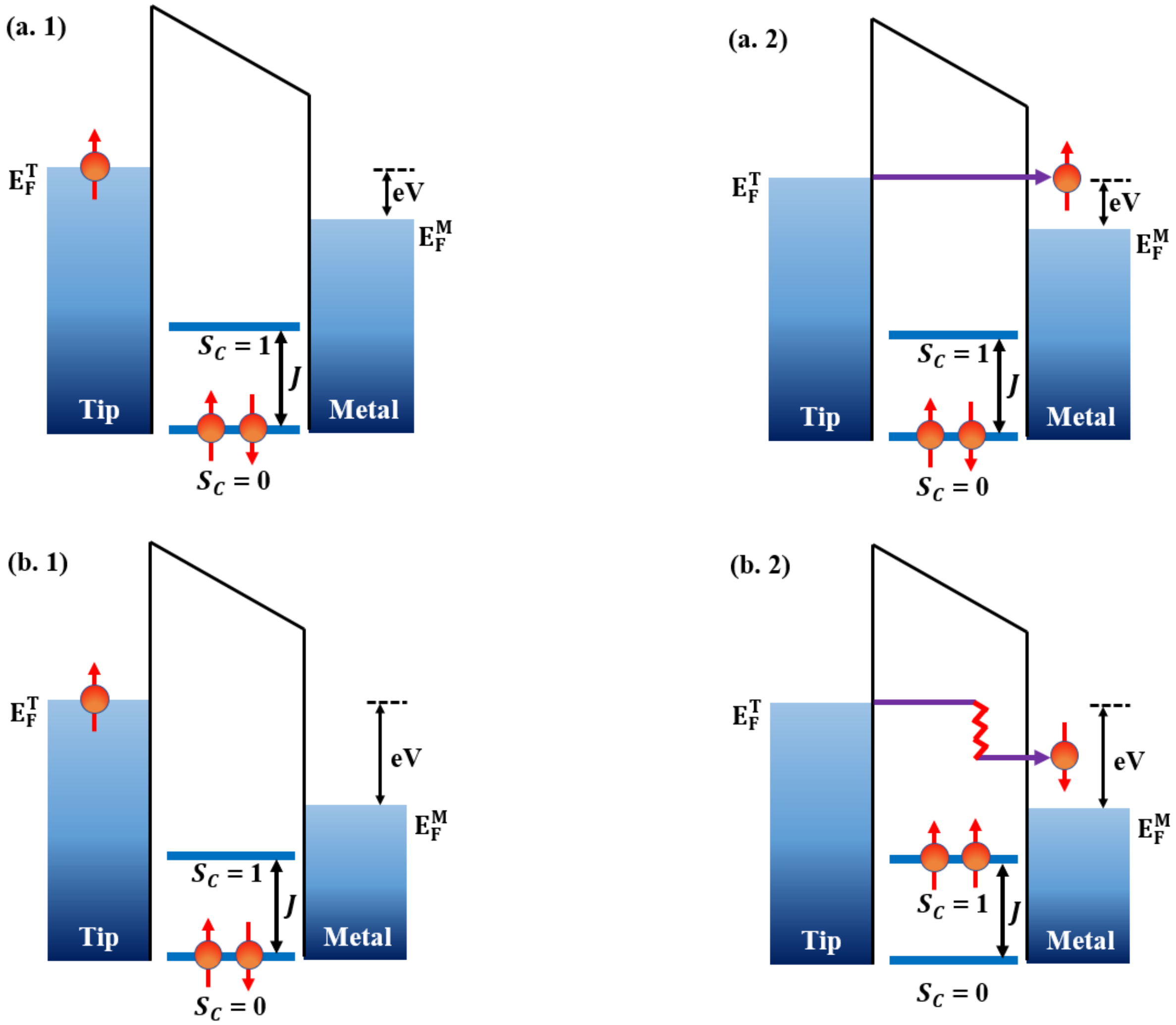

Figure 5.13. The schematization of the elastic and inelastic tunneling regimes for a 3ML long spin chain of CoPc with effective spin 1/2 for each ML. the 1st ML magnetization quenched by the ferromagnetic substrate Co, therefore with next two AFM coupled CoPc molecules the total effective spin of the 3ML spin chain becomes zero ($S_C = 0$) at the ground state. Panel (a.1 and a.2) schematizes the elastic tunneling regime, when the input voltage is lower than the threshold voltage (V_{th} = ±J/e) required to excite the inelastic spin-flip, in this case, the tunneling electron preserves its spin symmetry. Panel (b.1 and b.2) schematizes the inelastic tunneling regime, when the input voltage is equal to or higher than the threshold voltage ($V \geq V_{th}$, V_{th} = ±J/e), leading to a spin-flip excitation from $|m_s\rangle = -1/2$ to $|m_s\rangle = +1/2$. The figures are adapted from ref [26,166].

As soon as the energy of the injected electrons (e.V) reaches close to or surpasses the exchange energy (*J*) [see Fig. 5.13.b1 and b2], the tunneled electrons exchange or lose their energy with their environment and produce the spin-flip excitations. This spin-flip excitation causes a change in the total spin of a 3ML CoPc AFM chain grown on top of the Pb island, from $S_C = 0 \rightarrow S_C = 1$, and therefore opens additional inelastic conduction channels that are ultimately increasing the tunneling current (I). This inelastic tunneling regime corresponds to the input bias voltage equal to or greater than the threshold voltage ($\pm V_{th}$) i.e. $V \geq \pm V_{th}$ and is characterized by the step in the differential conductance (dI/dV) in its IETS equivalent [see Fig. 5.14]. Furthermore, performing the differential conductance (dI/dV) measurements under the applied external magnetic field (B) with $V > \pm V_{th}$ splits the total spin $S_C = 1$ energy level into triply degenerate Zeeman levels -1, 0, and +1 and increase the number of differential conductance steps with the selection rule $|\Delta S_C| = 0,1$[23,167].

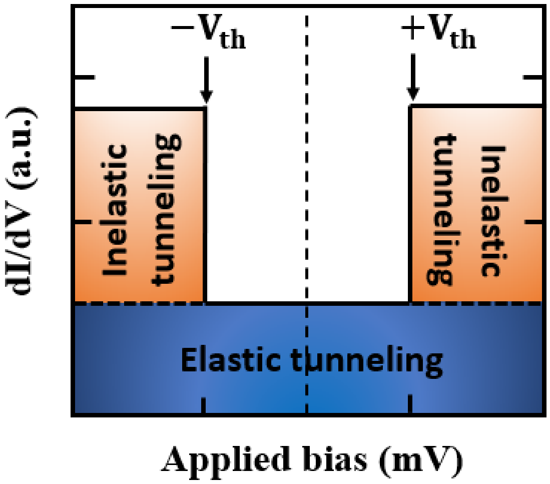

Figure 5.14. Schematic of differential conductance plot, equivalent to the elastic and inelastic (spin-flip) electron tunneling regime. The area filled with blue color with almost flat dI/dV represents the elastic tunneling regime whereas the area filled with brick red color with steps in dI/dV represents the inelastic tunneling regime. The figures are adapted from ref [23,26,166].

5.6.3 AFM ordering of spin chain and exchange bias

When an AFM material is grown as a bilayer, multilayer, or core-shell structure together with an FM material, this causes a shift in the coercivity (H_C) of FM material. This phenomenon is known as exchange bias or exchange anisotropy[168]. Exchange bias finds practical applications in technological devices such as spin valves, MTJs, and STT-MRAMs to provide the harder magnetic referential, by pinning the FM electrode [see Chapter-1]. AFM and FM materials lose their respective magnetic orderings and turn into paramagnets through a second-order or continuous phase transition at a certain temperature known as Néel temperature (T_N) and Curie temperature (T_C), respectively. Therefore to observe the exchange bias effect in a variety of FM|AFM structures, the magnetization measurements (M-H) must be carried out (i) after introducing a magnetic reference through an externally applied magnetic field (H_{FC}) during the cooling procedure known as field cooling (FC) and (ii) at a temperature ($T < T_N < T_C$) below the Néel temperature (T_N) of the AFM material and Curie temperature (T_C) of the FM material used. Here we present a phenomenological model[169] that describes how the FC procedure preserves both AFM and FM orderings within their respective magnetic materials in a given sample, giving rise to the exchange bias effect.

5.6.3.1. Field cooling and exchange bias

To understand the role of FC, we start with a simple picture where an AFM|FM bilayer is kept at the temperature $T_N < T < T_C$ [see Fig. 5.15.1]. In this case, since the temperature $T < T_C$, the bottom FM layer, as represented by the blue arrows (for spins), preserves its magnetic correlations i.e. the ferromagnetism, whereas the top AFM layer, as represented by the red arrows (for spins), does not exhibit any magnetic correlation (since $T > T_N$) and thus remains disordered. In this case, the FM layer is not magnetically influenced by the top layer (represented by the red arrows): the M-H curve has no shift in the coercivity (positive H_{C1} and negative H_{C2}) under the externally applied field.

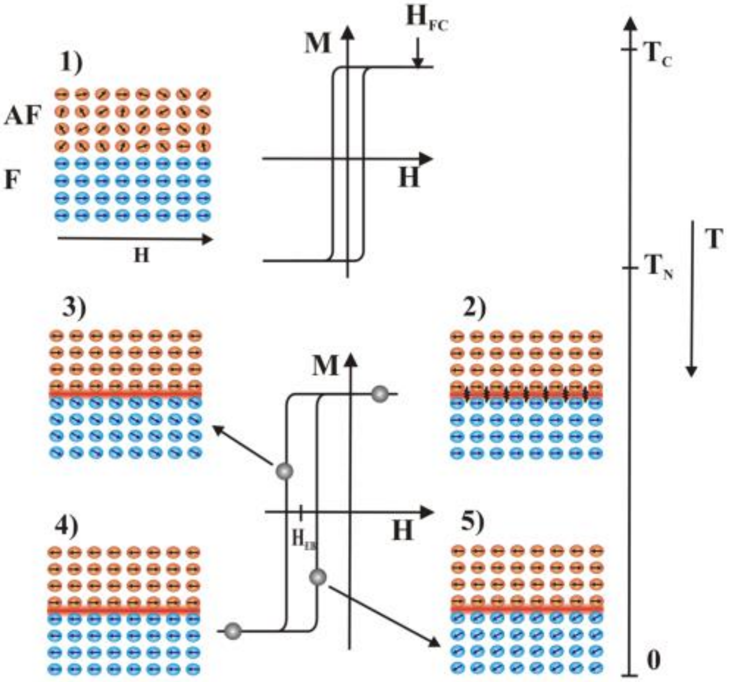

Figure 5.15. A phenomenological model for the exchange bias in an FM/AFM bilayer. The magnetic ordering with respect to the temperature (right side) is shown in panel (1) to panel (5). When the temperature T is below the Curie temperature (T_C) but higher than the Néel temperature (T_N) i.e. ($T_N < T < T_C$) the bilayer sample exhibit a symmetric M-H curve i.e. ferromagnetism, shown by the panel (1). Performing field cooling (FC) and measuring the M-H curve at the temperature $T < T_N < T_C$ causes a shift in the coercivity and produces a ferromagnetic loop that is altered exchange bias, shown by the panel (2). The figures are taken from ref [169].

However on applying an external magnetic field H_{FC}($H_{FC} > H_{C1,2}$) continuously and cooling the FM|AFM bilayer system, i.e. the FC process below both T_N and T_C ($T < T_N < T_C$), the magnetic correlations in both the FM and AFM materials are both preserved. This results in the appearance of exchange bias (EB) in these systems. The FC procedure produces an FM coupling between the FM and AFM interface that points in the direction of the positive applied H_{FC} as shown in Fig. 5.15.2. This FM coupling between the FM and AFM layer however gets a 360^0 reversal for the progressive sweeping of H_{FC} to the negative values [see Fig. 5.15.4]. This unidirectional anisotropy results in an AFM coupling between the interfacial spins of FM and AFM layer. If H_{C+} and H_{C-} are the coercivities for the +H_{FC} and -H_{FC} applied field respectively, the exchange bias for the FM|AFM system can be written as: $H_{EB} = (H_{C+} + H_{C-})/2$.

5.6.3.2. Exchange bias in FM|MnPc bilayers

As already described in Section 1.6.1, the paramagnetic MnPc molecular thin film grown on top of the ferromagnetic thin film sample Cu(100)||Co [where Cu (100) is the substrate] exhibits an antiferromagnetic ordering at room temperature[165]. Gruber et al.[165] performed the magneto-optical Kerr effect (MOKE) measurements at room temperature [Fig.5.16.a] and found a symmetric magnetization curve with no shift in the coercivity (represented by the red line for the temperature 300K). However, following a field cooling procedure at H_{FC} of +0.2T applied external field with simultaneously decreasing temperature produces the FM coupling between the 1st ML of MnPc and the ferromagnetic Co, along the direction of the applied H_{FC} while the successive monolayers of MnPc are antiferromagnetically coupled. The ferromagnetic Co and 1st ML of MnPc develops spin polarization and forms an entity called the spinterface. The spinterface is described in the Section 5.4.

The FC procedure resulted in an asymmetric magnetization curve with a shift in the coercivity of 60mT (represented by the blue line for the temperature 14K) towards negative values of the applied magnetic field. On increasing the temperature to 58K, a reduction in the asymmetry in the magnetization curve and the shift in the coercivity was found (represented by the green line). This asymmetry in the magnetization curve and the shift in the coercivity is the manifestation of exchange bias caused by the MnPc AFM chain on the ferromagnetic cobalt sample. The exchange bias gradually decreases with increasing temperature. This exchange bias due to the AFM ordering of the MnPc layer, and disappears above a certain temperature known as the “blocking temperature” (T_B) [Fig. 5.16.b]. It has been found that the uniaxial magnetic anisotropy induced by the AFM spin chain of MnPc completely vanishes at T_B. However, a fraction of the spin chain can be found AFM coupled even at room temperature[165]. From the temperature-dependent MOKE experiments Gruber et al.[165] found 100K as the blocking temperature for the Cu(100)||Co (20ML)|MnPc(25ML) bilayer sample. This T_B of 100K was found to be consistent with the T_B of ~106K, extracted out from exchange energy (J/K_B) measured experimentally from the magnetic susceptibility experiments performed Si by Serri et al.[24] on 200nm thick α-Phase CoPc sample (grown on silicon substrate). A significant increase in the T_B~150K was recently reported by Jo et al.[170], which is still lower than their inorganic counterparts. This, therefore, limits the use of these devices for technological applications at room temperature. A proper understanding of the interplay between the T_B and exchange energy (J/k_B), and improved quality of the FM|MPc interface could, however, yield devices with T_B close to room temperature.

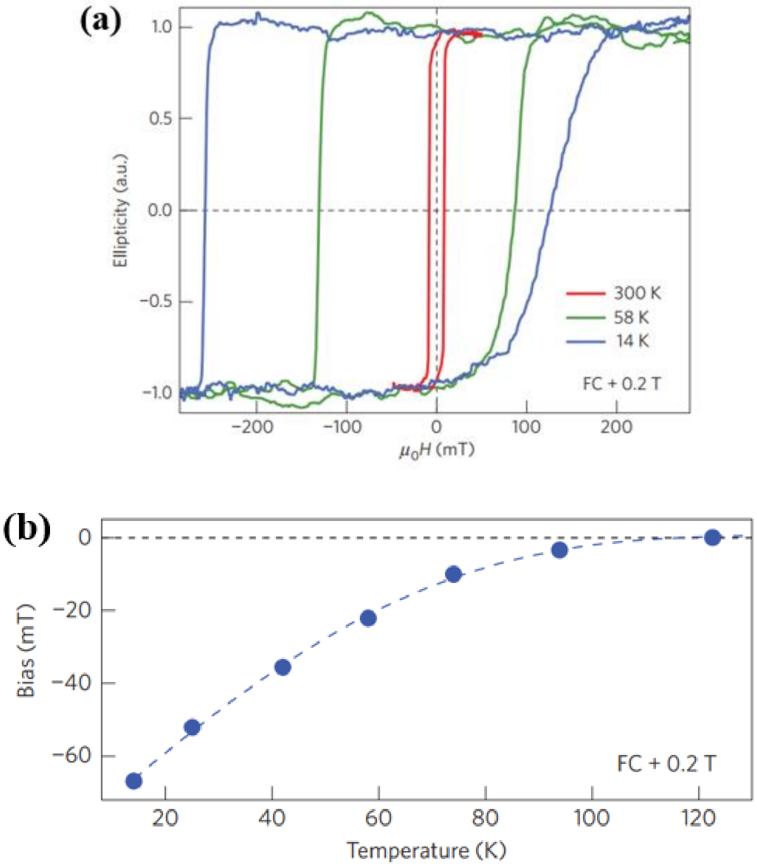

Figure 5.16. Exchange bias induced by MnPc AFM chain on the Co substrate and the blocking temperature. (a) Ellipticity as a function of the applied magnetic field (H) measured for Cu(100)||Co (20ML)|MnPc(25ML) bilayer sample measured from the magneto-optical Kerr effect microscope (MOKE) experiments. The red curve (300K) shows no asymmetry, therefore, no exchange bias. MOKE measurements performed after the field cooling procedure with H_{FC} = +0.2T, resulted in a shift in the coercivity (H_C) or the exchange bias, shown by the blue (green) curve at 14K (58K). From the temperature-dependent MOKE measurements, it was observed that the asymmetry in the magnetization curve or the exchange bias decreases with the increasing temperature. **(b)** Temperature-dependent exchange bias plot reveals extinction of the exchange bias after the blocking temperature (T_B) of ~100K. The figures are taken from ref [165].

5.7 Evolution of spinterface science

After the discovery of MR[18,19] in the spin valves composed of two ferromagnetic electrodes separated by an organic/molecular spacer layer, Sanvito et al.[171] provided the first theoretical description using the density functional theory (DFT) and later coined the term ‘spinterface’[20].

In his theoretical work, Sanvito et al.[171] observed an increased broadening and spin-splitting in the Tricene's (sandwiched between Ni leads) molecular orbitals upon decreasing the distance between the Ni-S, therefore, resulting in a modified interfacial spin polarization. The major milestone in spinterface science was achieved in 2010, when Barraud et al.[153] measured a large TMR of 300% at 2K, for their nanoscale vertical LSMO|Alq3|Co MTJ devices. This record TMR of 300% was found to be larger than what was expected within the Jullière model[36] given the spin polarization of the LSMO and Co electrodes. Furthermore, the positive sign could not be reconciled with prior experiments on inorganic MTJs with LSMO and Co electrodes[172]. Instead, this finding suggests an enhanced spin polarization of the FM electrodes due to the hybridization with the Alq3 molecular orbitals i.e. by the presence of the spinterface.

Although, after this remarkable work by Barraud et al., a significant interest in the spinterface science has been noticed, however, the technological challenges in the nanofabrication of these devices limited the progress of the spinterface science. Even to fabricate the nanoscale LSMO|Alq3|Co MTJs, Barraud et al.[153] employed an alternative lithography technique called AFM-nanoindentation developed by K. Bouzehouane et al.[173]. The nanofabrication process starts with the deposition of a protective layer to preserve the organic molecule Alq3, and is achieved by the spin coating of 30nm thick S1800 series positive photoresist on top of the LSMO|Alq3(10-30nm) bilayer. The photoresist-coated bilayer now indented from the top side (molecular layer coated with the photoresist) using the conductive tip-atomic force microscope (CT-AFM). During the indentation process, the thickness of the Alq3 molecular layer is controlled by the conductance measured between the AFM-tip and LSMO. After a desired thickness of Alq3 at the place of nanoindentation the remaining hole was filled by the Co sputter deposition. The schematic of the AFM-nanoindented vertical solid state MTJ with the TMR values is shown in Fig. 5.17.

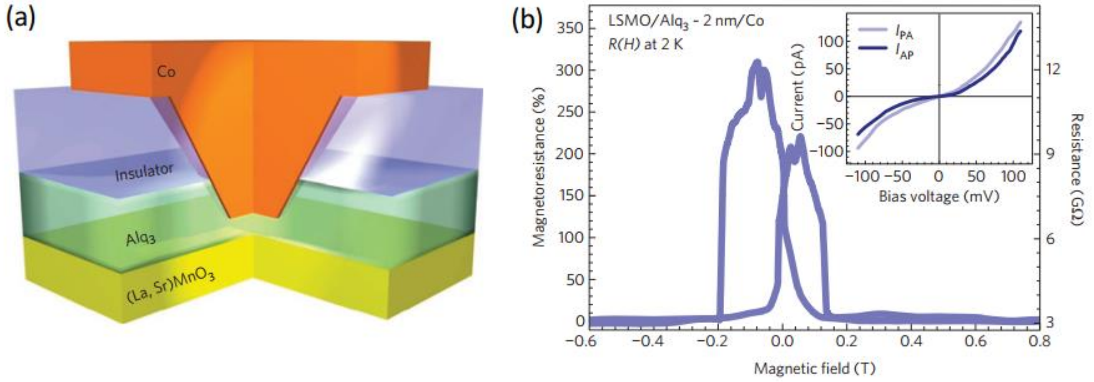

Figure 5.17. Nanoindented MTJ with measured TMR. (a) Nanosized LSMO|Alq3|Co organic magnetic tunnel junction. **(b)** Record TMR of 300% measured at 2K, is the direct evidence of highly spin-polarized spinterface.

The major challenge in the nanofabrication of these devices is to protect the organic or molecular spacer layer from the photoresists and organic solvents during the conventional lithography process. To completely avoid the use of photoresist and organic solvents (or limit them to enter into the molecular layer), we have developed our in-house technique which we call 'nanobead processing' is described in detail in Chapter-6.

5.7.1 MPc-based spinterfaces

We now discuss spinterfaces that integrate MPc molecules. The presence of an interfacial polarization was observed in W(110)||Fe|CoPc bilayers using spin-polarized scanning tunneling microscopy (SP-STM) experiments and DFT calculations performed by Brede et al.[25] , in agreement with the experimental findings of Iacovita et al.[174]. In 2012 Lach et al.[175] reported spin-resolved photoelectron spectroscopy (SR-PES) experiments and ab-initio calculations on a variety of such interfaces. Further, a large spinterface polarization was experimentally observed by Djeghloul et al.[176] for MnPc molecules chemisorbed on Co films [see Fig. 5.18]. These spectacular results obtained for MPc molecules deepened the interest of the spintronic research community towards the MPc molecules for technological device applications.

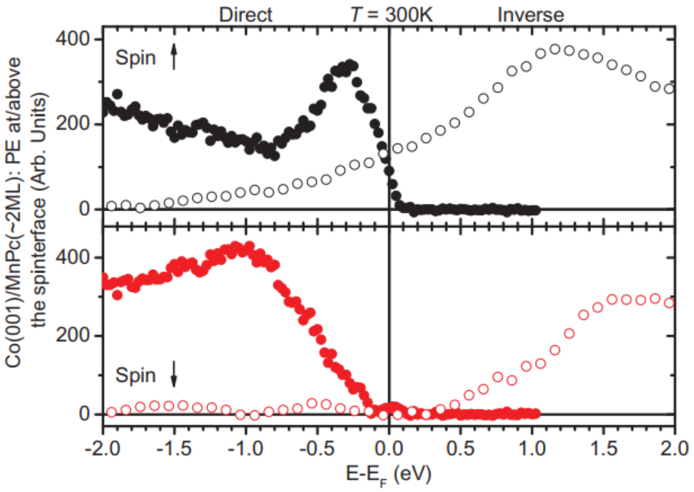

Figure 5.18. Spin-polarized direct (close symbols) and inverse (open symbols) photoemission (PE) spectra obtained for a Co|MnPc bilayer at 300 K. The interfacial band-structure is dominated by the majority channel, leading to P ≈ +80%. The Figure is taken from ref[176]

In the following years, Barraud et al.[177], again using the AFM-nanoindentation technique[173], crafted nanoscale Co|CoPc|Co magnetic tunnel junctions. From angle-dependent magnetotransport measurements performed on these MTJ devices, they observed tunneling anisotropic magnetoresistance (TAMR) between the 0^0 (with positive TMR) and 180^0 (with positive TMR) of applied external magnetic field and found it to be rooted with the spin-polarized tunneling asymmetry caused by the unidirectional magnetic anisotropy of the spinterface. In addition to the uniaxial magnetic anisotropy of the Co FM electrode, the unidirectional magnetic anisotropy at the spinterface is caused by interfacial hybridized electronic states between Co and an antiferromagnetic CoPc chain, found to be coexisting in these MTJ devices. The magnetotransport measured at 90^0 resulted in a negative TMR of 20%, which was never expected for the MTJs with nominally identical interfaces. They concluded that the inversion of MR sign (from positive to negative) is due to the formation of two different spinterfaces at Co|CoPc (bottom) and CoPc|Co (top). This conclusion fits with the basic understanding of the spinterface science developed so far, and according to which the coupling strength between the energy states of FM metal and molecule determines the spin polarization and therefore the spin-dependent tunneling [20,22]. These results are shown in Fig. 5.19.

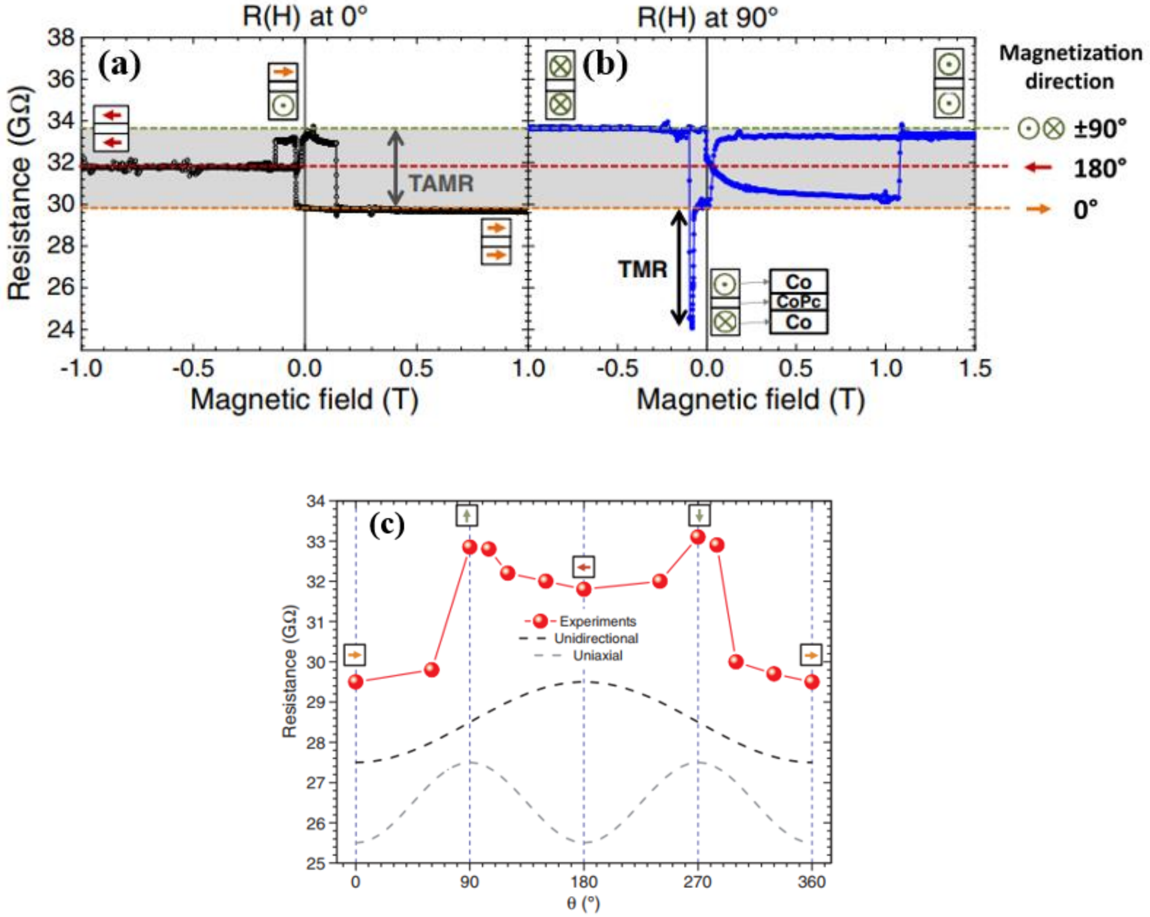

Figure 5.19. Angle dependent magnetotransport measurement performed and spinterfacial unidirectional magnetic anisotropy. (a) Magnetotransport performed at T = 2K and applied bias V = -200mV, with the external applied field at 0^0 and 180^0 (opposite direction of field) shows difference in the saturation magnetization thus resulting in a positive tunneling anisotropic magnetoresistance (TAMR), **(b)** The negative TMR at 90^0 for the symmetrical Co|CoPc|Co MTJ is due to the different interfacial hybridization at bottom Co|CoPc and top CoPc|Co spinterfaces. **(c)** Modification in the uniaxial anisotropy of Co due to the spinterface hybridization resulting in a unidirectional magnetic anisotropy. The figures are taken from ref[177].

In line with the above findings, in 2019, Jo et al.[170] reported the highest ever molecular exchange bias of 170mT for their Co|metalloporphyrin (MOEP, M = Ni, Cu, and Zn) hybrid bilayer thin film sample. The authors witnessed a wide range of interfacial coupling and exchange bias between the Co thin film and distinct MOEP molecular layers. The Co|(MOEP, M = Ni, Cu, and Zn) bilayer samples are schematically shown in Fig.5.20.a. The MOEP (M = Ni, Cu, and Zn) planar molecular layer of 8nm (shown by blue/red color) is deposited on top of the Co film of thickness 4nm and capped with an aluminum oxide layer (AlO_x). The M-H loops of these bilayer samples with M = Ni, Cu, and Zn are shown in Fig. 5.20. a, b, and c respectively.

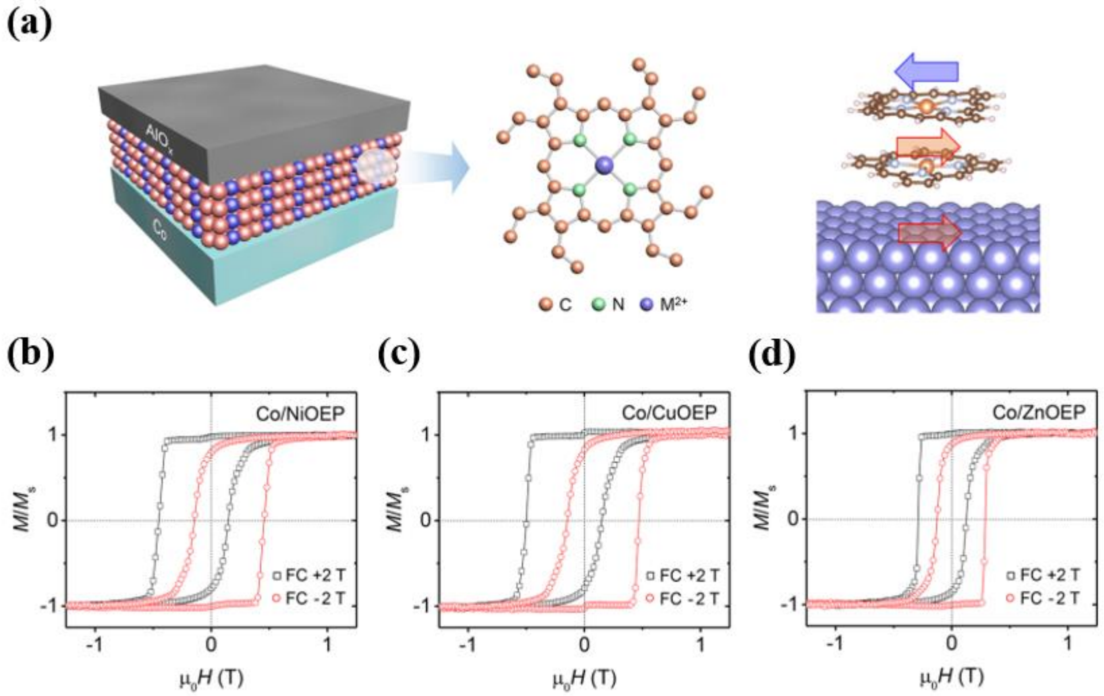

Figure 5.20. Co|MOEP (M = Ni, Cu, and Zn) hybrid bilayer system and the exchange bias. (a) Schematic representation of the Co|MOEP bilayer system and the magnetic coupling. The planar MOEP molecules (shown by blue/red color) are deposited on a Co(111) thin films. Panel (**b, c,** and **d**) are the M-H loops showing the molecular exchange bias for the Co(4nm)|MOEP(8nm)|AlOx bilayer capped systems with M = Ni, Cu and Zn respectively. The M-H loops with an open black rectangle (open red circle) correspond to the applied magnetic field of +2T (-2T) used for the field cooling (FC) procedure. For the M = Ni, Cu, and Zn systems, the magnitudes of exchange bias H_{EB} were measured to be -170, -162, and -95mT, respectively. The figure is taken from ref[170]

The M-H loops with an open black rectangle (open red circle) correspond to the applied magnetic field of +2T (-2T) used for the field cooling (FC) procedure. The width of the hysteresis loops for the Co|MOEP bilayers was found to be twice of the bare Co thin films. It has been observed that the positive (negative) magnetic field applied during the field cooling procedure shifts the M-H loop towards the opposite side i.e. negative (positive) direction of the applied field, indicating that the exchange bias is arising from the interfacial interactions between the Co and MOEP layers. Further, performing the transport measurements on the bilayer device Co|NiOEP, the transport asymmetry was observed in the angle-dependent resistance, anisotropic magnetoresistance (AMR), and planar Hall resistance (PHR).

The authors concluded that the asymmetrical transport is a manifestation of the molecular exchange bias. The effect of the spinterface formation on the magnetic anisotropy was also reported by Mallik et al.[178]. They experimentally observed a decrease in the uniaxial magnetic anisotropy of Fe for their sample Si|SiO*x*||Fe|C_{60} compared to that of the bare Fe thin films grown on top of the Si|SiOx substrate. They ascribed this decrease in the uniaxial magnetic anisotropy of Fe to the formation of the spinterface due to the π-d hybridization between the C (of C_{60}) and Fe atoms. In 2020, Mundlia et al.[179] reported a robust molecular exchange bias effect in zero field cooled Fe|MPc bilayers. According to them, the Fe|MPc spinterface forms a separate entity 'magnetic hard unit' that weakens the interlayer magnetic exchange coupling with the soft underlying magnetic unit Fe. They termed this mechanism a molecular 'crane-pulley effect'. The switching field for the magnetic hard unit was found to be larger than the 7T therefore on the one hand can be used as a potential alternative for the rare-earth free permanent magnets and on the other hand can also be used as the pinning layers for the soft ferromagnetic thin films. Recently Jo et al.[180] reported the emergence of multispinterface of a non Pc paramagnetic cobalt-octaethyl-porphyrin (CoOEP) layers in a Fe| CoOEP heterostructures. The emergence of the multi spinterface is found to be rooted in the interfacial layer and successive antiferromagnetic molecular spin chain. The authors concluded that the exchange bias, which is found to be tunable with the applied field cooling, is a manifestation of the molecular multispinterface coupled to the antiferromagnetic molecular spin chain.

Other than the spinterface induced molecular exchange bias, Barraud et al.[181] in 2016, reported the very first experimental results on spin-flip inelastic excitations (IETS) [see Section 5.6.2] obtained for the nanoscale vertical solid-state MTJ devices. These solid-state vertical MTJ devices of Co|H_2Pc|MnPc|Co structure with ~10 nm^2 cross-section were nanofabricated using the AFM-nanoindentation technique. Fig. 5.21 shows differential conductance measured for the Co|H_2Pc|MnPc|Co nanoscale MTJs, in which the higher resistance state exhibits the spin-flip inelastic excitations, whereas the lower resistance state does not show any such features.

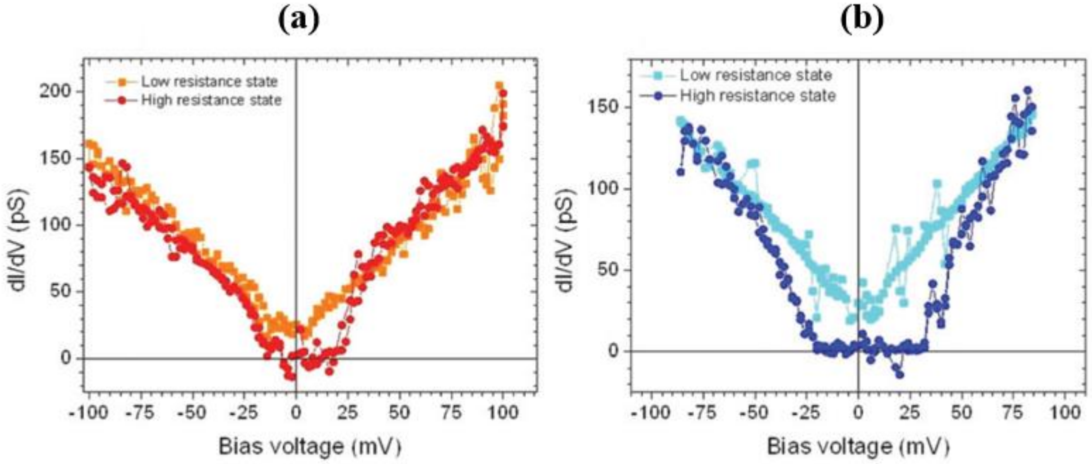

Figure 5.21. Differential conductance plots for Co|H_2Pc|MnPc|Co MTJs recorded at 2K and (a) at 0^0 and **(b)** 90^0. The dI/dV step at ~25mV is the threshold voltage for the spin-flip excitations in the MnPc spin chain and is consistent with the ~17meV reported by Hirjibehedin et. al.[182] The Figures are taken from ref[181].

In these devices, the H_2Pc molecule of ~1nm was used to magnetically decouple the top and bottom FM electrodes (Co) so that the AP state could be achieved. The formation of the spinterface at one side[181] rather than both sides of the tunneling layer[177] makes a comparatively simple picture to understand the impact of the spinterface formation and exchange bias in molecular solid-state spintronic devices.

5.8 Scientific Motivation

So far, we have discussed how the interfacial hybridization, between the atomic *d*-orbitals of the ferromagnetic metal and the molecular orbitals of a molecule adsorbed on top of it, forms a specific entity called a ‘spinterface’ and can induce the exchange bias, modify the amplitude and sign of the interfacial spin polarization and the interfacial magnetic anisotropy in the bilayer and trilayer solid-state hybrid devices. Further, from the local probe experiments[23,26,167] and the electrical transport measurements performed across the trilayer nanoscale vertical solid-state devices[181], it was observed that the inelastic excitations in these systems can be induced electrically. The inelastic excitations cause spin-flip in the molecular spin chain and allow the electron to transit from its ground state to an excited state (spin-flipped state). From the conservation of spin angular momentum and transition rules[26], the spin-flip process causes the minority spin states from the ferromagnetic electrode to be transported as a majority states, resulting in a large increase in the conductance. The large increase in the conductance due to the spin-flip inelastic excitations in the molecular spin chain have been experimentally characterized by the sharp steps in the differential conductance (dI/dV) plots. These spin-flip excited states are dynamical, therefore have a short lifetime, before spin angular momentum transfer to the transport electron causes the chain to return to its ground state[26]. The spin polarization of the spin excitation current is indirectly seen in scanning tunneling spectroscopy experiments by comparing the amplitudes of the resulting conductance peaks upon reversing the bias voltage[33]. In these STM experiments, the magnetic orientation of the isolated molecular spin chains is not set but can be influenced by a local[167,183,184] or external[185,186] magnetic field[33].

To exploit the spin-flip inelastic excitations for the technological device applications, one scheme could be to utilize the magnetoresistance (MR) that it is expected to generate. In inorganic solid-state devices such as spin valves and MTJs, the MR encodes the MTJ’s relative orientation of electrode magnetization into the change in the conductance (resistance). It has therefore been widely used for the magneto-resistive sensors and demonstrated for encoding and transmitting the spin or magnetic (electrical) information into the electrical (magnetic or spin) form[8]. Spin-polarized transport through a device's metallic/semiconducting antiferromagnetic layer can facilitate macroscale effects ranging from tunneling anisotropic magnetoresistance[187] and interface charging[188,189] to antiferromagnetic (AF) domain manipulations[190,191]. Moving from the macroscale to the quantum properties of the AF spin chain, indirect evidence indicates that MR can be used in a solid-state system to track changes in the quantum state of the AF spin chain[177,181]. Furthermore, spintronic devices with discrete spins that are being proposed for encoding quantum information[23,167,183,184,192–195], can also play an important role in harvesting thermal energy[29]. To demonstrate the aforementioned quantum phenomena and the capability in the vertical solid-state devices, we have further developed a resist-and solvent-free nanolithography technique called ‘nanobead processing’ that will be described in the following chapter, in detail.

6. Nanobead Processing: Realizing Hybrid Nanopillars

To visualize the quantum effects, the size of the devices must be scaled down to the nanometric scale. For a tri-layered/multilayered thin-film structure, the scaling down of the devices can be achieved by the nanolithography techniques. The commercially available nanolithography techniques such as the electron-beam lithography, focused ion beam etching, etc., however, have made the fabrication of industrial-grade inorganic nanoscale vertical junctions possible but the extensive use of the resist and organic solvents during the lithography steps limits these commercially available nanolithography techniques to be used for the nanofabrication of organic molecule-based hybrid junctions from their respective trilayer stacks. Many alternative techniques such as the point-contact method[113], AFM-based nanoindentation[153,181], dip-pen lithography[196], and nanosphere lithography[197] have also been invented so far. Among the abovementioned techniques, the first one is not a true nanolithography technique and does not scale down the complete vertical structure into the nanoscale regime. Furthermore, the latter three nanolithography processes either incorporate the resist or the organic solvent or both. To avoid the use of resist and minimize the use of organic solvents, we have developed an indigenous and modified nanosphere lithography that we call “nanobead processing”. The nanobead process uses silica nanobeads as the shadow mask to define the cross-section of the vertical nanopillars. The silica nanobeads can be deposited on the top capping layer of the hybrid trilayer stacks either in the dry form or using the microfluidic pen lithography technique with a very small quantity (picolitre volume) of solvent. In the microfluidic pen lithography technique, the use of highly localized drops of the solvent (~10μm size) to deposit the silica nanobeads on the top capping surface of the hybrid trilayer stack avoids all the possibilities of entering the solvent into the organic molecular spacer layer. In both the dry deposition technique and the microfluidic pen lithography technique, the quality of the organic molecular layer used as a spacer layer remains intact. Further, these deposited nanobeads can be precisely positioned on the desired location on the top surface (capping layer) of the hybrid trilayer stack, using the AFM-assisted lateral manipulations in the former case (dry deposition), and in the latter case (microfluidic pen lithography) by using a fine micropipette attached to the commercially available microinjectors and fixed to the automatic/manual manipulators, and a movable sample stage. The nanobead deposited capped trilayer hybrid stack is then subjected to a dry etching step to form an array of vertical nanopillars with the desired cross-section. The top electrodes for the devices are deposited using laser-cut shadow masks made of aluminum. Before heading to the lithography section, we will provide a brief knowledge regarding the growth of the trilayer hybrid stacks.

6.1 Growth of hybrid stacks

The growth process of the capped hybrid trilayer stack starts with the preparation of Si|SiOx substrate, where SiOx is a 150nm-thick thermally oxidized layer on top of the silicon (Si) substrate. To remove the possible contaminants on top of the surface, the substrate was subsequently cleaned with acetone, ethanol, and isopropanol (for 15 mins each) in an ultrasonic bath. Further to remove any possible carbon impurities the oxygen plasma was also used. After the cleaning process, the substrate was covered with a laser cut shadow mask (made of stainless steel) to define the bottom electrode. The whole trilayer structure growth happens through this shadow mask; therefore, the structure of the entire trilayer stack can be assumed as the periodic structure of the bottom electrode with successive layers of different materials along the upward direction. We have grown the two types of capped hybrid trilayer stacks: i) Si|SiOx||Cr(5)|Fe(50)|CoPc(20)|Co(10)|Cr(5), and ii) Si|SiOx||Cr(5)|Fe(50)|C60(*n* ML)|CoPc(3ML)|C60(5ML)|Fe(10)|Cr(50), with n =1,3. For both capped hybrid trilayer stacks: i) and ii), the numbers without any units written in the parentheses denote the thickness of the corresponding materials in nm. It is important to mention the thickness of each monolayer of organic molecular layers in the stack ii). For C60 and CoPc, a single ML corresponds to the thickness of 0.9nm and 0.34nm, respectively. The growth of these capped trilayer hybrid stacks was achieved in the ultra-high vacuum (UHV) multi-chamber cluster facility. This facility consists of a sputtering chamber (with a total of three sputtering guns with DC and/or RF power supply) in-situ connected with the ultra-high vacuum (UHV) molecular beam epitaxy (OMBE) chamber. The in-situ deposition avoids the possibility of the oxidation of the metallic layers and protects the organic molecular layer from possible environmental contaminants. The base pressure of the sputtering chamber and OMBE is always kept in 10^{-8} and 10^{-10} mbar respectively. To remove any water contamination, the substrate was annealed at 110^{0}C in the sputtering chamber and allowed to cool down naturally. The deposition of the metallic layers was done at the sputtering chamber while the deposition of the organic molecule for the spacer layer is achieved by the thermal sublimation process in the ultra-high vacuum (UHV) molecular beam epitaxy (OMBE) chamber. This ultra-high vacuum multi-chamber cluster is a rare facility of its kind worldwide. The thickness of the metallic films was monitored with a quartz microbalance during the sputter deposition, while the thickness of the organic layers was calibrated separately, from X-ray reflectivity (XRR) simulations using the test samples. The morphology of the thin films was verified with the atomic force microscope (AFM). The magnetic decoupling between the FM electrodes as a function of the spacer film thickness was confirmed from the AGFM (alternative field gradient magnetometer) and SQUID (superconducting quantum interference device) magnetometry measurements. These stacks were turned into the vertical nanopillars using the in-house developed and modified nanobead process (described in Section 6.3).

6.2 Shadow mask: Synthesizing SiO_2 nanobeads

To craft the nano junctions with a different cross-sectional area, the silica nanobeads of varying diameters were synthesized using the *surfactant mediated sol-gel synthesis technique*[198]. In this technique, we have used tetraethyl orthosilicate (TEOS) as a precursor while cetyltrimethylammonium bromide (CTAB) was used as a cationic surfactant. In this section, we will show how the surfactant's concentration, reflux process (single step or multistep), and reflux time determines the average size of the silica nanobeads. I would like to acknowledge one of our collaborators Dr. Damien Mertz from the Department of Chemistry and Inorganic Materials (DCMI) of CNRS-IPCMS for providing the guidance and allowing me to synthesize these silica nanobeads in his laboratory.

Sample 1: Aiming for the silica nanobeads of 300nm size [see Section 6.3.3], 1.07 gm of cetyltrimethylammonium bromide (CTAB) was completely dissolved in a mixture of 15% volume of propanetriol (PT 44.1 ml)/phosphate-buffered saline (PBS, 250 ml, pH 7: 1.715 gm KH_2PO_4 and 0.29 gm NaOH) solution at 95^0C under vigorous stirring using the magnetic bead. After attaining a clear, transparent, and homogeneous solution, the precursor TEOS of 4.5 ml was added dropwise and let the reaction run for the next 8hrs. After continuous stirring for 8 hrs, the as-synthesized milk-white precipitate was collected by centrifugation process (8000 rcf/8 min) and then washed three times with ethanol (8000 rcf/8 min). To remove the surfactant (CTAB), the as-synthesized material was calcinated at 550^0C for 6hrs. To check the size distribution, a small concentration of the synthesized silica nanobead powder dispersed in the ethanol solution was drop cast on the Si substrate, followed by a natural drying process placed inside the scanning electron microscope (SEM). Fig. 6.1.a shows the size distribution of the synthesized silica nanobeads.

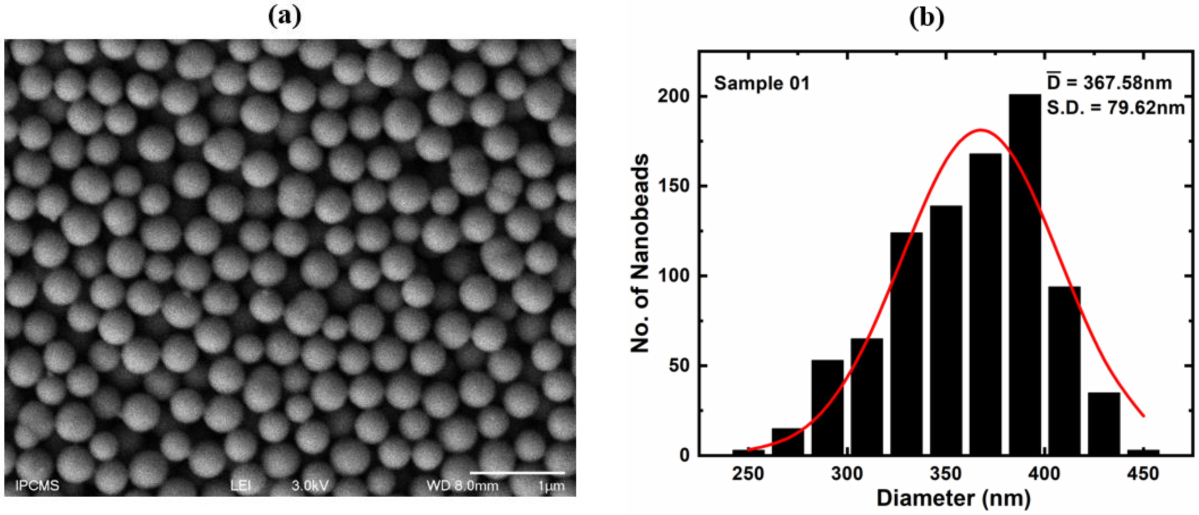

Figure 6.1. Optimization of size and dispersion of silica nanobeads. (a) SEM image shows monodispersed silica nanobeads, **(b)** Average size of the synthesized silica nanobeads was calculated using normal distribution fitting for the extracted values from ImageJ software[199,200]. The average size ($\overline{D}$) of the synthesized silica nanobeads was found to be 367.58nm with the standard deviation (S.D.) of 79.62nm.

Using ImageJ software[199,200], the diameter of 900 random nanobeads was extracted out. On fitting normal distribution [Fig. 6.1.b], the average diameter ($\overline{D}$) was found to be 367.58nm with the standard variation (S.D.) of ±79.62 nm. The synthesized silica nanobead thus exhibits a monodisperse morphology.

Sample 2: Since the average size of the synthesized nanobeads of sample 1 is larger than 300nm aimed in the beginning, therefore, to decrease the size of the silica nanobeads down to 300nm, the concentration of the surfactant solution was decreased from 15% to 12%. To proceed the reaction with modified reaction parameters, 1.035 gm (for 10 mM concentration) of cetyltrimethylammonium bromide (CTAB) was completely dissolved in a mixture of 12% volume of propanetriol (PT 34.1 ml)/ phosphate-buffered saline (PBS, 250 ml, pH 7: 1.715 gm KH_2PO_4 and 0.29 gm NaOH) solution at 95^0C under vigorous stirring using the magnetic bead. After attaining a clear, transparent, and homogeneous solution, 4.5 ml of TEOS was added dropwise and let the reaction run for the next 8hrs. After continuous stirring for 8 hrs, the as-synthesized milk-white precipitate was collected by centrifugation (8000 rcf/8 min) and then washed three times with ethanol (8000 rcf/8 min). To remove the surfactant (CTAB), the as-synthesized material was calcinated at 550^0C for 6 hrs. Fig. 6.2 shows the SEM image [panel (a)] and the measured average size [panel (b)] of the synthesized silica nanobeads. After decreasing the concentration of the surfactant (CTAB) solution from 15% to 12%, the average size ($\overline{D}$) of the silica nanobeads was decreased down to 201.29nm with the standard deviation (S.D.) of ±32.84nm. This reduction in the average size of the silica nanobeads was more than what we aimed for (300 nm). Further, from the SEM image [panel (a)], instead of the monodispersed distribution of the silica nanobeads, we observe agglomerates.

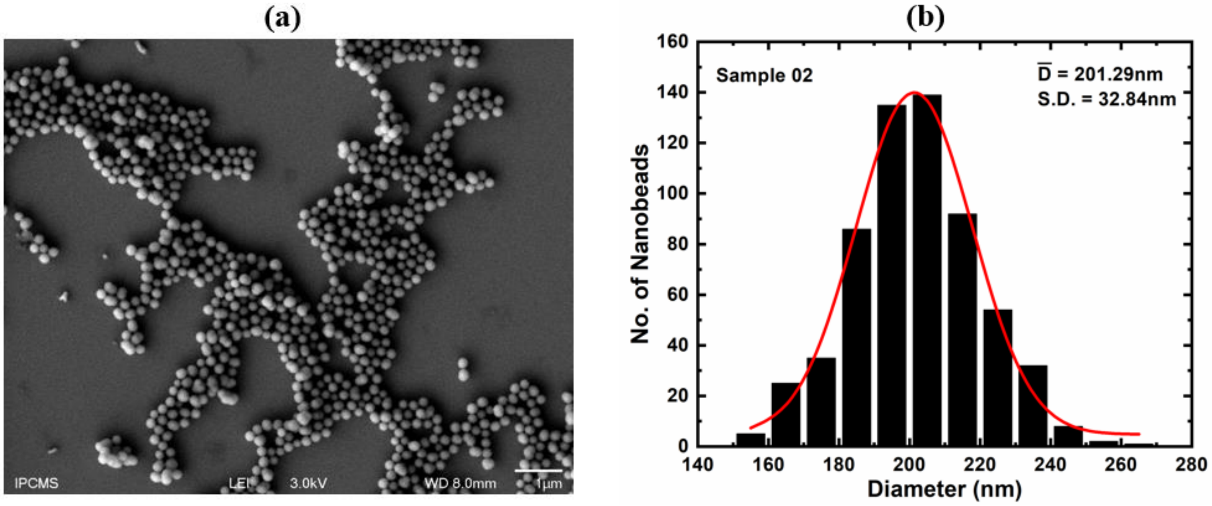

Figure 6.2 Optimization of size and dispersion of silica nanobeads. (a) SEM image indicates the formation of agglomerates of the silica nanobeads **(b)** Average size of the synthesized silica nanobeads was calculated using normal distribution fitting for the extracted values from ImageJ software[199,200]. The average size ($\overline{D}$) of the synthesized silica nanobeads was found to be 201.29nm with the standard deviation (S.D.) of 32.84nm.

Sample 3: To increase the size up to 300nm and improve the growth of the silica nanobeads, we kept the concentration of the surfactant (CTAB) solution fixed i.e., 12% but modified the process of adding the precursor solution (TEOS) and the reflux time. The existing single step addition of the precursor solution (4.5 ml of TEOS) in the surfactant solution, was replaced with the multistep addition process and the reflux time was increased from 8hrs to 12 hrs. The complete chemical reaction was performed in the following way: First, 1.035 gm (for 10 mM concentration) of cetyltrimethylammonium bromide (CTAB) was completely dissolved in a mixture of 12% volume of propanetriol (PT 34.1 ml)/ phosphate-buffered saline (PBS, 250 ml, pH 7: 1.715 gm KH_2PO_4 and 0.29 gm NaOH) solution at 95^{0}C under vigorous stirring using the magnetic bead. After attaining a clear, and homogeneous solution, 750 µl of TEOS was added dropwise and let the reaction run for the next 2 hrs. This dropwise addition of 750 µl of TEOS into the reaction was repeated for the next 5 more times. The total 6 times addition of 750 µl of TEOS thus equivalent to 4.5 ml TEOS addition but in a multistep process of total reflux time of 12hrs. Compared to the single addition, the multistep addition of TEOS provides better control on the growth of the silica nanobeads of the desired size of 300 nm. After continuous stirring for 12 hrs, the as-synthesized milk-white precipitate was collected by centrifugation (8000 rcf/8 min) and then washed 03 times with ethanol (8000 rcf/8 min). To remove the surfactant (CTAB), the as-synthesized material was calcinated at 550^{0}C for 6 hrs. To protect the silica nanobeads from environmental humidity, the calcinated powder was stored in an airtight vial. Fig.6.3.a shows the improved morphology of the silica nanobeads. The average diameter ($\overline{D}$) measured for 300 random silica nanobeads using the ImageJ software[199,200] and fitted with a normal distribution curve was found 297.40 nm with the standard deviation (S.D.) of ±38.24 nm [Fig.6.3.b]. The average values of the silica nanobeads with the standard deviations are very close to 300nm aimed for the nanolithography process.

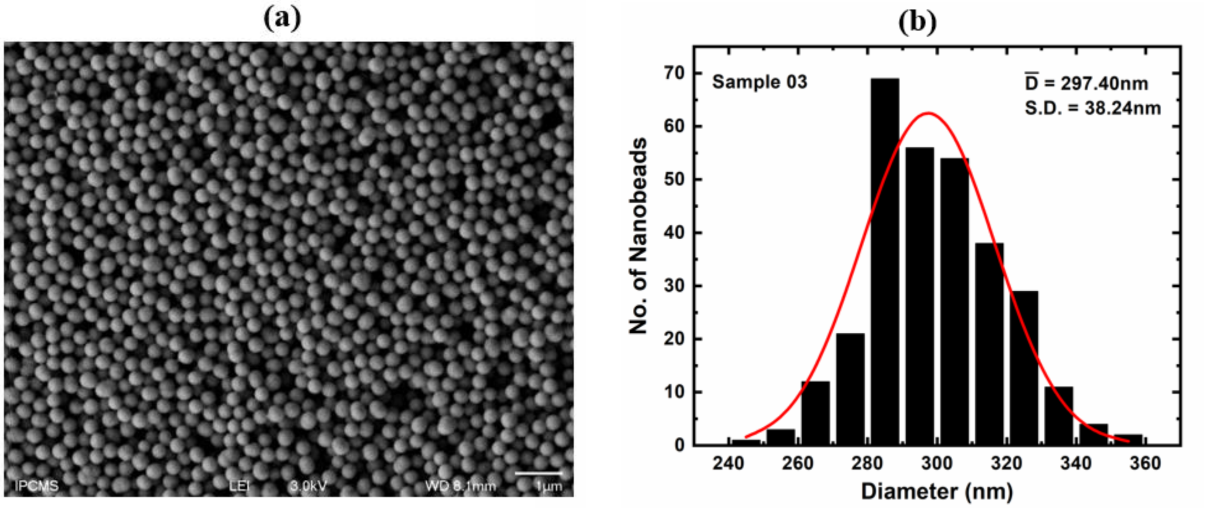

Figure 6.3. Optimization of size and dispersion of silica nanobeads. (a) SEM image shows monodispersed silica nanobeads, **(b)** Average size of the synthesized silica nanobeads calculated using normal distribution fitting for the extracted values from ImageJ software[199,200]. The average size ($\overline{D}$) of the synthesized silica nanobeads was found to be 297.40nm with the standard deviation (S.D.) of 38.24nm.

As was said earlier, the motivation behind synthesizing these silica nanobeads is to use them as a shadow mask for the fabrication of the vertical nanopillars. During the dry etching step (Ar^+ ion milling), these silica nanobeads placed on the top surface (capping layer) of a trilayer hybrid stack preserve the structure underneath, thus turning the trilayer stack into an array of vertical nanopillars. To complete the electrical circuit across these nanopillars the top electrode must fall on top of them. To make this happen, the precise positioning of both the silica nanobeads on the top surface (capping layer) of the tri-layered hybrid stack and the top electrode deposition must be done very precisely and carefully. The schemes for the precise positioning of the silica nanobeads are described in Section 6.4, and Section 6.5, while the alignment of the top electrodes is discussed in Section 6.3.4.

6.3 Nanobead process

To craft the vertical nanoscale pillars out of the capped hybrid trilayer stacks we performed a four-step lithography process called the nanobead process[201]. These four steps are: (i) Nanobead dispersal (ii) Ar^+-ion milling and nanopillars' definition, iii) device passivation and lift-off process, and iv) metallization process for the top electrodes.

6.3.1 Step I: Nanobead dispersal

In this step, the dry silica nanobeads are dispersed on the top surface (capping layer) of the hybrid trilayer stack using the dry deposition technique as explained in Section 6.3.1.1. The Step-I of the nanobead process performed on a hybrid trilayer stack is schematized by Fig. 6.4. The dark gray colored structure represents the substrate Si|SiOx, while the sky-blue colored C shape structure is the trilayer hybrid stack containing two FM electrodes (sky-blue colored), organic spacer layer (dark yellow color), and the nanobeads of silica (white color tiny spherical structures).

Figure 6.4. Schematic presentation of the nanobead process Step-I i.e., nanobead dispersal. The dark gray colored area represents the substrate (Si|SiOx), while the layers with sky-blue color represent the FM electrodes (top and bottom). The sandwiched dark yellow colored layer represents the organic molecular layer (or the spacer layer). The white spherical-shaped objects on the top surface (capping layer) of the hybrid trilayer stacks are the silica nanobeads, that will be used as a shadow mask to define the cross-section of the vertical nanopillars during the Ar+-ion etching step (Step-II).[33]

6.3.1.1 Dry deposition

This is the very first technique used by our research group to deposit the silica nanobeads on the top surface (capping layer) of the trilayer hybrid stacks. In this technique, developed by Dr. Etienne Urbain[201], the pre-processed silica nanobeads in the dry powder form are kept in a petri dish (silica nanobead reservoir) and the sample is kept facing downwards above it. This whole setup is placed in the ultrasonication bath, and an ultrasound pulse is applied to deposit the silica nanobeads onto the sample surface. By optimizing the distance between the sample and the nanobead reservoir, ultrasonic power, and ultrasonic pulse duration, the number of nanobeads deposited on top of the sample surface (capping layer) can be qualitatively controlled. A representative picture of the capped hybrid trilayer stack with nanobeads deposited on the top surface (capping layer) using the dry nanobead dispersal technique is shown in Fig. 6.5.

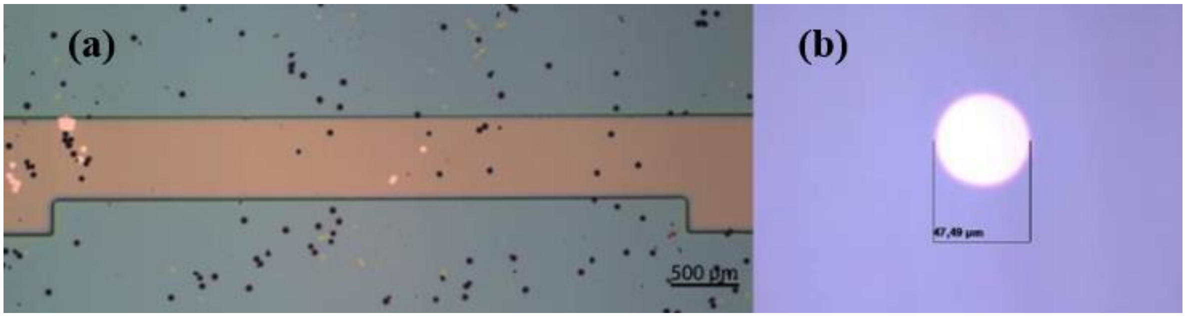

Figure 6.5. Dry nanobead dispersal. (a) a representative microscopic image of the dry bead process performed on a capped hybrid trilayer stack with **(b)** polystyrene microbeads of the size of approx. 45µm**.** The figure is taken from ref [201].

After optimizing the deposition parameters, the refined dry deposition technique was used to fabricate the hybrid nanopillars of 500nm cross-section, the experimental findings on which are described in Chapter-7. Although the dry deposition technique produces working nanopillars, since there is no control over the number of the nanobeads and their precise location on the top surface (capping layer) of the hybrid trilayer stack therefore this can result in parallel junctions underneath a top electrode [Section 6.3.4]. To control the number of silica nanobeads during the deposition process, the sample was covered with two copper TEM grids placed in crossed geometry acting as a sieve. Although this modification avoids bigger agglomerates of silica nanobeads from reaching the sample surface, this does not reduce the number of silica nanobeads adsorbed on the sample surface significantly. The second issue i.e., positioning silica nanobeads on the sample surface at the desired location, however, could not be resolved in the dry deposition scheme.

The Step-I of the nanobead process is one of the most crucial steps in nano junction processing. The main challenges associated with Step-I are: to deposit the silica nanobeads as a shadow mask and to control their quantity and location on the top surface (capping layer) of the hybrid trilayer stack. To overcome the abovementioned shortcomings of the dry nanobead deposition scheme, I have used AFM-nanomanipulations [Section 6.4] and developed a microfluidic pen lithography technique [Section 6.5].

6.3.2 Step II: Ar$^+$-ion milling and nanopillars' definition

In this step, the capped hybrid trilayer stack with the shadow mask (silica nanobeads) on the top surface (capping layer) is now etched down to the mid of the spacer layer (organic molecular layer). The Step-II of the nanobead process is schematically presented in Fig. 6.6. After a multistep Ar$^+$-ion milling process the nanobead dispersed capped hybrid trilayer stacks are turned into an array of the vertical nanopillars. The nanopillars are the preserved structures underneath the silica nanobeads, while the rest of the area is etched out down to the middle of the organic molecular (spacer) layer. The etching is done in the Ar$^+$ -ion/plasma milling chamber with subsequent depth profiling using the elemental analysis of the Auger electron spectroscope. For a detailed description of both the techniques i.e., Ar$^+$ ion etching and Auger electron spectroscopy, please have a look at Chapter-2.

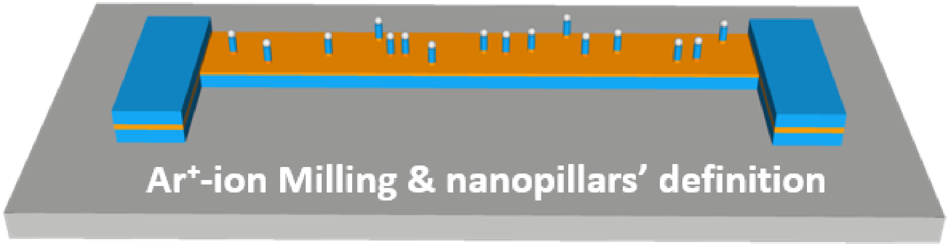

Figure 6.6. Schematic presentation of the nanobead lithography Step-II. During the Ar+-ion milling process, the silica nanobeads preserve the structure underneath thus turns the capped hybrid trilayer stack into an array of vertical nanopillars.[33]

A series of Auger scans collected after Ar$^+$-ion etching steps performed for a representative capped hybrid trilayer stack: Si|SiO$_x$||Cr(5)|Fe(50)|C60(2ML)|CoPc(3ML)|C60(5ML)|Fe(10)|Cr(100) structure is shown in Fig. 6.7. For the capped hybrid trilayer stack mentioned above, the numbers inside the small bracket denote the thickness in nm for the corresponding material/layer while ML is used as an abbreviation for monolayer. In Fig. 6.7, panel (a) shows the Auger scan performed after a five-step etching of a total of 95 min (30min+15min+15min+15min+20min) with the calculated total etching dose of ~93.97 mA.min. The high etching dose observed for panel (a) is obvious due to the large thickness of 100nm of the Cr capping layer. It was found that even after etching for more than 95 mins the capping layer (Cr) has not been completely etched out. The capped hybrid trilayer stack was further etched with a three-step etching process of a total of 29 mins (20 min+5min+4min) with a calculated total etching dose of ~25.18 mA.min, showing the signal of the molecular spacer layer (CoPc) and bottom electrode (Fe) as shown in the panel (b). To etch the molecular spacer layer down to its middle layer, a two-step etching process of a total of 6 min (2.5min+3.5min) with a total etching dose of ~6.39 mA.min was performed. This final etching is shown in panel (c), with an increased spectral weight of Fe (bottom electrode) combined with a decrease in C spectral that suggests that the etching has reached the mid-layer of the organic spacer layer.

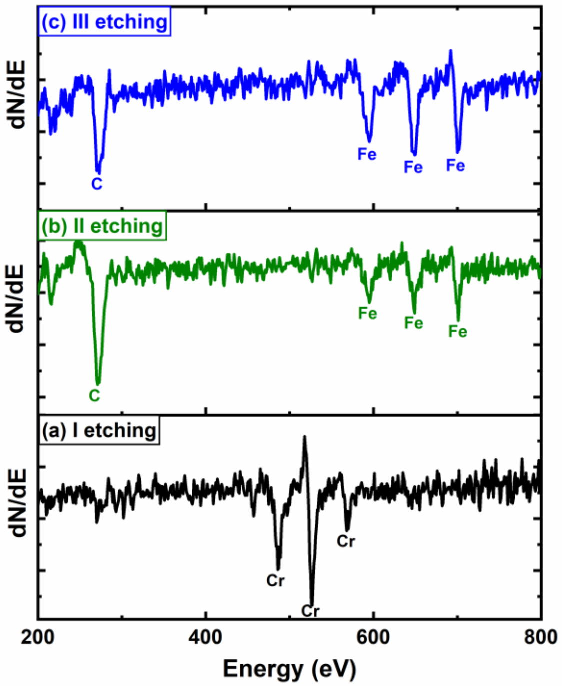

Figure 6.7. 1st order intensity derivative of Auger signal. after the subsequent etching of inorganic multilayer stack Si|SiO$_x$||Cr(5)|Fe(50)|C60(2ML)|CoPc(3ML)|C60(5ML)|Fe(10)|Cr(100) with silica beads of 350nm deposited on top surface (capping layer) using the microfluidic pen lithography technique [Section 6.5]. The numbers inside the bracket represent the thickness in nm. For clarity, only the highest intensity peaks are highlighted. The peaks at [272] eV, [489, 529, 571] eV, and [598, 651, 703] eV, and corresponds to C, Cr, and Fe respectively, with the highest intensity peaks at 272 eV, 529 eV, and 651 eV for C, Cr, and Fe respectively.

The Step-II of the nanobead process is schematically presented in Fig. 6.7. After a multistep Ar$^+$-ion milling process the nanobead dispersed capped hybrid trilayer stacks are turned into an array of the vertical nanopillars. The nanopillars are the preserved structures underneath the silica nanobeads, while the rest of the area is etched out down to the middle of the organic molecular (spacer) layer.

6.3.3 Step III: Passivation layer deposition and lift-off process

To protect the vertical nanopillars (formed after the etching Step-II) from short-circuiting, a thin passivation/encapsulating layer of insulating/dielectric material is to be deposited. During this step, the thin passivation layer covers all the etched area therefore in addition to the passivation also provides static stability to the vertical nanopillars. However, during the process of passivation, the silica nanobeads used as a shadow mask (in Step-I) also get buried underneath the thin passivation layer. To lift-off these buried silica nanobeads, we have developed a solvent-free dry lift-off process. The dry lift-off process that we have developed uses the blow of inert Ar gas to flush-off the silica nanobeads. The Step-III of the nanobead process is schematically presented by Fig. 6.8.

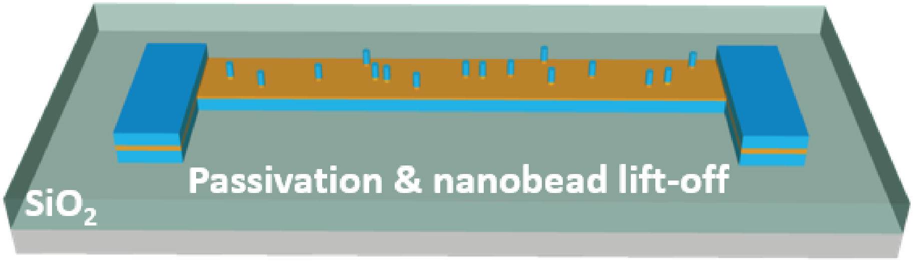

Figure 6.8. Schematic presentation of Step-III of the nanobead process. In this step, a thin dielectric layer of silica (SiO_2) was deposited to protect the nanopillars from short-circuiting. After the deposition of the passivation layer, to electrically access the nano junctions through the top electrodes (will be deposited in Step-IV), the buried nanobeads are lifted-off using Ar gas blow.[33]

This dry lift-off process only works when the thickness of the passivation layer is either equal to or less than the radius (half of the diameter or the size) of the silica nanobeads and can be written mathematically as: $t_{\text{passivation layer}} \leq D/2$, where $t_{\text{passivation layer}}$ and D is the thickness of the passivation layer and the diameter of the silica nanobeads respectively. This situation is schematically represented by Fig. 6.9.

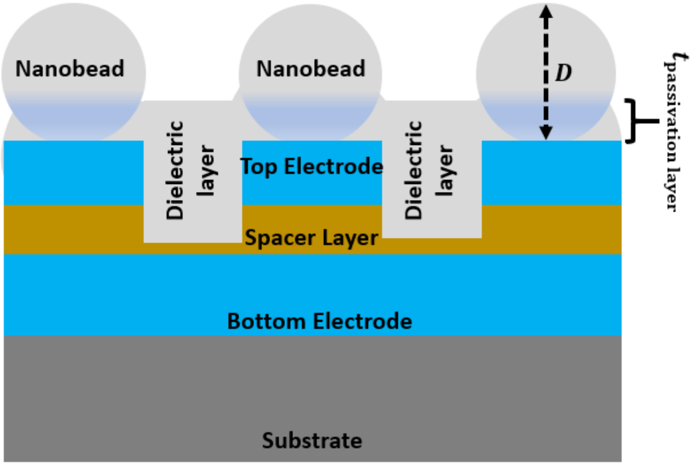

Figure 6.9. The front schematic view of the etched trilayer stack after the passivation process.

Further, the thickness of the passivation layer cannot be reduced on the cost of its dielectric property. Due to the unavailability of the atomic layer deposition (ALD) technique at the time this experimental work was performed, we had to use sputtered silica (SiO_2) thin film for the passivation layer. From a series of experiments, we have found that the room temperature sputtered silica thin films exhibit a measurable leakage current at V=80V below 110nm of film thickness. The constraint arising due to the dielectric property as a function of passivation layer film thickness limits our freedom to scale down the cross-sectional area of our vertical nanopillars below 220nm (in terms of radius 110nm). However, for a safer side and easy lift-off process, we have used silica nanobeads of 300nm (in terms of radius 150nm) shadow mask for the 130nm of silica thin film as a passivation layer. The passivation is done at room temperature by depositing 130 nm of SiO_2 layer using an RF sputtering system (EVA 300+).

6.3.4 Step-IV: Metallization process

After the successful lift-off process, the sample was covered with a laser-cut shadow mask made of aluminum. The aluminum mask was fixed and placed on the top surface (capping layer) of the sample in such a way that the processed nanopillars just reside underneath the transparent structures. The mask-covered sample was then placed inside the electron beam evaporator (Plassys MEB 550S) machine. A thin metallic layer deposition of Al110nm/Au35nm through the shadow mask thus patterns top electrodes. These top electrodes are patterned in a perpendicular geometry to the bottom electrode. The final picture after the metallization step of the processed hybrid trilayer stack turned into arrays of vertical nanopillars is schematically shown by Fig. 6.10.

Figure 6.10. Schematic presentation of Step-IV of the nanobead process. After the successful lift-off process, the top electrodes were deposited using the shadow mask. The top electrodes are shown with the structures with yellow color.[33]

The metallization step completes the nanobead process. The devices are now ready for electrical measurements. For the electrical measurements, the electrical contacts can be made either in 2-point or 4-point geometry using the wire bonder machine.

6.4 AFM-nano manipulations

To resolve the underlying issues with the previously mentioned dry deposition technique [Section 6.3.1.1], the atomic force microscope (AFM)-assisted nanomanipulation scheme was implemented. In this scheme the silica nanobeads are deposited on the top surface (capping layer) of the trilayer capped hybrid stack using the dry deposition technique mentioned earlier, Then, the number of the silica nanobeads and their location on the top surface (capping layer) of the stack can be controlled by an AFM-tip.

Atomic force microscope (AFM) is a surface characterization tool that uses the atomic force between the sample surface and the sharp AFM-tip connected to the flexible cantilever, to image the topography of the sample. During the AFM-operation the tip-sample force ($\vec{F}$), which is the sum of a positive repulsive force ($\propto r^{-12}$, r being the distance between the tip and the sample) and a negative attractive force ($\propto r^{-6}$), causes deflections in the cantilever. The tip-sample force can be written mathematically as:

$$\vec{F} \ = (A.r^{-12} - B.r^{-6})\,\hat{r} \tag{33}$$

Where A and B are the repulsive and attractive force constants and $\hat{r}$ is the unit vector along the direction of the tip-sample force ($\vec{F}$). To record the cantilever deflection, laser light is shined on the back of the cantilever. The light reflected by the cantilever contains the information of the sample topography and subsequently decoded into an image by a photo-sensitive diode. A schematic picture of the AFM is shown in Fig. 6.11.

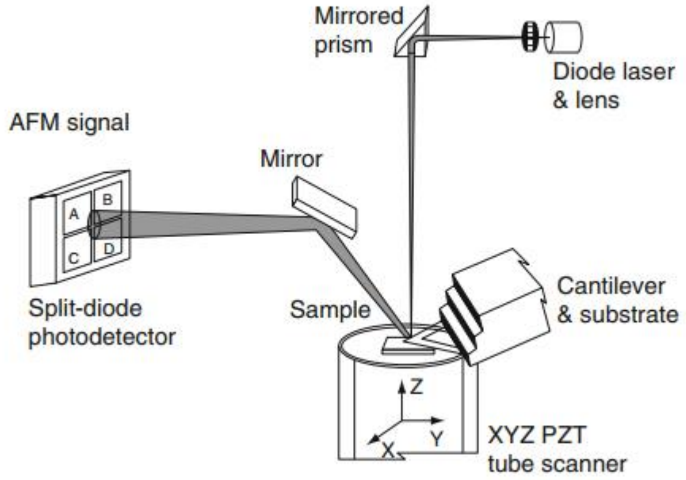

Figure 6.11. A schematic diagram of the Atomic Force Microscope (AFM). The tip-sample force is sensed by the deflections in the cantilever. To decode the deflections in the cantilever the laser light reflected is decoded into an image by the photosensitive diode. The figure is adapted from ref [202]

From equation (33) it is clear that, the tip-sample force ($\vec{F}$) is highly dependent on the tip-sample distance (r). Furthermore, depending upon the tip-sample separation (r), the AFM can be operated either in *contact* or *non-contact mode*. In contact mode, the AFM-tip remains in contact with the sample surface, causing a strong positive repulsive force (r^{-12}) on the cantilever. The contact mode provides the higher resolution images but at the same time causes damage to the sample surface. To avoid any possible damage to the sample surface from the AFM-tip in the contact mode, the non-contact mode is used. In non-contact mode, the AFM-tip remains at a certain distance away from the sample surface. The increase in the tip-sample distance in the non-contact mode thus causes the attractive force (r^{-6}) dominant, causing cantilever bending towards the sample surface. The non-contact mode although protects the sample surface from the AFM-tip but suffers due to the poor resolution.

To achieve higher resolution images without destroying the sample surface, the dynamic mode is used. In the dynamic mode, the AFM-tip remains at a certain small distance from the sample surface but oscillates along the z-direction. The dynamic mode can be achieved either by *amplitude* *modulation* (AM) or *frequency modulation* (FM). In the present work, the probe oscillation amplitude is used to control the feedback loop during the imaging step, while the manipulation step is achieved by reducing both the *amplitude setpoint* and the reactivity of the *feedback control* until a threshold for the particle movement has been reached. This particular kind of dynamic mode is known as the *tapping mode*. Since these silica nanobeads are loosely bound to the surface of the capped hybrid trilayer stack, they can therefore be displaced or moved laterally by the AFM-tip in *tapping mode.* The *amplitude setpoint* parameter defines the distance between the AFM-tip and the surface. Therefore, to not destroy both the sample and AFM-tip, the parameter must be optimized carefully. During the experiments, we have changed this parameter in a step of ±10% from the previously selected value. The feedback control mainly consists of two parameters: *integral gain*, and *proportional gain*. Both integral gain and proportional gain determine the interaction between the AFM-tip and the adsorbed silica nanobead on the sample surface. It has been found that, compared to the *proportional gain*, the *integral gain* has more impact on the nanomanipulation process. I acknowledge one of our collaborators Dr. Mircea Rastei from the Department of Organic Materials (DMO) of CNRS-IPCMS for his guidance and for allowing me to perform the AFM-manipulations in his laboratory. The AFM-nanomanipulation process is schematically presented by Fig. 6.12.

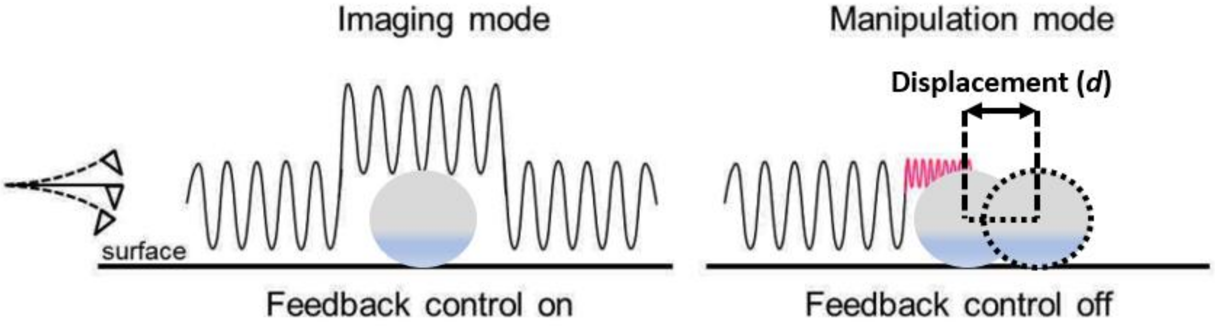

Figure 6.12. Schematic representation of the AFM-nanomanipulation achieved in tapping mode. During the imaging process, the feedback remains ON, while the lateral manipulation/displacement (d) is achieved by turning OFF the feedback control. The figure is adapted from ref [203].

In this AFM-based nanomanipulation scheme, we have used the following two strategies: i) wiping out the undesired silica nanobeads from the sample's surface by selecting a large manipulation area of 10µm, followed by ii) manipulating a single silica nanobead on the surface. The details of which are presented below:

6.4.1 Wiping out the undesired silica nanobeads

Figure 6.13 shows the displacement of the adsorbed silica nanobeads on top of the sample's surface (capping layer). The brown part represents the sample surface while the adsorbed nanobeads are represented by the white spherical shape-like objects. By proper tuning, the feedback parameters including the amplitude setpoint, the silica nanobeads in panel (a) were shifted towards the right direction [panel(b)]. Continuing the manipulation process over a large area of 10µm, we have reached the situation where most of the silica nanobeads have been moved towards the boundary on the right-side [panel (c)] and fewer silica nanobeads in the middle portion. Panel (d) shows the remaining silica nanobeads adsorbed on the sample's surface.

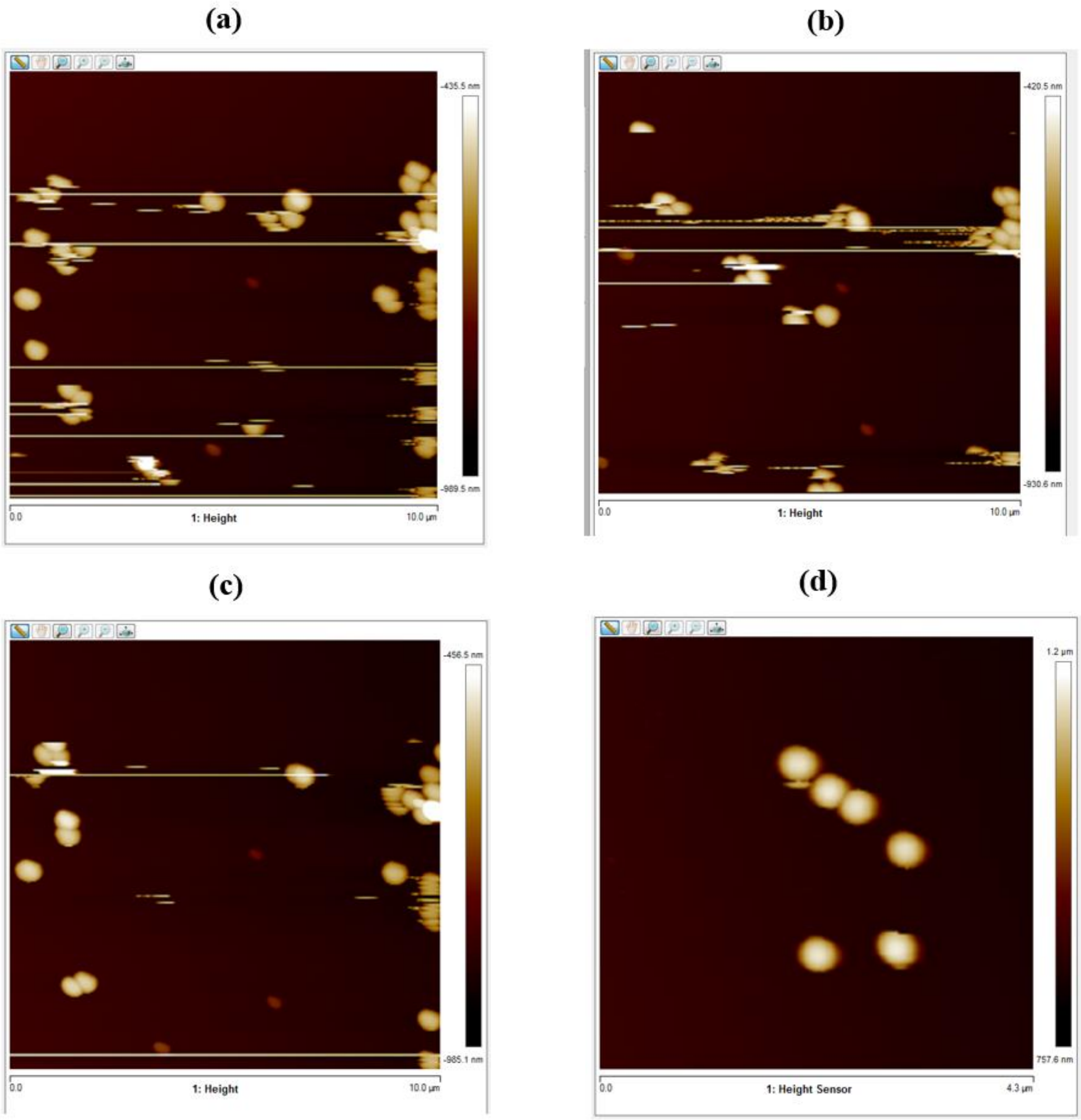

Figure 6.13. AFM images collected on the panel (d) after a series of lateral manipulations performed and on silica nanobeads of ~300 nm size loosely bound to the top surface (capping layer) of the capped hybrid trilayer stack shown by the panel **(a, b, c)**,

Comparing the initial distribution of adsorbed silica nanobeads [panel (a)] to the final situation [panel (d)], a significant reduction in the number of adsorbed nanobeads has been observed.

6.4.2 Manipulating a single silica nanobead

On applying the AFM-nanomanipulation techniques discussed in the previous subsection on a reduced scan/manipulation area of approximately 4x4μm^2 on the sample surface, we were able to move an adsorbed silica nanobead up to 1.45μm along the in-plane (*x*-*y*) direction. Fig. 6.14 shows the AFM images of the adsorbed silica nanobeads before [panel (a)] and after [panel (b)] the AFM-nanomanipulation scheme was implemented.

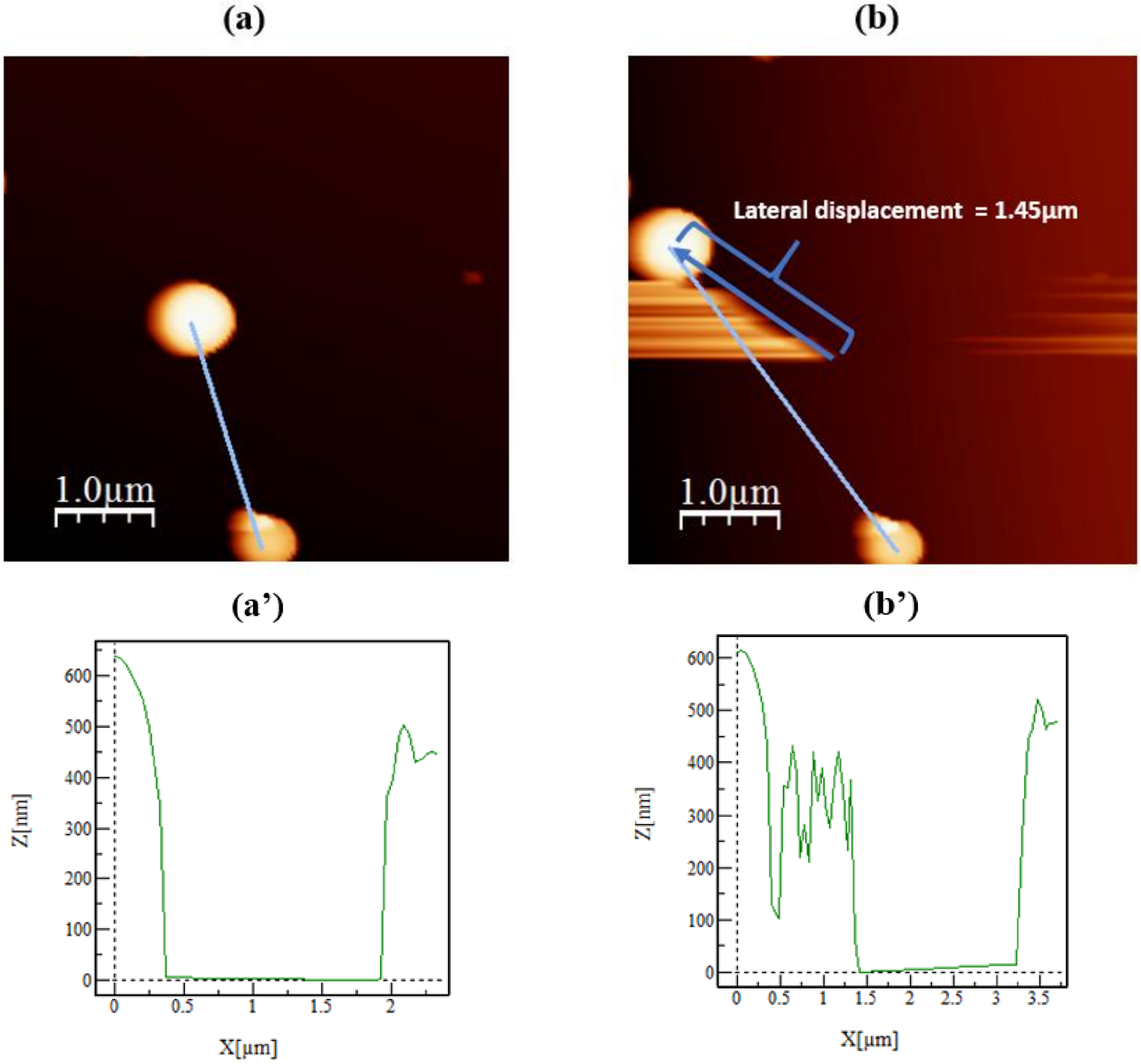

Figure 6.14. AFM image of a silica nanobead (a) during the imaging process, and **(b)** after the lateral manipulation, and calculated distance between the two nanobeads **(a')** during the imaging process and **(b')** after the lateral manipulation. The lateral manipulation displacement (*d*) of 1.45μm thus corresponds to approximately 5 times the size of the silica nanobead of 300nm size.

Using WSXM software[204], the distance between the two adsorbed silica nanobeads was calculated for both before and after the nanomanipulation. The distance before the nanomanipulation was found 1.55µm, while after performing the nanomanipulation it was found to be 3.00µm. This displacement of 1.45µm achieved after the AFM-nanomanipulation corresponds to approximately 5 times the size of a 300nm silica nanobead. Although the AFM-nanomanipulation technique was found to be very effective for laterally displacing the silica nanobeads adsorbed on the surface (capping layer) of a capped hybrid trilayer stack, for a stack with a comparatively large surface area, this is a very time-consuming process. This difficulty for the samples with larger surface areas arises due to the smaller scanning size (max ~10µm for good quality scans) and larger scan time (approx. 25-40 minutes for each scan) taken by AFM during both imaging and manipulation processes. To overcome this issue, we propose a nanomanipulation scheme done along the z-direction. In this process, AFM-tip would be used to pick a single silica nanobead from the reservoir and could be placed over the desired location on the top surface (capping layer) of the capped hybrid trilayer stack. We also tried in this direction but due to time constraints were not able to develop this approach.

6.5 Microfluidic pen lithography technique

As an alternative to AFM-manipulation, we developed a microfluidic technique in which a single silica nanobead is deposited over the desired location on the top surface (capping layer) of a capped hybrid trilayer stack. This technique utilizes the microfluidic principle to precisely place a single silica nanobead (serves as a shadow-mask) on the desired location on the top surface (capping layer) of the capped hybrid trilayer stack. The control over the number of silica nanobeads to be deposited is done with the help of a fine micropipette attached to the commercially available microinjector. The selection of the deposition location is done by the manual/semi-automatic manipulator and movable sample stage. The in-house developed setup of the microfluidic pen lithography is shown in Fig. 6.15.a, and its operation is schematized in Fig. 6.15.b. The manual/semi-automatic manipulator holds the micropipette while the sample stage holds the capped hybrid trilayer stack on which the deposition of silica nanobead is to be performed. Both manual/semi-automatic manipulator and sample stage have the translational degree of freedom in the *x-y* plane and the rotational degree of freedom of 360^0 at *y-z* and *x-y* planes, respectively. The entire process of the silica nanobead deposition is carried out under the optical microscope/digital camera with a sufficiently large working distance.

The size of the silica nanobead is chosen according to the junction size required. These silica nanobeads can be synthesized by optimizing the reaction parameters as mentioned in Section 6.2. The calcinated silica nanobead powder is dispersed in ethanol. Ethanol inhibits silica nanobeads from growing further and also acts as a carrier to flow within the micropipette. This parent solution needs to be further diluted in such a way that a single droplet of the solution ejected out from the micropipette contains only one silica nanobead. Since ethanol has a very low viscosity (~1.074 mPa.s at room temperature) therefore, to avoid the spilling of the droplets on the sample surface, we added 3ml of glycerol (viscosity~1.412 Pa.s at room temperature) into the 15ml ethanol solution containing nanobeads.

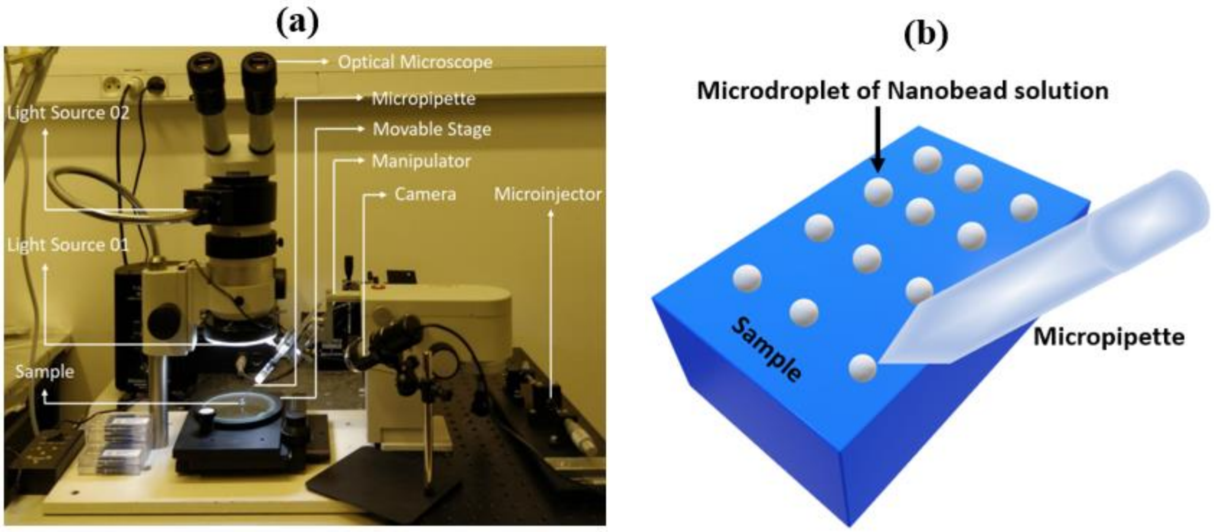

Figure 6.15. In-house developed 'microfluidic pen lithography' setup. (a) The in-house developed setup of microfluidic pen lithography, and **(b)** Schematic presentation of the working principle of microfluidic pen lithography

This ejected droplet of a few µm size (or picolitre volume) from the micropipette is placed on the desired location on the top surface (capping layer) of the capped hybrid trilayer stack and dried at a nominal applied temperature (~50^0C). After removal of the solvent during the drying process, the remaining adsorbed silica nanobeads act as a shadow mask. Note that we are using an organic solvent here, but in picolitre volume and atop the metallic capping layer of the heterostructure stack.

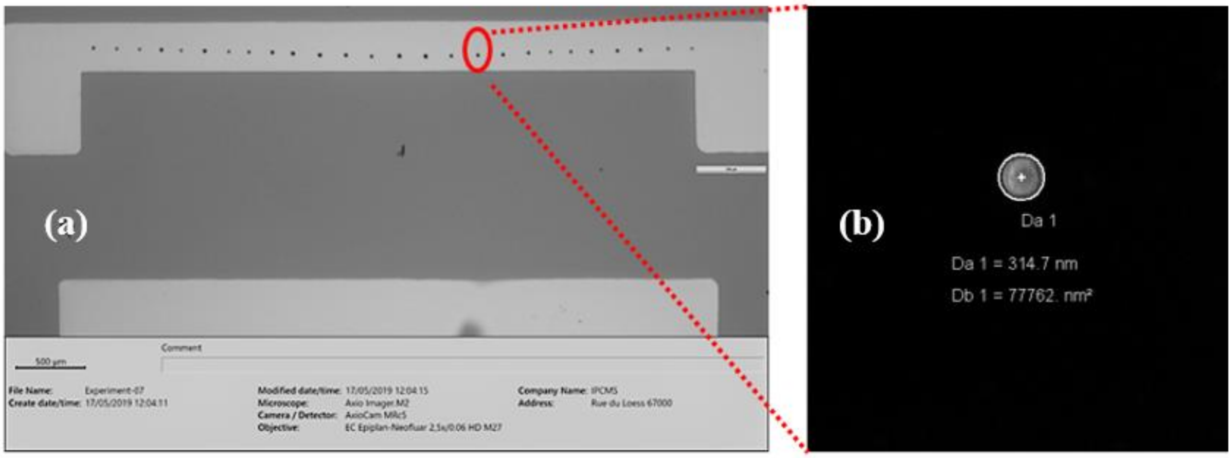

File Name: Experiment-07
Create date/time: 17/05/2019 12:04:11
Modified date/time: 17/05/2019 12:04:15
Microscope: Axio Imager.M2
Camera / Detector: AxioCam MRc5
Objective: EC Epiplan-Neofluar 2.5x/0.06 HD M27
Company Name: IPCMS
Address: Rue du Loess 67000

Figure 6.16. Controlled nanobead dispersal using 'microfluidic pen lithography'. (a) Optical image of the capped trilayer hybrid stack, after performing microfluidic pen lithography. In the image, the dark gray surface represents the Si|SiOx substrate while the lighter gray C shaped structure is the capped hybrid trilayer stack already pre-patterned into a lower electrode using shadow-mask disposition. The black dots on the capped trilayer hybrid stack are the micron size droplets of (picolitre volume) of the solution containing silica nanobead of ~300nm size. **(b)** SEM image of the nanobead left after the evaporation of the microdroplet.

This highly localized droplet deposition technique thus prevents the entry of the solvent into the molecular layer (spacer layer) from both the top surface (capping layer) and from the lateral sides of the capped hybrid trilayer stack. A representative optical image of the capped hybrid trilayer stack on which this lithography technique has been performed is shown in Fig. 6.16. In Fig. 6.16, the area with dark gray color represents the Si|SiOx substrate while the C type structure with white color is the capped hybrid trilayer stack, deposited through the laser cut SS bottom electrode mask in the ultra-high vacuum multi-chamber cluster facility. The islands with black color are the micron-sized droplets of picolitre volume containing silica nanobeads (shadow mask for defining the vertical nanopillars). The black color of the droplets is due to the reflection of light on the sample background. We have optimized the concentration of the solution in such a way that each micron-sized droplets of picolitre volume carry only one silica nanobead [panel (b)].

I must thank and acknowledge one of our collaborators Professor Bernard Doudin from Department of Magnetic Nanoobjects (DMONS), CNRS-IPCMS for providing me all the necessary equipment required to design and develop the microfluidic pen lithography setup.

6.6 The success rate of the microfluidic pen lithography technique

We performed the nanobead process using the microfluidic pen lithography technique on a series of capped hybrid trilayer stacks and found a good success rate of ~15%. We have considered only those devices as working devices which has the junction resistance more than that of the entire bottom electrode plus the resistance of the respective top electrode.

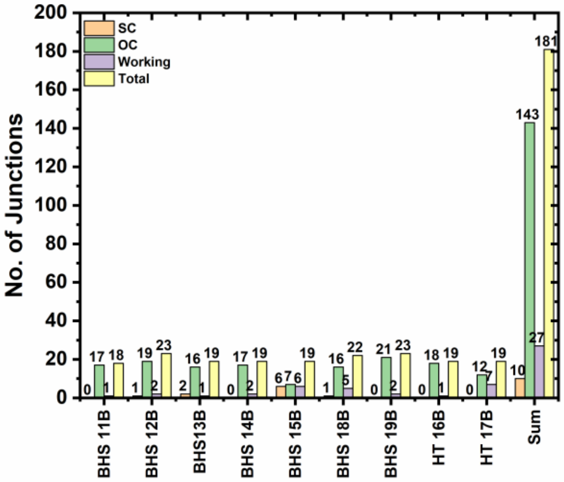

Figure 6.17. The success rate of ‘microfluidic pen lithography’ technique. Graphical representation of the prober results for the nanopillars fabricated from a series of capped hybrid trilayer stacks. The X-axis represents the beads processed capped hybrid sample, while the Y-axis shows the frequency of short-circuited (pink), open-circuited (green), working (purple) and total (yellow) nanopillars fabricated from different capped trilayer hybrid stacks.

All these electrical or probing measurements were performed in 4-point contact mode on the prober machine. Before the prober measurements, the Keithley multimeter was also calibrated with the standard resistances. Fig. 6.17, provides a graphical presentation of the prober data for the capped hybrid nanopillars fabricated from a series of capped hybrid trilayer stacks. This success rate is very high compared to the only one working device out of a total of 216 micropillar devices of the MgO/C type samples[29], although processed down by a proven and robust UV-photolithography technique.

6.7 Summary, and perspectives

Comparing the nanobead process performed using AFM-nanomanipulation [Section 6.4] and microfluidic pen lithography technique [Section 6.5] with the uncontrolled dry deposition technique [Section 6.3.1 and Fig. 6.5], a remarkable improvement over the control of the silica nanobeads (position, number) on the top surface (capping layer) of the capped hybrid trilayer stack has been observed. Although the initial motivation behind the development of the nanobead process was to protect the organic molecular (spacer) layer of the hybrid vertical nanopillars from the frequently used photoresists and organic solvents during the conventional nanolithography process (e-beam and focused-ion-beam lithography), it is also possible to craft the nanopillars for the inorganic devices. One such "hybrid scheme", in which the nanobead process is implemented with the UV-photolithography technique for crafting the vertical nanopillars, is shown in Fig. 6.18.

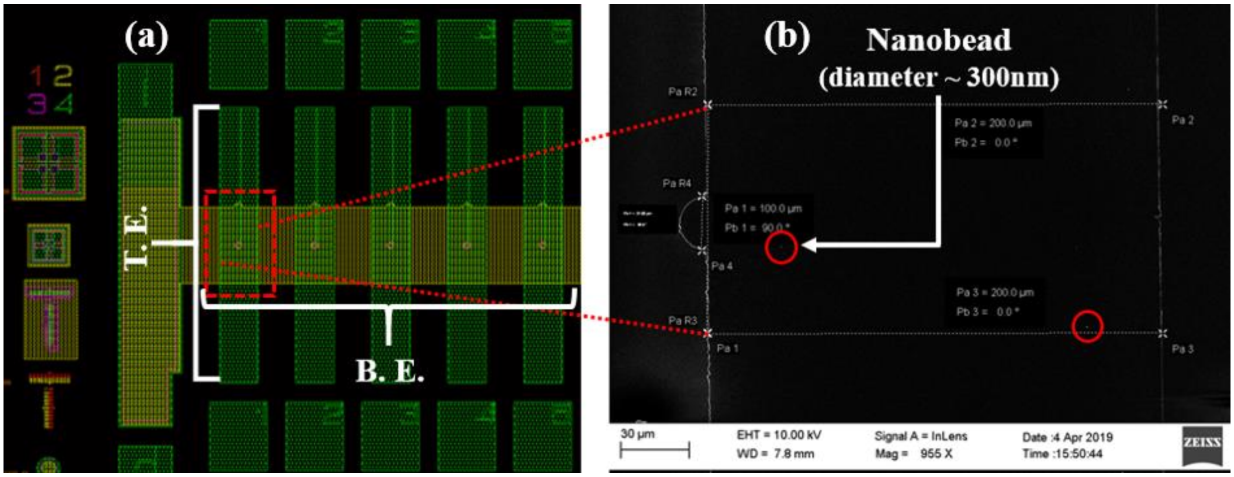

Figure 6.18. Integration of 'microfluidic pen lithography' with UV-Photolithography. (a) Zoomed image of an optical mask containing modified bottom electrodes (yellow-colored horizontal strip, only one presented here out of 10 in 7x5 mm^2) with semicircular identification marks of 24µm diameter at the top corner, and **(b)** The SEM image acquired after the microfluidic pen lithography process, shows the presence of ~300nm silica nanobeads at the cross-section of the bottom electrode (width 200µm) and top electrode (width 100µm, to be deposited in Step-IV lithography step).

It would be worth mentioning here that in UV-photolithography technique, the use of UV-light (λ= 365nm, Hg, i-line which is very large to the wavelength of the electrons ~10Å at 10kV) makes it incapable to pattern the nanoscale devices therefore to craft the vertical nanopillars one has to completely depend on the advanced nanolithography techniques such as the electron beam lithography. The electron beam lithography setup is very costly to purchase and maintain, requires sophisticated labs, skilled manpower, and proper maintenance. In that case, our in-house developed "hybrid scheme" might work as an alternative nanolithography technique. This technique is similar to the UV-photolithography technique as mentioned earlier in Section 2.1 of Chapter-2, except the silica nanobeads, are deposited to pattern the nanopillars. To align the etched nanopillars with the top electrodes, we modified the bottom electrode patterns on the optical mask. The modified bottom electrode's image is shown in Fig. 6.18.a. The additional semicircular geometries crafted on the bottom electrode acts as an identification mark for the locations where nanobeads are to be deposited. Step-III (passivation and nanobead lift-off) remains the same as for the nanobead process while Step-IV (metallization or top electrode deposition) is done using the UV-photolithography technique. Fig. 6.18.b, using the microfluidic pen lithography technique, we were able to deposit almost a single nanobead (if we don't consider the nanobead at the borderline) on the surface area of the 200x100 μm^2. The surface area of 200x100 μm^2 is the maximum allowable area where the nanopillars formed due to the silica nanobeads can be electrically accessed by the deposition of the top electrodes of 100 μm width.

7. Encoding Information on the Excited State of a Molecular Spin Chain

In Chapter-5, we have shown how the electrical transport across the lateral[192,205–209] and vertical solid state devices[153,177,181] including the local probe experiments[23,167,183,184,193–195] can be influenced by the quantum states due to the nanoobjects lying within. This opens-up the possibility of encoding the information in these devices at the quantum level by the electrically generated spin-flip excitations between the electron spins[23,167,183,184,193–195]. However, the short lifetime[26] and no defined magnetic orientation of this electronic state limits its use for technological device applications. We overcome these limitations and experimentally demonstrate the steady-state capability of this electronic state in the nanoscale vertical solid-state spintronic devices[33] fabricated from a trilayer hybrid stack consisting of two ferromagnetic electrodes Co (bottom) and Fe (top) separated by an antiferromagnetic spin chain of cobalt phthalocyanine (CoPc) molecular (spacer) layer. In the excited quantum state, the CoPc molecular spin chain coupled to the ferromagnetic electrodes[165], produces a distinct magnetic unit endowed with a coercive field. This distinct magnetic unit produces a specific steady-state magnetoresistance (MR) trace with an opposite sign to the ground state MR and mimics the differential conductance plot performed for the applied bias range, required to open the spin-flip conductance channel in the CoPc molecular spin chain. These experimental findings, along with the spin excitation transition rules, indicate that the observed excited state MR is originated due to the electrically generated spin-flip excitations in the CoPc molecular spin chain. Furthermore, the experimentally measured thermal energy barrier of ~5.9 meV (corresponding to the thermal energy k_BT at ~70K) between the ground and excited spin-flip state is confirmed by density functional theory (DFT) and a phenomenological theory of macrospin transport. This low-voltage control over a spin chain's quantum state (spin-flip) and spintronic contribution (spin-flip excited state MR) paves the way for transmitting spin wave-encoded information across molecular layers[210] in the solid states device and should augment quantum prospects for the antiferromagnetic spintronics and oxides electronics communities[211].

7.1 Device details

Utilizing the excited quantum state of a molecular spin chain (MSC) to encode the information in a technological way requires a steady magnetic state that can be manipulated independently. To realize this in a solid-state vertical device, a 20nm thin layer of antiferromagnetically coupled MSC formed by the CoPc molecules with S=1/2[23,24] was sandwiched between the Fe (bottom) and Co (top) FM electrodes. Here the ferromagnetic metal (FM) acts as a spin polarizer/analyzer and also used to set the spin referential of a MSC[165,180], whereas the CoPc molecular layer acts as an active spacer, rather than serving as an antiferromagnetic entity to magnetically pin the FM electrode[165] via the exchange bias mechanism[212]. As already discussed in Chapter-5, the MPc molecular thin films are dominated by the intrachain magnetic interactions rather than the very weak interchain interactions[24]. Furthermore, the transport in dielectric devices follows along a nanoscale path[140,213], and is therefore similar to the STM-assembled model junctions[23,26,167,183,184,193–195,206]. It is thus possible to observe the quantum transport effects due to the MSC in a nanoscale trilayer vertical solid-state device. Compared to the STM-assembled model junctions, these nanoscale trilayer solid state devices exhibiting quantum transport effects find their utility in technological device applications.

To fabricate these nanoscale vertical solid-state devices or the nanojunctions, the chromium (Cr)-capped FM|molecular layer|FM trilayer stacks of Si|SiOx||Cr(5)|Fe(50)|CoPc(20)|Co(10)|Cr(5-100) structure were grown in-situ through a C-shaped shadow mask (to define the bottom electrode) at ambient temperature in an ultra-high vacuum multichamber cluster using dc sputtering (metals) and thermal evaporation (CoPc) technique. Prior to deposition, the Si|SiOx|| substrate was annealed at 110°C and left to cool down naturally [Section 6.1, Chapter-6]. To probe the interface quality, the transmission electron microscopy (TEM) characterization was performed using an aberration (image) corrected Titan 80-300 (FEI Company) operated at 300 kV and equipped with a US1000 slow-scan CCD camera (Gatan Inc.). The cross-sectional sample preparation of the stack for the TEM characterization was achieved by focused-ion-beam (FIB) etching with a Strata 400-S (FEI Company). Initial cutting was performed at 30 kV followed by a fine polishing at 5kV with a current of 47pA and subsequently with 2kV and a current of 28pA. Scanning electron microscopy (SEM) imaging of the layers was minimized during the complete preparation procedure. Fig. 7.1.a shows a cross-sectional TEM image of our entire *in-situ* grown Si|SiOx||Cr(5)|Fe(50)|CoPc(20)|Co(10)|Cr(5) stacks. Despite some structural imperfections, the overall cross-sectional TEM image reflects the continuity of our layered heterostructure.

The nanojunctions were crafted from the aforementioned *in-situ* grown stacks using a novel, solvent-and resist-free technique, *nanobead processing*, inspired by nanosphere lithography[32]. The nanobead processing technique is described in Chapter-6 and was implemented using 500nm diameter SiO_2 nanobeads synthesized using a surfactant-mediated sol-gel reaction[198] [Section 6.2, Chapter-6]. The nanobead processing begins with the dispersal of nanobeads on top of the capping layer of the stack [Fig. 6.4, Chapter-6]. To achieve this, the dried silica nanobeads are made to jump by an ultrasonic energy pulse so that they stick on top of the capping layer of the stack via van der Waals interactions. To target only a few (1-3) nanobeads to be statistically present in the ~500x100 μm^2 region of the overlapping bottom and top electrodes, this step's parameters (nanobead powder dispersion in beaker, sample distance, ultrasound energy/time etc.) are calibrated by the scanning electron microscope (SEM). During the dry etching process, these nanobeads serve as a shadow mask to define vertical nanojunctions. Once Ar^+ milling to the CoPc layer is complete [Fig. 6.6, Chapter-6], the sample is encapsulated in sputtered SiO_2 and the beads are lifted-off by the Ar gas blow [Fig. 6.8, 6.9, Chapter-6]. This leaves a sub-diameter access to the nanopillars that can be accessed electrically by the top metallic contacts deposited through a shadow mask, in the final step of the nanobead processing [Fig. 6.10, Chapter-6].

After the nanobead processing, an array of the nanopillars or the vertical solid-state nanojunctions on the processed stack were wire-bonded to a sample chip and placed inside a cryo-free multifunctional magnetotransport bench (BMF). The magnetotransport measurements were performed in 4- point contact mode with applied positive (negative) bias on the top (bottom) electrode. During the transport measurements, the data acquisition time was selected on the order of 1s/point, with 1s between acquisitions.

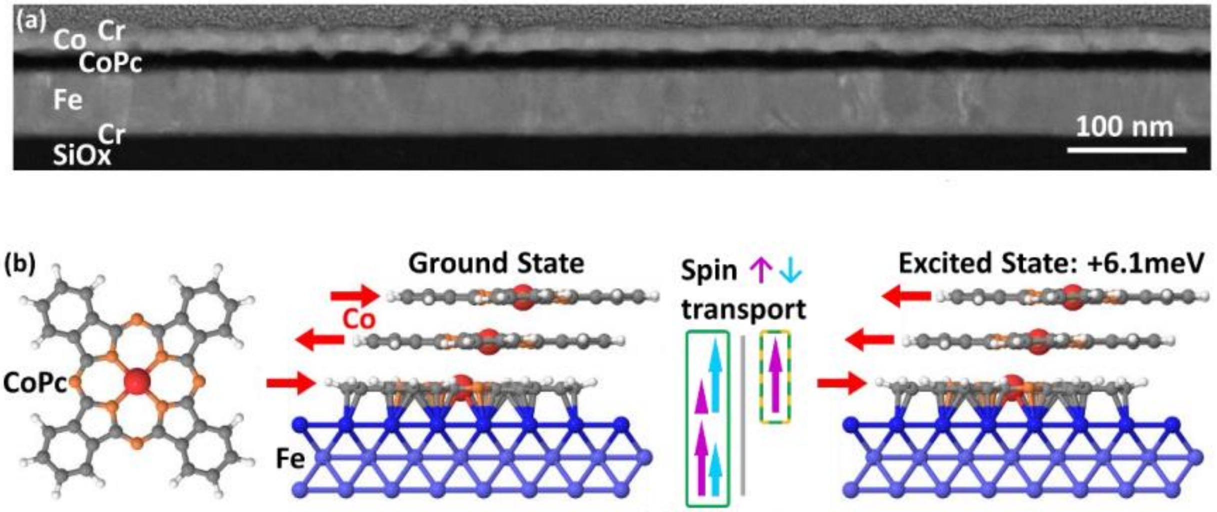

Figure 7.1. Ground and spin-flip excited state of CoPc molecular spin chain. (a) Cross-sectional TEM image of Si|SiOx||Cr(5)|Fe(50)|CoPc(20)|Co(10)|Cr(5) stack. **(b)** CoPc molecular spin chain adsorbed on top of bottom ferromagnetic Fe electrode. Spin-polarized transport across the spinterface and the molecular spin chain, with P<0 in its ground state (larger cyan arrow in the green box), further enhanced with P>0 in its excited state (magenta arrow within the yellow/green box). The ground and excited states of the CoPc molecular spin chain thus contribute to two different MR of reversed sign, $MR_{GS,}$ and MR_{ES} respectively.[33]

The CoPc molecule and spin-polarized transport proceeding from our nanoscale devices' lower Fe electrode across the MSC is shown in Fig. 7.1.b. The length of the magenta and cyan arrows are used to depict the amplitude of the spin ↑ and ↓ channels, respectively. On applying the input current across the device, the unpolarized current first gets converted into the spin-polarized current with a certain spin polarization P by the lower electrode Fe. The spin polarization P of the injected current further passing through the Fe|CoPc spinterface[22] gets modified with the larger value and a reversal in the sign (P<0)[214]. This current, with a modified spin polarization P<0 that then flows across the MSC in its ground state (large cyan arrow in green block), is anticipated to be augmented by a current with P>0[23,167,181,183,195] (large magenta arrow in yellow/green block) due to the spin-flip excitations across the MSc's excited state. The change in the sign of spin polarization P thus gives rise to two types of MR with opposite sign, MR_{GS} and MR_{ES} for the ground and excited state of the MSC respectively, upon flipping the magnetization of the top electrode (Co).

7.2 Electrical and magnetotransport measurements

From the temperature-dependent resistivity measurements (not shown) performed on Fe|CoPc(20nm)|Co nanojunction at 20mV applied bias, the resistance of the junction was found 11GΩ (32kΩ) at 17K (300K). The decrease (increase) in the junction resistance (conductance) with increasing temperature indicates thermally activated hopping transport[215,216] across the 20nm thin CoPc layer. In this section, the electrical and magnetotransport performed on these junctions will be discussed in detail.

7.2.1 Spin-flip excitation

The current-voltage (I(V)) characteristics of the processed nanojunction is shown in Fig. 7.2. The I(V) plot performed at 17K with or without applying the external magnetic field exhibits a conductance kink, after which a huge increase in the conductance is observed. This conductance kink is ascribed to the opening of a spin-flip excitation channel in the CoPc spin chain. This conductance kink was also observed for the I(V)s performed for the same nanojunction for the temperature range 17K < T < 90K and applied an external magnetic field of 2T. These I(V) plots are shown in Fig. 7.3. From the temperature-dependent I(V) measurements performed for the same nanojunction [Fig. 7.3], the bias position of the kink in the I(V) plots due to the spin-flip excitations decreases with increasing temperature. We attribute this to thermal smearing and thermally-assisted hopping effects. The kink disappears for T≈70K, in line with the calculated 5.9meV energy of the molecular spin chain [see Section 7.3].

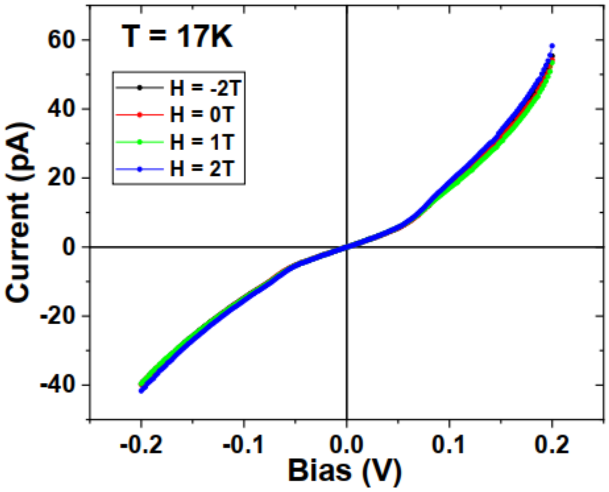

Figure 7.2. **Spin-flip excitation**. I(V) data at 17K for various magnetic field (H) values acquired for the nanopillar of size 500nm crafted from Si|SiOx||Cr(5)|Fe(50)|CoPc(20)|Co(10)|Cr(5) stack.[33]

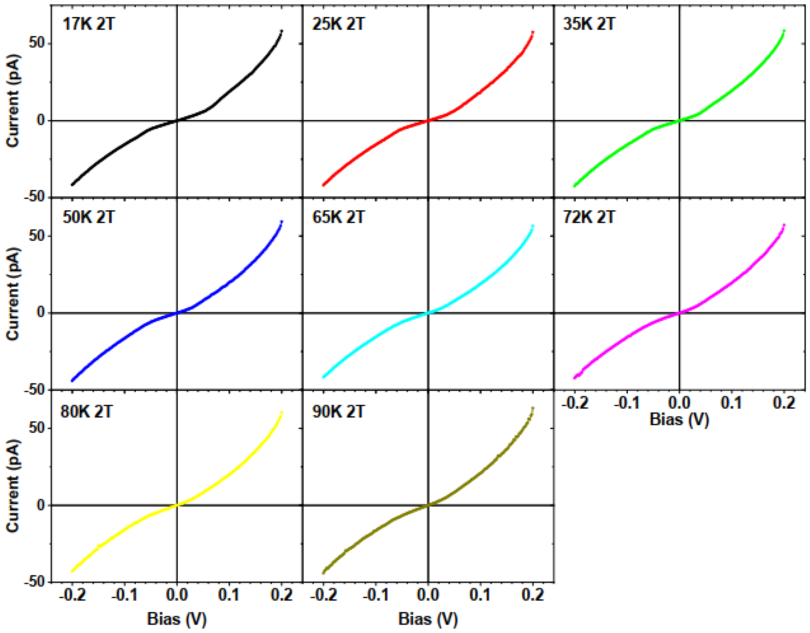

Figure 7.3. Spin-flip excitation. I(V) data at H=+2T for various temperature points (T) acquired for the nanopillar of size 500nm crafted from Si|SiOx||Cr(5)|Fe(50)|CoPc(20)|Co(10)|Cr(5) stack.[33]

However in the I(V)s performed the spectral weight of the conductance kink does not seem sharp therefore for a better resolution, using the same I(V) data the differential conductance (dI/dV) plot were calculated for different temperature range. The differential conductance (dI/dV) plots for the temperature range 17K < T < 90K are shown in Fig. 7.4. These dI/dV plots clearly show the spin-flip excitations in the CoPc molecular layer as a step in the differential conductance. The temperature dependence of the threshold bias (V_{th}, required to induce spin-flip excitations) and the differential conductance (dI/dV) also attains better resolution compared to the I(V) plots.

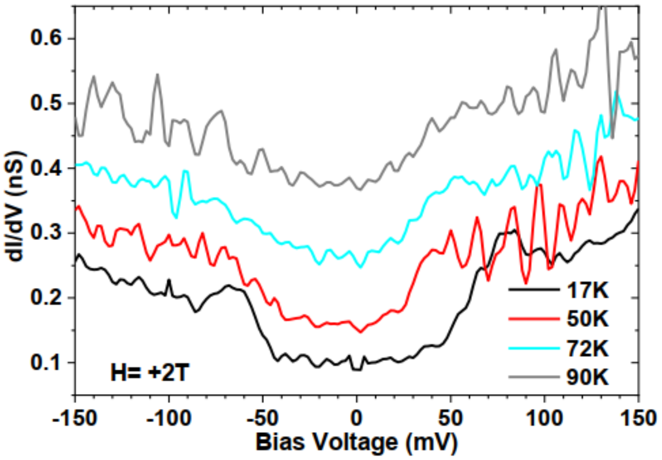

Figure 7.4. Spin-flip excitation. Differential conductance or dI/dV(V) data at H=2T for various temperature points (T) acquired for the nanopillar of size 500nm crafted from Si|SiOx||Cr(5)|Fe(50)|CoPc(20)|Co(10)|Cr(5) stack.[33]

7.2.2 Magnetotransport results at 60K and the identification of three distinct magnetic units

To identify the constituent magnetic units within our device and their role in the transport, we performed the field-dependent resistance, R(H) measurements at 60K. Fig. 7.5.a shows R(H) loops at an applied bias of 58mV, recorded after a field cooling (FC) procedure at H=-1T. The FC procedure helps the antiferromagnetically coupled MSC to align with the external field and allows it to exert its magnetic contribution at the interface with FM metal. As the applied magnetic field (H) is increased towards the positive values, the 1st resistance jump near H = 0 observed, followed by a 2nd resistance change centered around H=1.17T, both of which are reversible as long as the resistance baseline at H=-2T is not exceeded. Further increasing the magnetic field (H) towards the positive side, a 3rd resistance change is observed, and the overall R(H) loop becomes symmetric with respect to the applied field. These three resistance levels correspond to three magnetic configurations of the three magnetic units and are denoted by green and green/yellow arrows Fig. 7.5.a, and Fig. 7.5.b.

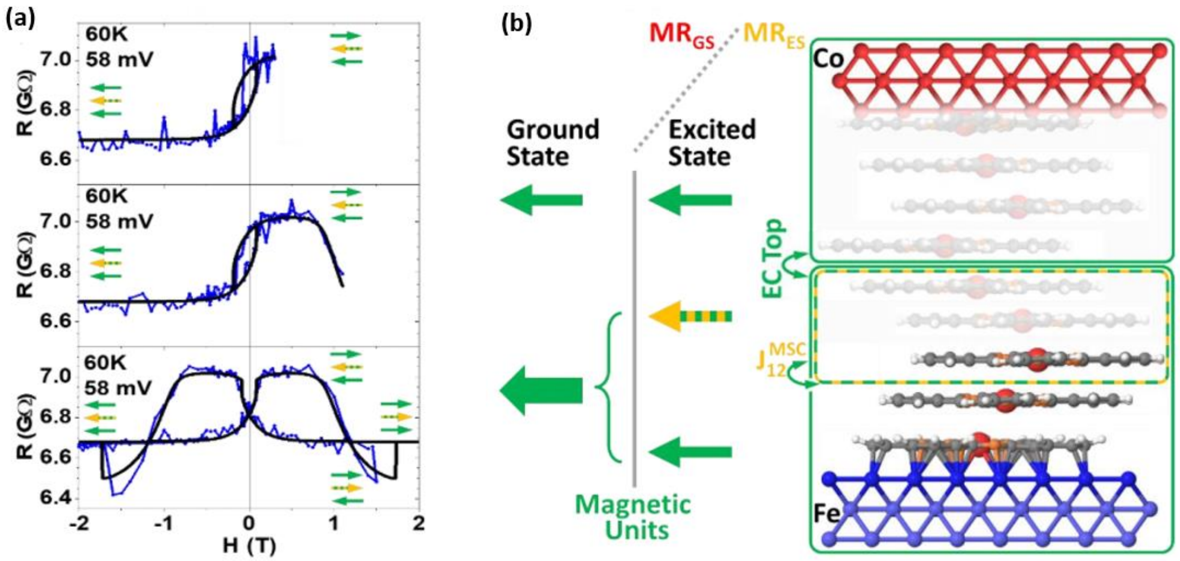

Figure 7.5. Spin-flip magnetoresistance. (a) Magnetotransport measurement performed at T=60K and V=58mV reveal three resistance switching due to the magnetization reversal of three magnetic units (green and green/yellow arrows). **(b)** Schematic of the magnetic units contributing to MR$_{GS}$ and MR$_{ES}$. In the ground state the CoPc molecular spin chain forms a relatively harder unit together with the Fe|CoPc spinterface and the underneath bottom Fe electrode (represented by the bottom large green box that also contains green/yellow box), however, in its spin-flipped excited state, the CoPc molecular spin chain acts as a distinct magnetic unit (represented by green/yellow box and arrow) with a coercive field and contributes only to MR$_{ES}$. The junction's imperfectly controlled portion appears semi-transparent. The macrospin model's coupling terms ECTop and J_{12}^{MSC} between the central and top/bottom units are shown. See the texts for more detail. The fit (shown by black line in panel (a)) was performed using the parameters K_t/M_t =0.26T, θ_{Mt}=60^0, K_b/M_b =4.95T, θ_{Mb}=-4^0, ECTop=-0.05T, J_{12}^{MSC} =1.28T, R$_0$=6.68GΩ, MR$_{GS}$ =-2.4% and MR$_{ES}$ =5.1%.[33]

These three magnetically distinct units that correctly explain the three-resistance levels [see next paragraph] in the R(H) loops [Fig. 7.5.a] are also found to be consistent with the subsequent transport measurements [Section 7.2.3], and are identified in Fig. 7.5.b thanks to an agreement between experiment and density functional theory (DFT) calculations [Section 7.3] and macrospin modeling [Section 7.5].

The 1st resistance jump near H = 0T occurs due to the magnetization reversal of the top magnetic unit [top green arrow in Fig. 7.5.a]. This unit comprises the top Co FM electrode with neighboring CoPc MSC underneath [Fig. 7.5.b]. At the top junction interface (Co|CoPc), the metal atoms are presumed to diffuse[217] into the molecular layer underneath with a different molecular stacking[165] from that of the junction's lower interface (Fe|CoPc). This complex top unit with moderate magnetic anisotropy calculated as per the macrospin modeling [Section 7.5], is schematically represented by a semi-transparent segment within the top green box in Fig. 7.5.b. The reversal of this top unit occurs relative to a magnetically hard unit comprised of the bottom unit (Fe electrode forming spinterface (Fe|CoPc) with the 1st ML of CoPc molecule) and central unit (antiferromagnetic CoPc MSC coupled with the bottom unit through exchange bias mechanism[159,165,179,180,218–221]). In the ground state of the central unit, the bottom and central units collectively represent a single magnetic entity i.e. the hard unit whose well-characterized physical properties can explain our main results. This so-called hard unit is schematically represented in Fig. 7.5.b by the comparatively bigger bottom solid green box containing a yellow-green box within. In its ground state, the magnetization of this bottom hard unit is represented by the solid thick green arrow. However, the antiferromagnetically coupled CoPc MSC, when in its electrically excited state, disentangles from the bottom unit and acts as a distinct steady-state magnetic unit. The electrically excited state of the CoPc MSC is schematically shown in Fig. 7.1.b whereas its presence within our device is conceptualized by the yellow-green arrow and box in Fig. 7.5.b. This central unit has very low magnetic anisotropy and is exchange-coupled to the bottom Fe electrode with exchange energy J_{12}^{MSC}. This exchange energy J_{12}^{MSC} leads to the exchange bias[159,165,179,180,218–221] that can switch the magnetic orientation of the central unit (CoPc MSC) in its excited state at the 2nd switching point $H \approx 1.1T$ [see yellow/green arrow in Fig. 7.5.a].

The 3rd change in the resistance at the higher positive field in Fig. 7.5.a is due to the reversal of the bottom unit comprised of Fe electrode and the spinterface formed between the Fe top layer and the 1st ML of the CoPc molecule, which is represented by the bottom green arrow in Fig. 7.5.a and thin green bottom arrow in Fig. 7.5.b. The exchange coupling between the top and the central magnetic unit is denoted by the ECTop parameter. The spin transport channel proceeding across the spin chain's quantum ground and excited states generate two magnetoresistance terms MR_{GS} and MR_{ES} respectively. In contrast to the MgO-based spintronic devices, the presence of an additional excited state magnetoresistance (MR_{ES}) term opens up the possibilities of these hybrid solid state devices to be used for encoding the information on the spin chain's quantum excited state.

7.2.3 Magnetotransport results at 17K and electrical excitation of the molecular spin chain

To further validate the presence of these aforementioned three distinct magnetic units within our hybrid solid-state device and their relationship with the observed ground state and excited state magnetoresistance, we now examine the magnetotransport measurements performed at 17K. Fig. 7.6.a-e shows the R(H) loops within the applied bias range 20< V(mV) < 80mV, followed by an FC procedure at -1T. Going from T=60K [Fig. 7.5.a] to T=17K [Fig. 7.6.d] causes the R(H) loop at 58mV to no longer be symmetric: the final reversal occurs for |H|>2T. From the magnetotransport measurements performed over the temperature range 17K-50K [see Fig. 7.7], we now define MR_{GS} = [{R(2T)/R(-2T)}-1] and MR_{ES} = [{R(H_f)/R(2T)}-1] [H_f = 1T for 17 < T(K) < 50, and H_f< 1T for T >50K]. A clear picture of the MR_{GS} and MR_{ES} is shown in the R(H) loop plotted at an applied bias of 80mV for the temperature point 17K [see Fig. 7.6.a]. Furthermore, it is clearly visible from Fig. 7.6 that reducing the applied bias causes MR_{ES} to decrease and finally disappear at 20mV. Similar results are obtained for the negative applied bias (data not shown).

The bias dependence of the differential conductance (dI/dV) plotted in Fig. 7.6.g (gray line) exhibits an almost constant amplitude of dI/dV within the applied bias range of -35mV < V < 35mV. A large increase in the dI/dV is observed after |V|>35mV with a peak centered around |V|≈70mV. The dI/dV amplitude further increases at higher applied bias values. This bias dependence of the dI/dV resembles previous literature[23,167,181] on STM assembled and solid-state-based transport across spin chains, i.e. is the characteristic feature of the spin excitation in the molecular spin chain (MSC). Moreover, from Fig. 7.6.g, we observe that the spin excitation induced magnetoresistance (MR_{ES}) across the MSC calculated from the R(H) data tracks the differential conductance (dI/dV). To the best of our knowledge, this is the first observation of a unique MR signal that is driven to appear due to the applied bias voltage, and whose amplitude follows the differential conductance. An electrically driven[158,222] generation of interfacial MR at a spinterface due to the so-called ‘magnetic hardening’ [179,180,218,220,221] beyond an electric field threshold isn’t expected to yield an MR term that scales with dI/dV[33]. See Section 7.3 for additional discussion on interfacial MR. This further confirms that the MR_{ES} that tracks the dI/dV, is solely arises due to the opening of additional spin-flip transport channels across the electrically quantum excited MSC.

The opposite sign of the spin polarization (P) of the MSC’s spin-flip excited sate transport channel to the ground state magnetotransport channel results in the sign reversal of MR_{ES} to the MR_{GS}. We show in Section 7.5.1 that the observed reversal in the MR sign is not due to our MR definitions but shows the influence of opposing MR effects upon flipping the magnetization of the top FM electrode [see Fig. 7.5.b]. If just electrically exciting the MSC opened an additional conductance channel with the reversed spin polarization P, then the MR in Fig. 7.6.e would also change signs, but the shape of the R(H) would remain the same.

The second resistance change at the applied magnetic field H=+1.2T only in the presence of the spin excitation current indicates the presence of a third magnetic unit that is related to enhancing the conductance [compare Fig. 7.6.d and 7.6.e]. This is the reason the scenario related to the ground [Fig. 7.6.e] and excited state [Fig. 7.6.d] of CoPc MSC's within our device are schematized by the two and three magnetic units, respectively [see Fig. 7.1.b and Fig. 7.5.b]. Thus, this magnetic unit responsible for MRES [yellow/green box of Fig. 7.5.b] is not only electrically driven to appear past a bias threshold, but has effective magnetostatic properties (e.g. its own coercive field).

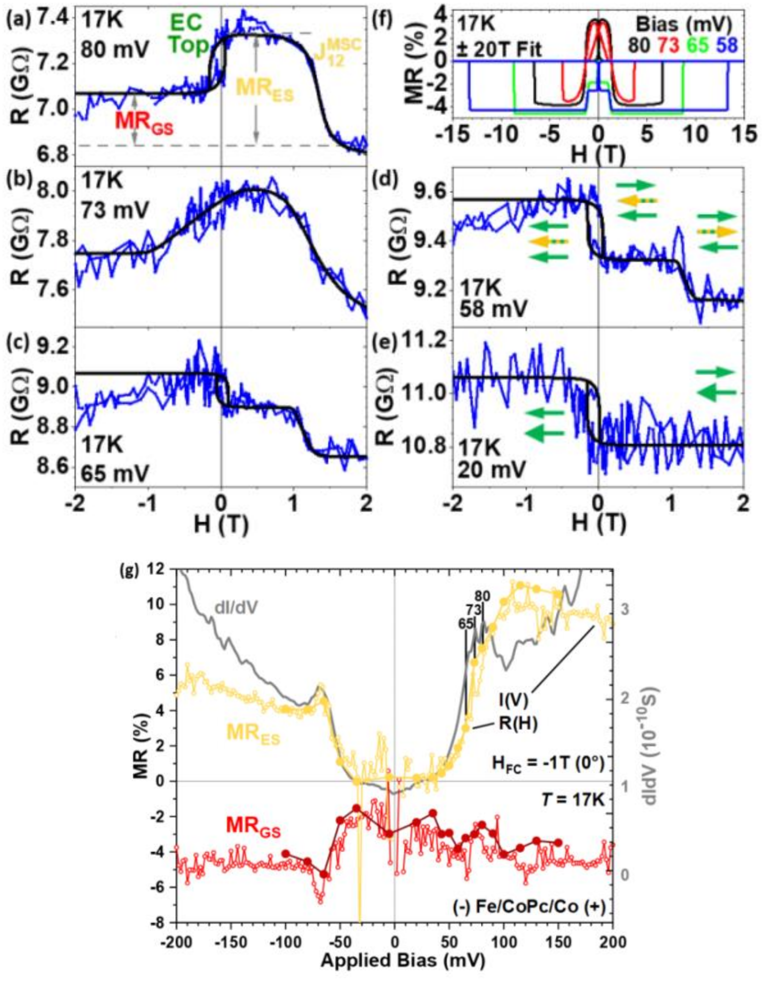

Figure 7.6. The electrical onset of spin-flip magnetoresistance. (a-e) Experimental (blue) R(H) loops performed at 17K for 20<V(mV)<80 with associated fits (black), also represented in panel (f) for ±20T. The yellow/green arrows denote the three distinct magnetic units. The larger green arrow in panel (e) represents a combined bottom unit (CoPc MSC together with Fe|CoPc spinterface and underneath bottom Fe electrode) in the absence of spin excitations [see Fig. 7.5.(b)]. **(g)** Bias dependence of dI/dV, and of MRGS/MRES inferred from I(V) and R(H) data. MRES tracks dI/dV and generates a specific R(H) trace. See text for details, and fitting parameters in Section 7.5.1.[33]

7.2.4 Thermal activation of the central magnetic unit

To study the energetics of the third (central) magnetic unit, the temperature-dependent magnetotransport measurements were performed at an applied bias higher than the threshold bias (Vth) required to observe the spin-flip excitations in the MSC. The temperature-dependent R(H) plots performed at 100mV over the temperature range 17K < T < 80K are shown in Fig. 7.7.a-e. From the R(H) plots performed over 17K < T < 55K (data at 55K not shown), below the applied magnetic field H| ≤ 2T, a similar kind of flipping for the top and bottom unit is observed. The R(H) plots become symmetric over the temperature range of 60K ≤ T(K) < 72K [see also Fig. 7.5.a]: here the bottom magnetic unit also flips for |H| ≤ 2T. A sharp change in the MR_{ES} contribution with respect to the applied field (H) is seen at T≈70K corresponding to the thermal energy E_{crit} = k_B.T ≈6meV. At T ≥ 80K, finally, the R(H) loop is collapsed, and only the low-field MR is observed until 100K.

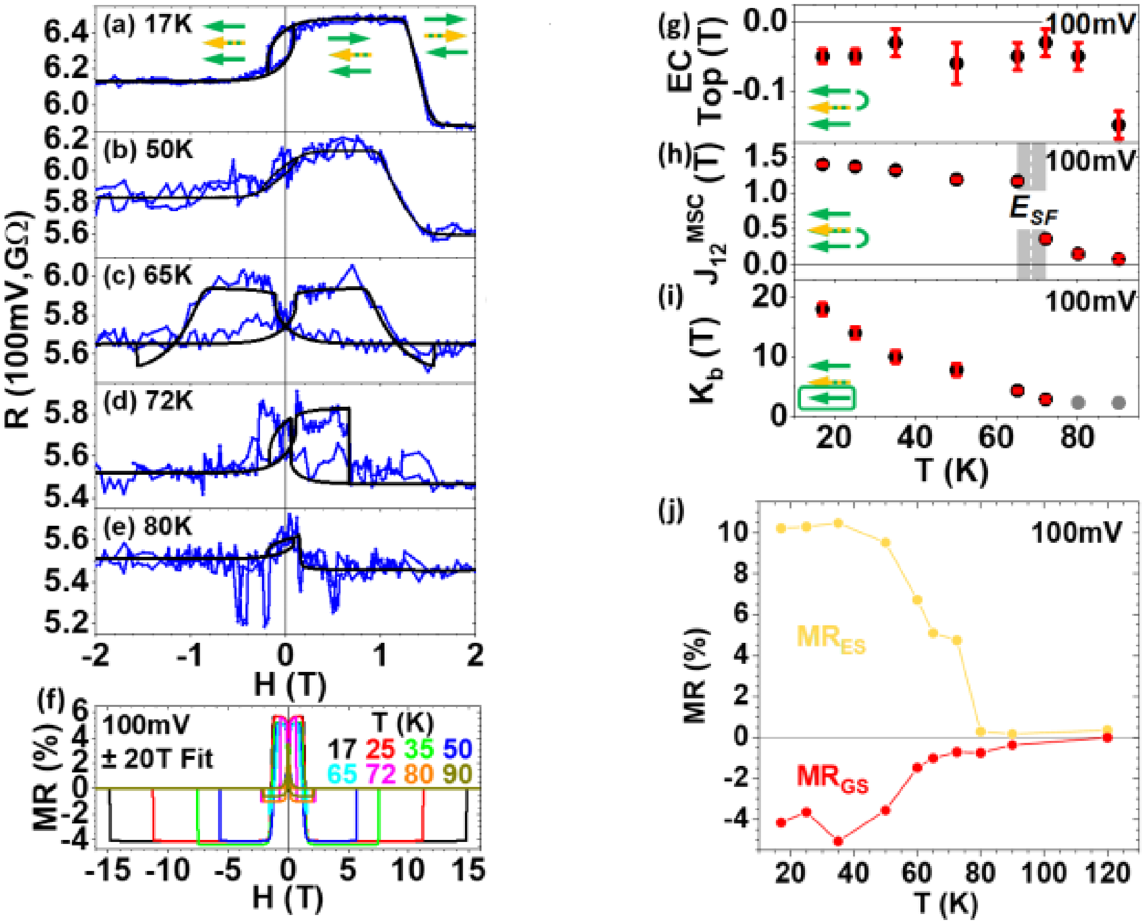

Figure 7.7. Thermal stability of the spin-flip magnetoresistance. (a-e) R(H) loops at 100mV for 17< T(K) <80. The blue/black line represents the experimental data/modeled fits and is also shown in panel **(f)** for ±20T. Temperature dependencies of **(g)** ECTop, **(h)** J_{12}^{MSC}, **(i)** K_b, and **(j)** of MR_{ES} and MR_{GS}. The gray data in panel **(i)** for T≥80K are the minimum values required to obtain R(- 2T)≠R(2T). The error bars for data in panels **g-i** are discussed in Section 7.5.1.[33]

7.3 Thermal activation and structural optimization using ab-initio calculations

To find the optimum structural geometry and magnetic property of the CoPc MSC adsorbed on top of the Fe(110) bottom electrode, density functional theory (DFT) calculations were performed by F. Ngassam and Professor M. Alouani using Vienna ab-initio simulation package(VASP)[141] and the projector augmented wave[143] (PAW) pseudopotentials included within. The exchange-correlation potential has opted with generalized gradient approximation parametrized by Perdew, Burke, and Ernzerhof[144], whereas the weak van der Waals (vdW) weak interactions were computed within the so-called GGA-D3 approach developed by Grimme[223,224] and later implemented in the VASP package[225]. For the plane-wave basis set, a kinetic energy cutoff of 450eV was chosen. The correlation effects due to the transition metal's 3d electrons were included by adding an additional Hubbard term (U) of 3eV with the DFT-GGA method[226].

7.3.1 Magnetic hardening scenario

We first looked at the so-called 'magnetic hardening' scenario[218] due to which the topmost monolayer of the bottom FM electrode together with the molecular layer adsorbed on top becomes magnetically anti-aligned relative to the FM layers underneath. As per the DFT calculations performed by Raman et al.[218] for the Co|zinc methyl phenalenyl (ZMP) bilayer system, on adsorption of the ZMP molecule on top of the Co film, a reduction in the interatomic magnetic exchange coupling from 8.54meV/atom to 1.34meV/atom between the surface Co atoms was observed. This strong modification in the surface magnetism due to the adsorbed ZMP molecule further reduces the energy difference required in order to anti-align the magnetization of the Co atoms from ΔE=190.9meV/atom to ΔE=26.4meV/atom. This allows the topmost Co layer and the ZMP molecule to magnetically decouple from the underlying Co film. In contrast to Raman et al. [218], on performing similar calculations for our bilayer bcc Fe(110)(5ML)|CoPc(1ML) system, we find that the adsorption of the CoPc molecule on top of the bcc Fe(110) film causes only a slight modification on the magnetic properties of the surface. The adsorption of the CoPc molecules onto Fe film reduces the magnetic moment of the Fe surface atoms only very slightly, from 2.68μ_B to 2.57μ_B. The energy required in order to magnetically decouple or anti-align the topmost Fe monolayer (and FM coupled CoPc layer) from the rest of the Fe film underneath was calculated to be ΔE= 200.5meV per iron atom. This value is just slightly reduced compared to the ΔE=242meV found for a bare surface Fe monolayer. The calculated ΔE= 200.5meV per iron atom corresponds[227] to the thermal energy of ~2400K, which is not at all compatible with the ~70K thermal energy [see Fig. 7.7.h] at which the electrically induced magnetic unit becomes coupled to the underlying FM electrode. Therefore from DFT calculations, we conclude that the so-called 'magnetic hardening'[218] scenario cannot explain our experimental results.

To further examine the impact of the CoPc MSC on the magnetic properties of Fe, we reduced the number of monolayers of Fe(110) film from 5ML to 3ML to save the computational energy and calculation time. To structurally optimize the CoPc MSC geometry on top of the Fe(110) film, we considered the following two scenarios: i) the ‘on-top’ scenario in which the 2nd CoPc molecule is centered atop the 1st CoPc molecule, with a 45^0 rotation [see Fig. 7.8.a], and ii) the ‘shifted’ scenario, in which the 2nd CoPc molecule is shifted without any rotation, relative to the 1st CoPc molecule [see Fig. 7.8.b]. The supercell structure Fe(110)(3ML)|CoPc(2ML) can be seen in Fig. 7.8.a-b.

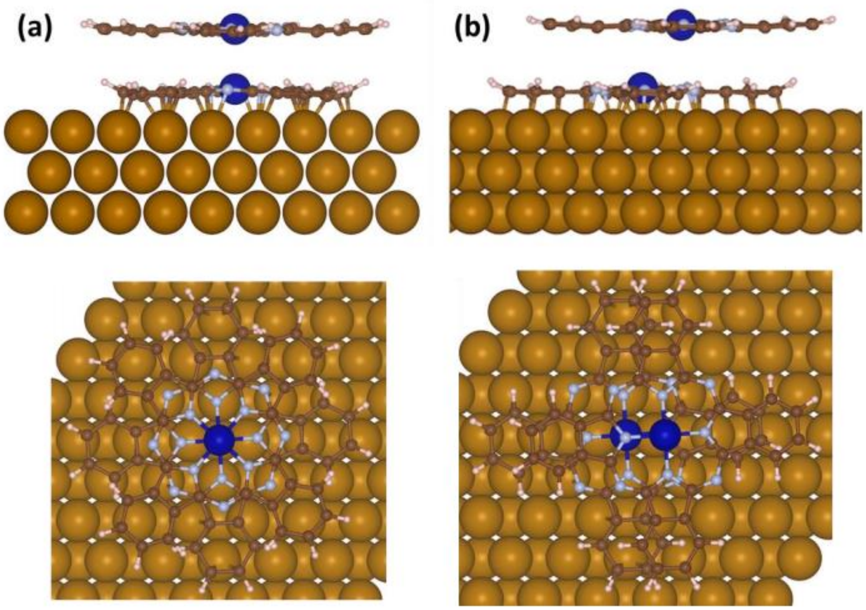

Figure 7.8. Adsorption geometries considered for the bcc Fe(110)(3ML)|CoPc(2ML): (a) ‘on-top’ and **(b)** ‘shifted’. From the DFT calculations the ‘shifted’ scenario is found to be more energetically favorable.[33]

For each scenario, i.e. ‘on top’ and ‘shifted’, the energy minimization in the ground (AFM) and excited (FM) states was achieved with respect to the intermolecular distance (d) between the successive CoPc ML. Table-7.1 and 7.2 summarizes these theoretically calculated parameters for the ‘on top’ and ‘shifted’ geometries, respectively. on comparing both the tables, we find that the ‘shifted’ scenario [Fig. 7.8.(b), Table 7.2] exhibits much lower energies with respect to the intermolecular distance between the two successive CoPc molecules, as compared to the ‘on-top’ scenario [Fig. 7.8.(a), Table 7.1]. this refers that that the ‘shifted’ scenario is more energetical favorable geometrical structure compared to the ‘shifted’ one.

For an intermolecular distance of 3.1 Å [shown in Fig. 7.9], between the successive CoPc molecules for the ‘shifted’ scenario, the magnetic anisotropy was found from the difference between the ground (AFM) and excited (FM) states was found to be 11.8meV.

Table 7.1. Calculated total energies for the ground state AFM and excited state of the *bcc* Fe(110)(3ML)|CoPc(2ML) system. The distance between the two CoPc molecules was varied. The total

energy of the system is shown when the top CoPc molecule's magnetic referential is aligned (FM) or anti-aligned (AFM) with that of the underlying CoPc molecule and Fe layer. Case (I) is when the second CoPc is on top of the first one by 'rotated by 45^0'. The total energy is with respect to reference energy of -2743 eV.[33]

$d_{CoPc\text{-}CoPc}$ (Å)	E_{AFM} (meV)	E_{FM} (meV)	ΔE (meV)
2.8	-448.20	-361.40	-86.81
2.9	-618.39	-536.20	-82.18
3.0	-681.14	-606.38	-74.76
3.1	-672.66	-607.52	-65.15
3.2	-616.76	-561.84	-54.92
3.3	-582.56	-483.22	-45.34
3.4	-420.51	-383.55	-39.96

Table 7.2. Calculated total energies for the ground state AFM and excited state of the *bcc* Fe(110)(3ML)|CoPc(2ML) system. The distance between the two CoPc molecules was varied. The total energy of the system is shown when the top CoPc molecule's magnetic referential is aligned (FM) or anti-aligned (AFM) with that of the underlying CoPc molecule and Fe layer. Case (II) is when the second CoPc is 'shifted' with respect to the first one. The total energy is with respect to reference energy of -2743 eV.[33]

$d_{CoPc\text{-}CoPc}$ (Å)	E_{AFM} (meV)	E_{FM} (meV)	ΔE (meV)
2.9	-918.12	-902.26	-15.86
3.0	-1030.35	-1016.63	-13.72
3.1	-1054.52	-1042.73	-11.80
3.2	-1019.19	-1009.9	-10.10
3.3	-945.09	-936.48	-8.60
3.4	-846.83	-839.52	-7.30

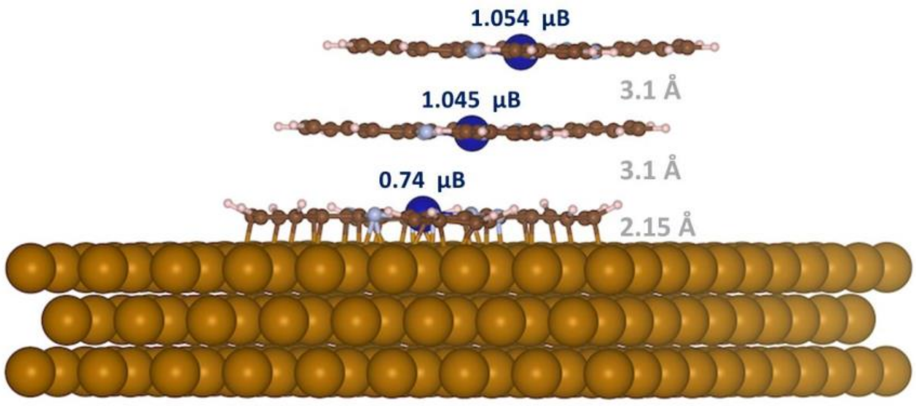

Figure 7.9. 'Shifted' adsorption geometry of bcc Fe(110)|CoPc(3ML). Molecular adsorption distances, and the amplitude of the magnetic moment on the Co atom of CoPc, are shown.[33]

The final structure bcc Fe(110)(3ML)|CoPc(3ML) shown in Fig. 7.9 exhibits the 'shifted' geometry of the adsorbed CoPc layers. The intermolecular distances between the successive CoPc monolayers and the magnetic moments of the Co within each CoPc ML are also shown. The magnetic moments of each Fe monolayers and the Co central metal atom in the adsorbed CoPc monolayers are tabulated in Table 7.3.

Table 7.3. The magnetic moment on Fe and Co atoms in the bottom FM electrode (Fe) and the CoPc molecular layer, respectively.[33]

	Ferromagnetic layer			Molecular layer		
	Fe (bottom)	Fe (middle)	Fe (top)	Co (bottom)	Co (middle)	Co (top)
Magnetic moment (μ_B)	2.68	2.46	2.57	0.74	1.05	1.05

The calculated on-site spin density in the ground (AFM) and excited (FM) state of the CoPc (3ML) MSC adsorbed on the Fe (110) 3ML is shown by the panel (a) and panel (b) respectively in **Fig. 7.10**. From the DFT calculations, the first spin-flip of the 3rd CoPc molecule costs 6.14 meV energy which is close to the 5.9meV thermal energy threshold for the magnetic decoupling, observed experimentally. The energy required to flip magnetization of the 3rd CoPc molecule, calculated using the DFT is tabulated in Table 7.4.

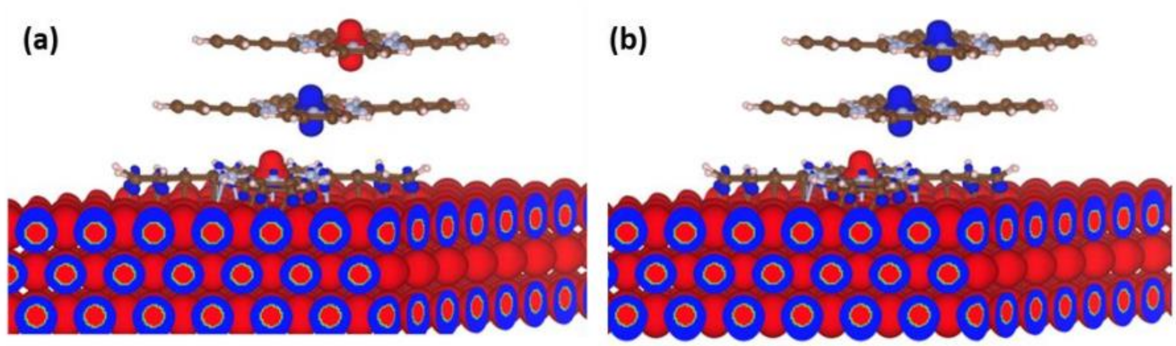

Figure 7.10. Spin density plots for Fe(110)(3ML)|CoPc(3ML). Spin ↑(↓) is represented by red(blue) color. **(a)** AFM (↑↓↑) ground state. (b) Lowest excited state (↑↓↓). The energy cost to flip the upper CoPc monolayer spin is found to be 6.14 meV.[33]

Table 7.4. Calculated total energies for the AFM ground state and first excited state of the bcc Fe(110) (3ML)|CoPc(3ML) system as shown in Fig. 7.9. The first row indicates for the case of three molecules are on top of each other's [see **Fig. 7.8.a**], and the second row for the case where the molecules are shifted [see **Fig. 7.8.b**] with respect to each other's. The difference between the ground and first excited state for the 'Shifted' scenario is found to be minimum.[33]

Configuration	$E_{\uparrow\downarrow\uparrow}$ (eV)	$E_{\uparrow\downarrow\downarrow}$ (eV)	ΔE (meV)
On-top	-3167.92256	-3167.91951	-3.05
Shifted	-3168.04920	-3168.04306	-6.14

To understand the spin excitation along the MSC, we performed DFT calculations and tested two possible scenarios for the molecular adsorption geometries and magnetization reversals, including one relating to 'magnetic hardening'[179,218,220,221] which was not consistent [see Section7.3] with our experimental findings. The spin excitation energy of ΔE=6.1meV, which was calculated by changing the magnetic coupling of the 3rd CoPc molecule from AFM to FM, relative to the 1st and 2nd monolayers of CoPc, was found to be consistent with the experimentally observed value (E_{crit} ~5.9meV). Note that, since the 1st CoPc molecule is chemisorbed onto Fe[23,228], the 1st CoPc molecule of the MSC is the 2nd CoPc ML atop Fe.

These results indicate that the magnetostatic properties of the MSC in its excited state appear due to the magnetic coupling with the FM electrode. The spinterface formed between both Fe and CoPc can set the spin referential for the AFM coupled CoPc MSC far above the onset of the exchange bias[165]. Moreover, the different magnetic anisotropies for the MSC's ground and excited states [229] play a major role to achieve magnetic decoupling and fixed spin referential.

7.4 Magnetic anisotropies along the nanotransport path

In this section, we will examine the symmetry of magnetic anisotropies along the nanotransport path with the field cooling procedure. The conclusion about the magnetic anisotropies present within our devices will be extracted out from the basic magnetotransport measurements R(H) plots with the field-cooling procedure, applied bias (below or above than the V_{th}), and the angle of magnetization. After a field cooling (FC) procedure starting from the initial temperature of 120K at a constant applied field of H=-1T along the in-plane direction (θ_H=0), the R(H) measurement was performed with an applied bias of 100mV (> V_{th}) at 25K, represented by red color. It was found that the R(H) plot performed at the same temperature and applied bias (at 17K with an applied bias of 100mV and shown by the blue color) flips about the H=0 axis, if the device was cooled down with an applied field of H=0+, after applying a field of H=2T at 120K [see Fig. 7.11.a]. A similar kind of flipping was also observed for the R(H) plots performed after an FC procedure at a constant applied field of H=-1T, with an applied bias of 100mV at 17K by switching the angle of the magnetic field to the sample (θ_H) from 0^0 to 180^0 [Fig. 7.11.b]. The black lines in Fig. 7.11.b represent the fitted data. Cooling down with H=1T applied at an in-plane angle of 90^0 instead of 0^0 did not change the R(H) loop (not shown).

To get an insight into the angular dependence of the magnetotransport data, the MR_{GS} was plotted as a function of the angle of the field cooling magnetic field to the sample (θ_H) at 17K, with an applied bias of -50mV (100mV) corresponding to the transport scenario without (with) spin-flip excitations [see Fig. 7.4 and 7.6.g] in the CoPc MSC. These plots are shown in Fig. 7.11.(c). The absence of the resistance plateau for an applied field 1.7T < H(T) < 2T (with restricted |H|<2T, due to the technical reasons) does not yield the magnetoresistance MR_{GS} for the applied field angle θ_H; $30^0 < \theta_H < 135^0$. We were not able to plot the angle dependence of the MR caused by the spin-flip excitations in the CoPc MSC (MR_{ES}) because the corresponding 1T resistance level becomes undetermined at intermediate angles. We noticed that the bias amplitude applied during the field cooling procedure does not alter the R(H) loop significantly (data not shown). From these datasets, we conclude that the magnetization direction of the FM electrodes during the cooldown procedure determines the uniaxial anisotropy along the nanotransport path.

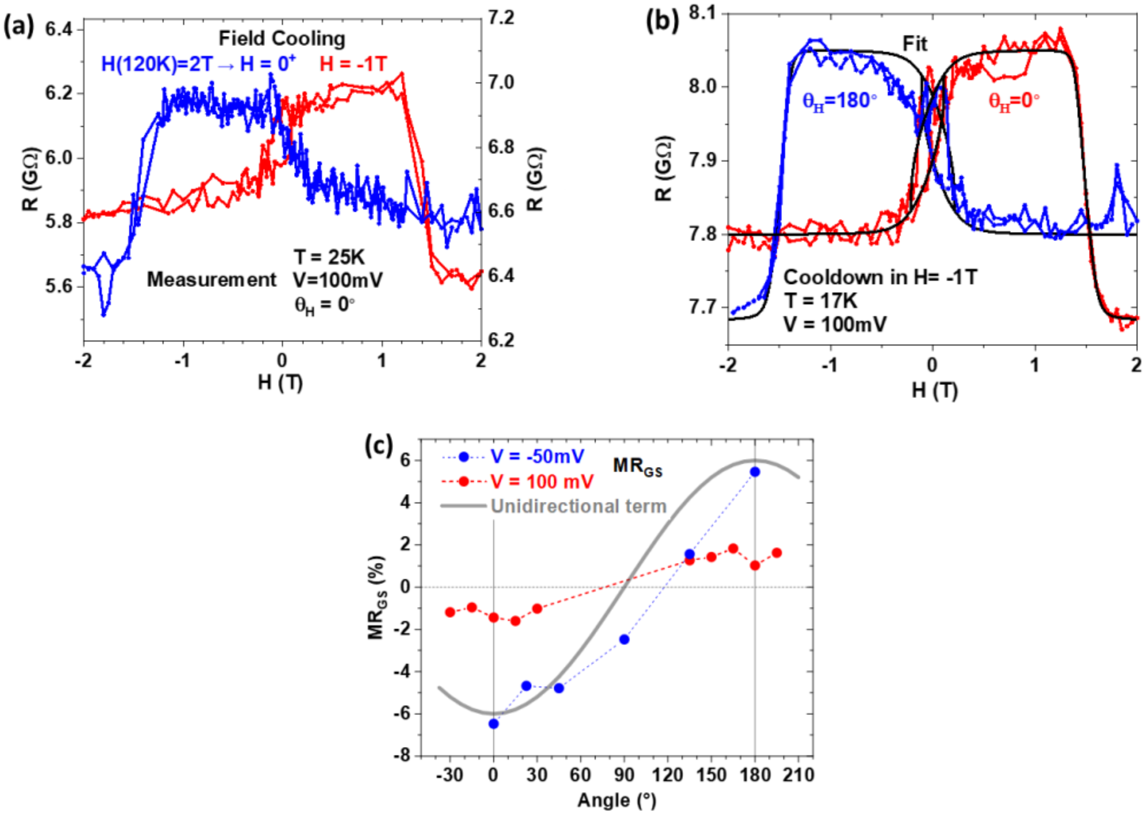

Figure 7.11. Determining magnetic anisotropy from magnetotransport. (a) R(H) loops acquired at 25K and 100mV (>V_{th} i.e. in the spin-flip excited state of MSC) after field cooling in H=-1T (red) and H=0+ T (blue; H=2T was first applied at 120K). Field-cooling at H<0 defines the in-plane angle θ=0. **(b)** R(H) loops acquired at 17K and 100mV for θ_H=0^0 (red) and 180^0 (blue). After fitting the θ_H=0^0 data, the same set of parameters were used, but the simulation was run for θ_H=180^0. **(c)** Angular dependence of MR_{GS} at 17K for V=- 50mV (<V_{th} i.e. in the ground state of MSC) and for V=100mV (i.e., (>V_{th} i.e. in the spin-flip excited state of MSC). Variations in R(H=-2T) between panels reflect a minor evolution of junction resistance during the ~100-hour measurement and across several field-cooling sequences. The fitting parameters in panel **(b)** were: K_t =0.28T, θ_t=70^0, K_b =21T, θ_b=-1^0, ECTop=-0.05T, J_{12}^{MSC}=1.49T, R_0=7.8GΩ, MR_{GS} =-1.4% and MR_{ES} =4.8%. Small differences between these parameters and those found in the main text reflect minor evolutions in junction magnetotransport during the measurement run.[33]

The R(H) plots performed at 17K temperature point with an applied bias 100mV (>V_{th}) and in-plane angle θ_H of the field cooling magnetic field are shown in Fig. 7.12. For $\theta_H \neq 0$, the R(H) fitting was performed by adjusting the in-plane angle of H while conserving the same parameters to only reproduce the features of the experimental R(H) qualitatively. For deviations from the field-cooling angle θ_H=0, the fitted R(H) obtained (black line) by simply adjusting the in-plane angle of H while conserving the same parameters only qualitatively reproduce features of the experimental R(H), whereas an exact fit (black line) is obtained when the fitting parameters found for θ_H=0^0 are used for θ_H=180^0 [see also Fig. 7.11.b]. Although magnetometry on FM|MPc bilayers showed a fatigue effect when the external magnetic field was repeatedly swept[159,165], no such fatigue effect was observed in magnetotransport [see Fig. 7.5.a][33]. This, along with the ability to replicate magnetotransport data using a macrospin model [see Fig. 7.5.a, Fig. 7.6.a-e, and Fig. 7.7.a-e], suggests that the nanotransport path within the 500nm nominal diameter is proceeding through a reduced number of grains[33].

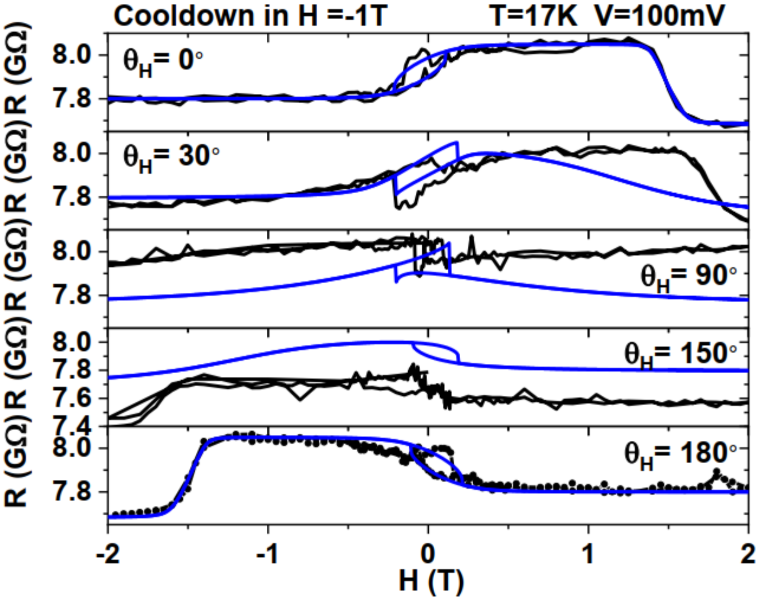

Figure 7.12. Angle-dependent R(H): experimental & fitted data. Parameters are the same as those in Fig. 7.16.b.[33]

7.5 Macrospin modeling of magnetotransport

To further support our experimental findings i.e. the presence of three distinct magnetic units within our device [see Fig. 7.5.b], later confirmed with the DFT calculations and described in Section 7.3, we phenomenologically model the magnetotransport results involving three macrospins. As previously described, in its excited state, the CoPc molecular spin chain (MSC) forms a separate magnetic entity from the rest of the bottom magnetic unit (Fe electrode and Fe|CoPc spinterface) that is represented by the yellow/green box in Fig. 7.5.b. Due to its magnetostatic properties (e.g. a coercive field), this bottom magnetic unit (CoPc MSC in its spin-flip excited state) could impact the magnetotransport which can be classically described as the deviation from the collinearity between the magnetic orientation of its spin referential. However, in its ground state, the CoPc MSC remains coupled to the bottom magnetic unit (comprising the bottom Fe electrode and the Fe|CoPc spinterface). This magnetically combined unit is shown by the large green box and the large green arrow in Fig. 7.5.b. Its uniaxial anisotropy field K_b is therefore large due to several mechanisms of magnetic exchange bias at the spinterface[159,165]. This is confirmed by field-cooling and angular studies [Section 7.4]. The central and bottom units are exchange-coupled by an exchange coupling energy J_{12}^{MSC}, such that we attribute a low anisotropy field K_C=5mT to the MSC in its excited state. The top magnetic unit which is comprised of the top Co FM electrode and few monolayers of CoPc MSC underneath with the diffused Co (top electrode) atoms within (shown by the gray area within the top green box in Fig. 7.5.b) [217]. Both the structural and magnetic studies[24,159] anticipate the existence of disjointed spin chains on the nano-transport route through the film thickness so that a weak ECTop exchange term of AF is present between the top and central magnetic units.

In order to model our magnetotransport data in a phenomenological manner, we first write the effective anisotropy field K of the nanotransport path across the top (i=t), central (i=c) and bottom (i=b) units as:

$$K = -\mu_0 \sum_{\boldsymbol{i = t,c,b}} \boldsymbol{H}.\boldsymbol{m_i} + \frac{1}{2} \sum_{\boldsymbol{i = t,c,b}} K_i \, sin^2(\theta_{Mi} - \theta_{Ki}) - \sum_{\boldsymbol{i = t,b}} C_{ci}.\boldsymbol{m_c}.\boldsymbol{m_i} \tag{34}$$

where H is the applied magnetic field, and for each magnetic units, m_i is the reduced magnetization, θ_{Mi} the magnetization angle, and K_i its uniaxial anisotropy field with an easy axis angle θ_{Ki}. Finally, C_{ci} is the coupling strength between the central (c) and outer (i=b,t) magnetic units. K, K_i and C_{ci} are expressed in Tesla. We define the coupling strengths, C_{ct} = ECTop and Ccb= J_{12}^{MSC}. For each H step, the uniaxial anisotropy field (K) is minimized to yield, for each magnetic unit, the magnetization's in-plane orientation. The resistance R due to non-collinear reduced magnetizations $\boldsymbol{m_t}$, $\boldsymbol{m_c}$ and $\boldsymbol{m_b}$ is:

$$R = R_0.\left[1 - \frac{MR_{GS}}{2}.(\boldsymbol{m_t}.\boldsymbol{m_b} - 1) - \frac{MR_{ES}}{2}.(\boldsymbol{m_t}.\boldsymbol{m_c} - 1)\right] \tag{35}$$

The magnetoresistance term MR_{GS} arises due to the magnetization flipping of the top magnetic unit relative to that of the magnetically hard bottom magnetic unit, whereas in the spin-flip excited state the magnetization flipping of the central unit (CoPc MSC) relative to the top magnetic unit produces the magnetoresistance term MR_{ES}. This association proceeds from the observation of the R(H) curves at 17K [Fig. 7.6] and 60K [Fig. 7.7] under the assumption of the sequential magnetization reversal of the three magnetic units.

7.5.1 Fitting R(H) data using the macrospin 3-unit model

This section details the procedure used to fit the R(H) data at 17K versus applied bias voltage [Fig. 7.6.a-e], and at 100mV versus temperature [Fig. 7.7.a-e]. Fig. 7.13.a, schematically shows the three potential MRs with their corresponding applied magnetic field (H) values, that can potentially fit the R(H) data. Out of the three MRs shown in Fig.7.13.a, we were able to fit our R(H) data using only two MR terms i.e. MR_{ES} Top/Central and MR_{GS} (Top/Bottom terms), as schematically shown in Fig.7.13.b.

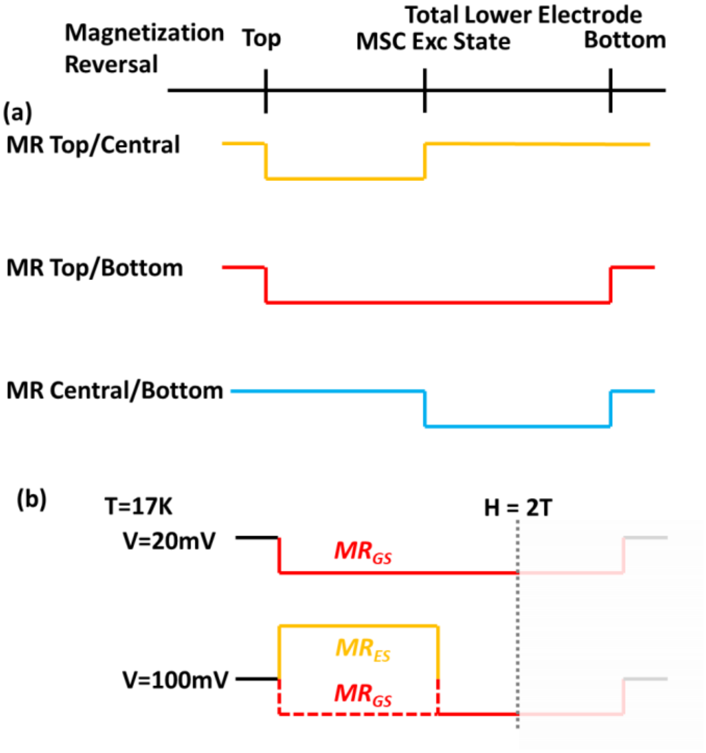

Figure 7.13. Rationalization of magnetization reversals and magnetoresistance (MR) terms. (a) MR traces upon flipping pairs of magnetic units. MR<0 is assumed in all cases for simplicity. **(b)** The experimental MR data for T=17K and V=20mV (<V_{th}, i.e. the ground state of the MSC) is most easily fitted using one MR Top/ Bottom term. Since the R change upon flipping the top unit magnetization switches from a decrease to an increase as V is increased, the MR trace at V=100mV (>V_{th}, i.e. the spin-flip excited state of the MSC) is most easily fitted by combining two MR Top/Bottom and MR Top/Central terms. Other combinations are possible but not straightforward as they would require the perfect cancellation of MR terms. For details, see the text.[33]

The ground state MR (called MR_{GS}) of the CoPc MSC (central unit), as experimentally visualized by the R(H) plot performed at 17K with an applied bias of 20mV [Fig. 7.6.e] can be understood by the magnetization flip of the top unit relative to the 'harder bottom unit' and fitted using only a single MR term MR_{GS} (Top/Bottom) [top panel of Fig. 7.13.b]. Further, increasing the applied bias more than the threshold voltage (V_{th}), as the case of R(H) performed at 17K, 100mV [Fig. 7.6.a], causes spin-flip excitations in the CoPc spin chain due to which the magnetization flip occurs in the CoPc MSC. The spin-flip excited state of the CoPc MSC forms a separate magnetic entity, 'central unit'. We were able to fit this data with the two MR terms, MR_{GS} (Top/Bottom) and MR_{ES} (Top/Central) [bottom panel of Fig. 7.13.b]. Noting that the AFM MSC has a vanishing magnetization compared to the other two FM layers, we also set a low magnetic anisotropy K_C=5mT for it. It thus acts as a 'free' layer.

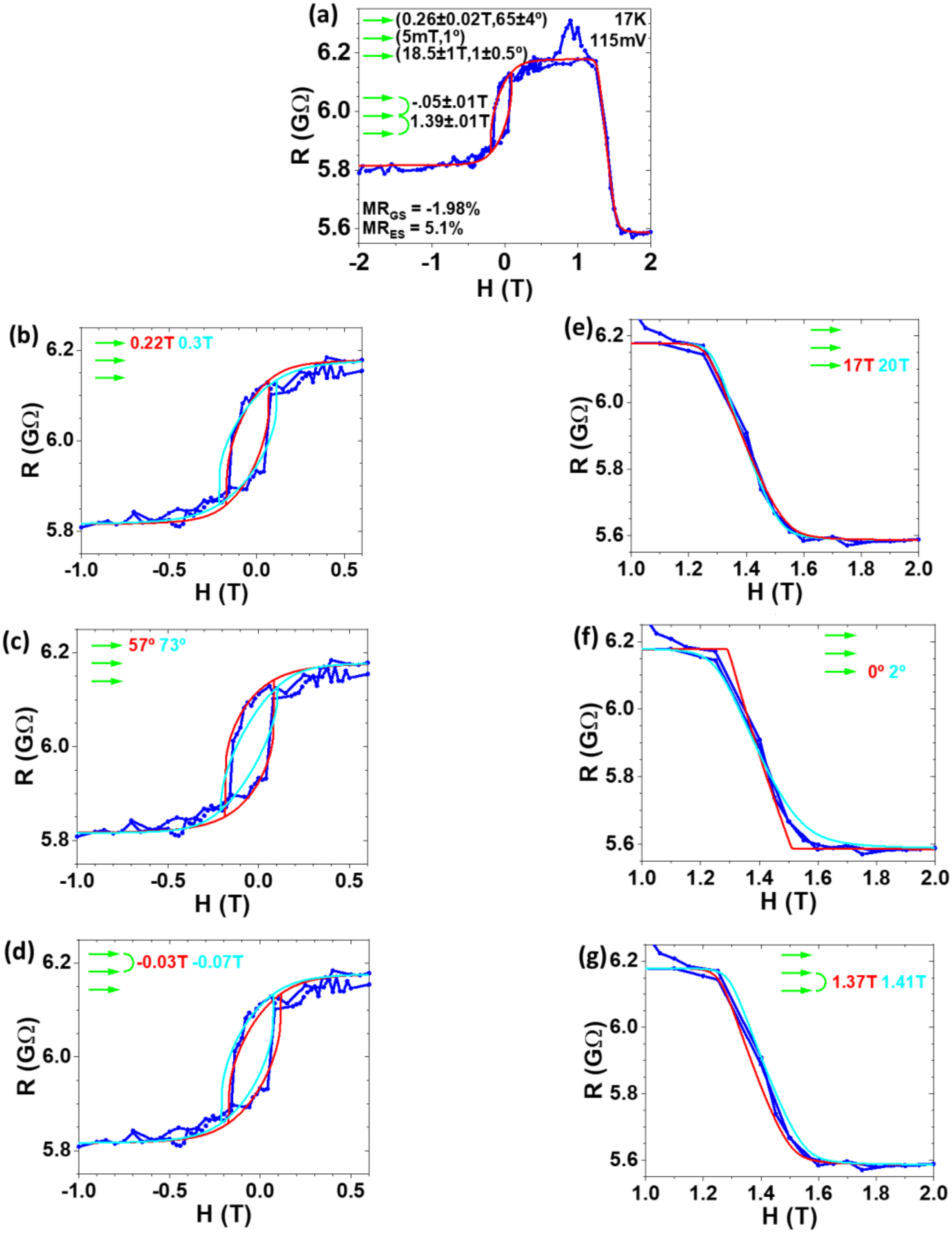

Figure 7.14. Determining the error bars of the fit. (a) The data and final fit for R(H) at 17K and 115mV (>V_{th} i.e. in the spin-flip excited state of MSC). Parameters with error bars are shown. Zooms on experimental data and two fits outside the error margin for **(b)** K_t, **(c)** θ_t, **(d)** ECTop, **(e)** K_b, **(f)** θ_b and **(g)** J_{12}^{MSC}.[33]

An example of the fitting of R(H) data at (17K, 115mV) is presented in Fig. 7.14. To fit the R(H) data the two magnetoresistance terms MR_{GS} and MR_{ES} are used. For 17K temperature point, within the applied magnetic field H|<2T, the R(H) traces at a lower applied bias (V) do not guarantee the full magnetization reversal. Therefore we have chosen here the R(H) data at a higher applied bias (17K, 115mV), for which the resistance is mostly flat not only at large H<0, but also for 1.7 < H(T) < 2, under the assumption that these plateaus imply full magnetization reversal. In the process of fitting the R(H) data, the evolution of the resistance plateau at 1.7T < H < 2T was monitored with respect to the change in V or T, and the two MR terms MR_{GS} and MR_{ES} were adjusted accordingly to mimic the R(H) slope in this field (H) region. The external magnetic field at which the magnetization of the central magnetic unit reverses is then driven mostly by its coupling J_{12}^{MSC} to the bottom magnetic unit [see Fig. 7.14.g].

Fig. 7.15 presents the experimental and fitted MR values for V>0. The fitted MR terms follow their experimental counterparts quite well, despite small deviations. This supports the MR_{GS} and MR_{ES} definitions described earlier in this chapter.

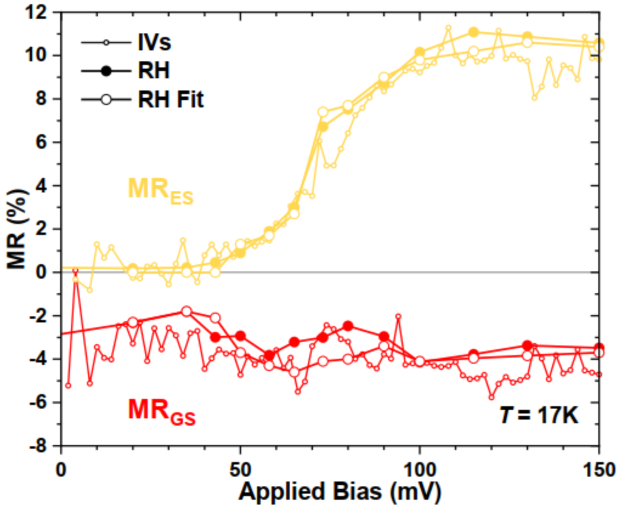

Figure 7.15. Experimental and fitted MR terms. Experimental MR_{GS} and MR_{ES} were obtained from I(V) and R(H) data, and fitted MR_{GS} and MR_{ES} parameters.[33]

The bias dependence of the parameters used to fit the R(H) data at 17K [shown Fig. 7.6] is presented in Fig. 7.16. As seen in panel (c), K_b scales with dI/dV and MR_{ES}.

The compartmentalization of our 3-macrospin model's parameters to R(H) features however fails at the critical points [point 'A'; (17K, 73mV); see Fig. 7.6.b, point 'B'; (17K, 80mV); see Fig. 7.6.a, and at point 'C'; (72K ,100mV); see Fig. 7.7.d]. These points 'A' and 'B' are also marked on the dI/dV plot, shown in Fig. 7.6.g. At point 'C', the magnetic anisotropy barrier between the bottom and central magnetic units is overcome by thermal fluctuations; this physically corresponds to the energy difference between the MSC's ground and excited states. At points 'B' and 'C', it is impossible to maintain 'free-layer' properties for the central magnetic unit: K_C~3000 and $\theta_C=13^0$. At points 'A' and 'B', $\theta_C \approx 11^0$. Also note the deviations in ECTop and θ_t at point 'A', which are associated with a jump in J_{12}^{MSC} to a higher, nearly constant value. These deviations are seen in Fig. 7.16. These mutual couplings of otherwise independent model parameters indicate that the three magnetic units become dynamically coupled at these critical points due to changes induced by the spin-polarized current in the spin-flip conductance channel's fully spin-polarized current, i.e., by spintronic anisotropy[230] (points 'A' and 'B') and by thermal fluctuations (point 'C'). This is also a feature of exchange-bias systems near criticality[231].

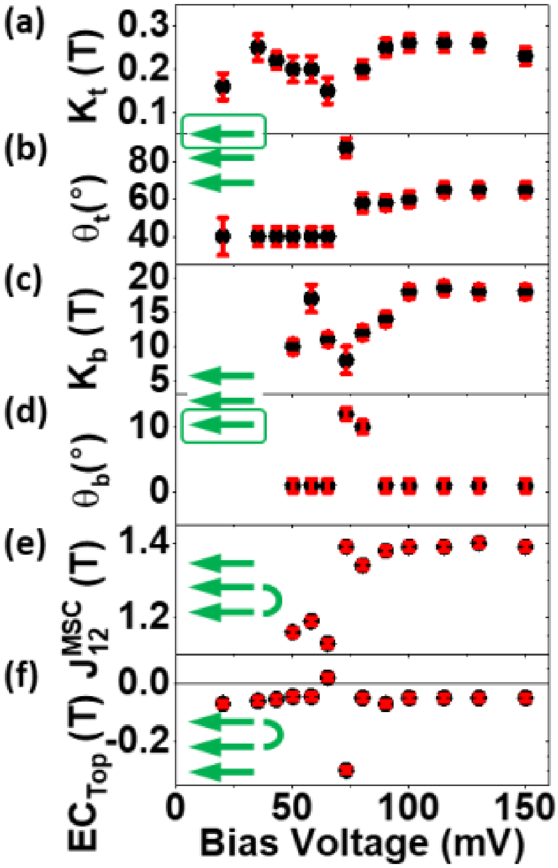

Figure 7.16. Bias dependence of fitting parameters at 17K. Bias dependencies of the strength and angle of the anisotropy field for the **(a-b)** top and **(c-d)** central magnetic units. Bias dependencies of the **(e)** J_{12}^{MSC} and **(f)** ECTop coupling terms. The MR_{ES} term tracks the dI/dV increase due to spin excitations. At the dI/dV peak, coupling between the MSCs of the top and central unit causes strong changes to their anisotropy parameters (panels **h-k**) and to the coupling parameters (panels **l-m**), which distorts the R(H) at 73mV (panel **b**).[33]

We successfully fit the key features (plateaus, reversals, coercive fields, loop form, etc....) of our peculiar R(H) dataset in (V,T) parameter space using the 3-macrospin model [see black lines in Fig. 7.5.a, Fig. 7.6.a-e, Fig. 7.7.a-e, Fig. 7.11.b, Fig. 7.12]. This model uses the two coupling terms ECTop and J_{12}^{MSC} for the coupling of the central magnetic unit (excited state of CoPc MSC) to the top (top Co electrode with the neighboring CoPc monolayer underneath with diffused Co atoms) and bottom (Fe|CoPc spinterface with the bottom Fe electrode) units respectively [see Fig. 7.6.a and Fig. 7.14.d, g]. This consequently describes the three units' sequential magnetization reversal [see corresponding green/yellow arrows in Fig. 7.5.a, 7.6.d, and 7.7.a]. We plot the R(H) phenomenology of the bias [Fig. 7.6.f] and temperature [Fig. 7.7.f] dependencies to explain the three reversals observed at 60K [Fig. 7.5.a]. The third resistance switch attributed to the magnetization reversal of a relatively harder 'bottom' unit is observed at |H|>2T.

The anisotropy energy for the top magnetic unit; $K_t \approx 0.2$T is over an order of magnitude stronger than that of a free layer [see Fig. 7.16.a] which confirms that the top unit not only consists the top Co electrode but also a part of the MSC [see Fig. 7.5.b]. From the temperature [Fig. 7.7.g] and bias dependence [Fig. 7.16.f] fits, the coupling term ECTop was found to be weakly negative and almost independent of the temperature and bias, therefore attributed to the antiferromagnetic coupling between the top unit and central unit [see Fig. 7.5.b]. In line with previous reports[177,179,181], the lower Fe electrode together with the Fe|CoPc spinterface and the exchanged coupled CoPc MSC with $K_b \approx$ 10-20T forms a magnetically hard unit at 17K. The bias dependence of the K_b i.e. K_b(V) plot [Fig. 7.16.c,] was found to mimic the differential conductance dI/dV(V) of the spin-flip current [see Fig. 7.6.g], while its temperature dependence K_b(T) [see Fig. 7.7.i] finds analogy with that of the exchange bias amplitude previously observed[159,165,179]. As compared to the weakly negative value of the ECTop, the exchange coupling energy term between the central and bottom magnetic unit i.e. J_{12}^{MSC} was found to be positive ($J_{12}^{MSC}>0$) resulting in a ferromagnetic coupling between the central and bottom magnetic unit, and is primarily responsible for the magnetization reversal of the spin-flip MSC for |H|>1T. This implies that an external magnetic field might also be controlling the MSC's transition from an excited spin state back to its ground state. Proving this point would require careful comparison of all three resistance levels [see Fig. 7.6.f] and dI/dV [see Fig. 7.6.g] at large H, when the hard bottom layer finally flips. As per our magnetotransport model, the evolution of MR_{ES} with respect to the applied magnetic field H [see Figs. 7.7.a-e] is associated with a sudden decrease in J_{12}^{MSC} for T>65K [see Fig. 7.7.h]. This thermal energy of T>65K corresponds to an E_{SF}=5.9±0.3meV magnetic anisotropy energy barrier, i.e. the threshold or the minimum amount of energy required to magnetically decouple the excited state of the molecular spin chain (MSC) from the bottom magnetic unit (Fe electrode together with Fe|CoPc spinterface). This magnetic anisotropy energy barrier of E_{SF}=5.9±0.3meV was found to be consistent with the DFT-calculated ΔE=6.1meV energy difference between the MSC's ground and excited spin states when coupled to the FM. These findings indicate a clear proof of spintronic anisotropy[29,230] in the magnetotransport, i.e., a shift in magnetic anisotropy is induced by a spin-polarized current[29,230], with modified spin polarization (P) due to the spin-flip excited state of the MSC.

Further, the magnetotransport was performed at 17K with an applied bias of 65mV [Fig. 7.6.c] resembles to that of the 80mV [Fig. 7.6.a], with a maximum spin-flip conductance at 73mV [Fig. 7.6.b]. To the best of our knowledge, this is the first evidence of how small bias changes can so drastically alter an R(H) loop. This experimental finding can be modeled only through the deviations in the model's parameter, particularly the magnetization angle of the bottom magnetic unit i.e. θ_{Mb}. The electrically driven dynamical coupling (from AFM to FM) in the CoPc molecular spin chain is reminiscent of an exchange bias system near a critical point[231] [see Section 7.6.1].

7.6 Summary, and perspectives

In conclusion, we have demonstrated how the shortcomings of an isolated molecular spin chain (MSC), with no intrinsic magnetic orientation and with an electrically excited quantum state possessing a short lifetime[26], can be overcome[159,165,219] by adjoining it to a ferromagnetic electrode. This spin-flipped quantum excited state not only reverses the sign of the spin polarization (P) of the current flowing across the Fe|CoPc spinterface, but also acts as a distinct magnetic unit with its own coercive field. It, therefore, generates a magnetoresistance MR_{ES} against the FM electrode. Using an in-house developed novel resist-and solvent-free nanolithography technique, i.e. 'nanobead processing', we further showed that the spin-flipped quantum excited state within the MSC of our nanoscale vertical solid-state devices can be utilized to encode information (i.e. MR_{ES}). The excited quantum state of the MSC identified experimentally by the thermal stability, was found to be consistent with the DFT calculations. To unravel the role of the magnetic coupling between the MSC and the FM electrode in promoting the MR_{ES} or the ability to encode the information, a classical 3-macrospin phenomenological model was also used. This work implements the exchange bias concept[212] at ferromagnetic metal/molecule interfaces[159,165,219] or the spinterface[22] within the device's active spintronic layer and connects it with the spin-flip spectroscopy[26] and spintronic anisotropy[29,230]. This work extends the prior magnetotransport study in the antiferromagnetic materials[187–191] into the quantum regime, leading to the fascinating magnetometry studies[232] of the spin chain's ground and excited states.

In contrast to the strategy of electrically altering[158,222] the charge transfer between the FM electrode and the adsorbed molecule, producing the spinterface[22] and interfacial MR[218], our strategy of electrically manipulating the quantum states of the MSC away from the spinterface benefits from the ability to electrically control the amplitude/sign of MR using low-voltage addressing, and to transmit spin-wave encoded[210] across an organic semiconductor using antiferromagnetic molecular spin chains in a pulsed voltage approach. This work may also the advantages of the quantum properties of multiferroic oxides used as the active spintronic spacer layer. Although the ability to encode the information in our nanoscale solid-state device was not observed beyond T≈70K, there are reports[24] mentioning the existence of the intermolecular exchange coupling beyond room temperature. This suggests their potential and bright future for technological applications at or beyond room temperature. One of these potential applications is to harvest energy due to the thermal fluctuations on the paramagnetic centers[29,233] of a molecular spin chain.

8. General Conclusion and Perspectives

To summarize, this Ph.D. thesis studies the localized states due to the defect states (that are either inherent or implemented by choice) in the spacer layer and their impact on the spintronic performance of nanoscale devices. Part-I of the thesis is dedicated to the study of the localized states appearing in the energy band diagram due to the oxygen vacancies within the MgO tunneling barrier. These oxygen vacancies are inevitable, therefore inherent to MgO. To characterize these oxygen vacancies and their impact on STT, the transport measurements are performed on the CoFeB|MgO|CoFeB nanopillar MTJs procured from two different laboratories (Prof. P. Freitas Lab at INL Portugal and TDK-Headway Inc. USA). The oxygen vacancies are characterized as the localized states relative to the Fermi energy (E_F), and can be mapped by the $\hat{I}$-techniques. For our CoFeB|MgO|CoFeB nanopillar devices, the localized states appeared only in the parallel (P) state. The appearance of broad peaks of the localized states in the $\hat{I}$-spectra suggests that these states are formed due to the chain of oxygen vacancies rather than the isolated ones. In a simplistic model, we assume that the chain is formed due to the single oxygen vacancies or F-centers. Additional characterizations of the localized states due to the oxygen vacancies are also performed using ST-FMR technique.

From the continuous mode STT switching experiments we observed that: i) P(AP) states of these devices exhibit ‘nearly ohmic’ (‘semiconducting’) features, ii) STT parameters (both P >AP and AP >P) decrease with an increase in the temperature, and iii) AP >P switching happens at relatively lower values of the critical current (voltage/current density) than P >AP switching. To know whether these results are a consequence of the oxygen vacancies, the DFT-calculations are performed. The charge density plots, incorporating the zig-zag oxygen vacancy chain (ZZCOV, as inferred from the $\hat{I}$- spectroscopy technique) formed due to the chain of single oxygen vacancies or F-center into the MgO layer, successfully addressed the ‘nearly ohmic’ and ‘semiconducting’ transport in the respective P and AP state. The decrease in the STT parameters (both P >AP and AP >P) with an increase in the temperature might be linked with the temperature-dependent magnetic anisotropy variation of FM electrodes. Although the incorporation of ZZCOV into the DFT calculations explains the observed two different modes of transport i.e. ‘nearly ohmic’ and ‘semiconducting transport’ in the nanopillar MTJs respective P and AP states, could not be able to explain explicitly why the AP >P switching happens at relatively lower input critical current density than its P >AP counterpart. To conclude, in our CoFeB|MgO|CoFeB nanopillar devices with R.A product of ~20-30 $\Omega.\mu m^2$, the low barrier heights (~0.7/0.4eV, measured experimentally from $\hat{I}$-plots, and ~0.45eV, calculated theoretically using Brinkman fit) and high TMR (~136%) leading to STT are more likely the results of a nanotransport path such as a zig-zag chain of oxygen vacancies that spans the junction’s MgO barrier.

Moving to part-II of the thesis, we have shown how the spintronic devices based out of the organic molecule (used as an active layer or spacer layer), can provide additional advantages over their inorganic counterparts. To experimentally realize these organic molecule-based inorganic-organic or the hybrid spintronic devices, I have designed a new setup for an alternative lithography technique called 'nanobead processing', chemically optimized the silica nanosphere size used as a shadow mask (to define the nanopillar underneath), and performed countless dry etching processes to fabricate the hybrid nanopillar junctions. To control the number of deposited silica nanobeads (served as a shadow mask during the etching step) and their precise location on the top of the capping surface of the hybrid stacks, the AFM nanomanipulations were also performed. To further improve the nanobead processing the 'dip-pen lithography' setup was designed, optimized, and demonstrated to achieve the working hybrid nanopillars. These processed hybrid nanopillar devices were studied for the 'information encoding' and 'energy harvesting' applications. Out of the aforementioned studies, this thesis contains only the former one i.e. the 'information encoding' application of these devices. The trilayer nanopillar devices of 500nm cross-sectional area, used in this study contain two FM electrodes Fe (bottom) and Co (top) separated by CoPc molecular layer (spacer layer). Using the inelastic tunneling spectroscopy (IETS) technique performed on the Fe|CoPc|Co nanopillar junctions, below a temperature corresponding to the molecular spin chain's magnetic anisotropy, the spin chain can be excited electrically. The electrically induced spin-flip excited state of the CoPc molecule causes a reversal in the sign of the total spin of the CoPc molecules therefore in the exchange coupling (*J*) between the adjacent CoPc molecules. The reversal of *J* modifies the magnetic correlations (AFM → FM) between the adjacent molecules of CoPc and contributes to an additional magnetoresistance (MR) term i.e. MR_{ES} (excited state MR). This additional MR term i.e. MR_{ES} has the opposite sign to the ground state MR (MR_{GS}), and spectroscopically tracks the differential conductance (dI/dV) of the spin-flip excitations. Since MR encodes the magnetic input signal into an electrical output signal, therefore the presence of the additional MR term i.e. the MR_{ES} in these hybrid spintronic devices brings additional advantages over the MgO-based spintronics devices or other inorganic counterparts. Furthermore, this MR_{ES} term appears only at or above a certain value of applied bias (required to drive the spin-flip excitations within CoPc molecules) hence is electrically driven and therefore can be considered as a potential alternative of the STT/spin-orbit torque.

These hybrid nanodevices with defect states (Co^{2+} paramagnetic centers) in the CoPc spacer layer have been found to generate spontaneous energy at room temperature[233]. The origin of the observed effect is of quantum nature and therefore these devices are popularly known as the 'quantum engines' or 'spintronic engines'[29–31]. The working mechanism of these spintronic engines however not very clear. We hope that this research work[233] including the past research works done by other groups, would inspire other researchers to better understand the working mechanism behind these devices to further increase their efficiency or output. We hope that this research direction would be able to mitigate the energy crisis of our society up to a certain extent.

Bibliography:

[1] Velev J P, Belashchenko K D, Jaswal S S and Tsymbal E Y 2007 Effect of oxygen vacancies on spin-dependent tunneling in Fe∕MgO∕Fe magnetic tunnel junctions *Applied Physics Letters* **90** 072502

[2] Velev J P, Zhuravlev M Ye, Belashchenko K D, Jaswal S S, Tsymbal E Y, Katayama T and Yuasa S 2007 Defect-Mediated Properties of Magnetic Tunnel Junctions *IEEE Transactions on Magnetics* **43** 2770–5

[3] McKenna K P and Blumberger J 2012 Crossover from incoherent to coherent electron tunneling between defects in MgO *Physical Review B* **86** 245110

[4] Taudul B, Monteblanco E N, Halisdemir U, Lacour D, Schleicher F, Montaigne F, Beaurepaire E, Boukari S, Hehn M, Alouani M and Bowen M 2017 Tunneling Spintronics across MgO Driven by Double Oxygen Vacancies *Advanced Electronic Materials* **3** 1600390

[5] Moodera J S, Kinder L R, Wong T M and Meservey R 1995 Large Magnetoresistance at Room Temperature in Ferromagnetic Thin Film Tunnel Junctions *Physical Review Letters* **74** 3273–6

[6] Slonczewski J C 1996 Current-driven excitation of magnetic multilayers *Journal of Magnetism and Magnetic Materials* **159** L1–7

[7] Berger L 1996 Emission of spin waves by a magnetic multilayer traversed by a current *Physical Review B* **54** 9353–8

[8] Kent A D and Worledge D C 2015 A new spin on magnetic memories *Nature Nanotechnology* **10** 187–91

[9] Torrejon J, Riou M, Araujo F A, Tsunegi S, Khalsa G, Querlioz D, Bortolotti P, Cros V, Yakushiji K, Fukushima A, Kubota H, Yuasa S, Stiles M D and Grollier J 2017 Neuromorphic computing with nanoscale spintronic oscillators *Nature* **547** 428–31

[10] Romera M, Talatchian P, Tsunegi S, Abreu Araujo F, Cros V, Bortolotti P, Trastoy J, Yakushiji K, Fukushima A, Kubota H, Yuasa S, Ernoult M, Vodenicarevic D, Hirtzlin T, Locatelli N, Querlioz D and Grollier J 2018 Vowel recognition with four coupled spin-torque nano-oscillators *Nature* **563** 230–4

[11] Ralph D C and Stiles M D 2008 Spin transfer torques *Journal of Magnetism and Magnetic Materials* **320** 1190–216

[12] Tsoi M 2008 Spin-torque measured up *Nature Physics* **4** 17–8

[13] Gibson A, Haydock R and LaFemina J P 1994 Stability of vacancy defects in MgO: The role of charge neutrality *Phys. Rev. B* **50** 2582–92

[14] Rosenblatt G H, Rowe M W, Williams G P, Williams R T and Chen Y 1989 Luminescence of F and F+ centers in magnesium oxide *Physical Review B* **39** 10309–18

[15] Rottländer P, Hehn M and Schuhl A 2002 Determining the interfacial barrier height and its relation to tunnel magnetoresistance *Phys. Rev. B* **65** 054422

[16] Kubota H, Fukushima A, Yakushiji K, Nagahama T, Yuasa S, Ando K, Maehara H, Nagamine Y, Tsunekawa K, Djayaprawira D D, Watanabe N and Suzuki Y 2008 Quantitative measurement of voltage dependence of spin-transfer torque in MgO-based magnetic tunnel junctions *Nature Physics* **4** 37–41

[17] Hohenberg P and Kohn W 1964 Inhomogeneous Electron Gas *Phys. Rev.* **136** B864–71

[18] Dediu V, Murgia M, Matacotta F C, Taliani C and Barbanera S 2002 Room temperature spin polarized injection in organic semiconductor *Solid State Communications* **122** 181–4

[19] Xiong Z H, Wu D, Vardeny Z V and Shi J 2004 Giant magnetoresistance in organic spin-valves *Nature* **427** 4

[20] Sanvito S 2010 The rise of spinterface science: Molecular spintronics *Nature Physics* **6** 562–4

[21] Schmaus S, Bagrets A, Nahas Y, Yamada T K, Bork A, Bowen M, Beaurepaire E, Evers F and Wulfhekel W 2011 Giant magnetoresistance through a single molecule *Nature Nanotechnology* **6** 185–9

[22] Delprat S, Galbiati M, Tatay S, Quinard B, Barraud C, Petroff F, Seneor P and Mattana R 2018 Molecular spintronics: the role of spin-dependent hybridization *J. Phys. D: Appl. Phys.* **51** 473001

[23] Chen X, Fu Y-S, Ji S-H, Zhang T, Cheng P, Ma X-C, Zou X-L, Duan W-H, Jia J-F and Xue Q-K 2008 Probing Superexchange Interaction in Molecular Magnets by Spin-Flip Spectroscopy and Microscopy *Physical Review Letters* **101** 197208

[24] Serri M, Wu W, Fleet L R, Harrison N M, Hirjibehedin C F, Kay C W M, Fisher A J, Aeppli G and Heutz S 2014 High-temperature antiferromagnetism in molecular semiconductor thin films and nanostructures *Nature Communications* **5** 3079–87

[25] Brede J, Atodiresei N, Kuck S, Lazić P, Caciuc V, Morikawa Y, Hoffmann G, Blügel S and Wiesendanger R 2010 Spin- and Energy-Dependent Tunneling through a Single Molecule with Intramolecular Spatial Resolution *Phys. Rev. Lett.* **105** 047204

[26] Loth S, Lutz C P and Heinrich A J 2010 Spin-polarized spin excitation spectroscopy *New J. Phys.* **12** 125021

[27] Thierschmann H, Sánchez R, Sothmann B, Arnold F, Heyn C, Hansen W, Buhmann H and Molenkamp L W 2015 Three-terminal energy harvester with coupled quantum dots *Nature Nanotech* **10** 854–8

[28] Sánchez R and Büttiker M 2011 Optimal energy quanta to current conversion *Phys. Rev. B* **83** 085428

[29] Katcko K, Urbain E, Taudul B, Schleicher F, Arabski J, Beaurepaire E, Vileno B, Spor D, Weber W, Lacour D, Boukari S, Hehn M, Alouani M, Fransson J and Bowen M 2019 Spin-driven electrical power generation at room temperature *Commun Phys* **2** 116

[30] Hai P N, Ohya S, Tanaka M, Barnes S E and Maekawa S 2009 Electromotive force and huge magnetoresistance in magnetic tunnel junctions *Nature* **458** 489–92

[31] Miao G-X, Chang J, Assaf B A, Heiman D and Moodera J S 2014 Spin regulation in composite spin-filter barrier devices *Nat Commun* **5** 3682

[32] Wang W G, Pearse A, Li M, Hageman S, Chen A X, Zhu F Q and Chien C L 2013 Parallel fabrication of magnetic tunnel junction nanopillars by nanosphere lithography *Scientific Reports* **3** 1948

[33] Katcko K, Urbain E, Ngassam F, Kandpal L, Chowrira B, Schleicher F, Halisdemir U, Wang D, Scherer T, Mertz D, Leconte B, Beyer N, Spor D, Panissod P, Boulard A, Arabski J, Kieber C, Sternitzky E, Da Costa V, Hehn M, Montaigne F, Bahouka A, Weber W, Beaurepaire E, Kübel C, Lacour D, Alouani M, Boukari S and Bowen M 2021 Encoding Information on the Excited State of a Molecular Spin Chain *Adv. Funct. Mater.* **31** 2009467

[34] Baibich M N, Broto J M, Fert A, Van Dau F N, Petroff F, Etienne P, Creuzet G, Friederich A and Chazelas J 1988 Giant Magnetoresistance of (001)Fe/(001)Cr Magnetic Superlattices *Physical Review Letters* **61** 2472–5

[35] Binasch G, Grünberg P, Saurenbach F and Zinn W 1989 Enhanced magnetoresistance in layered magnetic structures with antiferromagnetic interlayer exchange *Physical Review B* **39** 4828–30

[36] Jullière M 1975 Tunneling between ferromagnetic films *Physics Letters A* **54** 225–6

[37] Miyazaki T and Tezuka N 1995 Giant magnetic tunneling effect in Fe/Al2O3/Fejunction *Journal of Magnetism and Magnetic Materials* **139** L231–4

[38] Simmons J G 1963 Generalized Formula for the Electric Tunnel Effect between Similar Electrodes Separated by a Thin Insulating Film *Journal of Applied Physics* **34** 1793–803

[39] Brinkman W F, Dynes R C and Rowell J M 1970 Tunneling Conductance of Asymmetrical Barriers *Journal of Applied Physics* **41** 1915–21

[40] Meservey R and Tedrow P M 1972 Spin polarization of tunneling electrons from films of Fe, Co, Ni, and Gd *Solid State Communications* **11** 333–6

[41] Halisdemir U 2016 *Probing the impact of structural defects on spin dependent tunneling using photons* PhD Thesis (Université de Strasbourg)

[42] LeClair P R 2002 *Fundamental aspects of spin polarized tunneling : magnetic tunnel junctions and spin filters* PhD Thesis (Eindhoven University of Technology)

[43] Tedrow P M and Meservey R 1973 Spin Polarization of Electrons Tunneling from Films of Fe, Co, Ni, and Gd *Phys. Rev. B* **7** 318–26

[44] Yuasa S and Djayaprawira D D 2007 Giant tunnel magnetoresistance in magnetic tunnel junctions with a crystalline MgO(001) barrier *Journal of Physics D: Applied Physics* **40** R337–54

[45] Klaua M, Ullmann D, Barthel J, Wulfhekel W, Kirschner J, Urban R, Monchesky T L, Enders A, Cochran J F and Heinrich B 2001 Growth, structure, electronic, and magnetic properties of MgO/Fe(001) bilayers and Fe/MgO/Fe(001) trilayers *Physical Review B* **64** 134411

[46] Korringa J 1947 On the calculation of the energy of a Bloch wave in a metal *Physica* **13** 392–400

[47] Butler W, Zhang X-G, Schulthess T and MacLaren J 2001 Spin-dependent tunneling conductance of Fe|MgO|Fe sandwiches *Physical Review B* **63** 054416

[48] Landauer R 1987 Electrical transport in open and closed systems *Z. Physik B - Condensed Matter* **68** 217–28

[49] Büttiker M, Imry Y, Landauer R and Pinhas S 1985 Generalized many-channel conductance formula with application to small rings *Phys. Rev. B* **31** 6207–15

[50] Zhang X-G and Butler W H 2003 Band structure, evanescent states, and transport in spin tunnel junctions *Journal of Physics: Condensed Matter* **15** R1603–39

[51] Butler W H, Zhang X-G, Schulthess T C and MacLaren J M 2001 Reduction of electron tunneling current due to lateral variation of the wave function *Physical Review B* **63** 092402

[52] Tiusan C, Greullet F, Hehn M, Montaigne F, Andrieu S and Schuhl A 2007 Spin tunnelling phenomena in single-crystal magnetic tunnel junction systems *Journal of Physics: Condensed Matter* **19** 165201

[53] Mavropoulos Ph, Papanikolaou N and Dederichs P H 2000 Complex Band Structure and Tunneling through Ferromagnet/Insulator/Ferromagnet Junctions *Physical Review Letters* **85** 1088–91

[54] Dederichs P H, Mavropoulos Ph, Wunnicke O, Papanikolaou N, Bellini V, Zeller R, Drchal V and Kudrnovský J 2002 Importance of complex band structure and resonant states for tunneling *Journal of Magnetism and Magnetic Materials* **240** 108–13

[55] Butler W H 2008 Tunneling magnetoresistance from a symmetry filtering effect *Science and Technology of Advanced Materials* **9** 014106

[56] Zhang X-G and Butler W H 2004 Large magnetoresistance in bcc Co⁄MgO⁄Co and FeCo⁄MgO⁄FeCo tunnel junctions *Physical Review B* **70** 172407

[57] Papaconstantopoulos D A 2015 *Handbook of the Band Structure of Elemental Solids* (Boston, MA: Springer US)

[58] Bowen M, Cros V, Petroff F, Fert A, Martínez Boubeta C, Costa-Krämer J L, Anguita J V, Cebollada A, Briones F, de Teresa J M, Morellón L, Ibarra M R, Güell F, Peiró F and Cornet A 2001 Large magnetoresistance in Fe/MgO/FeCo(001) epitaxial tunnel junctions on GaAs(001) *Applied Physics Letters* **79** 1655–7

[59] Faure-Vincent J, Tiusan C, Jouguelet E, Canet F, Sajieddine M, Bellouard C, Popova E, Hehn M, Montaigne F and Schuhl A 2003 High tunnel magnetoresistance in epitaxial Fe/MgO/Fe tunnel junctions *Applied Physics Letters* **82** 4507–9

[60] Yuasa S, Nagahama T, Fukushima A, Suzuki Y and Ando K 2004 Giant room-temperature magnetoresistance in single-crystal Fe/MgO/Fe magnetic tunnel junctions *Nature Materials* **3** 868–71

[61] Herman M A and Sitter H 1989 *Molecular Beam Epitaxy* vol 7 (Berlin, Heidelberg: Springer Berlin Heidelberg)

[62] Parkin S S P, Kaiser C, Panchula A, Rice P M, Hughes B, Samant M and Yang S-H 2004 Giant tunnelling magnetoresistance at room temperature with MgO (100) tunnel barriers *Nature Materials* **3** 862–7

[63] Djayaprawira D D, Tsunekawa K, Nagai M, Maehara H, Yamagata S, Watanabe N, Yuasa S, Suzuki Y and Ando K 2005 230% room-temperature magnetoresistance in CoFeB⁄MgO⁄CoFeB magnetic tunnel junctions *Applied Physics Letters* **86** 092502

[64] Yuasa S, Suzuki Y, Katayama T and Ando K 2005 Characterization of growth and crystallization processes in CoFeB⁄MgO⁄CoFeB magnetic tunnel junction structure by reflective high-energy electron diffraction *Applied Physics Letters* **87** 242503

[65] Hayakawa J, Ikeda S, Lee Y M, Matsukura F and Ohno H 2006 Effect of high annealing temperature on giant tunnel magnetoresistance ratio of CoFeB⁄MgO⁄CoFeB magnetic tunnel junctions *Applied Physics Letters* **89** 232510

[66] Mathon J and Umerski A 2001 Theory of tunneling magnetoresistance of an epitaxial Fe/MgO/Fe(001) junction *Phys. Rev. B* **63** 220403

[67] Lee Y M, Hayakawa J, Ikeda S, Matsukura F and Ohno H 2007 Effect of electrode composition on the tunnel magnetoresistance of pseudo-spin-valve magnetic tunnel junction with a MgO tunnel barrier *Applied Physics Letters* **90** 212507

[68] Ikeda S, Hayakawa J, Ashizawa Y, Lee Y M, Miura K, Hasegawa H, Tsunoda M, Matsukura F and Ohno H 2008 Tunnel magnetoresistance of 604% at 300K by suppression

of Ta diffusion in CoFeB⁄MgO⁄CoFeB pseudo-spin-valves annealed at high temperature *Applied Physics Letters* **93** 082508

[69] Kittel C 2012 *Introduction to Solid State Physics, 8ed* (Wiley)

[70] David N, University C and Ashcroft N W 2003 *Solid State Physics* (New Delhi: Cengage)

[71] Meyerheim H L, Popescu R, Kirschner J, Jedrecy N, Sauvage-Simkin M, Heinrich B and Pinchaux R 2001 Geometrical and Compositional Structure at Metal-Oxide Interfaces: MgO on Fe(001) *Physical Review Letters* **87** 076102

[72] Zhang X-G, Butler W H and Bandyopadhyay A 2003 Effects of the iron-oxide layer in Fe-FeO-MgO-Fe tunneling junctions *Physical Review B* **68** 092402

[73] Bonell F, Andrieu S, Bataille A M, Tiusan C and Lengaigne G 2009 Consequences of interfacial Fe-O bonding and disorder in epitaxial Fe/MgO/Fe(001) magnetic tunnel junctions *Physical Review B* **79** 224405

[74] Mizuguchi M, Suzuki Y, Nagahama T and Yuasa S 2007 In situ scanning tunneling microscopy observations of polycrystalline MgO(001) tunneling barriers grown on amorphous CoFeB electrode *Appl. Phys. Lett.* **91** 012507

[75] Bean J J, Saito M, Fukami S, Sato H, Ikeda S, Ohno H, Ikuhara Y and McKenna K P 2017 Atomic structure and electronic properties of MgO grain boundaries in tunnelling magnetoresistive devices *Sci Rep* **7** 45594

[76] Read J C, Mather P G and Buhrman R A 2007 X-ray photoemission study of CoFeB⁄MgO thin film bilayers *Applied Physics Letters* **90** 132503

[77] Cha J J, Read J C, Egelhoff W F, Huang P Y, Tseng H W, Li Y, Buhrman R A and Muller D A 2009 Atomic-scale spectroscopic imaging of CoFeB/Mg–B–O/CoFeB magnetic tunnel junctions *Applied Physics Letters* **95** 032506

[78] Bai Z, Shen L, Wu Q, Zeng M, Wang J-S, Han G and Feng Y P 2013 Boron diffusion induced symmetry reduction and scattering in CoFeB/MgO/CoFeB magnetic tunnel junctions *Physical Review B* **87** 014114

[79] Wang Z, Saito M, McKenna K P, Fukami S, Sato H, Ikeda S, Ohno H and Ikuhara Y 2016 Atomic-Scale Structure and Local Chemistry of CoFeB–MgO Magnetic Tunnel Junctions *Nano Letters* **16** 1530–6

[80] Karthik S V, Takahashi Y K, Ohkubo T, Hono K, Ikeda S and Ohno H 2009 Transmission electron microscopy investigation of CoFeB/MgO/CoFeB pseudospin valves annealed at different temperatures *Journal of Applied Physics* **106** 023920

[81] Burton J D, Jaswal S S, Tsymbal E Y, Mryasov O N and Heinonen O G 2006 Atomic and electronic structure of the CoFeB⁄MgO interface from first principles *Appl. Phys. Lett.* **89** 142507

[82] Han Y, Han J, Choi H J, Shin H-J and Hong J 2012 Effect of Diffused B During Annealing on the Electronic Structure of the MgO Barrier in CoFeB/MgO/CoFeB Magnetic Tunnel Junctions *Appl. Phys. Express* **5** 033001

[83] Kurt H, Rode K, Oguz K, Boese M, Faulkner C C and Coey J M D 2010 Boron diffusion in magnetic tunnel junctions with MgO (001) barriers and CoFeB electrodes *Appl. Phys. Lett.* **96** 262501

[84] Mukherjee S, Knut R, Mohseni S M, Anh Nguyen T N, Chung S, Tuan Le Q, Åkerman J, Persson J, Sahoo A, Hazarika A, Pal B, Thiess S, Gorgoi M, Anil Kumar P S, Drube W, Karis O and Sarma D D 2015 Role of boron diffusion in CoFeB/MgO magnetic tunnel junctions *Phys. Rev. B* **91** 085311

[85] Taudul B 2017 *Impact of symmetry of oxygen vacancies on electronic transport in MgO-based magnetic tunnel junctions* PhD Thesis (Université de Strasbourg)

[86] Schleicher F, Halisdemir U, Lacour D, Gallart M, Boukari S, Schmerber G, Davesne V, Panissod P, Halley D, Majjad H, Henry Y, Leconte B, Boulard A, Spor D, Beyer N, Kieber C, Sternitzky E, Cregut O, Ziegler M, Montaigne F, Beaurepaire E, Gilliot P, Hehn M and Bowen M 2014 Localized states in advanced dielectrics from the vantage of spin- and symmetry-polarized tunnelling across MgO *Nature Communications* **5** 4547–55

[87] Miao G X, Park Y J, Moodera J S, Seibt M, Eilers G and Münzenberg M 2008 Disturbance of Tunneling Coherence by Oxygen Vacancy in Epitaxial Fe/MgO/Fe Magnetic Tunnel Junctions *Phys. Rev. Lett.* **100** 246803

[88] Mitani S, Moriyama T and Takanashi K 2003 Fe/MgO/FeCo(100) epitaxial magnetic tunnel junctions prepared by using *in situ* plasma oxidation *Journal of Applied Physics* **93** 8041–3

[89] Teixeira J M, Ventura J, Araujo J P, Sousa J B, Fernández-García M P, Wisniowski P and Freitas P P 2010 Evidence of spin-polarized direct elastic tunneling and onset of superparamagnetism in MgO magnetic tunnel junctions *Phys. Rev. B* **81** 134423

[90] Newton M D 1991 Quantum chemical probes of electron-transfer kinetics: the nature of donor-acceptor interactions *Chem. Rev.* **91** 767–92

[91] Taudul B, Bowen M and Alouani M 2020 Impact of single and double oxygen vacancies on electronic transport in Fe/MgO/Fe magnetic tunnel junctions *Journal of Applied Physics* **128** 143902

[92] Teixeira J M, Ventura J, Araujo J P, Sousa J B, Wisniowski P, Cardoso S and Freitas P P 2011 Resonant Tunneling through Electronic Trapping States in Thin MgO Magnetic Junctions *Phys. Rev. Lett.* **106** 196601

[93] Smogunov A, Dal Corso A and Tosatti E 2004 Ballistic conductance of magnetic Co and Ni nanowires with ultrasoft pseudopotentials *Phys. Rev. B* **70** 045417

[94] Giannozzi P, Baroni S, Bonini N, Calandra M, Car R, Cavazzoni C, Ceresoli D, Chiarotti G L, Cococcioni M, Dabo I, Corso A D, Gironcoli S de, Fabris S, Fratesi G, Gebauer R, Gerstmann U, Gougoussis C, Kokalj A, Lazzeri M, Martin-Samos L, Marzari N, Mauri F, Mazzarello R, Paolini S, Pasquarello A, Paulatto L, Sbraccia C, Scandolo S, Sclauzero G, Seitsonen A P, Smogunov A, Umari P and Wentzcovitch R M 2009 QUANTUM ESPRESSO: a modular and open-source software project for quantum simulations of materials *J. Phys.: Condens. Matter* **21** 395502

[95] Kim D J, Choi W S, Schleicher F, Shin R H, Boukari S, Davesne V, Kieber C, Arabski J, Schmerber G, Beaurepaire E, Jo W and Bowen M 2010 Control of defect-mediated tunneling barrier heights in ultrathin MgO films *Applied Physics Letters* **97** 263502

[96] Halisdemir U, Schleicher F, Kim D J, Taudul B, Lacour D, Choi W S, Gallart M, Boukari S, Schmerber G, Davesne V, Panissod P, Halley D, Majjad H, Henry Y, Leconte B, Boulard A, Spor D, Beyer N, Kieber C, Sternitzky E, Cregut O, Ziegler M, Montaigne F, Arabski J, Beaurepaire E, Jo W, Alouani M, Gilliot P, Hehn M and Bowen M 2016 Oxygen-vacancy driven tunnelling spintronics across MgO *SPIE* Spintronics IX vol 9931, ed H-J Drouhin, J-E Wegrowe and M Razeghi p 99310H

[97] Krzysteczko P, Münchenberger J, Schäfers M, Reiss G and Thomas A 2012 The Memristive Magnetic Tunnel Junction as a Nanoscopic Synapse-Neuron System *Advanced Materials* **24** 762–6

[98] Krishnan K M 2016 *Fundamentals and applications of magnetic materials* (Oxford, United Kingdom: Oxford University Press)

[99] Ogrodnik P, Wilczyński M, Świrkowicz R and Barnaś J 2010 Spin transfer torque and magnetic dynamics in tunnel junctions *Phys. Rev. B* **82** 134412

[100] Wang S-Z and Xia K 2016 Electric and thermal spin torque across disordered FeCo/MgO/FeCo magnetic tunnel junctions *Phys. Rev. B* **93** 184414

[101] Jia X, Xia K, Ke Y and Guo H 2011 Nonlinear bias dependence of spin-transfer torque from atomic first principles *Phys. Rev. B* **84** 014401

[102] Costa J D, Serrano-Guisan S, Lacoste B, Jenkins A S, Böhnert T, Tarequzzaman M, Borme J, Deepak F L, Paz E, Ventura J, Ferreira R and Freitas P P 2017 High power and low critical current density spin transfer torque nano-oscillators using MgO barriers with intermediate thickness *Scientific Reports* **7** 7237

[103] Dieny B, Prejbeanu I L, Garello K, Gambardella P, Freitas P, Lehndorff R, Raberg W, Ebels U, Demokritov S O, Akerman J, Deac A, Pirro P, Adelmann C, Anane A, Chumak A V, Hirohata A, Mangin S, Valenzuela S O, Onbaşlı M C, d'Aquino M, Prenat G, Finocchio G, Lopez-Diaz L, Chantrell R, Chubykalo-Fesenko O and Bortolotti P 2020 Opportunities and challenges for spintronics in the microelectronics industry *Nature Electronics* **3** 446–59

[104] Silva T J and Rippard W H 2008 Developments in nano-oscillators based upon spin-transfer point-contact devices *Journal of Magnetism and Magnetic Materials* **320** 1260–71

[105] Kiselev S I, Sankey J C, Krivorotov I N, Emley N C, Schoelkopf R J, Buhrman R A and Ralph D C 2003 Microwave oscillations of a nanomagnet driven by a spin-polarized current *Nature* **425** 380–3

[106] Mancoff F B, Rizzo N D, Engel B N and Tehrani S 2005 Phase-locking in double-point-contact spin-transfer devices *Nature* **437** 393–5

[107] Tiwari D 2018 *Spin Torque Ferromagnetic Resonance in Magnetic Tunnel Junctions and Ferromagnetic/Non-magnetic Bilayers* PhD Thesis (IIT-Delhi)

[108] Tulapurkar A A, Suzuki Y, Fukushima A, Kubota H, Maehara H, Tsunekawa K, Djayaprawira D D, Watanabe N and Yuasa S 2005 Spin-torque diode effect in magnetic tunnel junctions *Nature* **438** 339–42

[109] Sankey J C, Cui Y-T, Sun J Z, Slonczewski J C, Buhrman R A and Ralph D C 2008 Measurement of the spin-transfer-torque vector in magnetic tunnel junctions *Nature Physics* **4** 67–71

[110] Sankey J C, Braganca P M, Garcia A G F, Krivorotov I N, Buhrman R A and Ralph D C 2006 Spin-Transfer-Driven Ferromagnetic Resonance of Individual Nanomagnets *Phys. Rev. Lett.* **96** 227601

[111] Nembach H T, Shaw J M, Boone C T and Silva T J 2013 Mode- and Size-Dependent Landau-Lifshitz Damping in Magnetic Nanostructures: Evidence for Nonlocal Damping *Phys. Rev. Lett.* **110** 117201

[112] Maruyama T, Shiota Y, Nozaki T, Ohta K, Toda N, Mizuguchi M, Tulapurkar A A, Shinjo T, Shiraishi M, Mizukami S, Ando Y and Suzuki Y 2009 Large voltage-induced magnetic anisotropy change in a few atomic layers of iron *Nature Nanotech* **4** 158–61

[113] Tsoi M, Jansen A G M, Bass J, Chiang W-C, Seck M, Tsoi V and Wyder P 1998 Excitation of a Magnetic Multilayer by an Electric Current *Physical Review Letters* **80** 4281–4

[114] Wang C, Cui Y-T, Sun J Z, Katine J A, Buhrman R A and Ralph D C 2009 Bias and angular dependence of spin-transfer torque in magnetic tunnel junctions *Physical Review B* **79** 224416

[115] Tiwari D, Sisodia N, Sharma R, Dürrenfeld P, Åkerman J and Muduli P K 2016 Enhancement of spin-torque diode sensitivity in a magnetic tunnel junction by parametric synchronization *Appl. Phys. Lett.* **108** 082402

[116] Gonçalves A M, Barsukov I, Chen Y-J, Yang L, Katine J A and Krivorotov I N 2013 Spin torque ferromagnetic resonance with magnetic field modulation *Appl. Phys. Lett.* **103** 172406

[117] Bernos J, Hehn M, Montaigne F, Tiusan C, Lacour D, Alnot M, Negulescu B, Lengaigne G, Snoeck E and Aliev F G 2010 Impact of electron-electron interactions induced by disorder at interfaces on spin-dependent tunneling in Co-Fe-B/MgO/Co-Fe-B magnetic tunnel junctions *Physical Review B* **82** 060405(R)

[118] Tsunekawa K, Choi Y-S, Nagamine Y, Djayaprawira D D, Takeuchi T and Kitamoto Y 2006 Influence of Chemical Composition of CoFeB on Tunneling Magnetoresistance and Microstructure in Polycrystalline CoFeB/MgO/CoFeB Magnetic Tunnel Junctions *Jpn. J. Appl. Phys.* **45** L1152–5

[119] Schleicher F, Taudul B, Halisdemir U, Katcko K, Monteblanco E, Lacour D, Boukari S, Montaigne F, Urbain E, Kandpal L M, Arabski J, Weber W, Beaurepaire E, Hehn M, Alouani M and Bowen M 2019 Consolidated picture of tunnelling spintronics across oxygen vacancy states in MgO *J. Phys. D: Appl. Phys.* **52** 305302

[120] Schleicher F, Halisdemir U, Urbain E, Lacour D, Gallart M, Boukari S, Montaigne F, Beaurepaire E, Gilliot P, Hehn M and Bowen M 2015 MgO magnetic tunnel junctions of enduring F-type upon annealing *Journal of Physics D: Applied Physics* **48** 435004

[121] Zhang C, Zhang X-G, Krstić P S, Cheng H, Butler W H and MacLaren J M 2004 Electronic structure and spin-dependent tunneling conductance under a finite bias *Physical Review B* **69** 134406

[122] Yuasa S, Fukushima A, Kubota H, Suzuki Y and Ando K 2006 Giant tunneling magnetoresistance up to 410% at room temperature in fully epitaxial Co⁄MgO⁄Co magnetic tunnel junctions with bcc Co(001) electrodes *Applied Physics Letters* **89** 042505

[123] Ando Y, Miyakoshi T, Oogane M, Miyazaki T, Kubota H, Ando K and Yuasa S 2005 Spin-dependent tunneling spectroscopy in single-crystal Fe⁄MgO⁄Fe tunnel junctions *Applied Physics Letters* **87** 142502

[124] Gundlach K H 1973 Theory of metal-insulator-metal tunneling for a simple two-band model *Journal of Applied Physics* **44** 5005–10

[125] Heyd J, Scuseria G E and Ernzerhof M 2003 Hybrid functionals based on a screened Coulomb potential *The Journal of Chemical Physics* **118** 8207–15

[126] Ohtomo A, Muller D A, Grazul J L and Hwang H Y 2002 Artificial charge-modulationin atomic-scale perovskite titanate superlattices *Nature* **419** 378–80

[127] Halisdemir U, Schleicher F, Kim D J, Taudul B, Lacour D, Choi W S, Gallart M, Boukari S, Schmerber G, Davesne V, Panissod P, Halley D, Majjad H, Henry Y, Leconte B, Boulard A, Spor D, Beyer N, Kieber C, Sternitzky E, Cregut O, Ziegler M, Montaigne F, Arabski J, Beaurepaire E, Jo W, Alouani M, Gilliot P, Hehn M and Bowen M 2016 Oxygen-vacancy driven tunnelling spintronics across MgO *Spintronics IX* vol 9931 (International Society for Optics and Photonics) p 99310H

[128] Chen X and Victora R H 2007 Effect of pinholes in magnetic tunnel junctions *Appl. Phys. Lett.* **91** 212104

[129] Ventura J, Teixeira J M, Araujo J P, Sousa J B, Ferreira R, Freitas P P, Langer J, Ocker B and Maass W 2010 Influence of Pinholes on MgO-Tunnel Junction Barrier Parameters Obtained from Current–Voltage Characteristics *J. Nanosci. Nanotech.* **10** 2731–4

[130] Ventura J, Teixeira J M, Araujo J P, Sousa J B, Wisniowski P and Freitas P P 2008 Pinholes and temperature-dependent transport properties of MgO magnetic tunnel junctions *Phys. Rev. B* **78** 024403

[131] Teixeira J M, Ventura J, Carpinteiro F, Araujo J P, Sousa J B, Wisniowski P and Freitas P P 2009 The effect of pinhole formation/growth on the tunnel magnetoresistance of MgO-based magnetic tunnel junctions *Journal of Applied Physics* **106** 073707

[132] Lu Y, Tran M, Jaffrès H, Seneor P, Deranlot C, Petroff F, George J-M, Lépine B, Ababou S and Jézéquel G 2009 Spin-Polarized Inelastic Tunneling through Insulating Barriers *Phys. Rev. Lett.* **102** 176801

[133] Heine V 1965 Theory of Surface States *Phys. Rev.* **138** A1689–96

[134] Ikeda S, Miura K, Yamamoto H, Mizunuma K, Gan H D, Endo M, Kanai S, Hayakawa J, Matsukura F and Ohno H 2010 A perpendicular-anisotropy CoFeB–MgO magnetic tunnel junction *Nature Materials* **9** 721–4

[135] Slonczewski J C 1999 Excitation of spin waves by an electric current *Journal of Magnetism and Magnetic Materials* **195** L261–8

[136] Deka A, Rana B, Anami R, Miura K, Takahashi H, Otani Y and Fukuma Y 2020 Electric-field control of interfacial in-plane magnetic anisotropy in CoFeB/MgO junctions *Phys. Rev. B* **101** 174405

[137] Sato H, Chureemart P, Matsukura F, Chantrell R W, Ohno H and Evans R F L 2018 Temperature-dependent properties of CoFeB/MgO thin films: Experiments versus simulations *Phys. Rev. B* **98** 214428

[138] Katayama T, Yuasa S, Velev J, Zhuravlev M Ye, Jaswal S S and Tsymbal E Y 2006 Interlayer exchange coupling in Fe⁄MgO⁄Fe magnetic tunnel junctions *Applied Physics Letters* **89** 112503

[139] Hayakawa J, Ikeda S, Matsukura F, Takahashi H and Ohno H 2005 Dependence of Giant Tunnel Magnetoresistance of Sputtered CoFeB/MgO/CoFeB Magnetic Tunnel Junctions on MgO Barrier Thickness and Annealing Temperature *Jpn. J. Appl. Phys.* **44** L587

[140] Studniarek M, Halisdemir U, Schleicher F, Taudul B, Urbain E, Boukari S, Hervé M, Lambert C-H, Hamadeh A, Petit-Watelot S, Zill O, Lacour D, Joly L, Scheurer F, Schmerber G, Da Costa V, Dixit A, Guitard P A, Acosta M, Leduc F, Choueikani F, Otero E, Wulfhekel

W, Montaigne F, Monteblanco E N, Arabski J, Ohresser P, Beaurepaire E, Weber W, Alouani M, Hehn M and Bowen M 2017 Probing a Device's Active Atoms *Adv. Mater.* **29** 1606578

[141] Kresse G and Furthmüller J 1996 Efficient iterative schemes for ab initio total-energy calculations using a plane-wave basis set *Phys. Rev. B* **54** 11169–86

[142] Kresse G and Joubert D 1999 From ultrasoft pseudopotentials to the projector augmented-wave method *Phys. Rev. B* **59** 1758–75

[143] Blöchl P E 1994 Projector augmented-wave method *Phys. Rev. B* **50** 17953–79

[144] Perdew J P, Burke K and Ernzerhof M 1996 Generalized Gradient Approximation Made Simple *Phys. Rev. Lett.* **77** 3865–8

[145] Katcko K 2019 *Sondage des nano-trajets inorganiques et organiques par du transport résolu en spin* PhD Thesis (Université de Strasbourg)

[146] McClure D S 1952 Spin-Orbit Interaction in Aromatic Molecules *J. Chem. Phys.* **20** 682–6

[147] Dediu V A, Hueso L E, Bergenti I and Taliani C 2009 Spin routes in organic semiconductors *Nature Materials* **8** 707–16

[148] Krinichnyi V I, Chemerisov S D and Lebedev Ya S 1997 EPR and charge-transport studies of polyaniline *Phys. Rev. B* **55** 16233–44

[149] Bader K, Winkler M and van Slageren J 2016 Tuning of molecular qubits: very long coherence and spin–lattice relaxation times *Chem. Commun.* **52** 3623–6

[150] Yu Z G 2014 Impurity-band transport in organic spin valves *Nature Communications* **5** 4842

[151] Zuppiroli L, Bussac M N, Paschen S, Chauvet O and Forro L 1994 Hopping in disordered conducting polymers *Phys. Rev. B* **50** 5196–203

[152] Naber W J M, Faez S and Wiel W G van der 2007 Organic spintronics *J. Phys. D: Appl. Phys.* **40** R205–28

[153] Barraud C, Seneor P, Mattana R, Fusil S, Bouzehouane K, Deranlot C, Graziosi P, Hueso L, Bergenti I, Dediu V, Petroff F and Fert A 2010 Unravelling the role of the interface for spin injection into organic semiconductors *Nature Physics* **6** 615–20

[154] Bowen M, Barthélémy A, Bibes M, Jacquet E, Contour J P, Fert A, Wortmann D and Blügel S 2005 Half-metallicity proven using fully spin-polarized tunnelling *J. Phys.: Condens. Matter* **17** L407–9

[155] Xu W, Szulczewski G J, LeClair P, Navarrete I, Schad R, Miao G, Guo H and Gupta A 2007 Tunneling magnetoresistance observed in La0.67Sr0.33MnO3/organic molecule/Co junctions *Appl. Phys. Lett.* **90** 072506

[156] Vinzelberg H, Schumann J, Elefant D, Gangineni R B, Thomas J and Büchner B 2008 Low temperature tunneling magnetoresistance on (La,Sr)MnO3⁄Co junctions with organic spacer layers *Journal of Applied Physics* **103** 093720

[157] Ciudad D, Gobbi M, Kinane C J, Eich M, Moodera J S and Hueso L E 2014 Sign Control of Magnetoresistance Through Chemically Engineered Interfaces *Adv. Mater.* **26** 7561–7

[158] Cinchetti M, Dediu V A and Hueso L E 2017 Activating the molecular spinterface *Nature Mater* **16** 507–15

[159] Boukari S, Jabbar H, Schleicher F, Gruber M, Avedissian G, Arabski J, Da Costa V, Schmerber G, Rengasamy P, Vileno B, Weber W, Bowen M and Beaurepaire E 2018 Disentangling Magnetic Hardening and Molecular Spin Chain Contributions to Exchange Bias in Ferromagnet/Molecule Bilayers *Nano Lett.* **18** 4659–63

[160] Braun A and Tcherniac J 1907 Über die Produkte der Einwirkung von Acetanhydrid auf Phthalamid *Berichte der deutschen chemischen Gesellschaft* **40** 2709–14

[161] Gruber M *Electronic and magnetic properties of hybrid interfaces. From single molecules to ultra-thin molecular films on metallic substrates.* PhD Thesis (Université de Strasbourg)

[162] Ballirano P, Caminiti R, Ercolani C, Maras A and Orrù M A 1998 X-ray Powder Diffraction Structure Reinvestigation of the α and β Forms of Cobalt Phthalocyanine and Kinetics of the α → β Phase Transition *J. Am. Chem. Soc.* **120** 12798–807

[163] Ashida M, Uyeda N and Suito E 1971 Thermal transformation of vacuum-condensed thin films of copper-phthalocyanine *Journal of Crystal Growth* **8** 45–56

[164] Heutz S, Mitra C, Wu W, Fisher A J, Kerridge A, Stoneham M, Harker A H, Gardener J, Tseng H-H, Jones T S, Renner C and Aeppli G 2007 Molecular Thin Films: A New Type of Magnetic Switch *Adv. Mater.* **19** 3618–22

[165] Gruber M, Ibrahim F, Boukari S, Isshiki H, Joly L, Peter M, Studniarek M, Da Costa V, Jabbar H, Davesne V, Halisdemir U, Chen J, Arabski J, Otero E, Choueikani F, Chen K, Ohresser P, Wulfhekel W, Scheurer F, Weber W, Alouani M, Beaurepaire E and Bowen M 2015 Exchange bias and room-temperature magnetic order in molecular layers *Nature Materials* **14** 981–4

[166] Fu Y-S, Zhang T, Ji S-H, Chen X, Ma X-C, Jia J-F and Xue Q-K 2009 Identifying Charge States of Molecules with Spin-Flip Spectroscopy *Phys. Rev. Lett.* **103** 257202

[167] Muenks M, Jacobson P, Ternes M and Kern K 2017 Correlation-driven transport asymmetries through coupled spins in a tunnel junction *Nat Commun* **8** 14119

[168] Meiklejohn W H and Bean C P 1956 New Magnetic Anisotropy *Phys. Rev.* **102** 1413–4

[169] Radu F 2005 *Fundamental aspects of exchange bias effect in AF/F bilayers and multilayers* PhD Thesis (Ruhr-Universität Bochum)

[170] Jo J, Byun J, Oh I, Park J, Jin M-J, Min B-C, Lee J and Yoo J-W 2019 Molecular Tunability of Magnetic Exchange Bias and Asymmetrical Magnetotransport in Metalloporphyrin/Co Hybrid Bilayers *ACS Nano* **13** 894–903

[171] Rocha A R, García-suárez V M, Bailey S W, Lambert C J, Ferrer J and Sanvito S 2005 Towards molecular spintronics *Nature Materials* **4** 335–9

[172] Teresa J M D, Barthélémy A, Fert A, Contour J P, Lyonnet R, Montaigne F, Seneor P and Vaurès A 1999 Inverse Tunnel Magnetoresistance in Co/SrTiO3/La0.7Sr0.3MnO3: New Ideas on Spin-Polarized Tunneling *Physical Review Letters* **82** 4

[173] Bouzehouane K, Fusil S, Bibes M, Carrey J, Blon T, Le Dû M, Seneor P, Cros V and Vila L 2003 Nanolithography Based on Real-Time Electrically Controlled Indentation with an Atomic Force Microscope for Nanocontact Elaboration *Nano Letters* **3** 1599–602

[174] Iacovita C, Rastei M V, Heinrich B W, Brumme T, Kortus J, Limot L and Bucher J P 2008 Visualizing the Spin of Individual Cobalt-Phthalocyanine Molecules *Physical Review Letters* **101** 116602

[175] Lach S, Altenhof A, Tarafder K, Schmitt F, Ali Md E, Vogel M, Sauther J, Oppeneer P M and Ziegler C 2012 Metal-Organic Hybrid Interface States of A Ferromagnet/Organic Semiconductor Hybrid Junction as Basis For Engineering Spin Injection in Organic Spintronics *Advanced Functional Materials* **22** 989–97

[176] Djeghloul F, Ibrahim F, Cantoni M, Bowen M, Joly L, Boukari S, Ohresser P, Bertran F, Le Fèvre P, Thakur P, Scheurer F, Miyamachi T, Mattana R, Seneor P, Jaafar A, Rinaldi C, Javaid S, Arabski J, Kappler J-P, Wulfhekel W, Brookes N B, Bertacco R, Taleb-Ibrahimi A, Alouani M, Beaurepaire E and Weber W 2013 Direct observation of a highly spin-polarized organic spinterface at room temperature *Scientific Reports* **3** 1272

[177] Barraud C, Bouzehouane K, Deranlot C, Fusil S, Jabbar H, Arabski J, Rakshit R, Kim D-J, Kieber C, Boukari S, Bowen M, Beaurepaire E, Seneor P, Mattana R and Petroff F 2015 Unidirectional Spin-Dependent Molecule-Ferromagnet Hybridized States Anisotropy in Cobalt Phthalocyanine Based Magnetic Tunnel Junctions *Physical Review Letters* **114** 206603

[178] Mallik S, Mohd A S, Koutsioubas A, Mattauch S, Satpati B, Brückel T and Bedanta S 2019 Tuning spinterface properties in iron/fullerene thin films *Nanotechnology* **30** 435705

[179] Mundlia S, Chaudhary S, Peri L, Bhardwaj A, Panda J J, Sasmal S and Raman K V 2020 Robust Monolayer Exchange-Bias Effect in Molecular Crane-Pulley Response at Magnetic Surface *Phys. Rev. Applied* **14** 024095

[180] Jo J, Byun J, Lee J, Choe D, Oh I, Park J, Jin M, Lee J and Yoo J 2020 Emergence of Multispinterface and Antiferromagnetic Molecular Exchange Bias via Molecular Stacking on a Ferromagnetic Film *Adv. Funct. Mater.* **30** 1908499

[181] Barraud C, Bouzehouane K, Deranlot C, Kim D J, Rakshit R, Shi S, Arabski J, Bowen M, Beaurepaire E, Boukari S, Petroff F, Seneor P and Mattana R 2016 Phthalocyanine based molecular spintronic devices *Dalton Transactions* **45** 16694–9

[182] Hirjibehedin C F 2006 Spin Coupling in Engineered Atomic Structures *Science* **312** 1021–4

[183] Ormaza M, Abufager P, Verlhac B, Bachellier N, Bocquet M-L, Lorente N and Limot L 2017 Controlled spin switching in a metallocene molecular junction *Nat Commun* **8** 1974

[184] Yan S, Choi D-J, Burgess J A J, Rolf-Pissarczyk S and Loth S 2015 Control of quantum magnets by atomic exchange bias *Nature Nanotech* **10** 40–5

[185] Khajetoorians A A, Wiebe J, Chilian B, Lounis S, Blügel S and Wiesendanger R 2012 Atom-by-atom engineering and magnetometry of tailored nanomagnets *Nature Phys* **8** 497–503

[186] Warner B, El Hallak F, Prüser H, Sharp J, Persson M, Fisher A J and Hirjibehedin C F 2015 Tunable magnetoresistance in an asymmetrically coupled single-molecule junction *Nature Nanotech* **10** 259–63

[187] Park B G, Wunderlich J, Martí X, Holý V, Kurosaki Y, Yamada M, Yamamoto H, Nishide A, Hayakawa J, Takahashi H, Shick A B and Jungwirth T 2011 A spin-valve-like magnetoresistance of an antiferromagnet-based tunnel junction *Nature Materials* **10** 347–51

[188] Sefrioui Z, Visani C, Calderón M J, March K, Carrétéro C, Walls M, Rivera-Calzada A, León C, Anton R L, Charlton T R, Cuellar F A, Iborra E, Ott F, Imhoff D, Brey L, Bibes M, Santamaria J and Barthélémy A 2010 All-Manganite Tunnel Junctions with Interface-Induced Barrier Magnetism *Adv. Mater.* **22** 5029–34

[189] Bruno F Y, Grisolia M N, Visani C, Valencia S, Varela M, Abrudan R, Tornos J, Rivera-Calzada A, Ünal A A, Pennycook S J, Sefrioui Z, Leon C, Villegas J E, Santamaria J, Barthélémy A and Bibes M 2015 Insight into spin transport in oxide heterostructures from interface-resolved magnetic mapping *Nat Commun* **6** 6306

[190] Shi J, Lopez-Dominguez V, Garesci F, Wang C, Almasi H, Grayson M, Finocchio G and Khalili Amiri P 2020 Electrical manipulation of the magnetic order in antiferromagnetic PtMn pillars *Nat Electron* **3** 92–8

[191] Nair N L, Maniv E, John C, Doyle S, Orenstein J and Analytis J G 2020 Electrical switching in a magnetically intercalated transition metal dichalcogenide *Nat. Mater.* **19** 153–7

[192] Moreno-Pineda E, Godfrin C, Balestro F, Wernsdorfer W and Ruben M 2018 Molecular spin qudits for quantum algorithms *Chem. Soc. Rev.* **47** 501–13

[193] Bellec A, Lagoute J and Repain V 2018 Molecular electronics: Scanning tunneling microscopy and single-molecule devices *Comptes Rendus Chimie* **21** 1287–99

[194] Karan S, García C, Karolak M, Jacob D, Lorente N and Berndt R 2018 Spin Control Induced by Molecular Charging in a Transport Junction *Nano Lett.* **18** 88–93

[195] Loth S, von Bergmann K, Ternes M, Otte A F, Lutz C P and Heinrich A J 2010 Controlling the state of quantum spins with electric currents *Nature Phys* **6** 340–4

[196] Zhang Y, Berger R and Butt H-J 2012 Dip-Pen Nanolithography *Encyclopedia of Nanotechnology* ed B Bhushan (Dordrecht: Springer Netherlands) pp 565–72

[197] Haynes C L and Van Duyne R P 2001 Nanosphere Lithography: A Versatile Nanofabrication Tool for Studies of Size-Dependent Nanoparticle Optics *The Journal of Physical Chemistry B* **105** 5599–611

[198] He Q, Cui X, Cui F, Guo L and Shi J 2009 Size-controlled synthesis of monodispersed mesoporous silica nano-spheres under a neutral condition *Microporous and Mesoporous Materials* **117** 609–16

[199] Schneider C A, Rasband W S and Eliceiri K W 2012 NIH Image to ImageJ: 25 years of image analysis *Nat Methods* **9** 671–5

[200] Abramoff M D, Magalhães P J and Ram S J 2004 Image processing with ImageJ *Biophotonics international* **11** 36–42

[201] Urbain E 2017 *Utilisation de semi-conducteurs organiques comme barrière tunnel pour l'électronique de spin* These de doctorat (Université de Strasbourg)

[202] Aliano A, Cicero G, Nili H, Green N G, García-Sánchez P, Ramos A, Lenshof A, Laurell T, Qi A, Chan P, Yeo L, Friend J, Evander M, Laurell T, Lenshof A, Laurell T, Chen J, Lacroix J C, Martin P, Randriamahazaka H, Barnes W Jon P, Hoogenboom B W, Fukuzawa K, Hölscher H, Hölscher H, Bottos A, Astanina E, Primo L, Bussolino F, Gao X, Phan V-N, Nguyen N-T, Yang C, Abgrall P, Barth F G, Gurman P, Rosen Y, Auciello O, Kähler C J, Cierpka C, Rossi M, Bhushan B, Palacio M L B and Dezelah C L 2012 Ab Initio DFT Simulations of Nanostructures *Encyclopedia of Nanotechnology* ed B Bhushan (Dordrecht: Springer Netherlands) pp 11–7

[203] Craciun A 2017 *AFM force spectroscopies of surfaces and supported plasmonic nanoparticules* These de doctorat (Université de Strasbourg)

[204] Horcas I, Fernández R, Gómez-Rodríguez J M, Colchero J, Gómez-Herrero J and Baro A M 2007 WSXM: A software for scanning probe microscopy and a tool for nanotechnology *Review of Scientific Instruments* **78** 013705

[205] Gehring P, Thijssen J M and van der Zant H S J 2019 Single-molecule quantum-transport phenomena in break junctions *Nat Rev Phys* **1** 381–96

[206] de Bruijckere J, Gehring P, Palacios-Corella M, Clemente-León M, Coronado E, Paaske J, Hedegård P and van der Zant H S J 2019 Ground-State Spin Blockade in a Single-Molecule Junction *Phys. Rev. Lett.* **122** 197701

[207] Yoshida K, Hamada I, Sakata S, Umeno A, Tsukada M and Hirakawa K 2013 Gate-Tunable Large Negative Tunnel Magnetoresistance in Ni–C60–Ni Single Molecule Transistors *Nano Lett.* **13** 481–5

[208] Xin N, Guan J, Zhou C, Chen X, Gu C, Li Y, Ratner M A, Nitzan A, Stoddart J F and Guo X 2019 Concepts in the design and engineering of single-molecule electronic devices *Nat Rev Phys* **1** 211–30

[209] Scott G D and Hu T-C 2017 Gate-controlled Kondo effect in a single-molecule transistor with elliptical ferromagnetic leads *Phys. Rev. B* **96** 144416

[210] Gauyacq J P and Lorente N 2011 Excitation of spin waves by tunneling electrons in ferromagnetic and antiferromagnetic spin- 1 2 Heisenberg chains *Phys. Rev. B* **83** 035418

[211] Baltz V, Manchon A, Tsoi M, Moriyama T, Ono T and Tserkovnyak Y 2018 Antiferromagnetic spintronics *Rev. Mod. Phys.* **90** 015005

[212] O'Grady K, Fernandez-Outon L E and Vallejo-Fernandez G 2010 A new paradigm for exchange bias in polycrystalline thin films *Journal of Magnetism and Magnetic Materials* **322** 883–99

[213] Schleicher F, Studniarek M, Kumar K S, Urbain E, Katcko K, Chen J, Frauhammer T, Hervé M, Halisdemir U, Kandpal L M, Lacour D, Riminucci A, Joly L, Scheurer F, Gobaut B, Choueikani F, Otero E, Ohresser P, Arabski J, Schmerber G, Wulfhekel W, Beaurepaire E, Weber W, Boukari S, Ruben M and Bowen M 2018 Linking Electronic Transport through a Spin Crossover Thin Film to the Molecular Spin State Using X-ray Absorption Spectroscopy Operando Techniques *ACS Appl. Mater. Interfaces* **10** 31580–5

[214] Djeghloul F, Gruber M, Urbain E, Xenioti D, Joly L, Boukari S, Arabski J, Bulou H, Scheurer F, Bertran F, Le Fèvre P, Taleb-Ibrahimi A, Wulfhekel W, Garreau G, Hajjar-Garreau S, Wetzel P, Alouani M, Beaurepaire E, Bowen M and Weber W 2016 High Spin Polarization at Ferromagnetic Metal–Organic Interfaces: A Generic Property *J. Phys. Chem. Lett.* **7** 2310–5

[215] Boukari S, Ghaddar A, Henry Y, Arabski J, Da Costa V, Bowen M, Le Moigne J and Beaurepaire E 2007 Electrical transport across a structurally ordered phthalocyanine film: Role of defect states *Phys. Rev. B* **76** 033302

[216] Tong J, Ruan L, Yao X, Qin G and Zhang X 2019 Defect states dependence of spin transport in iron phthalocyanine spin valves *Phys. Rev. B* **99** 054406

[217] Fourmental C, Bellec A, Repain V, Lagoute J, Chacon C, Girard Y, Rousset S, Dappe Y J, Vlad A, Resta A, Garreau Y and Coati A 2019 Deep metallic interdiffusion in a model ferromagnetic/molecular system *Phys. Rev. Materials* **3** 083603

[218] Raman K V, Kamerbeek A M, Mukherjee A, Atodiresei N, Sen T K, Lazić P, Caciuc V, Michel R, Stalke D, Mandal S K, Blügel S, Münzenberg M and Moodera J S 2013 Interface-engineered templates for molecular spin memory devices *Nature* **493** 509–13

[219] Mallik S, Mattauch S, Dalai M K, Brückel T and Bedanta S 2018 Effect of magnetic fullerene on magnetization reversal created at the Fe/C60 interface *Sci Rep* **8** 5515

[220] Bairagi K, Bellec A, Repain V, Fourmental C, Chacon C, Girard Y, Lagoute J, Rousset S, Le Laurent L, Smogunov A and Barreteau C 2018 Experimental and theoretical investigations of magnetic anisotropy and magnetic hardening at molecule/ferromagnet interfaces *Phys. Rev. B* **98** 085432

[221] Moorsom T, Alghamdi S, Stansill S, Poli E, Teobaldi G, Beg M, Fangohr H, Rogers M, Aslam Z, Ali M, Hickey B J and Cespedes O 2020 π -anisotropy: A nanocarbon route to hard magnetism *Phys. Rev. B* **101** 060408

[222] Studniarek M, Cherifi-Hertel S, Urbain E, Halisdemir U, Arras R, Taudul B, Schleicher F, Hervé M, Lambert C-H, Hamadeh A, Joly L, Scheurer F, Schmerber G, Da Costa V, Warot-Fonrose B, Marcelot C, Mauguin O, Largeau L, Leduc F, Choueikani F, Otero E, Wulfhekel W, Arabski J, Ohresser P, Weber W, Beaurepaire E, Boukari S and Bowen M 2017 Modulating the Ferromagnet/Molecule Spin Hybridization Using an Artificial Magnetoelectric *Adv. Funct. Mater.* **27** 1700259

[223] Grimme S, Antony J, Ehrlich S and Krieg H 2010 A consistent and accurate ab initio parametrization of density functional dispersion correction (DFT-D) for the 94 elements H-Pu *The Journal of Chemical Physics* **132** 154104

[224] Grimme S, Ehrlich S and Goerigk L 2011 Effect of the damping function in dispersion corrected density functional theory *Journal of Computational Chemistry* **32** 10

[225] Bučko T, Hafner J, Lebègue S and Ángyán J G 2010 Improved Description of the Structure of Molecular and Layered Crystals: Ab Initio DFT Calculations with van der Waals Corrections *J. Phys. Chem. A* **114** 11814–24

[226] Bengone O, Alouani M, Blöchl P and Hugel J 2000 Implementation of the projector augmented-wave LDA+U method: Application to the electronic structure of NiO *Phys. Rev. B* **62** 16392–401

[227] MacLaren J M, Schulthess T C, Butler W H, Sutton R and McHenry M 1999 Electronic structure, exchange interactions, and Curie temperature of FeCo *Journal of Applied Physics* **85** 4833–5

[228] Javaid S, Bowen M, Boukari S, Joly L, Beaufrand J-B, Chen X, Dappe Y J, Scheurer F, Kappler J-P, Arabski J, Wulfhekel W, Alouani M and Beaurepaire E 2010 Impact on Interface Spin Polarization of Molecular Bonding to Metallic Surfaces *Physical Review Letters* **105** 077201

[229] Deshmukh M M, Kleff S, Guéron S, Bonet E, Pasupathy A N, von Delft J and Ralph D C 2001 Magnetic Anisotropy Variations and Nonequilibrium Tunneling in a Cobalt Nanoparticle *Phys. Rev. Lett.* **87** 226801

[230] Misiorny M, Hell M and Wegewijs M R 2013 Spintronic magnetic anisotropy *Nature Phys* **9** 801–5

[231] Pan W, Jih N-Y, Kuo C-C and Lin M-T 2004 Coercivity enhancement near blocking temperature in exchange biased Fe/FexMn1−x films on Cu(001) *Journal of Applied Physics* **95** 7297–9

[232] Verlhac B, Bachellier N, Garnier L, Ormaza M, Abufager P, Robles R, Bocquet M-L, Ternes M, Lorente N and Limot L 2019 Atomic-scale spin sensing with a single molecule at the apex of a scanning tunneling microscope *Science* **366** 623–7

[233] Chowrira B, Kandpal L, Mertz D, Kieber C, Joly L, Monteblanco E, Bahouka A, Vileno B, Bernard R, Garcia H P, Elidrissi S, Gavara M, Sternitzky E, Costa V D, Hehn M, Montaigne F, Choueikani F, Ohresser P, Lacour D, Weber W, Boukari S and Bowen M 2020 Spintronic harvesting of thermal fluctuations on paramagnetic molecular centers around a phase transition *arXiv:2009.10413v2, *The first two authors contributed equally*

KANDPAL Lalit Mohan

Localized States in the Spacer Layer of Spintronic Nanodevices

Résumé en français

L'effet de couple de transfert de spin (STT) permet de coder l'information magnétiquement en appliquant un courant d'entrée de haute densité. Cela fait du STT l'une des techniques les plus prometteuses pour réaliser des mémoires magnétiques à accès aléatoire (MRAM). Il a été rapporté que même pour la barrière de tunnel MgO la plus fine, la densité de courant requise pour piloter le mécanisme STT dans une jonction tunnel magnétique (MTJ) ne peut être atteinte que si la hauteur de la barrière est bien inférieure à celle du MgO intrinsèque. Les calculs ab-initio combinés aux expériences ont révélé que cette réduction de la hauteur de la barrière est due aux vacances d'oxygène situées dans la barrière de tunnel du MgO. Nous avons caractérisé le paysage énergétique exact des vacances d'oxygène situées dans la barrière de tunnel du MgO et étudié leur impact sur le STT. Nous avons étendu nos études aux dispositifs nanospintroniques organiques fabriqués à l'aide d'une technique de nanolithographie développée en interne, appelée "traitement des nanobilles", et avons démontré avec succès leur potentiel pour l'application de codage de l'information.

Mots clés : Couple de transfert de spin, lacunes d'oxygène, mémoires magnétiques à accès aléatoire, jonctions tunnel magnétiques, nanolithographie, traitement des nanobilles, codage de l'information, spintronique organique

Summary in English

The spin transfer torque (STT) effect allows one to encode the information magnetically by applying an input current of high density. This makes STT as one of the promising techniques to realize the magnetic random-access memories (MRAMs). It has been reported that even for the thinnest MgO tunneling barrier the current density required to drive the STT mechanism in a magnetic tunnel junction (MTJ) can only be achieved if the barrier height is far below to that of the intrinsic MgO. Ab-initio calculations combined with experiments revealed that this reduction in the barrier height is due to the oxygen vacancies lying within the MgO tunneling barrier. We characterized the exact energetic landscape of the oxygen vacancies lying within the MgO tunneling barrier and studied their impact on STT. We further extended our studies on organic nanospintronic devices crafted using an in-house developed nanolithography technique called 'nanobead processing', and successfully demonstrated their potential for the information encoding application.

Keywords : Spin transfer torque, oxygen vacancies, magnetic random-access memories, magnetic tunnel junctions, nanolithography, nanobead processing, information encoding, organic spintronics